Universidad Pública de Navarra
Nafarroako Unibertsitate Publikoa

Universidad Pública de Navarra
Electric and Electronical Engineering department

Contributions to the development of Brillouin distributed sensors for structural health monitoring

PhD Dissertation by

Jon Mariñelarena Ollacarizqueta

Advisor

Alayn Loayssa Lara

Pamplona, July 2019

Agradecimientos / Acknowledgements

Ante todo, a mi familia, Enrique, Mari Jose y Mikel, que siempre habéis confiado en mí a pesar de poner objetivos un poquito exigentes. También a Fabiola y Lorea, que han conseguido hacer más fácil este largo e intenso proceso gracias a su incondicional apoyo y positiva presencia. Gracias por haberos preocupado y alegrado en tantos duros e intensos días de trabajo, ya que sin vosotros este trabajo no hubiera sido lo mismo.

A mis compañeros y amigos de fatigas, Juanjo y Javi, que desde un principio me habéis resuelto tantas dudas sobre el papel y pizarra, en el despacho y en el laboratorio, y hasta alguna que otra vez de viaje y con una cerveza en la mano. Gracias por tantas risas y bromas Juanjo, muchas de ellas absurdas y frikis, pero que en realidad alegraban y suavizaban las tensiones del trabajo. A pesar de que estos últimos meses me has visto menos por el despacho, todo tiene un por qué..., echaré mucho de menos la alegría y salero que le pones a la vida. Así que, ¡no cambies, sigue así!

A todos los que hemos compartido numerosas horas de trabajo en el laboratorio, despacho y/o conferencias: Haritz, Dani, Mikel, Santi, Aitor, Verónica, Aitor J., Manolo, Rosana y un largo etcétera. En especial a tí Rosana, que en muchas ocasiones me has escuchado y ayudado mientras hablábamos y relajábamos tomando alguna cerveza, té o vermut después de las largas horas de trabajo. Gracias en general a todo el grupo de Comunicaciones Ópticas por permitirme disfrutar de los buenos momentos pasados en los congresos a los que hemos asistido por distintos países y continentes del mundo: Brasil, Corea del Sur, Irlanda, Suiza, Estados Unidos...

Gracias también a Nerea y Diego en esta recta final del doctorado. Vuestra compañía a la hora de comer, junto con la de Juanjo, han sido un punto de inflexión en cada día de trabajo, ya que a pesar de que hubiera mucho que escribir, casi siempre hemos tenido ese tiempo justo y necesario para las carcajadas y piques sanos entre unos y otros.

A special thanks is expressed to Proffesor Kwang Yong Song, who was my advisor during three and half months at the Chung-Ang University of Seoul. I was delighted with your kind attention and warm hospitality during my stay in Korea. I thank you for teaching me about BOCDA systems and Korean culture. It was a wonderful pleasure to visit Korea and have the chance to travel in so different and gorgeous country. A special thanks is expressed also to Yong Hyun, who was a really good friend from the first to the last day, who helped me with all the Korean paperwork that was required to live there during three months. I wish we could see some day in Spain. Thanks as well to the rest of my collegues and friends in the Chung-Ang laboratory: Che-Ho and Hyung Joon.

Además, quiero agradecer a las instituciones que han permitido que esta tesis se pudiese desarrollar: Universidad Pública de Navarra a través del programa de ayudas para la formación de personal investigador y ayudas a la movilidad; Ministerio de economía y competitividad a través de los proyectos TEC2013-47264-C2-2-R y TEC2016-76021-C2-1-R; Gobierno de Navarra-Departamento de Desarrollo Económico por los proyectos I-SEN 0011-1365-2016-00069 y WINSOLAR 0011-1365-2017-000122.

Finalmente, y con un agradecimiento muy especial, a Alayn, quien ha sido un gran director de tesis y ha sabido transmitir su amplio conocimiento en comunicaciones ópticas y principalmente en los sensores distribuidos Brillouin. Muchas gracias por tu aportación, ya que el resultado de esta tesis viene en parte dado gracias a tus habilidades como profesor e investigador, nivel de exigencia y gusto por el buen hacer de las cosas. Muchas gracias por el asesoramiento, enseñanzas y consejos, tanto dentro como fuera del trabajo.

Pamplona, July 2019

Jon Mariñelarena

Abstract

Distributed optic fiber sensors (DOFS) are a very interesting technology for industrial monitoring applications due to their capability of performing measurements that provide a multitude of measurement positions along a sensing fiber. Among the DOFS, those based on stimulated Brillouin scattering (SBS) are especially interesting due to the possibility of measuring temperature and strain simultaneously. In particular, Brillouin optical time-domain analysis (BOTDA) sensor is one of the most developed and studied Brillouin-based DOFS due to their capability of performing long-range measurements of temperature and strain with high spatial resolution. Moreover, they can also provide very fast measurements in short length of fibers. During the last years there have been many important advancements in improving the BOTDA performance by proposing techniques to enhance their accuracy, measurement range, spatial resolution, and acquisition time. However, there are constraints that still limit the performance of these sensors. This thesis has been focused on overcoming several of these constraints.

Firstly, a technique has been developed to mitigate the non-local effects related to the limited extinction ratio of pump pulses, which induce important detrimental effects and errors in the measurement results. This method is based on the dithering of the light source used to generate the pump and the probe waves in BOTDA sensors. Another contribution that improves the BOTDA sensors performance has been presented to mitigate an unsolved issue when they deploy pump pulse coding techniques. The problem lies on the nonlinear amplification experienced by the probe wave when long sequences of pulses are used. This solution is based on a simple post-processing calculation performed on the detected signal.

Similarly, this thesis has contributed also to the enhancement of dynamic BOTDA sen-

sors, especially, the self-heterodyne detection BOTDA sensors. This particular technique, which is based on a phase-modulated probe wave and coherent detection, has been studied in detailed. A theoretical and experimental study is presented in this thesis where the dependence of the detected radiofrequency phase-shift spectrum on large Brillouin gain variations is analyzed. Then, the limitation of the dynamic range of these sensors is investigated. In order to overcome this constraint, two different methods are investigated and presented. One of them is based on the pulse-shortening method and the second one relies on the generation of multiple frequency components of the pump pulses.

Another important type of DOFS based on SBS are the Brillouin optical correlation-domain analysis sensors, whose particular advantage lies on the high spatial resolution they provide and the possibility of the random access to the measuring position along the sensing fiber. As in BOTDA sensors, multiple limitations and constraints have been overcome during the last years, although, there are others that still limit their performance. In this thesis, research has been carried out to solve the limitation of the maximum amplitude of the frequency modulation (FM) that can be deployed to modulate the light source in linearly-configured BOCDA (LC-BOCDA) sensors. This problem has been addressed and overcome deploying an alternative setup based on a dual-probe wave and a control of the correlation order. The proposed method has demonstrated the possibility of extending the FM amplitude, and thus, the number of resolving points and spatial resolution of the LC-BOCDA.

Finally, this thesis has contributed to close the gap between research and practical applications of Brillouin distributed sensors. In this sense, a monitoring system to monitor the effects of wind on photovoltaic solar trackers has been developed. This novel measuring system has demonstrated, for the first time, distributed measurements of bending and torsional strain along the beams that made these structures. A particular layout for the deployment of the optical fiber has been devised. Experimental measurements are performed in the laboratory facilities demonstrating dynamic measurements of strain along a solar tracker beam and an in-field installation of the measuring system has been carried out in a solar plant.

Contents

List of Figures

List of Tables

List of acronyms

AWG	Arbitrary waveform generator
ASE	Amplified spontaneous emission
BFS	Brillouin frequency shift
BGS	Brillouin gain spectrum
BOCDA	Brillouin optical coherent-domain analysis
BOCDR	Brillouin optical coherent-domain reflectometry
BOFDA	Brillouin optical frequency-domain analysis
BOFDR	Brillouin optical frequency-domain reflectometry
BOTDA	Brillouin optical time-domain analysis
BOTDR	Brillouin optical time-domain reflectometry
CW	Continuous wave
CP	Correlation peak
DBA	Distributed Brillouin amplifier
D-BOTDA	Dynamic-BOTDA
DC	Direct current
DFB	Distributed feedback laser
DOFS	Distributed optical fiber sensors
DPP	Differential pulse-width pair
DSA-BOTDA	Double-slope-assisted BOTDA
DSB-SC	Double-sideband suppressed-carrier
EDFA	Erbium doped-fiber amplifier
ER	Extinction ratio
FBG	Fiber Bragg grating
FM	Frequency modulation
FWM	Four wave mixing

FWHM	Full-width half-maximum
LC-BOCDA	Linearly-configured BOCDA
LD	Laser diode
LIA	Lock-in amplifier
IM	Intensity modulation
MI	Modulation instability
MSS	Microwave sweep synthesizer
MZ-EOM	Mach Zehnder-Electrooptic modulator
NLE	Non-local effects
OFDR	Optical Frequency Domain Reflectometry
PD	Photo-detector
PS	Polarization scrambler
PSW	Polarization switch
PV	Photovoltaic
RF	Radiofrequency
SA-BOTDA	Slope-assisted BOTDA
SBS	Stimulated Brillouin scattering
SMF	Single mode fiber
SNR	Signal-to-noise ratio
SOA	Semiconductor optical amplifier
SOP	State-of-polarization
SPM	Self-phase modulation
SpBS	Spontaneous Brillouin scattering
SSB-SC	Single-sideband suppressed-carrier

CHAPTER 1

Introduction to the thesis

1.1. Motivation of the thesis

It is already more than forty years that optical fibers are being used for sensing applications apart from their common optical communication purposes. Since it was found that multiple physical quantities such as strain, temperature, magnetic and electric field, gas concentration, humidity, etc., could be monitored by the effect that these measurands induce on the propagation of the light along the fiber, the research and development on this technology has been continuously growing. Compared to conventional sensing technologies, optical fiber sensors offer numerous advantages such as small size, a very wide operating range, installation simplicity, multiplexing capabilities, etc. Moreover, optical fiber consists in a dielectric material, offering the advantage of being a suitable material for measurement in harsh environments prone to be affected by electromagnetic interference. Therefore, thanks to the great capability of detecting a wide range of measurands by simply using an optical fiber cable, optical fiber sensing has become in a very valuable and competitive technology for monitoring in numerous applications where other technologies are not suitable or cannot be deployed.

Among the different optical fiber sensors developed during the last decades, there are point sensors, such as fiber fiber Bragg grating (FBG) or interferometric sensors, and distributed fiber sensors. The main difference between these two type of sensors is that point sensing employs all the fiber link, from the sensing position to the sensor interrogator,

as a light propagation medium to bring the light signal to the desired location, whereas distributed optical fiber sensors (DOFS) deploy the fiber link as multiple and distributed sensing elements. The great capability of using the optical fiber as a sensing element allows distributed optical fiber sensors to provide information of the measurand at each location of an optical fiber. This technology has demonstrated very good performance and, in addition, allows to replace thousands of the conventional discrete sensors. As a result, a reduction of the overall cost of the monitoring network and its maintenance is achieved, as well as a reduction of the installation complexity. DOFS also allows the monitoring in remote inhospitable and isolated locations thanks to the large range of their measurements.

DOFS are based on different kinds of scattering phenomena such as Raman, Rayleigh or Brillouin scattering. Among the different sensors based on the scattering phenomena, those based on stimulated Brillouin scattering (SBS) are of great interest. Brillouin-based DOFS have centered the attention of many researchers during the last years with significant and multiple contributions to overcome their limitations and enhance their performance. With this technology, resolutions in the millimeter range can be achieved in short length of fibers. Moreover, Brillouin sensors stand out due to their capability of performing long range and fast measurements, since measurements over more than 100 km have been achieved and dynamic measurements at kHz-range in optical fibers of several kilometers have been successfully performed.

As a result of the community research work and the increasing interest and effort of diverse industries on developing and implementing these type of monitoring systems in industrial applications, DOFS are currently being deployed in applications like:

- Structural health monitoring in: buildings, dams, railways, bridges, aircraft wings, ships, etc.
- Temperature monitoring for: fire alarm systems, electric power supply cables monitoring, etc.
- Leakage detection in: water, oil or gas pipelines.
- Smart structures: embedded sensors in composite to monitor the state of materials.

The multiple and important applications that require Brillouin-based sensors along with the interest of other industries to install this type of monitoring systems are the main motivation to further improve their performance.

1.2. Objectives of the PhD thesis

The main objectives of this thesis is to contribute to the enhancement of the performance of DOFS based on SBS by analyzing their limitations and proposing solutions to overcome their current constraints. The dissertation has been focused on improving different aspects of dynamic and static Brillouin optical time-domain analysis (BOTDA) and Brillouin optical coherent-domain analysis (BOCDA) sensors. Moreover, this research work has tried to contribute to reduce the existing gap between the investigation of DOFS and their industrial applications, demonstrating the capability of these sensors to provide efficient and valuable measurements in real application scenarios.

In particular, the objectives of this dissertation are:

- Enhance the signal-to-noise ratio (SNR) constraints faced by of BOTDA sensors by proposing alternative setups or post-processing solutions to achieve better performance.
- Analyze and study the dynamic self-heterodyne detection BOTDA sensor recently presented by our research group to try to improve its performance by proposing solutions to their constraints and alternative setups.
- Research on the limitations of a particular single-ended access BOCDA sensor setup with the aim of enhancing its performance.
- Design, develop and implement novel measuring systems to deploy the investigated DOFS in real applications and demonstrate their capabilities.

1.3. Structure of the thesis

The contents of this dissertation are divided in six chapters.

The first chapter contains an introduction to the Brillouin scattering phenomena and, in particular, to SBS, with the aim of explaining the working principle of this effect. Then, the two most important methods deployed to perform distributed optical fiber measurements are described: BOTDA and BOCDA sensors. Finally, a summary of their limiting factors and a state of the art for both techniques are introduced.

The second chapter starts with a brief explanation to one of the most limiting effects in BOTDA sensors, the non-local effects (NLE). First and second-order NLE are presented along with several solutions that have been demonstrated in the last years to mitigate them. Then, a more detailed explanation of a recently presented NLE is given. Then, a

technique that allows to overcome the constraints imposed by NLE is presented, allowing to enhance the SNR in BOTDA sensors.

In the third chapter, a simple solution to solve the impairments faced by BOTDA sensors that deploy coding technique with long codewords is presented. This is based on a simple post-processing calculation applied to the detected signal.

In the fourth chapter, the dynamic self-heterodyne detection BOTDA sensor based on a phase-modulated probe wave is studied and enhanced. Firstly, the dependence of this measuring system on large Brillouin gain variations is investigated and compared to the dependence of direct-detection BOTDA systems. Then, the dynamic range limitation of these systems is studied, and two alternative schemes are proposed to enlarge the dynamic range of self-heterodyne detection BOTDA sensors.

Chapter five presents a design, development and implementation of a monitoring system that has allowed to dynamically monitor the effects of wind over the photovoltaic (PV) solar tracker structures. In particular, a mechanical study to devise the fiber optic installation and measurement process to obtain bending and torsional strain in beams is accomplished. Finally, an in-field installation of the monitoring system in a solar plant is shown.

In the sixth chapter a brief introduction to BOCDA sensors is given along with some of the main advancements presented since they were first devised. Then, the a limitation of a particular linearly-configured BOCDA (LC-BOCDA) sensor is studied and a solution is proposed to mitigate the impairments and enhance the performance.

To conclude, a summary chapter where the main conclusions of the different research works accomplished during this thesis is presented along with the open lines of this thesis.

CHAPTER 2

Distributed optical fiber sensors based on Brillouin scattering

DOFS are playing an essential role in many structural health monitoring applications since they were presented for the first time more than 30 years ago [1]. The possibility of using an optical fiber as a sensing element allows the user to retrieve remotely the measurand information at each position of the optical fiber. This special feature makes DOFS a powerful measuring system in comparison to traditional sensors that provide the physical parameter of interest in only one location.

DOFS rely on one or more of the Rayleigh, Raman and Brillouin scattering effects. The scattering of the incident light wave can be originated in an optical fiber by fluctuations of the optical properties of the medium caused by the interaction with inhomogeneities in the material, molecular vibration or acoustic waves generated in the medium. The latter, for example, induces the Brillouin scattering effect, in which part of the incident light is scattered due to local variations of the refractive index that appear along the fiber. Depending on the scattering effect used for sensing, the sensor allows to measure different physical quantities such as temperature or strain. For instance, Brillouin scattering process offers the capability of retrieving either temperature and strain of the sensing fiber, while Raman scattering only allows to obtain temperature variations. Among the Brillouin scattering processes, two different types can be distinguished, the spontaneous Brillouin scattering (SpBS) and SBS. In this thesis, the research work is especially focused on the study of those sensors based on the stimulated generation of the Brillouin scattering.

In this sense, this chapter briefly introduces the basics of the Brillouin scattering and the SBS effect in order to gain a better understanding of the fundamentals of

Brillouin-based DOFS. Then, different types of sensors that rely on the latter scattering process are introduced along with the main features and limiting factors that constrain the performance of these sensors. In particular, a more detailed explanation will be given for BOTDA and BOCDA configurations, which are the measuring systems that have been studied during this thesis research.

2.1. Stimulated Brillouin scattering in optical fiber

Brillouin scattering is an inelastic scattering process in which the incident light is scattered from acoustic waves, that is, from propagating density waves. In particular, SpBS is originated in optical fibers when an incident light wave, called pump wave, propagates through the fiber interacting with thermally driven material-density fluctuations that travel at the speed of sound v_a [2]. Due to the thermal agitation, the moving acoustic wave generates a periodic perturbation of the refractive index in the fiber, modulating the index as a moving Bragg grating. Then, a small portion of the incident light is scattered through Bragg diffraction. This scattered light can emerge at either lower or higher frequency than the incident light. If the scattered light emerges at a lower frequency it is known as Stokes scattering, while if the scattered light emerges at higher frequency than the incident waveis called anti-Stokes scattering [3]. The frequency shift between the scattered light and the incident wave is the Brillouin frequency shift (BFS), given by:

$$\nu_B = \frac{2nv_a}{\lambda_p} \tag{2.1}$$

where λ_p is the wavelength of the pump wave and n is the refractive index of the fiber.

Figure 2.1 (a) depicts a schematic description of the generation of SpBS effect in an optical fiber that is originated by simply launching the pump wave from one end of the fiber. However, under some particular conditions, such as the deployment of high optical power level or the interaction of two counter-propagating optical signals, this scattering process can be stimulated and becomes more intense, giving rise to the nonlinear phenomena known as SBS, which is schematically represented in Fig. 2.1 (b).

SBS is described as a nonlinear interaction between two optical waves, the pump wave and the Stokes wave, and an acoustic wave [5]. The SBS effect occurs when the pump and Stokes waves are counter-propagated in an optical fiber, where they interact and generate an acoustic wave through electrostriction process, which is the tendency of dielectric materials to compress and become denser in those areas where an electric field is applied [3]. In this process, the acoustic wave also propagates at a velocity v_a, generating

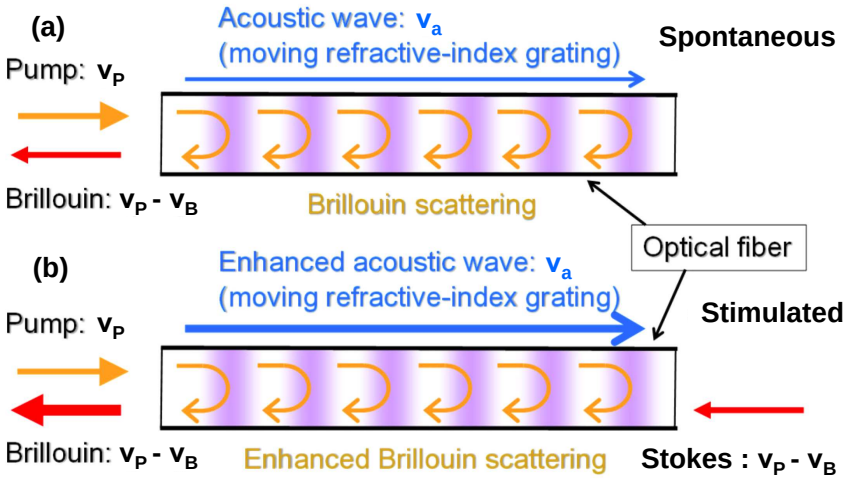

Figure 2.1: Brillouin scattering effect along an optical fiber: (a) Spontaneous Brillouin scattering and (b) stimulated Brillouin scattering. © 2019, Appl. Sci. [4].

a periodic perturbation on the refractive index. Then, part of the incident pump wave is transferred through Bragg diffraction to the Stokes wave, shifting the frequency of the transferred light to lower frequencies due to Doppler effect and the acoustic wave velocity. The transfer of power between both waves gives rise to an amplification of the Stokes wave, that simultaneously strengths the acoustic wave that further stimulates the SBS process. As a result of this interaction, the Stokes wave experiences a power amplification and the pump wave experiences depletion.

From the point of view of the quantum mechanics, SBS consist in the destruction of a pump photon to create simultaneously a Stokes photon and an acoustic phonon. The three waves must fulfill the energy conservation condition relating their frequencies:

$$\omega_a = \omega_P - \omega_S \tag{2.2}$$

and the conservation of the momentum:

$$k_a = k_P - k_S \tag{2.3}$$

where the sub-indexes a, P and S are referred to the acoustic, the pump and the Stokes waves respectively. It is important to remark that the acoustic wave is efficiently generated when the Stokes wave counter-propagates with the pump and their frequency difference is near the BFS of the optical fiber, ν_B, giving rise to a reinforced scattering process and

higher transfer of power to the Stokes wave.

Coupled-wave equations for SBS

As explained, the SBS process relies on the interaction of two counter-propagating optical waves, the pump and the Stokes wave (from now on called probe wave), $E_P(z,t)$ and $E_S(z,t)$, and the acoustic wave, $Q(z,t)$. The propagation of these three waves can be modeled (under the assumption of plane-wave interaction) by the following system of coupled equations [3]:

$$\left[\frac{\partial}{\partial z}+\frac{n}{c}\frac{\partial}{\partial t}+\alpha_P\right]E_P\left(z,t\right)=\frac{i\omega_P\gamma_e}{2nc\rho_0}QE_S(z,t) \tag{2.4a}$$

$$\left[-\frac{\partial}{\partial z}+\frac{n}{c}\frac{\partial}{\partial t}+\alpha_S\right]E_S\left(z,t\right)=\frac{i\omega_S\gamma_e}{2nc\rho_0}Q^*E_P(z,t) \tag{2.4b}$$

$$\left[-2iqv_a^2\frac{\partial}{\partial z}-2i\Omega\frac{\partial}{\partial t}+\left(\Omega_B^2-\Omega-i\Omega\Gamma_B\right)\right]Q(z,t)=\epsilon_0\gamma_e q^2E_P(z,t)E_S^*(z,t) \tag{2.4c}$$

where c is the light velocity in vacuum, γ_e is the electrostrictive constant, ϵ_0 is the dielectric permittivity in the vacuum, ρ_0 is the density of the medium, Γ_B is the phonon decay rate and q its wave vector and Ω is the frequency of the acoustic wave. While ω_P and ω_S are the pump and probe wave frequencies, respectively; α_P and α_P are the respective attenuation coefficients for the pump and the probe wave. In single mode fiber (SMF) the typical attenuation value is $\alpha = 4.6\cdot10^{-5}$ Neper/m ($\alpha \approx$0.2 dB/km) [5].

An expression to represent the evolution of the probe wave $E_S(z,t)$ when it is subjected to SBS interaction is derived solving the three-wave equations system using the steady-state approach. The deducted expression will be then deployed for the study of the different types of Brillouin-based distributed sensors. Firstly, it is considered that the interaction time between probe and pump waves is longer than the acoustic phonon lifetime (τ_p), so, the steady-state approach is assumed and, all time derivatives can be neglected. Then, the acoustic wave is considered as a static wave due to its lower velocity with respect to light velocity, vanishing after propagation over a few optical wavelengths. Consequently the spatial derivative in Eq. (2.4c) is set equal to zero. Considering that the optical frequencies of pump and probe waves are in similar range, their attenuation can be taken approximately equal as well, $\alpha = \alpha_S \approx \alpha_P$. Then, defining the intensity as $I(z) = 2n\epsilon_0 c|E(z)|^2$, the coupled intensity equations for the pump and probe signals can be expressed as [3, 5]:

$$\frac{d}{dz}I_P(z) = -g_B(\Delta\nu)I_P(z)I_S(z) - \alpha I_P(z) \tag{2.5a}$$

$$\frac{d}{dz}I_S(z) = -g_B(\Delta\nu)I_P(z)I_S(z) + \alpha I_S(z) \tag{2.5b}$$

where I_P and I_S are the intensities of the pump and probe waves, respectively, and $g_B(\Delta\nu)$ represents the Brillouin gain coefficient for the probe wave due to its SBS interaction with the pump wave, which depends on the frequency detuning of the probe frequency from the BFS, $\Delta\nu$. Notice that the SBS interaction exhibits a frequency dependence, increasing the energy transfer from the pump to the probe wave for detuning frequencies near the BFS of the optical fiber. As it will be explain in next section, this frequency dependence of the SBS effect, along with the BFS dependence on the temperature and strain, allows Brillouin-based sensors to retrieve the distribution of measurands along the optical fiber, and indeed, perform distributed measurements.

In the following expression, the function of the Brillouin gain coefficient, $g_B(\Delta\nu)$, is represented for an incident pump wave, which shows a Lorentzian dependence [5]:

$$g_B(\Delta\nu) = g_0 \frac{(\Delta\nu_B/2)^2}{\Delta\nu^2 + (\Delta\nu_B/2)^2}. \tag{2.6}$$

where $\Delta\nu_B$ is the Brillouin gain linewidth and g_0 is the Brillouin gain coefficient, given by [3]:

$$g_0 = \frac{\gamma_e^2\omega^2}{n v_a c^3 \rho_0 \Gamma_B}, \tag{2.7a}$$

$$\Delta\nu_B = \frac{1}{2\pi\tau_p}, \tag{2.7b}$$

These two parameters, g_0 and $\Delta\nu_B$, along with the BFS, ν_B, characterize the Brillouin gain given in Eq. (2.6). The typical values in 1550 nm band for SMF fibers are $g_0 \approx 2.5 \cdot 10^{-11}$ m/W, $\nu_B = 11$ GHz, and $\Delta\nu_B = 30$ MHz [3].

Figure 2.2 depicts the Brillouin gain amplitude and phase-shift spectra with respect to the frequency detuning. Notice that, not only the magnitude of the stimulated Brillouin amplification is frequency dependent, but also its phase, which shows a sharp transition at the line center, as highlighted in Fig. 2.2 (b).

In order to obtain an expression for the intensity probe wave at a given location in the fiber after its interaction with the pump wave, Eq. (2.5b) is solved assuming that no

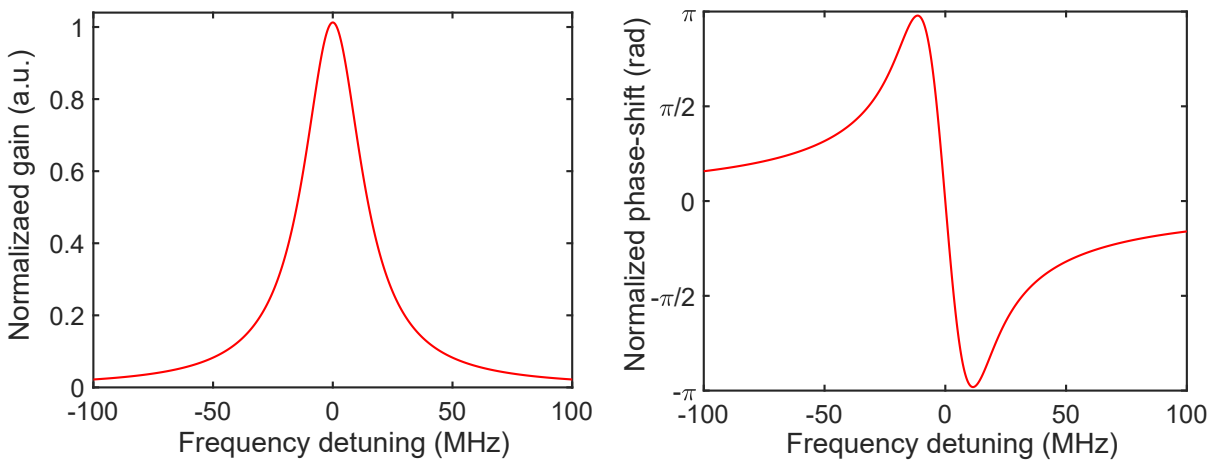

Figure 2.2: Magnitude (a) and phase (b) of the Lorentzian shaped Brillouin spectrum in a regular silica optical fiber. A FWHM of 30MHz is assumed

depletion is observed on the pump wave. This means that the pump wave only experiences the attenuation due to the propagation in the fiber, so that, its intensity exponentially decays along the fiber as follows $I_P(z) = I_{P_{in}} e^{-\alpha z}$, being $I_{P_{in}}$ the intensity at the input of the fiber ($z = 0$). Then, substituting the pump wave expression in Eq. (2.5b), and assuming constant distribution of BFS along the fiber, the intensity of the probe wave at position z can be expressed as:

$$I_S(z) = I_{S_{in}} exp\big[-\alpha(L-z)\big] exp\Big[g_B(\Delta\nu) I_{P_{in}} L_{eff}\Big] \tag{2.8}$$

where $I_{S_{in}}$ is the injected optical intensity of the probe wave at the far end of the fiber, from where the pump wave is injected ($z = L$). While L_{eff} is the effective length of the optical fiber parameter, which is defined as [5]:

$$L_{eff} \equiv \frac{1 - \exp\big(-\alpha(L-z)\big)}{\alpha} \tag{2.9}$$

From Eq. (2.8) is observed that the probe wave intensity increases exponentially with distance due to SBS along its propagation. At the same time, the probe intensity is attenuated due to the absorption coefficient of the optical fiber. Observe that, in order to obtain the expression for $I_S(z)$, it has been assumed a backward direction of propagation of the probe, starting from $z = L$ and ending at $z = 0$.

SBS threshold

As observed in Eq. (2.8), the probe intensity follows an exponential increment as it propagates along the optical fiber, basically due to the Brillouin amplification that occurs as a result of the commented SBS process. However, as explained before, in absence of the incident probe wave, the Stokes wave can grow spontaneously from Brillouin scattering, which is generated by thermal agitation of the medium by the pump wave injected in the fiber. If the incident pump power is high, the Stokes components can start to act as a counter-propagating wave, interacting with the incident pump and being amplified by SBS, giving rise to an amplification of the Stokes component and rapidly depleting the pump signal.

During the design of fiber optic communication systems or fiber optic monitoring system, the Brillouin threshold must be considered, which is the maximum pump power level that can be injected in the fiber before the SBS induces deleterious effects. The maximum power is that at which the Stokes components at the input of the pump wave equals the output pump power at $z = L$. The critical pump power P_{th}^{SBS} is determined by the following expression [5]:

$$P_{th}^{SBS} \approx 21 \frac{A_{eff}}{g_0 L_{eff}} \tag{2.10}$$

where A_{eff} is the effective area of the fiber. The typical values for these parameters in SMFs at 1550 nm are: A_{eff} =80 μm^2, $L_{eff} \approx$ 22 km. Therefore, the critical power is approximately 5.6 mW, making SBS a dominant nonlinear process in optical fibers.

2.2. Brillouin-based distributed optical fiber sensors

As commented, DOFS based on the Brillouin scattering effect are currently being employed for a wide range of applications that require the measurements of temperature or strain variations in a distributed manner. This is possible basically thanks to the dependence of the BFS on the local environment temperature and strain conditions of the optical fiber. The expression that relates BFS variations with strain and temperature changes is given by [6, 7]:

$$\nu_B(T, \delta\epsilon) - \nu_{B0} = A \cdot \delta\epsilon + B \cdot \Delta T \tag{2.11}$$

where ν_{B0} is the BFS measured at reference temperature and loose state of the fiber, $\delta\epsilon$ is the strain difference, ΔT is the temperature change, while $A = 0.048$ MHz/$\delta\epsilon$ and

$B = 1.07$ MHz/°C are the strain and temperature coefficients, respectively.

Thus, by monitoring the BFS changes it is possible to retrieve the distribution of the measurands over long sensing fiber distances [5]. It has been proved that the BFS dependence on these physical parameters shows excellent linearity for a wide operating range [8, 9].

Brillouin-based DOFS rely on detecting variations of the BFS value by tracking the frequency of the Brillouin gain spectrum (BGS) peak. There exist a classification of DOFS depending on the method used to obtain the distributed measurement of the BFS and the way of retrieving the BFS at a localized position along the sensing fiber. These different techniques are based on either the time-domain, correlation-domain or frequency-domain. Then, if the monitoring system is based on reflectometry techniques, deploying a single-ended access to the fiber and measuring the reflected incident light power due to SpBS, we have for instance the Brillouin optical time-domain reflectometry (BOTDR), Brillouin optical coherent-domain reflectometry (BOCDR) and Brillouin optical frequency-domain reflectometry (BOFDR). On the contrary, if two optical waves are counter-propagated in the sensing fiber generating a SBS interaction between them, we can classify these DOFS depending on the type of analysis performed: if it is in the correlation domain, we have the BOCDA sensors, in the frequency domain, there are named as Brillouin optical frequency-domain analysis (BOFDA) sensors, and in time domain, the well-known BOTDA sensors.

During the following subsections, the BOTDA and BOCDA sensors will be described since those are the techniques deployed during the research of this thesis.

2.2.1. Fundamentals of Brillouin optical time-domain analysis sensors

BOTDA sensors were first demonstrated in 1990 for temperature [10] and strain [11] monitoring. Since then, BOTDA sensors have been the most widely used DOFS among the different Brillouin-based distributed sensors, deploying numerous monitoring systems for diverse industrial applications [12, 13, 14, 15]. In this section of the thesis, the fundamentals of two different BOTDA techniques are presented: the direct-detection BOTDA sensors and the self-heterodyne detection BOTDA sensors. The former technique is the most common and widely studied configuration, permitting to deploy long-range distributed measurements with high accuracy and spatial resolution, while the second one employs a slight modification on the probe wave and a coherent detection system that permits to perform fast acquisition measurements over large distances, allowing to develop real-time DOFS tolerant to pump power variations.

Direct-detection Brillouin optical time-domain analysis sensors

The fundamentals of direct-detection BOTDA sensors operation are schematically outlined in Fig. 2.3. These sensors are based on the SBS effect in which a pump pulse in injected into a SMF and induces a gain spectrum to a continuous wave (CW) probe that counter-propagates with it. During the propagation of the two waves along the fiber, an exchange of energy between both optical waves is generated via SBS effect. The energy transfer depends on the relative optical frequency of the pump and probe waves: the probe wave experiences amplification if $\nu_P - \nu_S \approx \nu_B$ (Brillouin gain configuration), as shown in Fig. 2.3, while it undergoes depletion along the fiber if $\nu_S - \nu_P \approx \nu_B$ (Brillouin loss configuration).

The direct-detection BOTDA sensors rely on the measurement of the Brillouin gain/loss experienced by the probe wave at the output of the sensing fiber. For instance, Fig. 2.4 depicts the detected probe wave power at the output of the fiber as a function of time or distance in a gain configuration and, for a given frequency difference between the pump pulse and probe wave. Observe that the probe wave detected at the end of the fiber has been amplified by the pump pulse in every location of the fiber. This temporal evolution of the probe wave, the BOTDA trace, can be directly translated to position-dependent information using the round-trip time relation:

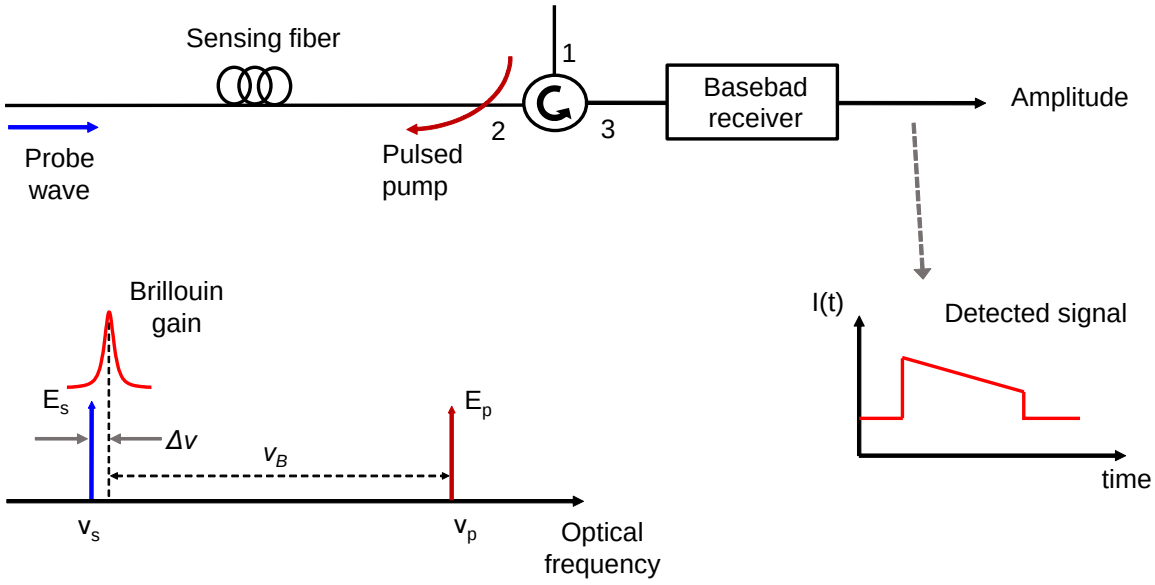

Figure 2.3: Fundamentals of BOTDA sensor: a pulsed signal and a CW signal counter-propagate through an optical fiber with a frequency difference around the BFS.

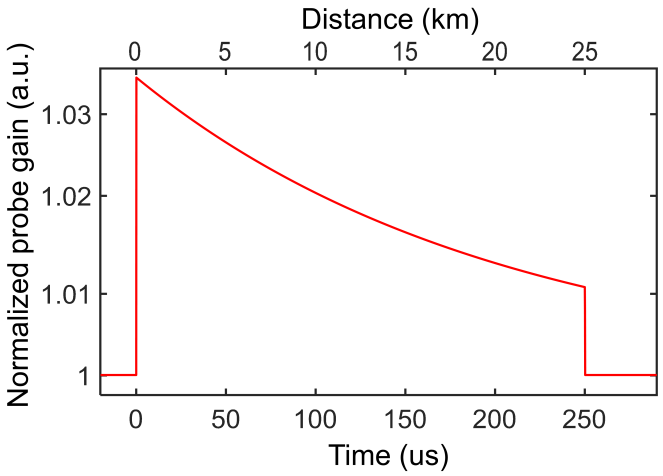

Figure 2.4: Detected probe wave power at the output of the fiber in a BOTDA sensor for a given frequency difference between probe and pump waves.

$$z = \frac{c}{2n}t \tag{2.12}$$

where t is the measured time since the pulse signal enters the fiber and z the location where the pulse and probe waves meet. Therefore, from the BOTDA trace, it is possible to retrieve the Brillouin gain experienced by the probe at each position of the sensing fiber.

As explained before, the Brillouin gain depends on the frequency detuning of the probe wave from the maximum of the Brillouin interaction. So, the amplitude of the retrieved probe signal will vary depending on either the frequency difference between probe and pump or the BFS of the fiber section evaluated. Thus, in order to obtain the BFS of the fiber, it is necessary to determine the frequency difference at which the maximum Brillouin gain is induced at each position of the sensing fiber.

There exist two methods to attain this, the first one is based on performing a frequency sweep of the detuning frequency, $\Delta\nu$, storing all the probe wave time-domain traces and then sorting all the data to reconstruct the Brillouin gain distribution, as shown in Fig. 2.5. Then, the BFS for each position of the sensing fiber is retrieved by fitting the measured spectra to the theoretical model of the Brillouin gain presented in Eq. (2.6). Once the distributed BFS is obtained, the measurands of interest are directly calculated [16, 17, 18, 19].

This method has been widely studied by researchers and multiple advancements have been presented during the last years. As a result of this work, this type of sensors are currently being used in several industries for structural health monitoring applications

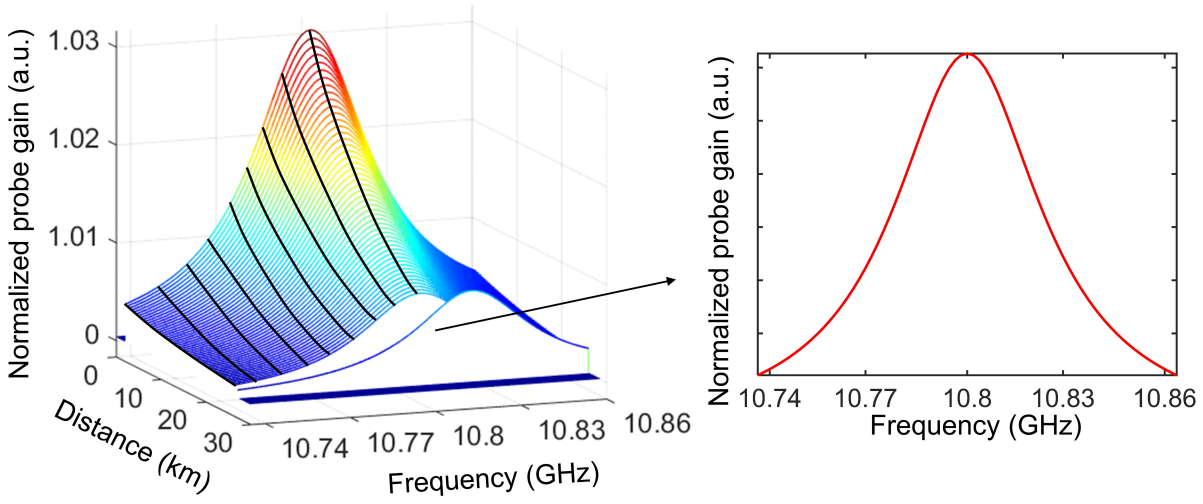

Figure 2.5: Retrieved Brillouin gain spectrum distribution along the sensing fiber. The inset shows the BGS measured at a particular position of the fiber.

thanks to the enhanced accuracy and measurement range that they offer with respect to traditional measuring systems [12, 14, 15]. However, there is a physical constraint that cannot be overcome when using direct-detection BOTDA sensors based on the BGS scan, which is the large measurement time [19]. The reason is that the measurement time is limited by the need to scan the Brillouin spectra by changing the frequency difference between pump and probe, which is a time-consuming process, preventing this type of sensors from performing real-time measurements.

The second method to retrieve the BFS of the sensing fiber using the direct-detection BOTDA configuration is based on the frequency discriminator working principle, which permits to obtain the BFS without the need to scan the BGS, reducing significantly the measurement time. Fig. 2.6 depicts the basics of this technique, the so-called slope-assisted BOTDA (SA-BOTDA) sensors [20]. Basically, the frequency of the probe wave is fixed to a certain value ensuring that the frequency detuning, $\Delta\nu$, matches with the frequency of the BGS slope. Then, continuous measurements at that single frequency are performed, detecting fast amplitude variations that are translated to frequency changes for each position of the sensing fiber, allowing real-time measurements of temperature or strain [20, 21, 13]. However, this technique also undergoes several constraints. One of the most significant is the dependence of the BGS amplitude on the optical pump power. As a consequence, slight variations of the optical pump power due to, for instance, changes in the attenuation of the fiber, may be wrongly interpreted as BFS variations caused by temperature or strain changes. This impairment has been partially mitigated with the

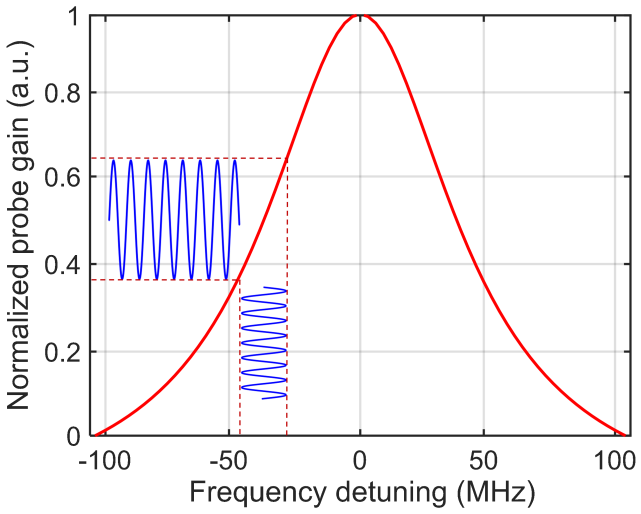

Figure 2.6: Fundamentals of SA-BOTDA sensors.

double slope-assisted BOTDA (DSA-BOTDA) technique [22], where both BGS slopes are measured, although the measurement time is also doubled. Another practical constraint is the dynamic sensing range that direct-detection SA-BOTDA sensors offer, which is limited to the linear region of the gain slope [23].

In order to get a better understanding of the Brillouin gain experienced by the probe wave, we analytically represent the probe wave power at the receiver solving the steady-state coupled intensity equations presented in Eq. (2.5) [24]. As it has been shown in the scheme of Fig 2.3, the pump pulse is injected from $z = 0$ and propagates to $z = L$, while the probe wave propagates from $z = L$ to $z = 0$, with an injected optical power of P_{Pin} and P_{Sin}, respectively. After their interaction, the amplified/depleted CW is directed to a receiver where the probe wave is detected. The detected power of a probe wavefront that has interacted with the pump pulse at a given position z can be expressed as follows [11, 25]:

$$P_S(z)\Big|_{rx} = P_{S_{in}} \exp(-\alpha L) \exp\left(\frac{g_0}{A_{eff}} \frac{(\Delta\nu_B/2)^2}{(\Delta\nu_B/2)^2 + \Delta\nu^2} P_{Pin} \exp(-\alpha z)\, \Delta z\right) \tag{2.13}$$

where $\Delta z = T_P \cdot c/2n$ is the spatial resolution of the system, T_P is the temporal pulse duration. Since the pump wave is pulsed in BOTDA sensors, the interaction length in the fiber between both waves is negligible, thus, it has been assumed that the pump pulse only experiences attenuation during its propagation, while the Brillouin interaction experienced by the pump wave is negligible, and hence the pulsed signal maintains its

amplitude. Then, assuming that the Brillouin gain is very small, it can be considered that BOTDA sensors operate in small signal regime and a linear dependence between the detected probe and the Brillouin gain is obtained:

$$P_S(z)\Big|_{rx} \approx P_{Sin}\exp(-\alpha L)\left[1+\frac{g_0}{A_{eff}}\frac{(\Delta\nu_B/2)^2}{(\Delta\nu_B/2)^2+\Delta\nu^2}P_{Pin}\exp(-\alpha z)\,\Delta z\right] \tag{2.14}$$

where the first term corresponds to a DC component generated by probe wave that has not been modified by Brillouin interaction, being independent of the fiber position, and the second term represents the Brillouin gain experienced by the probe signal at position z due to its interaction with the pump pulse. From this expression, we observe that the Brillouin gain is proportional to the Brillouin gain coefficient, the local pump power, and the pulse duration [19]. Notice also that the gain shows an exponential decrease as a function of distance, being scaled by a factor of $exp(-\alpha z)$. Therefore, the worst-case sensor precision is found to be at the far end of the fiber, where the detected optical power of the probe wave is given by [19]:

$$P_S(L)\Big|_{rx} \approx P_{Sin}\exp(-\alpha L)+\frac{g_0}{A_{eff}}\frac{(\Delta\nu_B/2)^2}{(\Delta\nu_B/2)^2+\Delta\nu^2}P_{Pin}P_{Sin}\exp(-2\alpha L)\,\Delta z \tag{2.15}$$

Observe that, after the amplification of the probe wavefront, the signal must propagate back to the receiver, and thus, the fiber attenuation turns to be doubled as shown in Eq. (2.15). This fact is essential to understand how the sensing distance influences on the detected signal of BOTDA traces at the far end of the fiber [19].

Once the fundamentals and theoretical model of the direct-detection BOTDA sensors are presented, the following section introduces the alternative measuring method, the self-heterodyne detection BOTDA sensor.

Self-heterodyne detection Brillouin optical time-domain analysis sensors

As mentioned, there is an alternative BOTDA sensor configuration that deploys a coherent detection of the probe signal, the self-heterodyne detection BOTDA sensor, which was recently presented by our research group. This technique is based on the use of a probe wave that is phase modulated at a radiofrequency (RF) frequency and, after its propagation along the fiber, it is detected deploying a self-heterodyne detection system [26]. Basically, this measuring system relies on measuring the BFS of the fiber using the RF phase-shift changes, translating these phase variations into frequency changes using the

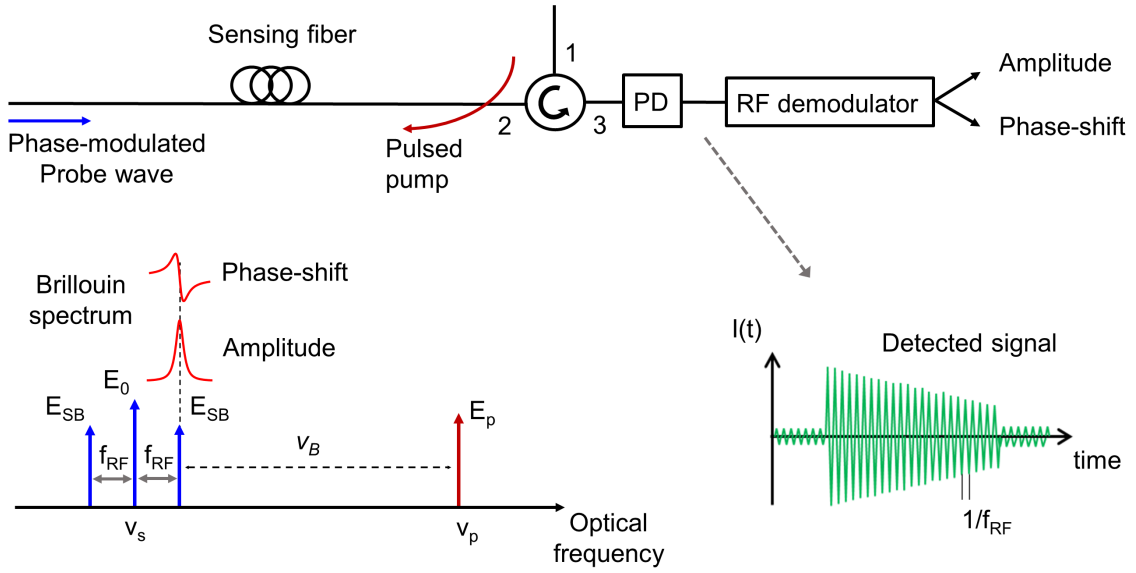

Figure 2.7: Fundamentals of the BOTDA sensor based on phase-modulated probe wave and self-heterodyne detection.

frequency discriminator method.

This technique was first presented deploying a single sideband modulated probe wave to demonstrate the enhanced capabilities obtained when coherent-detection is applied in BOTDA systems, improving the SNR without the need to increase the pump and probe powers [26]. In this section, we center our research on the use of the advanced setup that deploys the phase-modulated probe wave. The fundamentals of this type of SA-BOTDA sensor are schematically depicted in Fig. 2.7. Basically, a phase-modulated probe wave is injected from one end of an optical fiber while the pump pulse is introduced from the other end. The phase-modulated probe wave interacts with the pump pulse via SBS. However, in this case, only the upper frequency sideband of the probe wave interacts with the pulse, while the lower frequency sideband propagates without experience any interaction. Thus, the optical field detected at the photo-detector (PD) as a result of the interaction with the pulse at a particular location, z, can be expressed as [27]:

$$\begin{aligned} E_T(t)\Big|_{rx} = & -E_{SB_i} \exp\left(i2\pi(\nu_0 - f_{RF})t\right) \exp\left(-\frac{\alpha}{2}L\right) \\ & + E_{0_i} \exp(i2\pi\nu_0 t) \exp\left(-\frac{\alpha}{2}L\right) \\ & + E_{SB_i} \exp\left(i2\pi(\nu_0 + f_{RF})t\right) H_{SBS}(z, \Delta\nu) \exp\left(-\frac{\alpha}{2}L\right) \end{aligned} \tag{2.16}$$

where E_{0_i} and E_{SB_i} are the amplitudes of the optical fields of the carrier and sidebands of the phase-modulated probe wave, ν_0 is the optical frequency of the carrier and f_{RF} the RF deployed for the modulation. $\Delta\nu(z) = \nu_0 + f_{RF} - \nu_P + \nu_B(z)$ represents the detuning frequency along the fiber, ν_P the frequency of the pump wave and H_{SBS} is the complex Brillouin spectrum given by:

$$H_{SBS}(z, \Delta\nu) = \exp\left(\frac{g_0}{A_{eff}} \frac{\Delta\nu_B}{\Delta\nu_B + 2i\Delta\nu} P_P(z)\Delta z\right) = G_{SBS} \exp(i\varphi_{SBS}) \tag{2.17}$$

where $G_{SBS}(z, \Delta\nu)$ and $\varphi_{SBS}(z, \Delta\nu)$ are the modulus and phase-shift of the Brillouin spectrum that can be expressed as:

$$G_{SBS}(z, \Delta\nu) = \exp\left(\frac{g_0}{A_{eff}} \frac{\Delta\nu_B^2}{\Delta\nu_B^2 + 4\Delta\nu^2} P_P(z)\Delta z\right) = \exp(g_{SBS}) \tag{2.18a}$$

$$\varphi_{SBS}(z, \Delta\nu) = -\frac{g_0}{A_{eff}} \frac{2\Delta\nu_B\Delta\nu}{\Delta\nu_B^2 + 4\Delta\nu^2} P_P(z)\Delta z \tag{2.18b}$$

being $P_P(z) = P_{P_i} \exp(-\alpha z)$ the pump power at the position z considering that there is no pump depletion.

Notice that there is an important difference with respect to the direct-detection method where only one optical signal arrives in the PD. In this case, instead of receiving a single probe signal, three different components arrive in the receiver at the same time, the carrier and two sidebands of the probe wave. The detected optical power at the heterodyne frequency is given by the beating of these signals [26]:

$$P(t)\Big|_{f_{RF}} = 2E_0E_{SB}\Big[G_{SBS}\cos(2\pi f_{RF}t + \varphi_{SBS}) - \cos(2\pi f_{RF}t)\Big] \tag{2.19}$$

Note that, Eq. (2.19) represents the interference of two terms resulting from the beating between the optical carrier and each of the sidebands of the phase-modulation upon detection. As explained before, just one of the sidebands experiences the SBS interaction, and hence, only one of the terms is amplified/depleted. In the absence of Brillouin gain, both terms interfere destructively and no signal is detected. This is schematically depicted in the phasorial diagram in Fig. 2.8, where the two blue phasors represent the two signals that result from the beating of each of the two sidebands with the carrier, and the red phasor is the resultant RF signal detected at the PD.

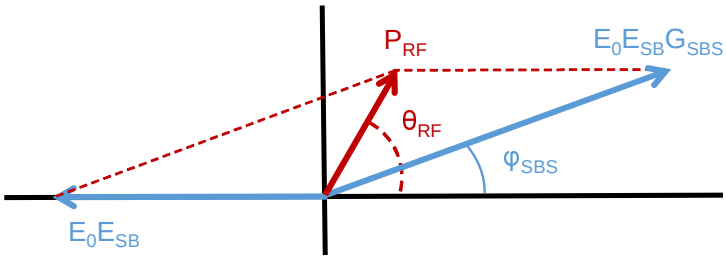

Figure 2.8: Phasorial representation of SBS interaction for a self-heterodyne detection BOTDA sensor based on a phase-modulated probe wave.

If we assume small gain and Lorentzian Brillouin gain, the expression in Eq. (2.19) can be approximated as [27]:

$$P(t)\Big|_{f_{RF}} \approx \frac{2E_0E_{SB}g_0\Delta\nu_B}{\sqrt{\Delta\nu_B^2+(2\Delta\nu)^2}} \cdot \cos\left[2\pi f_{RF}t - \arctan\left(2\frac{\Delta\nu}{\Delta\nu_B}\right)\right] \tag{2.20}$$

Note that, under this approximation, the RF phase-shift of the detected signal, θ_{RF}, is independent of the peak Brillouin gain, confirming that this method is tolerant to Brillouin gain variations.

Finally, the probe wave is detected in a PD and the recovered RF signal is demodulated to obtain its amplitude and phase-shift. The interesting property of this signal is that, as it is schematically depicted in Fig. 2.9, the measured RF phase-shift depends monotonically on the detuning frequency, and thus, on the BFS of the fiber. Moreover, this relation does not depend on the power of the pump pulse. Therefore, the frequency difference between

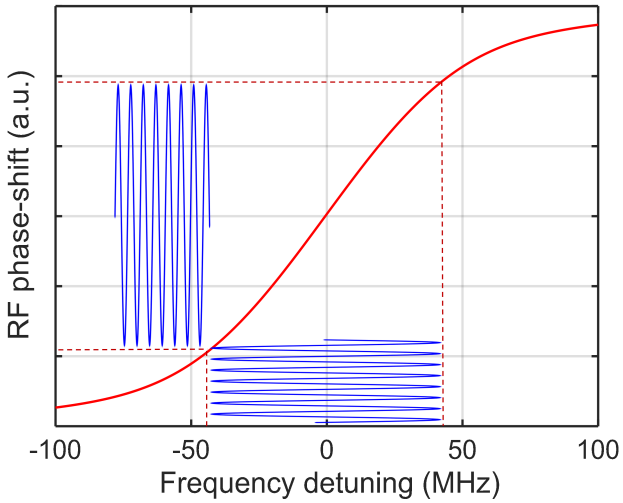

Figure 2.9: Working principle of the SA-BOTDA sensor based on phase-modulated probe and self-heterodyne detection.

the pump and probe can be fixed and then, the frequency discriminator principle can be used to convert dynamically the measured RF phase-shift into BFS changes, without the need to scan the Brillouin spectra [27]. This system has demonstrated to successfully monitor strain variations at kHz-frequencies along hundreds of meters of sensing fibers with BFS precision in the MHz range [28].

2.2.2. State of the art for the BOTDA sensors

In the previous section, the fundamentals of DOFS based on SBS interaction and time-domain have been presented, showing their working principles and the basics of their configuration setups. In this section, there will be introduced some of the contributions that have been presented in the literature related to this type of sensors since they were initially devised. The different limitations that constrain their performance are also introduced and explained. In addition, several solutions recently attained to overcome these restrictions will be briefly explained to provide the reader with an updated state of the art of BOTDA sensors.

As explained, the objective of BOTDA sensors is to determine the strain or temperature distribution along the optical fiber using the BFS variation. Since the optical waves experience a power attenuation during their propagation along the fiber, the performance of BOTDA sensors is constrained. Recently, an expression that characterizes the accuracy of this type of sensors has been established, relating the standard deviation of the retrieved BFS with the measured Brillouin spectrum parameters [19]:

$$\sigma_{BFS}(z) = \frac{1}{SNR(z)} \sqrt{\frac{3 \cdot \delta \cdot \Delta\nu_B}{8\sqrt{2}(1-\zeta)^{3/2}}} \tag{2.21}$$

where δ is the frequency scanning step of the BGS and ζ is the fraction of the peak level over which the quadratic least-square fitting is carried out, while the SNR relates the power level of the output BOTDA signal to the power level of the background noise (total noise power of the system) for each position of the sensing fiber, z. Notice that the accuracy of the sensor depends on the SNR, the Brillouin linewidth, the frequency step of the BGS scan and the data used for the parabolic fit. Therefore, in order to enhance the performance of BOTDA sensors, it is necessary to improve the SNR by either rise the probe power, increase the pump power, increment the number of the measurement averages or enlarge the pulse duration. Another option is to reduce the scanning frequency step. However, all these alternatives bring some constraints to the measuring system, such as the distortion of the output signal that worsens the accuracy of the system, the

increment of the measuring time or the worsening of the spatial resolution. Therefore, there is a restrictive trade-off between the accuracy of the sensor, its spatial resolution, and the measurement time that must be considered to obtain the desired features of the BOTDA sensor.

Limitation of the probe optical power

As it has been explained in section 2.2.1 and shown in Eq. (2.15), the detected probe wave power is directly proportional to the injected probe power, while the Brillouin gain experienced by the probe is, at the same time, proportional to the pump pulse peak power. Therefore, the SNR of BOTDA systems can be enhanced by increasing either of these two signals power.

However, the maximum power level of the probe and pump waves that can be launched into the sensing fiber is constrained and cannot be freely increased. For instance, the maximum probe wave power that can be deployed is firstly restricted by the onset of the so-called NLE [29, 17, 30], and secondly by the onset of the Brillouin threshold [31].

The origin of NLE resides on the continuous interaction of the counter-propagating probe and pump optical waves and the exchange of energy via SBS between them during their propagation along the fiber. Basically, it has been found that the interaction between both signals induces a transfer of power that is dependent on the frequency detuning, generating a distortion of the pump pulses during their propagation, which eventually leads to measurement errors [29, 17]. Moreover, it has been identified that the impairments caused by NLE are dependent on the probe wave power injected to the fiber.

There have been identified three different types of NLE that directly restrict the maximum power that can be injected into the fiber. First-order NLE were initially noticed due to the depletion of the pump pulses observed at the output of the sensing fiber when the probe power was risen [29, 17]. Then, the detrimental effects of second-order NLE were recognized, observing a distortion of the temporal shape of the pump pulses at the output of the fiber that depends on the frequency detuning [32, 33]. Recently, in part as contribution of this thesis, extinction ratio-related NLE have been found due to the interaction of the pump pulse pedestal with the probe wave signal, which induces a similar detrimental effects and measurement errors to the other NLE. In addition, it has been found that the transient response of the Erbium doped-fiber amplifiers (EDFA) deployed for the amplification of pump pulses generates a distortion on the retrieved signal, generating also similar impairments to the other NLEs [34].

Since the constraints imposed by NLE in BOTDA sensors are of paramount importance, they have been part of the investigation of this thesis. In chapter 3, we first explain

in detail the origin and the constraints brought by the mentioned NLE. Several solutions presented during the last years to mitigate some of their impairments are also described. Then, as a result of the investigation of this thesis, a relevant contribution attained to successfully overcome the impairments brought by the ER-related NLE is presented, which successfully mitigate the detrimental effects brought by all type of NLE, allowing to inject the maximum possible probe wave power into the sensing fiber.

Despite the multiple proposed solutions to mitigate the detrimental effects of NLE, the probe wave power is ultimately limited by the onset of the Brillouin threshold, which is caused by the amplification of thermally-induced SpBS waves [31, 35]. As will be shown in the next chapter, the Brillouin threshold has been also enhanced with the technique developed in this thesis work.

Limitation of the pump optical power

As mentioned, the SNR of BOTDA sensors can be enhanced increasing the injected pump power. However, if high-power pump pulses are injected into the fiber, it has to be taken into account that the maximum allowable pulse peak power is limited by the onset of nonlinear effects such as modulation instability (MI) or four wave mixing (FWM) [36, 37, 17]. MI effect induces a depletion on the effective pump power distorting the response of the sensor due to the interplay between anomalous dispersion and the Kerr effect in the fiber [36, 37, 38, 39]. This effect generates two symmetric sidebands around the frequency of the pump pulse, inducing a power exchange between these sidebands and the pump pulse frequency when it propagates along the fiber. As a consequence, power fluctuations of the pump pulse are induced, which are directly translated into a reduction of the Brillouin gain, and consequently, measurement errors are experienced due to the decay of the SNR. This effect can produce such a broadening of the pump power that can completely suppress the Brillouin gain, generating important impairments in the BOTDA sensor accuracy.

It has been observed that the amplified spontaneous emission (ASE) increases the detrimental effects of MI [36]. So, in order to reduce the detrimental influence of this noise, typically generated by the EDFA deployed to amplify the pump pulses, an optical filter is deployed right before the injection of the pump wave to the fiber [40]. The power of the pump pulse is constrained by MI to around 20 dBm (for lengths longer than 22 km and SMF). In order to mitigate the deleterious effects of MI, a slight modification on the BOTDA scheme has been recently presented by our research group, which relies on the use of orthogonal polarization pulses to decrease the pump power fluctuations due to MI [33].

FWM is another nonlinear effect that is induced when three or more optical waves copropagate simultaneously along an optical fiber. As a consequence, a degradation of the original signals due to nonlinear crosstalk of the optical waves is observed. This is a relevant effect in the study if this type of DOFS since some of the BOTDA configurations deploy multiwavelength pump signals to enhance their performance, as for example, to extend the dynamic range or to reduce the measurement time [41]. In order to avoid FWM, the total pump peak power injected into the fiber should be properly adjusted, limiting again the SNR of BOTDA sensors.

Finally, another limitation of the performance of BOTDA sensors that is related to the power and the temporal shape of the pump pulse is the onset of self-phase modulation (SPM). If the temporal pulse shape is not completely rectangular, i.e., the rising and falling edges are not sharp enough and SPM can appear [42]. Basically, this nonlinear effect induces a spectral broadening of the pump pulses that can generate a severe distortion on the measured Brillouin spectrum, reducing the accuracy of the sensor. This effect can be easily avoided by using perfectly shaped rectangular pump pulses with sharp rising and falling edges or by deploying the differential pulse-width pair (DPP) technique [43].

Signal-to-noise ratio of BOTDA sensors

As explained at the beginning of this subsection 2.2.2, the precision of BOTDA sensors can be improved by enhancing the SNR. We have already explained that one solution to enhance the SNR and compensate the optical attenuation due to the propagation losses is to optimize the probe and pump wave powers that are injected into the sensing fiber. In this sense, several solutions and techniques proposed to attain the optimum working conditions have been already introduced. Another way to improve the accuracy of these sensors is to reduce the δ (frequency step) or to increase the number of averages. However, both of these solutions directly worsen the measurement time, which restricts the capabilities of performing dynamic measurements.

In spite of these difficulties, in order to enlarge the measurement range of BOTDA sensors, great effort has been done during the last years to improve the SNR without worsening the measuring time, obtaining important advancements. For instance, some schemes have reached to measure up to 150 km fiber length in loop configuration or up to 200 km using a leading fiber to monitor the farthest point at 100 km [44, 45]. One of the proposed methods to attain these improvements requires in-line amplification of the probe and/or pump waves along the sensing fiber. Several EDFA must be deployed to compensate the fiber losses [44], which is a drawback of this technique due to the need for power supply in remote locations, increasing the complexity of the measuring sys-

tem. Other solutions are based on deploying first and second-order Raman amplification methods, which rely on the generation of distributed gain amplification along the fiber. This amplification can act separately or simultaneously over the probe and pump waves, which interact in the SBS process [46, 47, 48]. The use of distributed Brillouin pump amplification to increase the pulse power is another effective solution to improve the SNR of BOTDA sensors [49, 50, 51].

An alternative method to increase the SNR and hence, the sensing range, is the use of coding techniques, such as Simplex coding [52], cyclic coding [53], bipolar coding [45] or color coding [54, 55]. The basic concept of pulse compression coding is to generate a sequence of pulses in a particular way that propagate in the sensing fiber and interact with the probe wavefronts, resulting in overlapped return signals. Since multiple pulses are launched into the sensing fiber without increasing the pump peak power, nonlinear effects are avoided, while the average pump energy is increased, as well as the backscattered signal. Then, deploying a particular decoding process, the return signal can be restored to a waveform that is equivalent to a single pulse but of much higher energy. In this way, one aims to improve the SNR of the measurement [2].

Recently, a solution presented by our research group has permitted to increase the performance of mono-color cyclic coding technique thanks to the combination of the dithering of the probe wave method with coded pulses [56]. This novel scheme has demonstrated to successfully retrieve the BFS distribution along an 82-km sensing fiber, with a spatial resolution of 1 m and an accuracy of 3 MHz. In this thesis work, the constraint of nonlinear amplification that coding techniques experience when long codewords are deployed [57] has been studied. In chapter 4, a practical solution is presented to simply solve this limitation, allowing to deploy larger codes, and thus, further enhance the SNR.

Number of resolved points: the spatial resolution

Since there exist applications that require monitoring systems with high spatial resolution such as aircraft wing monitoring or cracks detection, the pulse duration is shortened to enhance the spatial resolution. However, as it has been also mentioned before, there is a restrictive trade-off between the SNR and the spatial resolution of the measuring system. The spatial resolution, Δz, of the BOTDA sensors is determined by:

$$\Delta z = \frac{T_P \cdot c}{2n} \tag{2.22}$$

where T_P is the temporal pulse duration.

From this expression, it is observed that, the shorter the pulse duration, the better the spatial resolution of the sensor. However, the use of short pulses introduces two important limitations. The first one is that, as the Brillouin interaction between the probe and the pump pulse is now shorter, the resultant Brillouin gain amplitude is also reduced (see Eq. (2.15), giving rise to a degradation of the SNR. The second problem is related to the broadening experienced by the Brillouin linewidth when the pulse duration is shorter than the phonon lifetime (∼10 ns), which can lead to a worsening of the accuracy of the sensor [58, 43].

Therefore, once again, great effort has been devoted to find alternative solutions that allow enhancing the spatial resolution without compromising the SNR of the BOTDA sensors. As a result, several advancements have been demonstrated during the last years to improve spatial resolution in different manners. Some of these methods are the so-called bright-pulse technique, the dark-pulse technique or the pulse pre-pumping technique [59, 60, 61], which are based on the pre-excitation of the acoustic wave, allowing to reach a steady-state response and maintaining a narrow linewidth of the Brillouin spectrum. The previously mentioned DPP technique was also devised to enhance the spatial resolution [43]. It is based on the subtraction of two different Brillouin spectra that are measured sequentially using two pulses with slightly different duration. The duration of the pulses is set to be long enough to correctly measured with a narrow Brillouin linewidth, obtaining two different BGS measurements with high SNR but low spatial resolution. Then, the difference of the detected spectra is calculated, obtaining a resultant spectrum that provides measurements with a spatial resolution equals the difference of the duration of the two pulses, thus, allowing to considerably enhance the spatial resolution.

In relation to the broadening of the spectrum shape due to the shortening of the pulse duration, notice that is not always a deleterious effect. Since the SA-BOTDA sensors are based on measuring the amplitude or phase-shift changes observed on the linear region of the spectra, the broadening of their spectra can permit to enlarge the linear region where these techniques perform their measurements. Thus, the dynamic range of dynamic BOTDA sensors is directly enlarged when the pulse is shortened [62]. This particular effect has been also studied during this thesis to propose a technique that allows to extend the dynamic range of self-heterodyne BOTDA sensors, as it will be shown in section 5.4.

Measurement time and dynamic sensing

As explained before, the measurement process to retrieve the distributed Brillouin spectra along the sensing fiber requires to sweep the frequency difference between probe

and pulse waves. This is a very time-consuming procedure that prevents BOTDA sensors from performing dynamic measurements. During the last years, there has been thorough research on this limitation due to the growing interest and the increasing number of applications that require fast measurements to quickly detect the measurands variations. For instance, the renewable energy industry, and in particular, wind-turbine manufactures and wind farm owners, are currently deploying optical fiber sensors to detect damages in their wind-turbine blades. Specifically, there are specific wind-turbine blade tests that require to dynamically monitor the state of their asset. As a consequence of this increasing demand, several fast acquisition systems have been successfully implemented to monitor vibrations in a different type of structures.

Some of these schemes have been already introduced in section 2.2.1 and section 2.2.1, with the SA-BOTDA sensors that employ the slope of the gain or phase-shift spectra to discriminate the BFS changes. Some examples of this technique are the previously presented SA-BOTDA with constant probe frequency and the DSA-BOTDA sensor [20, 22]. Additional configuration setups based on the same working principle with slight variations have been also deployed to perform fast measurements. For instance, a tailored probe wave was used to compensate the impairments brought by optical fibers with non-uniform BFS [21]. Basically, this technique generates a probe wave whose frequency varies along the fiber, so that, the probe is always set at the skirt of the Brillouin spectrum even if the BFS changes along the fiber. A different method is the so-called fast BOTDA sensor, which is based on the fast switching that provides an arbitrary waveform generator (AWG) to perform the BGS scan [63]. Each frequency of the probe wave is launched one after the other with a period given by the round-trip time. Consequently, the measurement time is only given by the product of the round-trip time, the number of frequencies used to scan the Brillouin spectrum and the number of averages. Finally, a swept-free BOTDA sensor was developed, in which a comb probe with different and constant frequency counter-propagates with the pump wave [64]. Then, each pair of probe and pump waves obtain the Brillouin gain for their corresponding detuning, allowing to reconstruct the BGS without the need of a sweep. The measurement time is only limited by the round-trip time (without including the post-processing).

Recently, the so-called single-shot distributed BOTDA sensor has been presented [65]. In this analyzer, the whole sensing fiber can be monitored with only one-shot measurement. This method is based on generating a dual-polarization probe with orthogonal frequency-division multiplexing modulation, allowing to retrieve the BFS profile without the need for neither frequency scanning, nor polarization scrambling, nor averaging.

As mentioned previously in section 2.2.1, there are alternative dynamic measurement

techniques that rely on the phase-shift changes, which have already been described in the previous section and will be further studied in chapter 5.

2.2.3. Fundamentals of Brillouin optical correlation-domain analysis sensors

BOCDA sensors are under continuous research since they were first presented in 1999 by Professor Kazuo Hotate [66]. This technique also deploys two counter-propagating signals, a pump signal and a probe wave frequency-shifted by the BFS. However, the main difference of this method with respect to BOTDA sensors, is that both signals are CW and the light source deployed to generate the pump and probe signals is frequency modulated with a sinusoidal signal using the direct current of a laser diode (LD). Contrary to the time-domain configuration, where the measurement is sequentially done from one fiber end to the other and allowing a distributed measurement mode, in BOCDA sensors, the measurement is done at a specific position [66]. Basically, in this particular type of DOFS, SBS is excited position-selectively along the sensing fiber by applying the coherence manipulation technique to the continuous pump and the probe waves, which travel in opposite directions in the fiber [66]. As a result, the output signal of a BOCDA sensor shows the Brillouin gain generated by the SBS interaction induced all along the in the fiber, being only significant those positionswhere the correlation between the pump and probe waves is high, the so-called correlation peak (CP). As in BOTDA sensors, the measured BGS is deployed to obtain the BFS of the sensing fiber, and thus, the measurands variations. The position under test, the CP, can be easily shifted by simply modify the modulation frequency of the light source. Therefore, "random accessibility" to multiple points that are selected arbitrarily along the fiber provides the possibility of performing simultaneous dynamic strain measurements at the selected points. The "random accessibility" is a unique feature offered by BOCDA sensors, while it cannot be realized by any other time-domain technologies [66].

In BOCDA sensors, the gain experienced by the probe wave that counter-propagates the pump along the optical fiber is determined by the overlap integral of the Brillouin gain spectrum, $g_B(\zeta\nu)$, and the pump-probe beat spectrum, $S_b(\zeta\nu)$, given by [66, 67]:

$$g = \frac{\nu_g \bar{P}_1}{A_{eff}} \int_{-\infty}^{\infty} d\zeta \int_{-\infty}^{\infty} \frac{d\nu}{2\pi} g_B(\zeta,\nu) S_b(\zeta,\nu) \tag{2.23}$$

where S_b is the beat spectrum that has the delta function-like shape, which is generated by the frequency modulation (FM) of the laser along the fiber position ζ and $\bar{P}_1$ is the

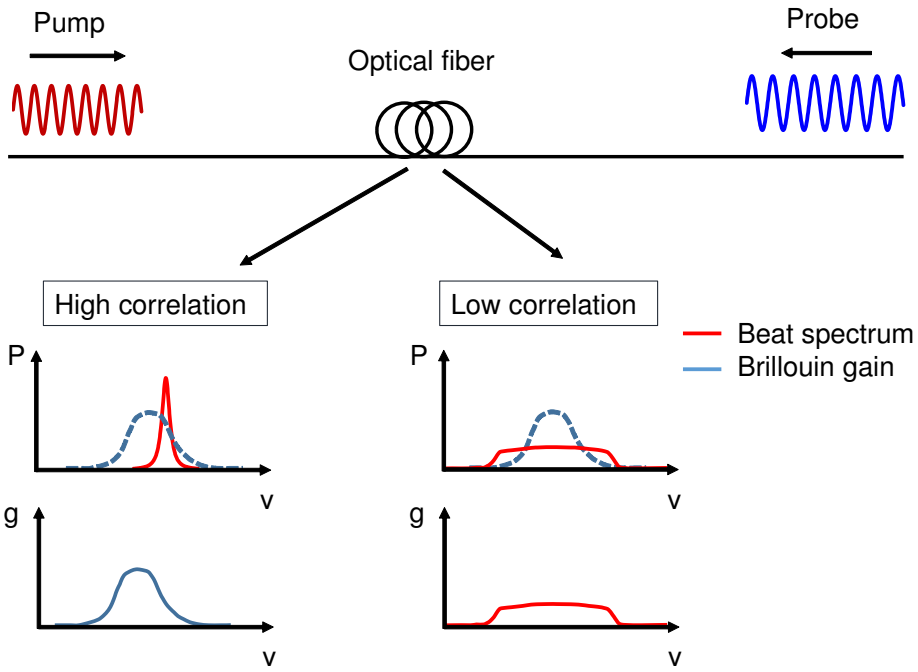

Figure 2.10: Schematic illustration of SBS interaction between pump and probe waves in a BOCDA sensor. The gain of the probe wave (lower graphs) is determined by the overlap integral of the Brillouin gain spectrum with the power spectrum of the pump-probe beat.

time-averaged pump power.

Figure 2.10 highlights the propagation of the two optical waves along the sensing fiber. Then, the intrinsic Brillouin spectrum and the pump-probe beat spectrum for correlated and un-correlated positions of the fiber are also shown. Brillouin spectrum follows a Lorentzian shape, while the beat spectrum in BOCDA sensors depends on the correlation between the two counter-propagating waves. In those positions of the fiber where both waves are highly correlated, the beat spectrum S_b is approximately delta function of frequency. So, if the pump-probe frequency difference is swept, the gain experience by probe wave at the CP can be scanned and retrieved. On the other hand, the beat spectrum S_b is severely broadened at those positions of the fiber where probe and pump waves are not correlated. In this case, when the beat spectrum is shifted, the gain for the probe wave remains small and almost constant, giving rise to a noisy gain contribution.

Figure 2.11 shows the Brillouin gain experienced by the probe wave at each position of the fiber. As it can be observed, those locations that correspond to CP positions in the fiber both waves have efficiently interacted via SBS and a clear BGS is generated. Therefore, the output signal of a BOCDA sensor is characterized by showing two different contributions: the resultant Brillouin gain that is only efficient in those positions of

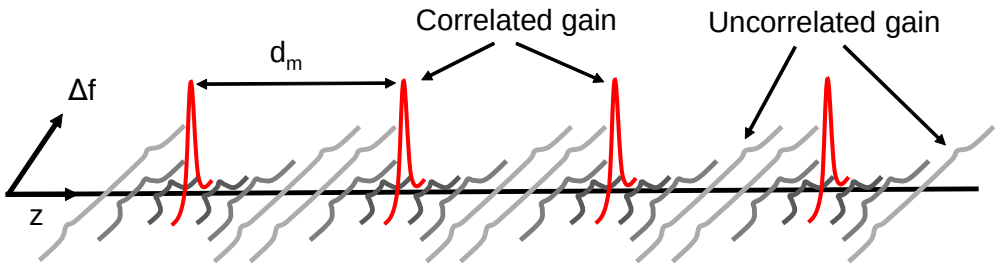

Figure 2.11: Schematic diagram of the SBS along the sensing fiber in BOCDA sensors.

the fiber where the correlation between both waves is high, and the un-correlated gain contribution for the rest of the sensing positions, which generate a broadened background signal. As a result, a Lorentzian shape spectrum is added to a "mountain-shape" background noise. As in BOTDA sensors, the BGS of the CP is reflected on the variation in the probe power at the output of the fiber, allowing to detect the Brillouin gain peak, and hence, the BFS for each position of the optical fiber when the fiber scan is performed.

Since the modulation of the probe and pump waves is sinusoidal and periodical, CP are periodically generated along the sensing fiber with a distance interval given by [66]:

$$d = \frac{c}{2nf_m} \tag{2.24}$$

The distance between the CP determines the measurement range in the basic BOCDA system, limiting the monitoring distance to have only one CP in the sensing fiber.

Since the interaction is given by two CW signals at a localized position, the spatial resolution has no limitations like in BOTDA sensors and is determined by [66]:

$$\Delta z = \frac{c \cdot \Delta\nu_B}{2\pi n f_m \cdot \Delta f} \quad \text{for} \quad \Delta\nu_B > f_m \tag{2.25a}$$

$$\Delta z = \frac{1.52c}{2\pi n \Delta f} \quad \text{for} \quad \Delta\nu_B < f_m \tag{2.25b}$$

where f_m is the laser modulation frequency and Δf is the amplitude of the FM.

2.2.4. State of the art for the BOCDA sensors

Like BOTDA, BOCDA technology has attracted increasing attention in research and applications related to civil engineering during the last years, and as a result, multiple performance improvement schemes have been recently presented [68, 69], along with sev-

eral application tests [70, 71]. For instance, a BOCDA sensor with just three-cm spatial resolution was deployed for cracks detection in a reinforced concrete specimen that was subjected to bending. A tiny crack was detected on the surface of the steel-reinforced concrete specimen before visual recognition using a centimeter-order spatial resolution of the BOCDA system [71]. Notice that these types of events are not detectable with low spatial resolution systems, such as BOTDA sensors. In this sense, BOCDA sensors have demonstrated enhanced performance in terms of spatial resolution.

Apart from deploying BOCDA sensors for high spatial resolution measurements, these types of DOFS have been also deployed for the dynamic strain monitoring of a tall building model subjected to an earthquake waveform vibration, observing small strain variations at a sampling rate of 10 samples/s [72]. BOCDA sensors have been also applied in the structural health monitoring for aircraft wings and bodies, performing in-flight tests in which the sensing fiber was set on the body material and a strain distribution change between the in-flight and on-ground situation was successfully measured [73, 74]. In this case, the random accessibility provided data for simultaneous dynamic strain measurements at arbitrarily selected multiple points along the fiber nerve.

In order to successfully develop BOCDA sensors capable of performing the mentioned sensing measurements, several constraints have to be taken into account. Some of these constraints have been already overcome, while others still limiting the performance of BOCDA sensors.

Background noise spectrum

As explained before, the BOCDA output spectrum is obtained by the integration of all the spectra that are generated at each position along the fiber. Therefore, the total BOCDA output spectrum consists of two clearly differentiated components; one is the signal component corresponding to the correlation peak position, and the other one is given by all the uncorrelated gain contributions of those positions of the sensing fiber where the pump and probe waves show low correlation between both waves [4]. As a result, the detected BOCDA spectrum shows a "mountain-like" background spectrum that is added to the signal spectrum corresponding to the CP position, which has a tower-like shape. This means that the useful signal employed for sensing in BOCDA sensors is affected by a background noise that strongly reduces their dynamic range and spatial resolution [4, 75].

Regarding this constraint, a modified BOCDA configuration, named "intensity modulation scheme" was presented to successfully overcome this important limitation. By the FM modulation on the LD with a sinusoidal waveform, the time-averaged LD power

spectrum has peaks at both sides of the spectrum shape. These side lobes can be reduced by manipulating the time-averaged LD power spectrum shape, so that, the mountain-like background spectrum is successfully reduced, canceling the detrimental effects of those uncorrelated gain contributions [75].

An alternative solution to ameliorate the detrimental effects of all the uncorrelated positions of the sensing fiber is the differential measurement scheme devised by Professor Kwang Yong Song et al. [76]. In this scheme, phase modulation is applied to either the pump or probe waves. Thanks to the phase modulation, the shape of the spectrum obtained at the CP position is significantly attenuated, whereas the background spectrum shape is nearly the same. Then, by calculating the difference between the BOCDA spectra of the two cases with and without the phase modulation, the background spectrum is notoriously reduced, retrieving a sharp and clear spectrum from the CP signal. This technique, presented in 2012 provided a five-fold enhancement of the spatial resolution, apart from the improvement attained in terms of the dynamic range in BOCDA sensors due to the suppression of the background spectrum [76].

Measurement range and spatial resolution

Like in BOTDA sensors, the measurement range is also constraint in BOCDA sensors. Since the measurement range is determined by the CP distance, it is a parameter that cannot be freely modified due to the fact that it is inversely related to the FM of the light source. As said before, multiple CP are periodically generated along the sensing fiber, and the measurement range is limited to the distance between the neighbor CP positions in the basic BOCDA system. The range can be elongated if a lower FM was deployed, however, the spatial resolution would be directly reduced, as indicated in Eq. (2.24). Therefore, there exists an important trade-off between the measurement range and spatial resolution that has to be taken into account when a BOCDA sensor is designed.

An initial approach to extend the measurement length of the fiber is to implement the temporal gating scheme based on modulating the amplitude of the pump wave to have a pulse shape with a width equal to the CP distance [77, 78]. Then, the BOCDA output is also gated with the same frequency to select only one CP position, which allows to enhance the measurement range. An alternative and improved way to enlarge the range is to deploy a more advanced setup that relies on generating a double modulation scheme. Basically, the modulation of the light source is performed with two modulated frequencies, whose frequencies ratio is an integer. In particular, the lower frequency determines the measurement range and the higher frequency improves the spatial resolution. In this manner, the measurement range can be elongated while a high spatial resolution is main-

tained. This technique can be carried out even when the ratio between both modulation frequencies is not an integer [79].

Another important drawback in correlation-based systems that has been limiting the sensing performance is the noise induced by the backward reflection of the pump waves. As it has been explained, the SBS process requires the interaction of two counter-propagating waves, a strong pump wave and a weak probe wave, which are propagated along an optical fiber system where there are several fiber connection points or splicing points that may back-reflect the signal. These reflections act as noise, which cannot be completely eliminated by an optical filter, generating a deleterious effect in the SNR of the system. To avoid these drawbacks, the best approach is to deploy a double lock-in detection scheme within the BOCDA sensing system, which is based on chopping the pump and probe waves simultaneously with two different lock-in frequencies. These frequencies are then used to synchronize the detection system and remove the backward reflection of pump waves from the probe signal without using any optical filter [80]. This not only permits to reduce the noise and hence, improve the SNR but also allows to deploy a large FM amplitude, $\Delta f > \nu_B/2$, enhancing the spatial resolution.

Measurement time and dynamic sensing

One of the main particularities of BOCDA sensors is the capability of arbitrarily select the measuring position along the sensing fiber. However, some applications require fast measurements of the whole sensing fiber to retrieve dynamically the distributed measurand information. In common BOCDA sensors, locking-detection schemes are usually adopted, which require a minimum time to correctly retrieve the measured signal, restricting the possibility of deploying a fast measuring system. A couple of solutions have been presented to overcome this restriction, leading to the development of BOCDA sensors capable of monitoring dynamic strain variations [81, 82]. The first alternative scheme is based on sweeping the CP position along the sensing fiber while keeping the frequency difference between the pump and probe waves fixed; then, the frequency difference is changed. This process is repeated to scan all the frequencies of the BGS at any positions along the fiber [83]. In these schemes, the random accessibility cannot be realized, but the measurement speed has been significantly enhanced to correctly monitor the entire measurand distribution of 120-m length fiber with an accuracy of ±2.5 MHz, a spatial resolution of 0.5 m and a frequency acquisition of 20 Hz. A second solution relies on the implementation of the differential FM technique that has experimentally demonstrated an enhanced performance of dynamic measurements using BOCDA sensors, as it has been mentioned before.

Polarization-induced noise

Another limiting factor of BOCDA sensors is the polarization-induced noise, which is caused by the Brillouin gain dependence on the state-of-polarization (SOP) of the optical waves, affecting directly on the SNR of the measuring system. This problem was also solved thanks to the fact that the SOP can easily be changed when SMF is deployed as sensing fiber. In this case, the time-division polarization diversity scheme was proposed to overcome this detrimental effect [84]. Specifically, the probe wave polarization is switched between the two orthogonal SOP and both BOCDA output signals are measured. Then, the two detected signals are squared and added together to compensate the fluctuation of the Brillouin interaction due to the SOP.

Simplification of the measurement systems

Finally, as every DOFS, the simplicity of the measurement system is one of the main objectives in order to make accessible the use of these sensors to the users. As it has been explained along this chapter, SBS interaction process requires very particular conditions to be successfully used for sensing purposes, and even more when correlation-based systems are deployed. Thus, it is important to either reduce the complexity of their systems and the deployment of the sensing fiber. For the latter, there have been some proposals to enable the one-end access measurement instead of using both ends of the fiber to propagate the two signals [85, 86]. This is achieved, for example, in the LC-BOCDA sensor that simplifies the sensing fiber installation by using a reflection mirror at the far end of the fiber to make the signals propagate backward, and thus, counter-propagate with the incoming waves, generating the SBS interaction. This type of configuration has been particularly studied in this thesis, where a proposal to enhance the current performance of the LC-BOCDA sensors has been investigated and experimentally demonstrated, as it will be introduced in chapter 7.

CHAPTER 3

Compensation of non-local effects due to limited ER pump pulses in BOTDA sensors

3.1. Introduction

DOFS are playing an important role among the different monitoring systems available nowadays for structural health monitoring. In particular, those sensors based on the SBS effect that offer the capability of providing a large number of simultaneous measurement positions with high spatial resolution are being specially investigated due to the numerous real applications capable of monitoring. This is, for example, the case of the civil engineering industry, that is using DOFS to control the state of, for example, dams, bridges or tunnels. Other industries such as oil, gas or electricity transportation are also deploying DOFS to monitor pipelines leakages, 3rd part intrusions and preventive maintenance of their assets.

The BOTDA technique is the most investigated and developed configuration of DOFS based on SBS. As mentioned in chapter 2, one of the most important limitations of BOTDA sensors is the maximum probe power that can be injected into the fiber due to the appearance of the previously introduced NLE [29, 87, 34]. This power limitation directly degrades the SNR of the BOTDA sensor, which is the parameter that characterizes the performance of the sensor. Several solutions have been presented during the last years to mitigate first and second-order NLE detrimental effects, however, our research group has recently found that BOTDA sensors still undergo NLE constraints when limited extinction ratio (ER) pump pulses are deployed [34]. In particular, it has been demonstrated that limited ER pump pulses and the transient response of the EDFA in-

duce important detrimental effects on the determination of the BFS of the sensing fiber, limiting the performance of BOTDA sensors.

In this context, the research contribution introduced in this first chapter of the thesis is focused on presenting a practical solution to ameliorate the constraint related to the deployment of limited ER pump pulses in BOTDA sensors. This solution is based on the dithering of the light source technique, which has been demonstrated that allows to overcome NLE caused by limited ER pump pulses and the transient response of the EDFA. Moreover, it is proved that this method successfully solves either first-order NLE and second-order NLE, being the first and unique technique capable of solving all existing NLE at once.

This chapter contains a review of the state of the art of first and second-order NLE is firstly presented. Then, the detrimental effects of deploying limited ER pump pulses in BOTDA configuration are summarized along with the constraints brought by the transient response of EDFA. Afterward, the fundamentals of the research accomplished during this part of the thesis are carefully explained, introducing the dithering technique and experimentally demonstrating the enhanced performance of the proposed method. It is shown how this powerful technique allows to mitigate all the detrimental effects of NLE, allowing to deploy limited ER pump pulses and any kind of EDFA to amplify the pulsed signal. Finally, it is proved that the dithering technique is a very useful method for the implementation of cost-effective distributed sensors, as well as measuring systems with high spatial resolution deploying the DPP technique.

3.2. NLE in BOTDA sensors

In this section, a review of the physical origins of NLE and their consequences to BOTDA measurements is carried out, with special emphasis on the recently presented detrimental effects related to the use of limited ER pump pulses. In addition, techniques that have been presented to mitigate the impairments of NLE are introduced.

3.2.1. First-order NLE in BOTDA sensors

As explained in chapter 2, in a conventional gain-BOTDA sensor configuration, an optical probe wave is injected into the sensing fiber and counter-propagated with a pulsed pump wave which is injected from the other end of the fiber. During the propagation, there is an interaction between both waves via SBS that generates a narrow gain spectrum on the probe. This transfer of energy only occurs at a certain location of the fiber during the time interval of the pump pulse duration, generating a gain spectrum when the pump

wave has a higher frequency than the probe, which is separated in frequency by the BFS. Simultaneously, the pump wave amplitude is slightly depleted due to the Brillouin interaction at each section of the fiber. However, the cumulative interaction of the pump pulse with the probe all along the sensing fiber, induces a more significant effect on the pulse than on the probe [29, 17]. The effect of the Brillouin interaction over the pulsed signal can be calculated solving Eq. (2.5a). The optical pump power at the output of fiber after the Brillouin interaction during the propagation can be expressed as:

$$P_P(L) = P_{Pi}\exp(-\alpha L)exp\left(-\frac{g_B(\Delta\nu)}{A_{eff}}P_{Si}L_{eff}\right) \tag{3.1}$$

where P_{Pi} and P_{Si} are the injected optical powers of the pump pulse and probe waves, α is the attenuation of the fiber, L_{eff} is the effective length of the fiber, A_{eff} is the effective area of the fiber and $g_B(\Delta\nu)$ is the Brillouin gain coefficient defined in Eq. (2.6), which depends on the frequency detuning from the maximum of the Brillouin gain, $\Delta\nu$.

Notice that, in Eq. (3.1), apart from the attenuation that the pump pulse experiences due to the propagation along the fiber, the pump power is depleted showing a dependence on frequency, which is due to the natural response of the Brillouin interaction that follows a Lorentzian function shape. This means that, due to the cumulative interaction of the pump pulse with probe, the resultant depletion of the pulse at the end of the fiber will be more severe at frequencies near the BFS of the fiber, giving rise to pump pulses of different amplitude depending on the frequency detuning, $\Delta\nu$. The depletion that the pump pulse experiences from its entry to the end of its propagation in the sensing fiber can be expressed with a dimensionless coefficient, the so-called depletion factor, as follows [29]:

$$d(L) = \frac{P_{P_0}(L) - P_P(L)}{P_{P_0}(L)} \tag{3.2}$$

with P_{P_0} and P_P the pump power in the absence and presence of Brillouin interaction at the output of the fiber, respectively. Since the pump pulse depletion depends on the frequency detuning, a sensing fiber with uniform BFS will generate a more deleterious effect than a non-uniform fiber. Let's consider the situation where there is a slightly variation of the BFS at the end of the fiber, this section will undergo lower SBS interaction at those frequencies where the pump pulse has been more depleted, leading to measurement errors in the determination of the BFS. As an example, Fig. 3.1 shows the BGS of a short section fiber located at the far end, with slightly different BFS to the rest of the uniform

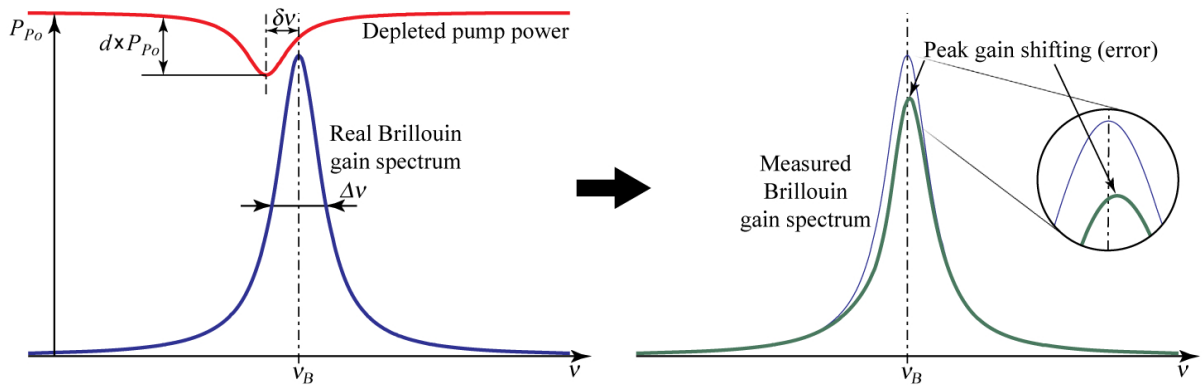

Figure 3.1: Distortion of the Brillouin gain spectrum due to the effect of pump pulse depletion frequency dependence, when scanning a fiber section displaced $\delta\nu$ MHz from the BFS of the fiber. © 2013 Optical Society of America [29].

sensing fiber. As it can be observed, the higher depletion of the pulse at certain frequencies induces a distortion on the retrieved gain spectrum that, consequently, generates a frequency shift of the BGS peak, and hence, an error on the determination of the BFS.

Notice that the depletion of the pump pulse takes place all along the sensing fiber, thus, the distortion of the BGS is more severe at the end of the propagation of the pump pulse, appearing the detrimental effects more significantly at the end of the fiber. This means that, the pulse depletion impairment occurs in a different location to where the depletion is actually originated. This is why this impairment is denominated as a non-local effect. Using Eq. (3.1) and Eq. (3.2), it is possible to express the depletion factor as a function of the probe power and the effective length of the fiber [29]:

$$d(L) = 1 - exp\left(-\frac{g_B}{A_{eff}} P_{Si} L_{eff}\right) \tag{3.3}$$

Note that the previous expression considers the maximum depletion of the pump signal, which occurs at the peak frequency of the Brillouin spectrum. Observe that the pulse depletion depends only on the probe power injected into the fiber, while it is independent on the pump power level and pulse duration. Therefore, the higher the probe power deployed, the higher the energy transferred, and hence, the larger the pump pulse depletion. Since the maximum depletion occurs at the frequency of the BFS and it is an cumulative effect, the most limiting probe power would be given when an uniform optical fiber is evaluated. From Eq. (3.3), it is easy to express the maximum tolerable injected probe power for a given depletion factor as follows [29]:

$$P_{Si} = -ln(1 - d(L))\frac{A_{eff}}{g_B L_{eff}} \tag{3.4}$$

Then, the error that is incurred on the determination of the BFS due to the distortion generated by the pulse depletion can be calculated. Assuming that we have a small depletion factor, $d < 0.2$, and the measurement error is much smaller than the full-width half-maximum (FWHM) of the gain spectrum, the error can be obtained from the following expression [29]:

$$\nu_e \cong \frac{-d\ \delta\nu}{\left(1 + 4\left(\frac{\delta\nu}{\Delta\nu_b}\right)^2\right)^2 - 2d\left(1 + 2\left(\frac{\delta\nu}{\Delta\nu_b}\right)^2\right)} \tag{3.5}$$

where $\delta\nu$ represents the BFS frequency difference between the long uniform sensing fiber and the short final fiber section with slightly different BFS. The minus sign indicates that the Brillouin gain peak is shifted to higher frequencies when the gain peak of the long segment is located at frequencies lower than that in the short segment. From Eq. (3.5), it is found that the error is maximum when the frequency difference between both fiber sections is approximately 1/4 of the FWHM [29]. On the contrary, the error is negligible when the BFS of the whole fiber is fairly uniform or, there is a large enough frequency difference that ensures there is no overlap between both spectra. Fig. 3.2 depicts the dependence of the maximum tolerable depletion factor d_{max} for a given normalized frequency error on the estimation of the BFS for a long sensing fiber ($L > L_{eff} = 22km$).

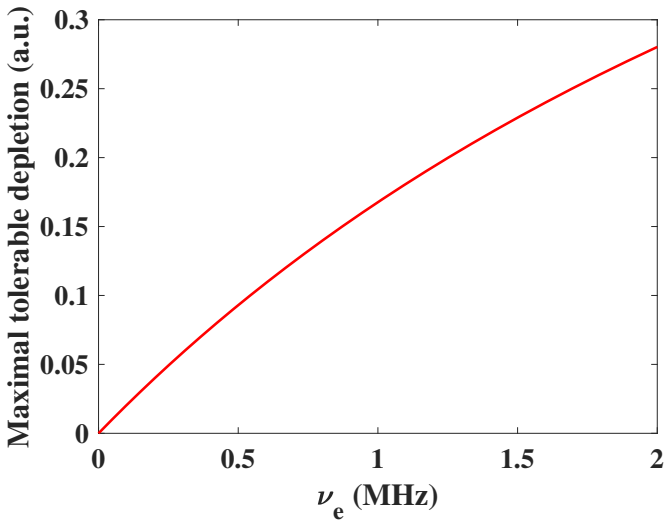

Figure 3.2: Maximum tolerable pump pulse depletion factor dependence on the BFS frequency estimation error.

As explained, pump pulse depletion directly imposes a limitation on the maximum probe wave power that can be injected into the sensing fiber, reducing the SNR of the measuring system. In order to mitigate the pump pulse depletion effect, many research contributions have been presented to solve this limitation during the last years. One of the first successful techniques that was proposed is the deployment of two balanced probe waves, the so-called dual-probe [88]. The fundamentals of the dual-probe wave configuration are depicted in Fig. 3.3. It is based on generating a balanced Brillouin interaction between both of the probe waves and a the pump wave that is equally separated in frequency from them. The advantage of using two symmetric probe waves is that the power transfered from the pump to the lower frequency probe in the gain process is compensated by the loss interaction with the higher frequency probe, giving rise to a negligible pump depletion [88]. Consequently, the net gain induced by the dual-probe wave upon the pump pulse is zero, mitigating and, even, completely canceling the pump depletion effect observed previously.

Another successful approach to supress first-order NLE is the use of the previously described self-heterodyne detection BOTDA sensor, which is a technique based on deploying a probe wave that is phase-modulated at a RF frequency [28]. The working principle is similar to a conventional BOTDA sensor, however, the interaction of the pump wave with one of the probe waves and subsequent RF detection, gives rise to a RF signal, whose phase-shift is strongly tolerant to any pump pulse power variation. The fundamentals of this technique have been introduced in chapter 2 and it will described in detail in chapter 5, as it has been also part of this thesis work.

Finally, one of the latest solutions presented to ameliorate NLE in BOTDA sensors implies the use of modulation or "dithering" of the optical wavelength of the light source [89]. Thanks to the wavelength modulation of the laser, a virtual BFS is generated along the fiber that allows to extend to a range of frequencies the effective SBS interaction between the pump pulse and the probe, and thus, reduce the depletion of the pump pulse. This

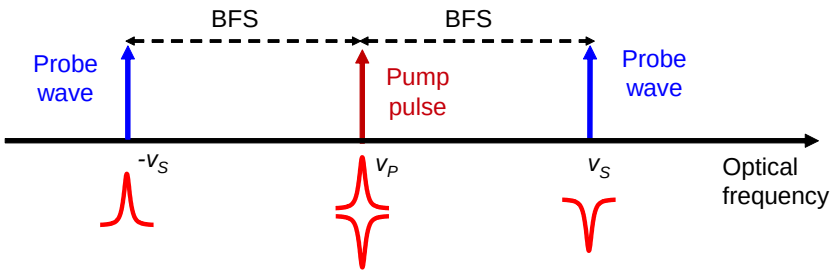

Figure 3.3: Brillouin interaction in a dual-probe wave BOTDA sensor. ν_S and ν_P are the optical frequencies of the probe and pump waves.

technique has been also devised by our research group and has demonstrated to completely compensate the detrimental effects of first-order NLE. The fundamentals of this method will be introduced in section 3.3.

3.2.2. Second-order NLE in BOTDA sensors

As it has been mentioned, one of the simplest and most successful methods to mitigate the detrimental effect of first-order NLE is the dual-probe wave configuration. However, in recent contributions, it has been shown that the compensation of the dual-probe wave technique is only valid to the first order. In particular, it has been found that there is a distortion of the pump pulse spectrum that is caused by the non-ideal overlap of the gain and loss spectra generated by the two probe waves [32].

The origin of this spectral distortion is represented in Fig. 3.4. As it can be observed, both probe waves are tuned to match the Brillouin gain and loss spectra of the pump pulse. As shown in Fig. 3.4 (a), there is a perfect overlap when the frequency difference between the pump and probe waves, $\nu_P - \nu_S$, equals the BFS, leading to an undistorted pump pulse spectrum. In contrast, if probe frequency is slightly up-shifted as displayed in Fig. 3.4 (b), or down-shifted as shown in Fig. 3.4 (c), the low frequencies of the pump pulse experience Brillouin loss, while higher frequencies experience Brillouin gain, and vice versa. This can occur for example during the scanning process, and thus, the resultant

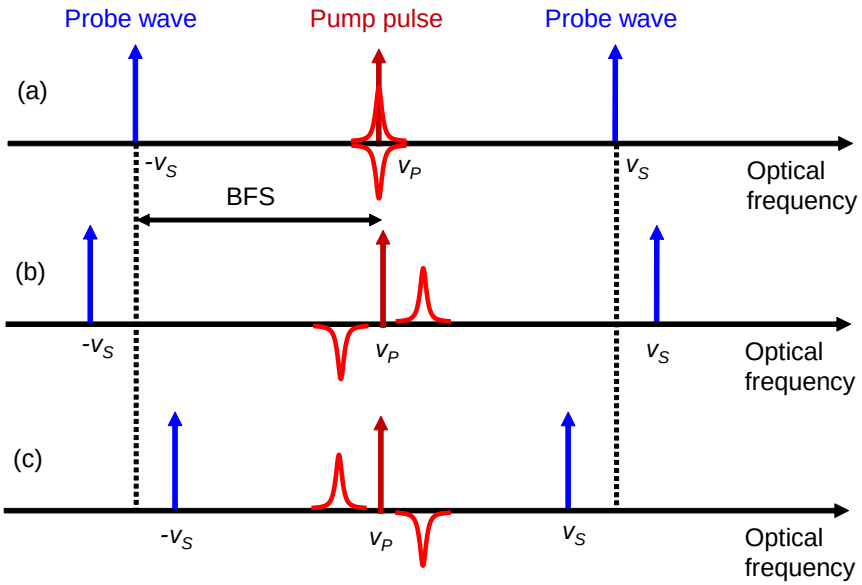

Figure 3.4: Brillouin interaction on the pump pulse in a dual-probe wave BOTDA sensor when the frequency difference between pump and probe waves is changed during the scanning process: (a) $\nu_P - \nu_S = \nu_B$, (b) $\nu_P - \nu_S > \nu_B$ and (c) $\nu_P - \nu_S < \nu_B$.

pump pulse spectrum is distorted, leading to a slightly up-shifted or down-shifted BGS spectrum. As a consequence, measurement errors on the determination of the BFS of the sensing fiber are experienced [87].

It has been found that this distortion of the pump pulses has a strong impact on the measured BGS, which worsens as the probe wave power increases, generating a distorted BGS mainly at the end of the fiber. Actually, in order to reach 1-MHz measurement error for a typical SMF, the maximum probe wave power that can be deployed was found to be -3 dBm per each probe wave [32]. This limit of power is far from the that imposed by the Brillouin threshold, which is around 7 dBm for typical SMF, corresponding to the ultimate probe wave power that can be deployed.

As a result of the community research effort, several solutions have been proposed to overcome the pump pulse spectral distortion. One of them is the modification of the scanning method by fixing the spectral separation between the probe waves [90]. In this scheme, the pump wave frequency is swept to acquire the BGS information, avoiding any spectral distortion of the pump pulse and providing an undistorted pump pulse spectrum. Moreover, it allows to increase the power of the probe waves up to the Brillouin threshold. However, this solution is only valid if the BFS of the sensing fiber is fairly uniform. For instance, if there are two long fiber segments with different BFS, the frequency detuning of the probe waves must be adjusted to coincide with one of the BFS of the fibers. So, both probes will be correctly tuned with the pump pulse when they counter-propagate along the first fiber section, compensating the pump pulse depletion distortion. In contrast, during the second fiber section, the frequency detuning of both probes does not match with the BFS, leading to the onset of the same problem as before and obtaining similar results to the conventional single-tone probe wave setup [29, 91].

A better approach is the use of two pairs of orthogonally-polarized dual-tone probe waves with opposite frequency scanning direction, which allows to reach a zero net gain and solve the pump pulse distortion problem even if the sensing fiber has two different BFS sections [92]. Nevertheless, this method increases significantly the complexity of the setup.

In this line, our research group has demonstrated a mitigation method to overcome the NLE caused by the pulse distortion. The proposed solution is based on the same working principle to the dithering of the light source technique mentioned before, although in this case, the frequency modulation is generated in the probe wave instead of the LD [87]. Fig. 3.5 (a) depicts the fundamentals of the dithering technique when the probe wave is modulated for instance with a saw-tooth shape waveform [50]. Different waveforms can be deployed as well [87].

In this technique, the modulated dual-probe wave varies its frequency around the BFS of the fiber following a saw-tooth shape. This signal is synchronized with the pump pulse generation process, so that, series of pump pulses that propagate along the fiber experience the same wavelength of the probe waves at periodic locations. Since the probe wave frequency follows a saw-tooth shape, its frequency varies in every position of the fiber, so that, the effective SBS gain induced by the pump pulse to the frequency modulated probe wave gives rise to a virtual BFS profile with the shape of the FM.

Figure 3.5 (b) depicts the BGS scanning process for the dithering of the probe wave technique. Since the delay between the FM of the probe wave and the generation of the pump pulse can be easily controlled, the BGS at a given position of the sensing fiber can be retrieved by simply varying the delay between both signals [87]. Note that, in a probe-dithering setup, the number of delay steps is equal to the number of scanned frequencies on the BGS. This is determined by the relation between the peak-to-peak modulation frequency applied to the probe wave (equal to the total frequency range scanned) and the desired frequency step. Therefore, this means that there is no penalty on measurement time in comparison to the conventional BOTDA frequency scan.

Overall, the modulation of the probe wave has the benefit of spreading the Brillouin interaction to a larger frequency range, giving rise to a reduction of the depletion of the pump pulse during its propagation along the sensing fiber. Moreover, when a double probe wave is deployed, both probes induce a broad gain and loss spectrum upon the pump pulse that compensates each other, avoiding the spectral distortion of the pump

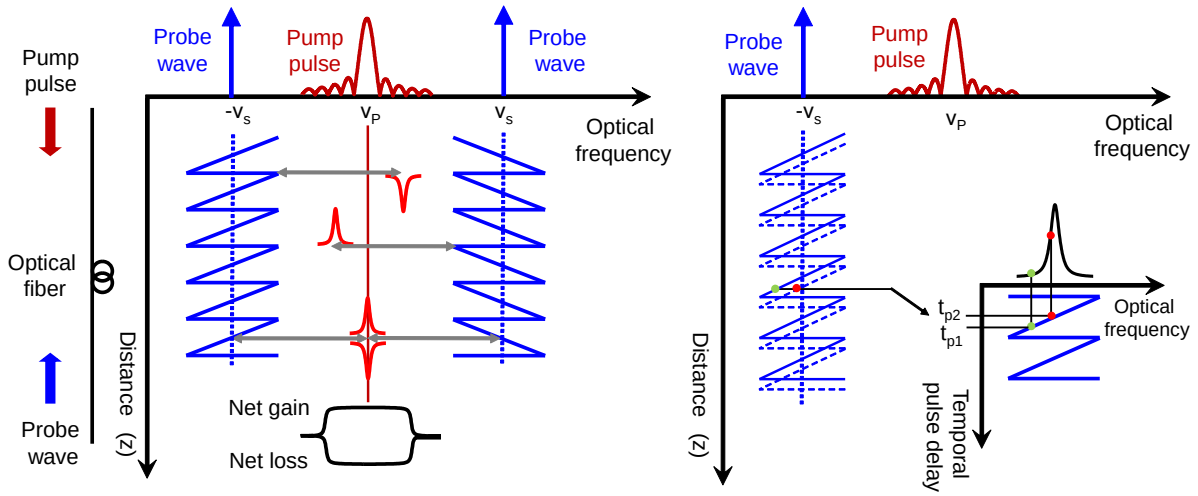

Figure 3.5: (a) Fundamentals of the Brillouin interaction in a dual-probe wave BOTDA sensor using the dithering technique and (b) scanning process of the BGS using the delay of the FM probe.

pulse [87, 50]. Furthermore, another advantage of modulating the wavelength of the probe is to increase the effective Brillouin threshold of the fiber, allowing to further increase the probe wave power injected in the fiber, up to 12 dBm [87].

As a result of the investigation in this thesis, a new BOTDA scheme is presented in chapter 4, in which the dithering of the probe wave is combined with pulse coding techniques to demonstrate a devised solution to solve the impairment of the nonlinear amplification undergone by BOTDA sensors deploying coding techniques.

3.2.3. NLE induced by limited ER pump pulses in BOTDA sensors

As it has been already mentioned in the introduction of this chapter, another significant constraint for BOTDA sensors comes from the limited ER of the pump pulses and the transient response of the EDFA deployed to amplify the pump pulsed signal. Several limitations have been recently reported by our research group with important consequences regarding the use of limited ER pump pulses [34].

In order to clearly understand this problem, it is necessary to clarify that, in real applications, the most common devices used to generate pump pulses have a limited ER. This means that the pump pulse is not perfectly generated, and consequently, it is on top of continuous pump power, called pedestal of the pump wave. As it is depicted in Fig. 3.6 (a), the pump pulse is composed by three parts: a continuous wave called leading pedestal, which is followed by the pulse itself, and another section of CW called trailing pedestal. Therefore, there are three sequential Brillouin interactions during the

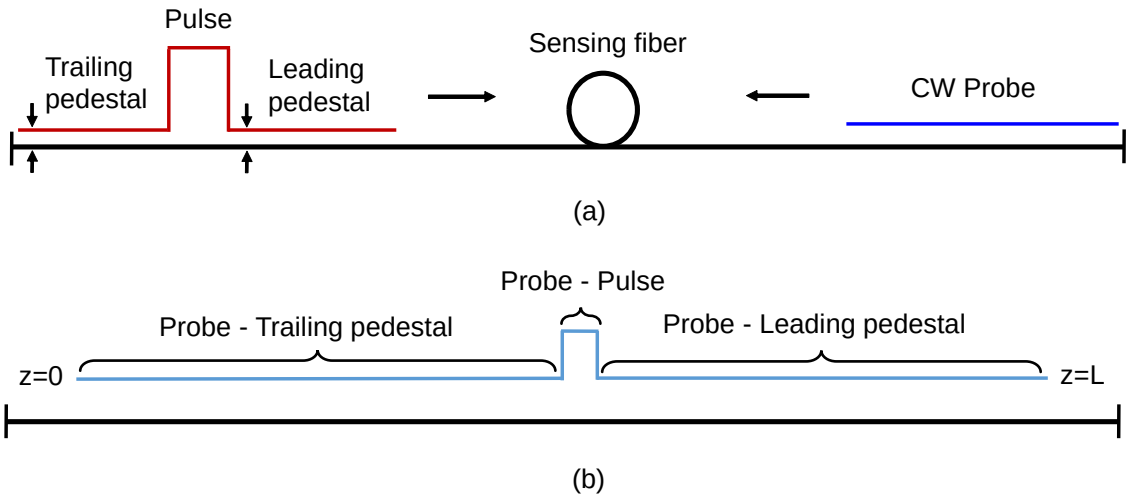

Figure 3.6: (a) Schematic depiction of probe and pump pulse waves and (b) SBS interaction along the sensing fiber.

propagation of the pump along the sensing fiber.

Figure 3.6 (b) represents the SBS interaction between probe and pump waves along the sensing fiber at a given time, t. Observe that, when the pump is injected into the optical fiber, firstly, the leading pedestal interacts with the probe, generating a Brillouin amplification and increasing the probe power. Then, the probe meets the pulse itself, leading to another energy transfer from the pump to probe wave, which is the gain commonly used in BOTDA sensors to obtain the sensing information. Finally, the trailing pedestal that follows the pulse, counter-propagates with the probe wave generating an additional amplification of the probe.

Therefore, it is clear that the resultant Brillouin amplification of the probe wave is larger when a pump pulse with limited ER is deployed [93]. Actually, the extra gain suffered by the probe due to the interaction with the pedestal of the pump is useless, and it has been shown to degrade the SNR and precision of the BFS measurement [94]. Fig. 3.7 schematically shows the Brillouin gain that corresponds to the interaction between probe and pump pedestal (blue line), and the Brillouin gain due to the pulse (red line). Notice that the useful signal to obtain the BFS measurement corresponds just to the Brillouin gain in red color, which can be recovered subtracting the gain produced by the former part to the latter and normalizing using the detected probe signal without the pulse contribution. However, this measurement process leads to an important waste of the full-scale dynamic range of the signal acquisition device, generating a higher quantization noise on the measurement and degradation of the BFS measurement [93].

Apart from this limitation, our research group, including work performed during this

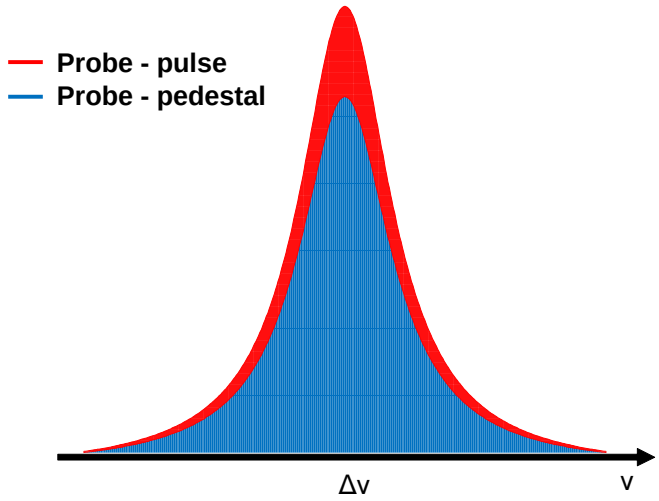

Figure 3.7: Brillouin gain spectrum due to the interaction between probe and pump wave with limited ER.

thesis, has recently found two new impairments that probably were previously observed in experiments many times by other researchers, but whose origins and limitations for the performance of BOTDA sensors had not been analyzed [34]. Moreover, it has been shown that these constraints induce detrimental effects to either single-probe or dual-probe BOTDA setups.

The first detrimental effect is caused by the increased depletion experienced by the trailing pedestal, due to its interaction with probe wavefronts that have been previously amplified by the pulse itself, giving rise to a reduced amplification of the probe in its interaction with the trailing pedestal. Basically, the problem is originated on the additional amplification that the probe wave experiences when it meets the pump pulse. Since the probe wave interacts via SBS with the pump pulse, the energy transferred from the latter to the probe wave leads to an extra amplification of the probe. This means that, when the trailing pedestal that follows the pump pulse counter-propagates with the amplified probe wave, the latter will further deplete the former, and its power will be reduced. Thus, the SBS interaction between the probe and the depleted trailing pedestal, gives rise to a lower amplification of the probe wave with respect to the leading pedestal, leading to a severe distortion of the BGS measurements. In order to understand the origin of this measurement distortion, it is necessary to remember that, as explained previously, the normalized BOTDA trace is obtained by subtracting the gain measured when there is no pulse in the fiber, i.e., before the input of the pulse, from the total measured gain. Since the probe wave has experienced a lower amplification during its interaction with the trailing pedestal, the gain measured without pulse is actually larger than the portion of probe gain due to the pedestal.

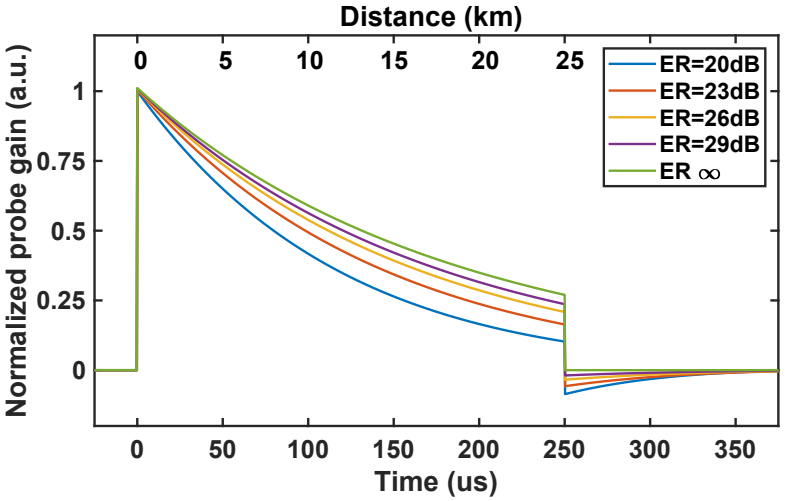

Figure 3.8: Calculation of the Brillouin gain profile influenced by pump pedestal depletion.

Figure 3.8 displays the calculated Brillouin gain profile for different ER pump pulses using a theoretical model developed in a previous research work [34]. As it is observed, when the pulse enters the sensing fiber, the gain profile is completely independent of the ER of the pulse. This is because there is no interaction between probe and trailing pedestal, or at least, very small. So, the gain without a pulse in the fiber is similar to the gain generated by the pedestal, and the normalization process to obtain the Brillouin gain is correct. However, when the pulse propagates along the sensing fiber, there is a larger interaction between probe and trailing pedestal, leading to a smaller amplification of the probe and generating an overestimation of the pedestal gain, giving rise to an apparent reduction of the measured Brillouin gain profile after normalization. Note that the detected probe wave power right after the pulse has left the fiber experiences an abnormal gain. This feature depicts an abrupt fall to negative gains followed by a slow recovery. This response is caused by the fact that the probe wavefronts that enter into the fiber after the pulse has exited the sensing fiber, meet the depleted trailing pedestal suffering a reduced Brillouin gain. These impairments are more severe for lower ER of the pump pulses, as it can be observed in the simulation shown in Fig. 3.8. Moreover, with the help of work performed during this thesis, it has been demonstrated that these constraints introduce a distortion in the measured BGS similar to that induced by the pump pulse depletion, generating an analogous impairment on the determination of the BFS of the fiber [34].

The second impairment related to the limited ER of the pump pulses that we have found is due to the interaction between the pulse pedestal and the transient response of the EDFA that are normally deployed to amplify the pump wave before its injection into the sensing fiber. It is well known that most of EDFAs have a transient response when amplifying pulsed signals, which is due to the long recovery time of the population inversion of the erbium ions after amplifying an optical pulse [95, 96]. The problem of using this type of EDFAs in BOTDA sensors with low ER pulses is that the transient response distorts the pump wave shape as it provides a different instantaneous gain before and after the arrival of the pulse. In particular, when the pulse enters the EDFA, the population inversion in the EDFA is depleted and, consequently, the amplification of the pump wave suffers an instantaneous reduction, showing less gain for the trailing pedestal than for leading pedestal. Then, the amplification is progressively recovered, however, the resultant trailing pedestal power undergoes a distortion as shown in Fig. 3.9 (a). This alteration of the pump pedestal level induces additional NLE on the pulse. The net effect of these two constraints is the generation of an error in the determination of the BFS along the sensing fiber that is increased for smaller ER [34].

It has been demonstrated that the impairments caused by the distortion of the pump pulse pedestal due to the transient response of the EDFA are similar to those originated by the trailing pedestal depletion [34]. In fact, the detected Brillouin gain is reduced when the probe wave interacts with the distorted trailing pedestal, generating an additional depletion factor that induces new NLE caused by the particular response of the EDFA deployed in the system. The interaction between the probe and the distorted pump wave is schematically depicted in Fig. 3.9 (b) and (c).

The described constraints due to the use of limited ER pump pulses and the transient response of EDFAs are particularly relevant when selecting the devices used to shape the pump pulses in BOTDA sensors. These, are primarily of two types: semiconductor optical amplifier (SOA), which is used as optical switch, and Mach Zehnder-Electrooptic modulator (MZ-EOM). SOA switches offer large ER, most of them over 45 dB. Therefore, the impairments related to ER-induced measurement errors can be negligible in sensor configurations that employ SOA to generate the pulsed signal. However, the rise time of commercially available SOAs is typically restricted to around 1 ns, limiting the spatial resolution of the sensor. Especially when spatial resolution below 1 m is targeted

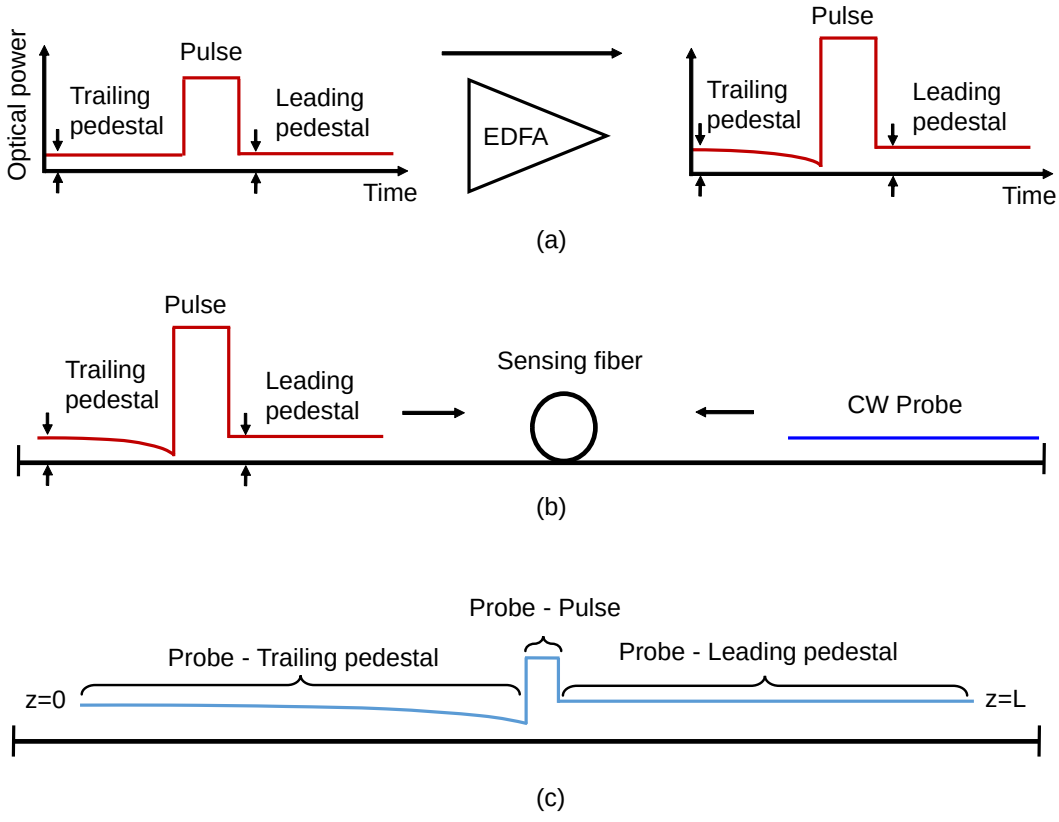

Figure 3.9: Fundamentals of the detrimental effect caused by EDFA transient response.

by deploying high-resolution techniques such as differential pulse pair [43]. The other alternative is the deployment of MZ-EOM to generate the pump pulses, which tend to be more cost-effective than SOA. Moreover, they have a broad modulation bandwidth and are able to generate extremely sharp pulses. However, the ER of standard MZ-EOMs is in the 20 to the 30-dB range, which has been shown to be insufficient to get rid of ER-related detrimental effects [34]. In the market, there are available MZ-EOMs with high ER, however, in order to obtain the maximum suppression signal for the "off" state, fine tuning on the device is necessary, leading to a cost rising. This is undesirable, as cost-effectiveness is of paramount importance to provide widespread adoption of the BOTDA technology outside current niche applications.

In this sense, during this thesis research work, a method to mitigate ER-related NLE has been devised and demonstrated. This solution relies on the same working principle than the one explained in section 3.2.2, the probe dithering technique. However, in this case, the dithering is applied to the light source used to generate both probe and pump waves, obtaining a further benefit. The rest of this chapter is focused on presenting this technique that is based on reducing the interaction between the probe wave and pedestal of the pump wave, allowing to ameliorate or even completely cancel, the distortion of the Brillouin interaction between the pump wave and the probe wave used for sensing.

3.3. Fundamentals of the dithering method for compensation of ER-related NLE

The fundamentals of the proposed technique are schematically depicted in Fig. 3.10. As it is shown, the method relies on the modulation of the optical frequency, f_m, of the pump and probe waves. The simultaneous modulation of both waves confines the effective Brillouin interaction between the pulse pedestal and the probe wave to specific locations along the sensing fiber, compensating the detrimental effects of deploying limited ER pump pulse. In addition, as it will be demonstrated, the simultaneous modulation of pump and probe waves permits to mitigate first and second-order NLE, which are originated by pulse depletion and pump pulse distortion, respectively, being the first method capable of mitigating all NLE at once. As it will be seen in chapter 7, the working principle is similar to the principles followed in BOCDA sensors, localizing the Brillouin interaction to those locations where the measurement is desired [66].

One way to perform the simultaneous modulation of pump and probe waves is to take advantage of the chirp (wavelength modulation) associated with the direct current modulation of a semiconductor laser used as a common source for both waves. Since

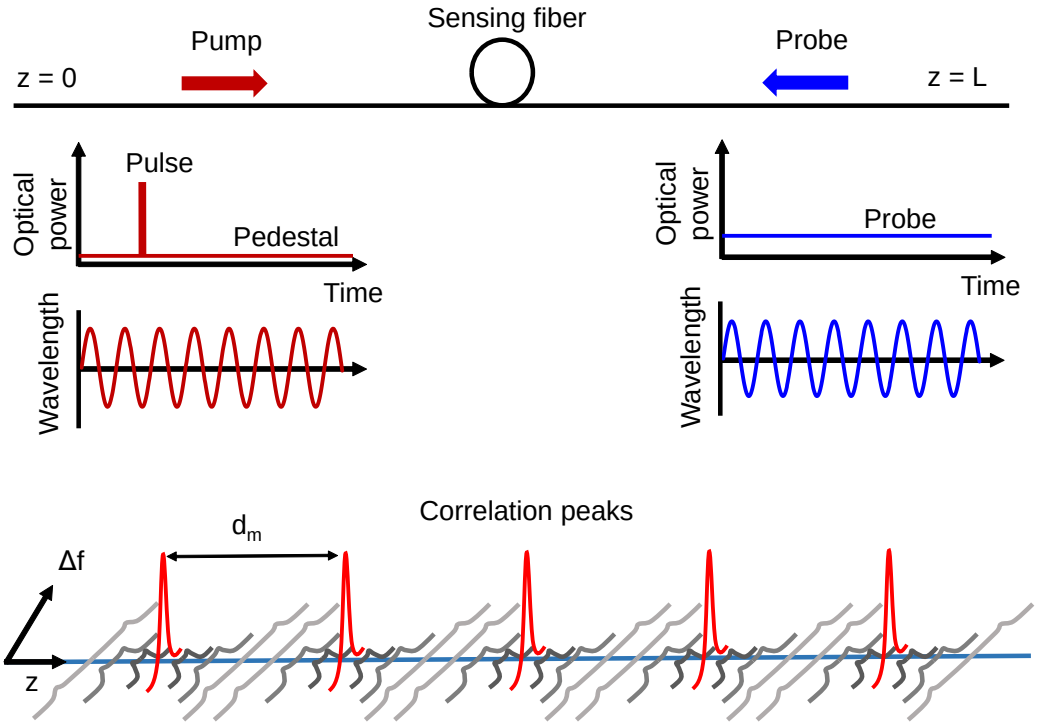

Figure 3.10: Fundamentals of the light source wavelength modulation technique to compensate ER-originated NLE.

pump and probe waves are modulated with the same sinewave signal of frequency f_m before being counter-propagated in the sensing fiber, their particular frequency at any given instant t and a certain location z along the fiber can be expressed as:

$$f_{pump} = \Delta f_0 + \Delta f_p \cdot cos(2\pi f_m t) \tag{3.6a}$$

$$f_{probe} = \Delta f_p \cdot cos(2\pi f_m t + \Delta\theta) \tag{3.6b}$$

where Δf_p is the peak frequency deviation of the FM modulation introduced on the pump and probe waves, Δf_0 is their static frequency difference, which is swept during the measurement process in order to scan the Brillouin spectra and $\Delta\theta$ is the phase difference between the two counter-propagated optical waves. The frequency difference between both propagating waves at a certain time t and position z can be calculated from Eq. (3.6a) and Eq. (3.6b):

$$\Delta f(t,z) = \Delta f_0 \mp 2\Delta f_p \cdot cos\left(2\pi f_m t \pm \frac{\Delta\theta}{2}\right) \cdot sin\left(\frac{\Delta\theta}{2}\right) \tag{3.7}$$

Therefore, the frequency difference between the pump pedestal and the probe becomes a

sinusoidal function along the fiber that behaves like a standing wave. There are positions where the frequency difference between both waves is constant, which corresponds to fiber positions where both are high correlated. As a result, the Brillouin interaction between the pump pedestal and the probe at these CP is highly efficient, whereas outside these locations the resultant interaction becomes negligible. This means that the probe wavefront will experience significant Brillouin interaction with the pedestal of the pump wave just at certain locations of the fiber. In contrast, at all other locations in the fiber, the pedestal and the probe wavefronts become uncorrelated, reducing strongly the energy transfer between both waves. Hence, the devised method permits to successfully reduce the effective Brillouin interaction between probe and pump pedestal and mitigate the impairments previously explained: the NLE-related to limited ER pump pulses and the detrimental effects of the EDFA transient response. Apart from this beneficial effect, the dithering of the light source also permits to increase the Brillouin threshold and compensate the first and second-order NLE, as it is demonstrated in section 3.5.3.

Notice that the modulation frequency used to dither the light source defines the distance between CP, identically to the method that is used in BOCDA sensors [66]. Hence, the width of the CP, Δz, and the distance between peaks, d_m, are given by [66]:

$$\Delta z = \frac{v_g \cdot \Delta\nu_B}{2\pi f_m \cdot \Delta f_p} \tag{3.8}$$

$$d_m = \frac{v_g}{2f_m} \tag{3.9}$$

where $\Delta\nu_B$ is the Brillouin gain linewidth and ν_g is the velocity group. Therefore, the ratio between both quantities can be regarded as a measurement of the reduction of the total interaction between the pump pedestal and the probe wavefronts during the propagation along the fiber:

$$\frac{\Delta z}{d_m} = \frac{\Delta\nu_B}{\pi \cdot \Delta f_p} \tag{3.10}$$

From this expression, it is possible to conclude that the larger the frequency deviation of the FM of the pump and probe waves, the larger the mitigation of ER-related impairments. Thus, a solution to successfully overcome NLE would be to increase the frequency deviation. However, the maximum Δf_p is limited, as it implies a larger frequency scan range, and thus, an increment of the measurement time.

It has been observed that the modulation of the frequency of the probe wave has an

equivalent effect to the synthesis of a virtual BFS profile along the fiber [89]. For instance, if the probe wave was modulated with a sinusoidal signal and a sensing fiber with uniform BFS was measured with a BOTDA sensor, the retrieved BFS distribution would appear as if it had a sinewave shape along the fiber distance. The amplitude of the sinusoidal BFS distribution depends on Δf_p. Therefore, an increment of Δf_p would lead to a need for increasing the frequency scan range of the BOTDA sensor. Hence, a measurement time penalty is induced in the measurement system, given by:

$$T = \frac{2\Delta f_p + \Delta f_T}{\Delta f_T} \tag{3.11}$$

where Δf_T is the frequency range that would be swept in the conventional BOTDA when the dithering technique is not deployed. However, in a real application, this penalty can be rather small. For instance, if we assume a typical long-range measurement with Δf_T=1 GHz, a realistic range to cover sensing fibers with different BFS, and Δf_p=100 MHz, the penalty would be just a 20% increment in the measurement time. Thus, contrary to the dithering of the probe wave, in this technique there is a penalty on measurement time in comparison to the conventional BOTDA frequency scan. This is the main disadvantage of this technique with respect to the dithering of the probe wave described previously.

The value of the f_m is conditioned by the interaction between the probe and the pump wave along the sensing fiber. Actually, f_m is determined by similar trade-offs than when probe dithering is deployed to mitigate conventional NLE [89]. In particular, if f_m is excessively increased in order to reduce NLE, a penalty would be induced on the accuracy of the sensor due to the interaction of the pump pulse with a segment of probe wave with a range of frequencies, reducing the Brillouin interaction measured. Whereas, if f_m value is reduced under a given value, NLE would not be completely compensated due to the fact that the Brillouin gain is not spread into enough frequencies and pulse depletion and pulse distortion would appear. This value depends on the sensing fiber length, L, and Δf_p.

This technique offers good performance when fibers with different BFS are tested, however, if the difference is large, it may be necessary to deploy another technique that has been recently deployed for tracking BFS changes [97].

Finally, note that the source optical dithering method presented in this chapter not only reduces the NLE originated by the limited ER of pump pulses, but also retains the advantages in terms of mitigation of both NLE originated by pump depletion and

NLE originated by pump spectral distortion as well as providing an increased Brillouin threshold [89].

3.4. Experimental setup

Figure 3.11 depicts the dual-probe BOTDA setup that was deployed to experimentally demonstrate the compensation of the NLE caused by the limited ER of the pump pulses and the effect of the transient response of the EDFA. Note that this is a conventional dual-probe BOTDA setup with the only addition of the chirp modulation of the optical source.

The optical source was a 1560-nm distributed feedback laser whose injection current was modulated by a 80-kHz sinusoid from a signal generator that was synchronized to the pulse generator. The amplitude of this modulation was set to get a peak frequency deviation for the laser chirp of 100 MHz. The modulated optical signal was divided by a coupler into two branches. In the upper branch, the pump pulse wave was shaped by using either a SOA, when deploying pulses with a high ER of 45 dB, or a MZ-EOM, when generating pulses with 26-dB ER. In both cases, the corresponding optical device was driven by an electrical pulse generator. Then, an EDFA was used to amplify the pump pulses. Its output was filtered to reduce the ASE and directed to a polarization scrambler (PS) before launching into the sensing fiber.

Two different EDFAs were deployed in the experiments presented in the next section to compare their influence on NLE. The first one, which we will denominate EDFA I, was a specialty EDFA designed for pulse amplification (Amonics Ltd. Pulsed EDFA) that offered a minimal transient response and hence negligible trailing pedestal distortion [34]. The second amplifier, EDFA II, was a conventional optical amplifier (MPB Communica-

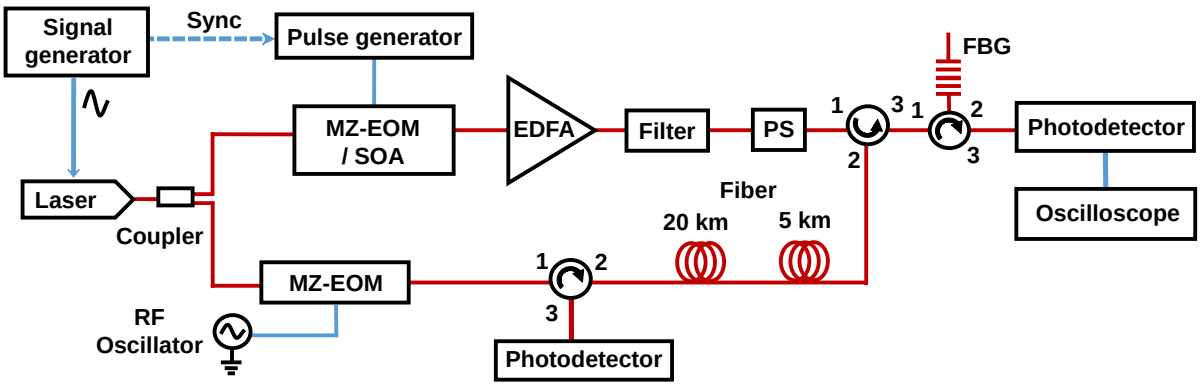

Figure 3.11: Experimental setup deployed to demonstrate the capabilities of the technique to mitigate ER-related NLE in BOTDA sensors.

tions Inc.) with a significant transient response. In both cases, the pump peak power was limited to 20 dBm, in order to avoid MI effects in the fiber [36], and the pump pulse duration was set to 20 ns, corresponding to approximately 2-m spatial resolution for the sensor.

In the lower branch of the setup, the probe wave was generated using another MZ-EOM driven by a RF generator that provided modulation frequencies close to the BFS of the fiber. This modulator was biased for minimum transmission so as to generate a double-sideband suppressed-carrier (DSB-SC) modulation. Thus, a dual-probe wave with a power of -3 dBm per sideband was injected into the fiber. In fact, this is the threshold for the onset of significant second-order NLE [32]. Finally, once the probe wave exited the sensing fiber, the highest wavelength of the probe wave was filtered and captured in a detector followed by an oscilloscope.

Since the particular frequency shift between the pulse and the probe wave at each location of the fiber needs to be known and controlled to retrieve the BGS, the pump pulse generation must be synchronized with the FM of the optical waves.

The experimental measurements that we performed to validate the proposed method were carried out along two concatenated standard SMF (ITU G.652) spools of 5-km and 20-km length. Both spools had fairly uniform BFS distribution, but slightly different Brillouin gain coefficient. In addition, two hotspots were prepared along the sensing link using a climatic chamber: one after the first spool, at z=5 km, and another at the end of the link at z=25 km. These hotspots were held in a thermal bath at a temperature 10°C over the rest of the fiber.

3.5. Experimental results

Experimental measurements were performed to demonstrate the capabilities of the optical source modulation technique to overcome for the first time to our knowledge, all the detrimental effects caused by first-order and second-order NLE along with the impairments caused by the used of limited ER pump pulses in BOTDA sensors.

3.5.1. Distributed Brillouin gain measurements compensation

Figure 3.12 depicts measurements of the probe gain profile along the fiber for a frequency separation between pump and probe waves close to the mean BFS of the sensing fiber. Different measurements are shown for the two EDFAs (EDFA I and EDFA II) deploying either high or medium ER pulses. Both graphs include the measurement of the probe gain profile for pulses with a high ER of 45dB generated using the SOA switch.

These measurements serve as a reference (blue line), inasmuch as the high ER pump pulses ensure that there is no distortion due to ER-related NLE [34]. Notice that there is a small discontinuity in gain at z=5 km, which is due to a slight difference of the Brillouin gain coefficient for the two fiber spools deployed in the sensing link.

Figure 3.12 (a) depicts the measurement without using optical source dithering. Observe that the green trace shows the measurement for a pump pulse ER of 26 dB, which has been amplified using EDFA I that has a negligible transient response. In this case, only the detrimental effects of the increased depletion of the pump pulse and pulse pedestal by the probe are observed [34]. The depletion effect is displayed as a gradual reduction of the gain along the fiber and also by the existence of a gain variation of the probe wavefronts even after the pulse has exited the fiber. The gain reduction along the fiber is partly due to the increased depletion of the pulse by the interaction with a probe wave that has been previously amplified by the leading pedestal of the pulse, and partly due to the depletion

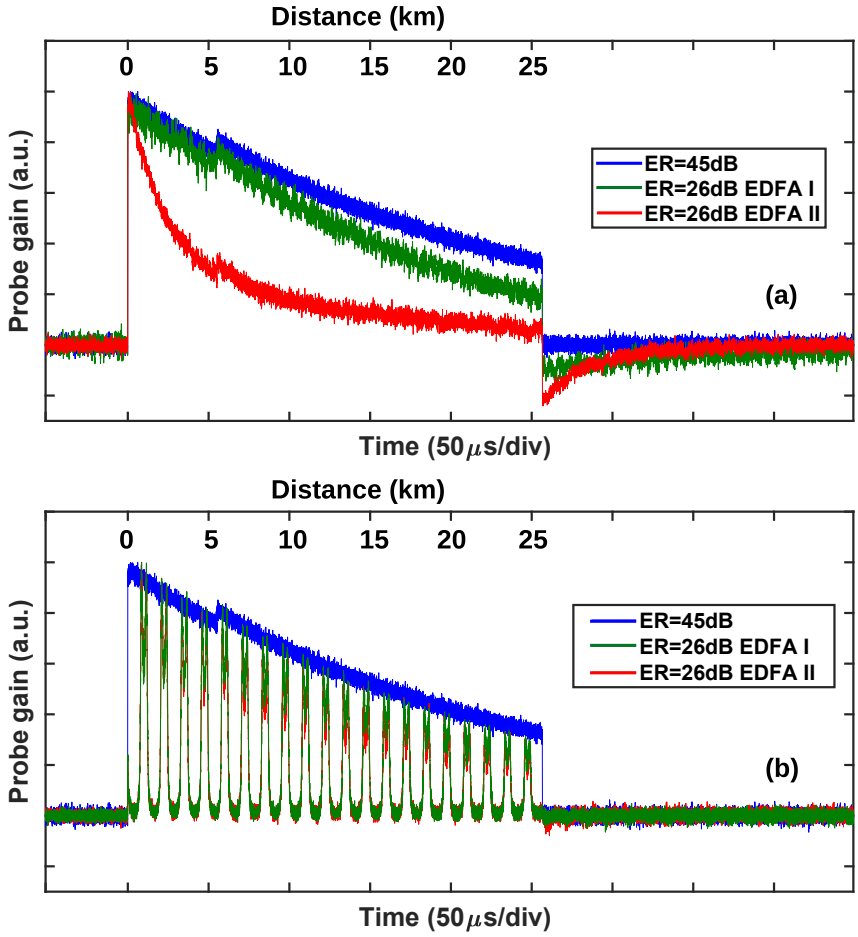

Figure 3.12: Probe gain profile measured along the fiber for different ER values of the pump pulse, using either EDFA I or EDFA II, (a) without dithering of the light source and (b) when the dithering is turned on.

of the trailing pedestal; whereas the sharp variation feature at the end of the fiber is solely originated by the depletion of the trailing pedestal of the pulse [34].

In case the conventional EDFA (EFDA II) is deployed to amplify the pump pulses, the gain profile measured along the fiber distance suffers even stronger distortion (red line). In this case, the gain measured along the whole fiber is severely affected by the distortion from the very first kilometers. Moreover, the gain reduction after the pulse has left the fiber is sharply increased, followed by a slow recovery of the measured gain. These impairments are caused by the distortion suffered on the trailing pedestal of the pulse when it is amplified in the conventional EDFA, generating a transient response on the amplified signal [34]. As it will be shown, these distortions of the measured probe gain lead to great errors in BFS measurements, particularly at the second hotspot where the detected signal is more distorted.

Figure 3.12 (b) depicts the measurement of the distributed Brillouin gain when the optical source frequency is dithered. It can be observed that, contrary to previous results, the measurements for the low ER pump pulses (26 dB) are identical in this case for both EDFA. Notice that the Brillouin gain traces display a series of "spikes" along the sensing fiber. The reason for these peaks is explained in Fig. 3.13, where the full Brillouin gain spectra distribution measured along the fiber is presented. This figure highlights the virtual BFS profile that is created by the probe wave wavelength modulation [89]. For a fiber with an approximately uniform BFS, this synthesized BFS profile follows the shape of the modulation, a sinusoid in this case. The correct BFS is obtained after subtraction

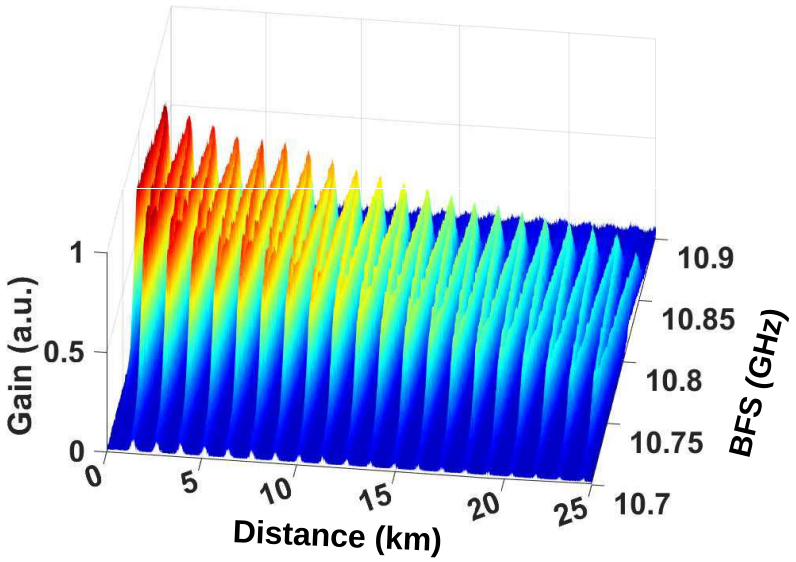

Figure 3.13: Brillouin spectra distribution measured along the fiber when the light source frequency is modulated with a sinusoid.

of the known sinusoidal modulation from the measured BFS.

In Fig. 3.12 (b), the Brillouin gain along the fiber for just one of the frequency differences between the pump and probe during the scanning process is displayed. As it is observed, gain peaks appear at positions given by the sinusoidal variation of the BFS along the fiber. Nevertheless, it can be seen that the gain peaks obtained with the dithering method perfectly match with the gain distribution measured for high ER pulses. This means that the gain distortion introduced by ER-originated NLE is correctly compensated applying the dithering technique. Furthermore, another demonstration of the good performance of the proposed method is that the probe gain detected right after the pulse has exited the fiber is completely flat. Contrary to the measurements obtained with the conventional system, the sudden change in amplitude and slow recovery seen in Fig. 3.12 (a) disappears when the light source is dithered.

Additionally, it has been also observed that the Brillouin gain experienced by the probe wave due to the interaction with the leading pedestal of the pulse when the dithering method is deployed in the 26-dB ER pulse case, is reduced by 7.45 dB (from 18.24 dB to 10.79 dB).

3.5.2. Pump pulse depletion compensation

In order to experimentally demonstrate the compensation of the pump depletion effect undergone in previous measurements, the optical pulse power was acquired after their propagation along the sensing fiber. Fig. 3.14 depicts the depletion of the pump pulses for different combinations of ER of the pump pulses, EDFA type, and use or not of the dithering method.

For instance, Fig. 3.14 (a) depicts the depletion of the 45-dB ER pump pulses generated with the SOA when using the EDFA I to amplify the pulses (blue line). The pump pulses were detected at the output of the sensing fiber and its shape was also measured when the probe wave was off. It is displayed to highlight that pulse depletion is negligible when a the SOA is deployed. Therefore, it is clear that the dual-probe setup is able to completely compensate the depletion of the pulses and that there are no problems related to the ER of these pump pulses.

Figure 3.14 (b) depicts the depletion of the 26-dB ER pulses generated using the MZ-EOM and two different EDFAs to amplified the pulse. Similarly, measurements turning on and off the probe wave were performed to quantify the depletion. In this case, there is a depletion of the pump pulse that reaches a maximum of around 10%. This depletion is similar for both EDFAs. This means that depletion of the pump pulses de-

pends neither on the transients effects of the EDFA nor on the trailing pedestal of the pulse. In fact, the increasing depletion of the pulses caused by first-order NLE is only due to their interaction with probe wavefronts that have been previously amplified by the leading pedestal of the pulse [34].

Finally, Fig. 3.14 (c) depicts the pump depletion once the dithering of the optical source is activated. Observe that, deploying the dithering technique, apart from mitigating the impairments brougt by deploying limited-ER pump pulses, the pump depletion due to first-order NLE is also suppressed, with a less than 1% residual depletion.

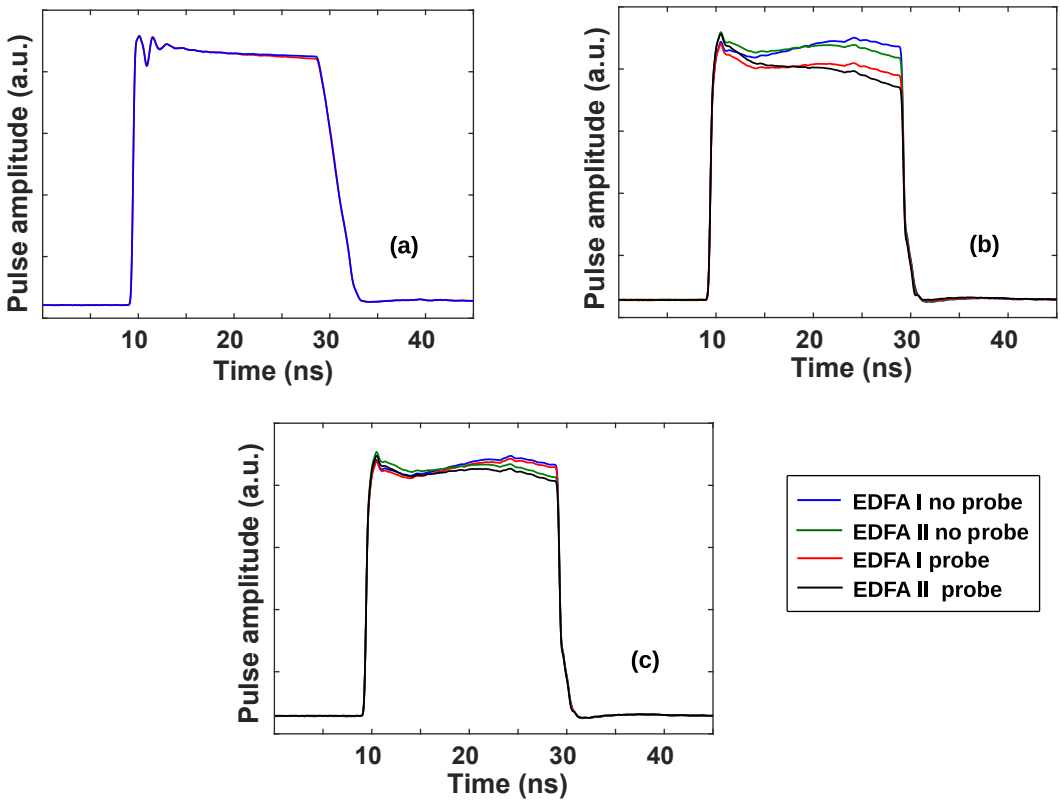

Figure 3.14: Depletion of the pump pulses at the output of the fiber (a) using the SOA to generate the pulses, (b) using the MZ-EOM to generate the pulses and (c) using the MZ-EOM to generate the pulses and deploying the source dithering technique.

3.5.3. Pump pulse spectral distortion compensation

As said previously, the proposed technique also compensates the impairments brought by second-order NLE. In order to demonstrate this, the probe wave power was slightly increased over the second-order NLE power threshold, to around -1 dBm per sideband. In the same way as for the pump depletion compensation, Fig. 3.15 depicts the beneficial effects of the dithering technique on the distortion of the pump pulses shape. These

figures show the pump pulses shape after their propagation along the sensing fiber for all the scanned frequencies.

Figure 3.15 (a) displays the detected pump pulses when a SOA is used to generate pulses with 45-dB ER and the EDFA I was deployed to amplify the pulses. As it can be observed, the detected pulse shape is similar for all the scanned frequencies, showing a negligible dependence of the pulse distortion on the frequency detuning. Whereas, Fig. 3.15 (b) depicts the similar measured pump pulses shape when pulses with 26-dB ER are deployed. In this case, the modulation to the light source was not applied, and consequently, an important distortion of the pump pulses shape is detected, observing severe power variations depending on the frequency detuning deployed. In order to quantify this impairment, the depletion of the pump pulses has been measured, reaching values near the 30%. Furthermore, the depletion experienced using the two EDFAs was measured, retrieving a similar response, which means that the detrimental effect induced by the EDFAs is independent on the trailing pedestal depletion. Finally, Fig. 3.15 (c) highlights

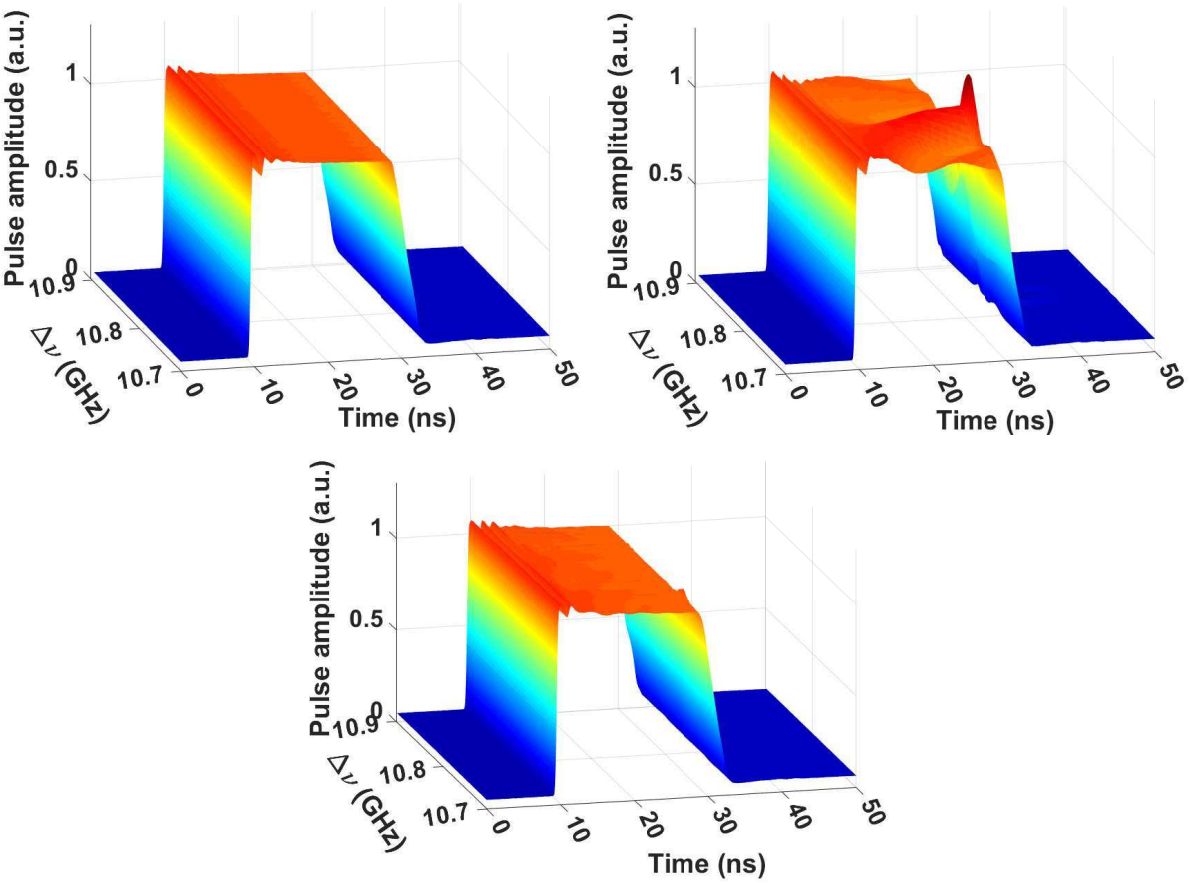

Figure 3.15: Distortion of the pump pulses at the output of the fiber (a) using the SOA to generate the pulses, (b) using the MZ-EOM to generate the pulses and (c) using the MZ-EOM to generate the pulses and deploying the dithering technique.

the compensation of the pump pulse distortion caused by second-order NLE when the dithering technique is applied. As it is observed, the retrieved shape of the pump pulses is very similar to the one obtained with high ER pump pulses, shown in Fig. 3.15 (a). Therefore, the dithering of the light source sucessfully mitigates the detrimental effects of the pulse distortion, reducing the depletion factor from 30% to 2%.

3.5.4. BFS measurements compensation

As it has been explained in section 3.2, NLE are a major origin of errors on the determination of the BFS in BOTDA sensors. In this section, the improvement in the final performance of BOTDA sensors deploying the source dithering technique is evaluated. To do this, the BFS distribution along the optical fiber was measured in order to accurately quantify the final measurement performance improvement obtained using the dithering of the light source. In order to determine the BFS measurement error, the BFS measurement obtained with pump pulses generated with the SOA (high ER) has been taken as reference.

Figure 3.16 depicts the measurement of the BFS when EDFA I is deployed to amplify the pump pulses. Notice that pump pulses with different ER were generated and dithering was activated and deactivated to compare the results. As shown in section 3.5.1, the transient effects of EDFA I are not very significant, thus, the observed BFS errors are only due to the trailing pedestal depletion effect. In particular, it can be seen that the BFS obtained using 26-dB ER pulses and without dithering, increasingly differs from the reference along the fiber. This is consistent with the result observed in Fig. 3.12 (a),

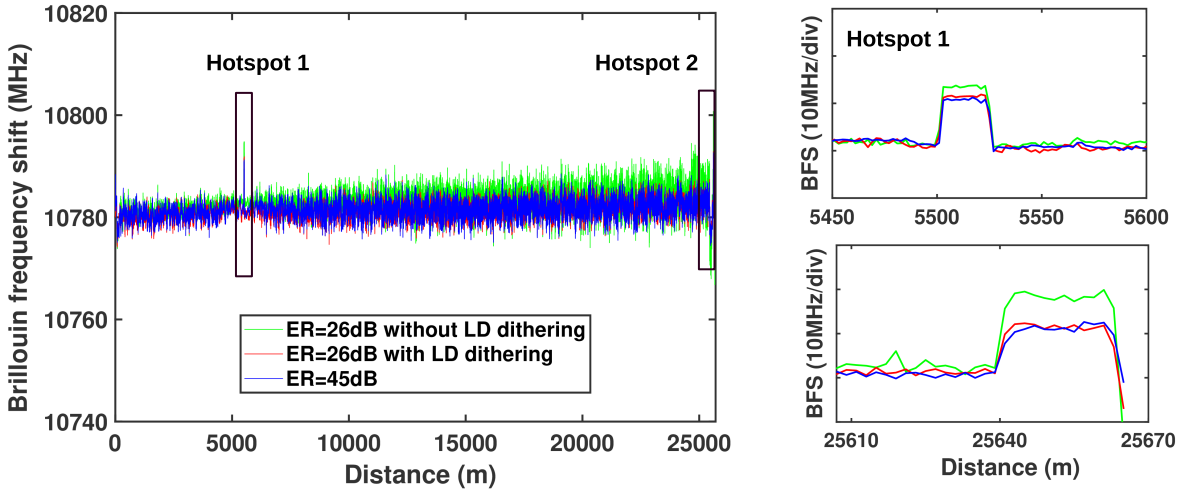

Figure 3.16: Brillouin frequency shift distribution measured along the optical fiber when using EDFA I (negligible transient response) for pump pulses with ER of 45 dB (blue line), 26 dB (green line) or 26 dB with dithering of the optical source (red line). The insets highlight the details of the measurement around the two hotspots.

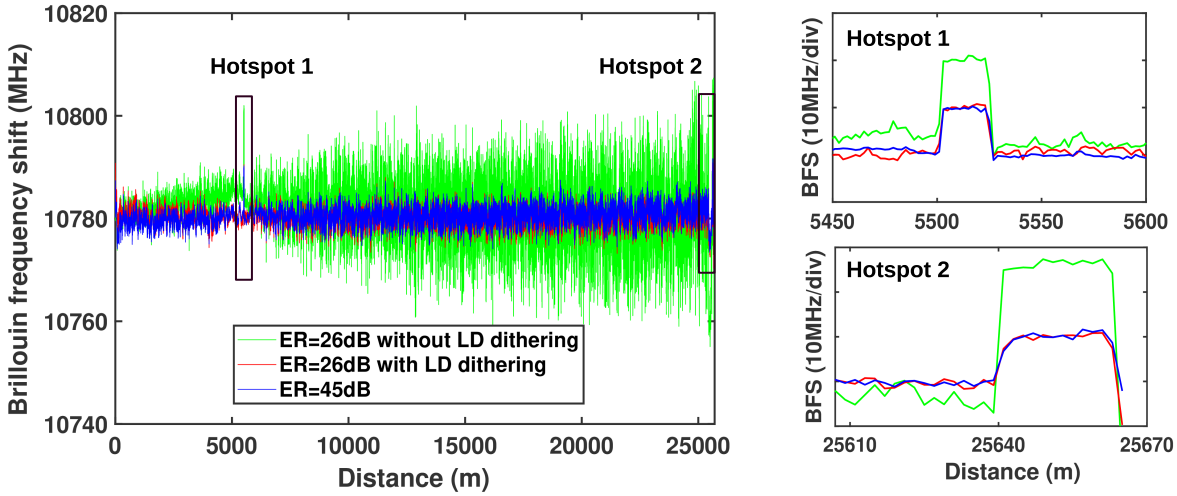

Figure 3.17: Brillouin frequency shift distribution measured along the optical fiber when using EDFA II (conventional amplifier) for pump pulses with ER of 45 dB (blue line), 26 dB (green line) or 26 dB with dithering of the optical source (red line). The insets highlight the details of the measurement around the two hotspots.

where an increased distortion of the measured probe gain along the fiber due to the effects of the pump pulse and trailing pedestal depletion is depicted. On the contrary, if the source dithering technique is implemented along with pump pulses of 26-dB ER, the BFS measurement coincides with the reference, showing no error on the BFS determination. This is verified in the insets of Fig. 3.12, which displays a zoom of the BFS measured in the two hotspots at z=5 km and z=25 km. At the first hotspot, there is a small BFS error of approximately 2.5 MHz for the measurement with medium ER and no dithering. Whereas the error drastically increases to around 7 MHz at the second hotspot. In contrast, with our source dithering method, the BFS errors are perfectly compensated in both hotspots.

On the other hand, Fig. 3.17 displays the measurements performed when the conventional amplifier with significant pulse amplification transients, EDFA II, is deployed. Similar trends are observed, but this time the BFS error with reduced ER pulses is dramatically increased due to the transient effects of the amplifier. Furthermore, the insets for the BFS distribution around the two hotspots highlight a very large error in both cases (10 MHz and 15 MHz, respectively). Despite this severe distortion, again, the use of the source dithering method is able to compensate for the BFS errors, showing a complete reduction of the BFS measurement error.

3.6. Conclusions

In summary, in this chapter of the thesis, a simple technique to reduce the NLE originated by the deployment of pump pulses with limited ER in BOTDA sensors has been presented. The method is based on introducing a wavelength modulation to the common optical source used for the pump and probe waves. This technique has demonstrated that is able to compensate for the different types of NLE related to the ER of the pump pulses:

- First, the NLE originated in the increased depletion of the pump pulse induced by probe wavefronts that have been previously amplified by the leading pedestal of the pump pulse.
- Secondly, the NLE originated by the distortion of the measured probe gain due to the increment depletion of the trailing pedestal of the pump pulse caused by probe wavefronts that have been previously amplified by the pump pulse.
- In addition, it has been demonstrated that second-order NLE that originates the spectral distortion of the pump pulses due to the un-balanced net gain induced by the dual-probe wave are also mitigated.
- Finally, the NLE that appear due to the distortion of the measured probe gain originated in the distortion of the trailing pedestal of the pulse by the transient response of the EDFA used to amplify the pump wave.

Moreover, the source dithering technique had previously demonstrated compensation of NLE associated with the depletion of the pump pulse by the probe wave [89]. Therefore, it can be said that this technique constitutes a comprehensive tool to compensate every type of NLE that impair BOTDA sensors performance as well as to increase the Brillouin threshold of the sensing fiber. This is, to our knowledge, the first and unique technique capable of solving all the detrimental effects of NLE, allowing to deploy higher probe power in the sensing link, and thus, improving the detected probe SNR and enhancing the measurement precision. All this is achieved with very little complexity added to the dual-probe wave setup, simplifying the deployment of this method.

It has been demonstrated that the dithering technique is very useful method for the implementation of cost-effective distributed sensors due to the capability of alleviating the impairments brought by the deployment of MZ-EOM with limited ER. With this technique it is also possible to deploy this type of devices to pulse the pump signal to obtain measuring systems with high spatial resolution based on the DPP technique that requires short rise and fall times for the pulse shape.

Lastly, as a result of the research described in this chapter of the dissertation, a paper has been published in the Optics Express international journal with the manuscript title of: "Compensation of nonlocal effects induced by the extinction ratio of pump pulses in Brillouin optical time-domain analysis sensors", by Mariñelarena et al.

CHAPTER 4

Linearization method for mono-color cyclic coding in BOTDA sensors

4.1. Introduction

Over the last years, DOFS have been attracting a great deal of attention thanks to the wide range of practical applications they offer, as well as the important advantages they can provide with respect to conventional temperature and strain sensors. It has been demonstrated that DOFS can provide really good performance and reliability for monitoring large structures, even those reaching up to hundreds of kilometers.

However, the maximum sensing range of BOTDA sensors is limited by the SNR of the systems, which is determined mainly by the optical power signal detected in the receiver. The amplitude of the received probe signal is limited due to the attenuation loss experienced by the probe wave during its propagation along the fiber. As explained in previous chapters, the probe and pump wave power that can be injected into the fiber is constrained by the onset of nonlinear and NLE that distort the measured signal. Thus, the performance of these sensors is ultimately restricted by the maximum probe and pump power that can be launched into the fiber.

Multiple solutions have been proposed to enhance the measurement range in BOTDA sensors, among them, the dithering of the probe wave, as presented in chapter 3. This method permits to reach the ultimate allowable probe wave power level to inject into the fiber, and thus, enhance the SNR. An alternative solution proposed in this chapter to improve the SNR of the measured BOTDA signal is the use of the optical pulse coding technique. This method allows to enhance the SNR of BOTDA systems by using a coded

pulsed signal based on launching, in a particular way, multiple pulses into the sensing fiber without increasing the pump peak power [98, 52, 99, 45, 100, 53, 55]. Instead, the average pump energy is increased, as well as the backscattered signal. Thus, nonlinear effects are avoided while the SNR is enhanced.

However, there are several constraints that have been limiting the performance of BOTDA sensors that deploy coding techniques since they were introduced. The first limitation relies on the need for generating coded pump pulses with the same optical peak power; otherwise, errors in the decoding process appear, and the distributed Brillouin gain cannot be properly obtained. This problem is caused by the optical amplifiers employed for the amplification of the pump pulses, which generate a transient response and a distortion in the amplitude of the pump pulses sequence [96]. This constraint has been recently solved by implementing a postprocessing solution based on weighting the peak power of the coded pump pulses and introducing corrective factors in the decoding matrix [101, 54].

Another important limitation of BOTDA sensors that make use of coded pump pulses is the onset of NLE. Similarly to conventional BOTDA sensors, coding methods also undergo the critical problem of the pump pulse depletion. It is important to remark that this detrimental effect, is even more severe for those sensors deploying coding techniques than for the ones without coding. As it has been explained in chapter 3, the dithering technique, of either the probe wave or the light source, allows to mitigate the detrimental effects of first and second order NLE in conventional BOTDA sensors. In a similar way to conventional systems, the pump depletion constraint in coding techniques has been also successfully overcome thanks to the deployment of the probe wave dithering technique [56]. This advancement has been lately demonstrated by our research group using a BOTDA system with mono-color simplex cyclic coding. There is an alternative solution to mitigate NLE, the color coding, which also offers the capability of ameliorating the negative impact of pump pulse depletion thanks to the generation of pulses with different frequencies, reducing the gain induced in the probe at frequencies near the BFS [55].

In spite of all these contributions, there is a constraint that is still limiting the performance of BOTDA sensors that deploy coding techniques. As it is well known, every time a long codeword is deployed using coded pulses, multiple pump pulses are successively launched into the fiber, inducing Brillouin gain on the probe and increasing its optical power. So, when long length codes are employed, the accumulative Brillouin gain experienced by the probe wave can induce stronger energy transfer from the pump to the probe by the SBS interaction, giving rise to nonlinear amplification. The nonlinear amplification of the probe generates a distorted probe wave signal that dramatically limits the enhancement of SNR. So, in order to ameliorate this constraint, a practical solution

has been devised during the realization of this thesis to cancel the detrimental effects of nonlinear amplification. The proposed linearization method is based on a postprocessing calculation, in which, the natural logarithm of the detected signal is calculated. This simple solution has been demonstrated with a BOTDA sensor that deploys a probe dithering technique and mono-color cyclic coding, allowing to experimentally demonstrate the linearization technique along with long-range sensing measurements.

In this chapter, firstly, a brief introduction to coding techniques is given and, in particular, the the mono-color cyclic coding method is introduced. Then, the origin of the onset of nonlinear amplification is explained and the proposed practical solution is described in detail. Experimental results highlight the validity of the proposed method to mitigate the nonlinear amplification, showing a reduction of the distortion and measurement errors induced when long codewords are deployed. Finally, it is experimentally demonstrated that the linearization technique along with the dithering of the probe wave, permits to successfully perform long-range distributed measurement using BOTDA sensors.

4.2. Optical pulse coding techniques in BOTDA sensors

As mentioned, one of the most widely explored approaches to enhance the SNR of BOTDA sensors is the use of optical pulse coding techniques [98, 53]. These methods rely on increasing the average pump energy in the fiber, without raising the peak pulse power and maintaining equal the pulse duration, so, it does not compromise the spatial resolution of the sensor. This is actually attained by launching into the fiber pulse sequences with some particular properties instead of a single pulse. Then, using a particular decoding process, this technique allows retrieving the impulse response of the sensing fiber, hence, the BFS.

During the last years, several pulse coding techniques have been applied to BOTDA sensors to extend the sensing range of DOFS. Among these coding methods, there are the complementary-correlation Golay codes [100], Simplex coding [98, 52], bipolar coding [99, 45, 100], cyclic coding [53] and color coding [54, 101]. Coding techniques have demonstrated to offer good capabilities to perform long-range measurements, and hence improve the SNR, maintaining the spatial resolution that is determined by the duration of each pulse contained in the sequence. All of these coding techniques are classified depending on the pulse sequence properties and their particular features, advantages and disadvantages.

For instance, the basic concept of complementary-correlation Golay coding method

is to transmit a sequence of pulses that has particular auto-correlation properties [2, 100]. These pulses generate overlapped Brillouin interactions that are detected as for a single pulse. Then, the detected signal is correlated with the original sequence and, the backscattered signal can be recalculated to a waveform that is equivalent to that generated by a single pulse, but of much higher energy. In this process, the SNR of the measurement is importantly increased.

Simplex pulse coding method is based on the use of pulse sequences that follow specific patterns according to particular codes, which are derived in this case from the Hadamard matrix [98, 102]. These are linear codes and the measured coded traces correspond to the linear combination of the single-pulse traces. Each of these traces is delayed in time according to the code sequence itself. Simplex codes, as well as complementary-correlation Golay codes, are implemented in BOTDA sensors using unipolar codes, which comprise sequences of '1s' and '0s', where 1 represents the presence of a pulse, while 0 represents absence off a pulse, that is, on/off intensity modulation of the pump pulses. In order to retrieve the BFS of the fiber, a linear decoding process is followed, according also to the specific code sequence used in the system. In both of these methods, the BOTDA trace retrieved after the decoding process offers a significantly enhanced SNR compared to the single-pulse measurement.

An alternative method to unipolar codes are the bipolar pulse sequences, in which bits of '1s' and '-1s' are required [45, 99]. In order to deploy bipolar codes in BOTDA sensors, it is necessary to implement the bits equal to 1 as pump pulses at frequencies higher than the probe wave, which induce Brillouin gain on the probe wave. While the bits equal to -1 are implemented as pump pulses at lower frequencies than the probe wave, inducing Brillouin loss on the probe wave. Due to the double intensity contrast provided by bipolar codes, the influence of the noise during the decoding process is reduced, and hence, the resultant coding gain is enhanced 3 dB in comparison with unipolar codes [99]. Moreover, it has been demonstrated that bipolar pulse coding method offers inherent robustness to pump depletion due to the compensation between gain and loss processes [99]. However, it requires considerable data processing due to a large number of sequences that have to be deployed. In addition, it requires a BOTDA setup with increased complexity for the implementation of this configuration [45].

Another coding technique is the color coding, which is based on the frequency coding of the pump pulses [54, 101]. Basically, while in previously described coding techniques applied to BOTDA sensors all the pulses of the code sequence have the same frequency, in color coding each of the bits of the code sequence that is associated to a pump pulse, has a different frequency. The different coding techniques presented up to now, Simplex and

bipolar coding, and the cyclic coding that will be presented next, can be combined with the color coding method, deploying multiple frequencies for the code bits, giving rise to simplex color coding technique [101] or cyclic color coding technique [54]. In color coding, the number of sequences necessary to retrieve the BGS is equal to the number of discrete frequencies scanning the BGS. This allows to highly reduce the measurement time with respect to other methods, leading to an optimization of the BOTDA systems that deploy coding in terms of SNR and acquisition time.

Mono-color cyclic coding technique

As mentioned, the main objective of the research work of this chapter has been to proposed and demonstrate a solution to overcome the impairments caused by the nonlinear amplification of the Brillouin gain when long code sequences are deployed. In order to experimentally prove the devised method, the mono-color cyclic coding technique has been deployed in a dual-probe wave BOTDA sensor configuration, in which, the probe has been frequency modulated as explained in section 3.2.2. Thus, a detailed explanation of the working principle of the mono-color cyclic coding technique is provided subsequently.

Mono-color cyclic coding technique is based on the Simplex coding method previously explained, although, deploying quasi-periodic simplex bit sequences and allowing real-time decoding in less than one fiber transit time [53, 103]. The main advantage of cyclic codes in comparison to Simplex, is that only one coded sequence is required to perform a distributed measurement. Since the code is periodic, this sequence is continuously generated, and thus, the measurement time is reduced. Therefore, cyclic codes allow performing fast distributed measurements over several kilometers of fiber [53].

Basically, the code sequence employed for the generation of the pump pulses in cyclic coding is based on a circulant matrix of dimension L_C, where L_C is a prime number [53, 54]. The elements of the code sequence are composed of 1's and 0's, which are generated following the recurrence expression [53, 54]:

$$\begin{cases} u_1 = 0 \\ u_{n+1} = (u_n + n) \bmod L_C \end{cases} \tag{4.1}$$

where n is an integer $n \in [1, \frac{L+1}{2}]$ and *mod* is the modulo operation. From this expression, the positions of the pulses in the first line of the code matrix are obtained. In particular, the positions for bits equal 1, p_n, are simply given by the relation: $p_n = u_n + 1$. Then, the rest of the matrix is derived by shifting one position of the first line (codeword). For

instance, $L_C = 7$ gives the following positions: {1, 2, 4, 7}, corresponding to the positions of "1's" in the first code matrix row. As an example, the code matrix for a code length of seven is represented as follows:

$$S_7 = \begin{pmatrix} 1 & 1 & 0 & 1 & 0 & 0 & 1 \\ 1 & 0 & 1 & 0 & 0 & 1 & 1 \\ 0 & 1 & 0 & 0 & 1 & 1 & 1 \\ 1 & 0 & 0 & 1 & 1 & 1 & 0 \\ 0 & 0 & 1 & 1 & 1 & 0 & 1 \\ 0 & 1 & 1 & 1 & 0 & 1 & 0 \\ 1 & 1 & 1 & 0 & 1 & 0 & 0 \end{pmatrix} \tag{4.2}$$

A BOTDA sensor with cyclic coding uses a pump wave shaped by multiple pulses following the sequence of bits from which the entire code matrix is obtained. This code sequence modulates the pump wave following an M-bit binary pattern, generating series of on/off pulses. Let's consider each row of the code matrix as an M bit pattern $P = \{P_0, ..., P_{M-1}\}$ with $P_j = 0$ or 1 for $j = 0, 1, ..., M-1$. Then, each row of the matrix is the right-shifted copy of the previous one.

In order to perform a coded BOTDA trace measurement, this multi-pulse pattern is periodically launched into the sensing fiber with a repetition period equal to the fiber round-trip time. This means that, when it propagates along the sensing fiber, each of the wavefronts of the probe must interact with the pulses referred to a certain row of the matrix, but never with any other additional pulse. The sequence must fulfill that all the pulses of a particular row of the matrix fill the entire fiber length.

An illustration of the obtained BOTDA trace detected at the receiver for a particular cyclic code of length $L_C = 7$ (using the bit sequence {1 1 0 1 0 0 1 1 1 0 1 0 0}) is depicted in Fig. 4.1. As shown in the figure, the obtained coded BOTDA trace (black solid line) is the combination of the Brillouin gain contributions induced by the successive pulses of the sequence that interact with the probe at a given sampling instant. The dashed lines of different colors represent the gain of each of the pulses of the sequence in an individual manner [104]. Observe that the detected probe signal, lower graph, corresponds to a linear combination of the Brillouin gain contributions generated by the multiple pulses composing the coded pump signal. This feature allows to use the linear decoding process to retrieve the original probe gain trace [52, 98].

A useful parameter that permits to characterize every coding method is the coding gain, which is the increment of SNR obtained when coded pulses are deployed. This

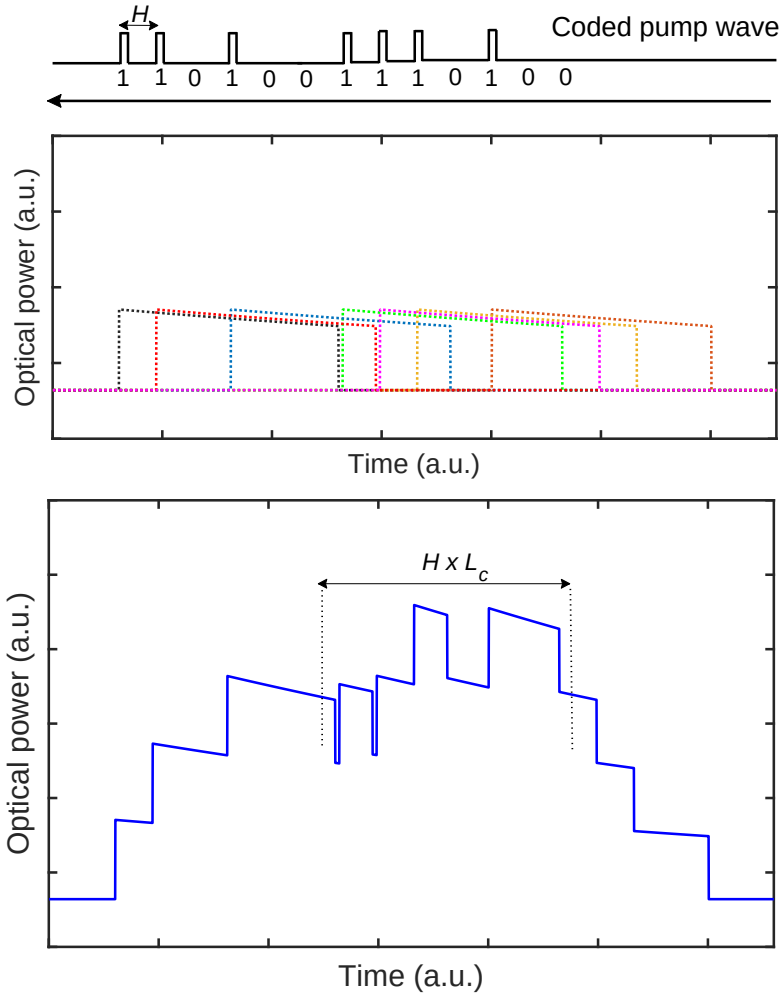

Figure 4.1: Obtained BOTDA trace as a function of time when using a particular cyclic code sequence of bits of length $L_C = 7$.

parameter directly depends on the number of bits used in the pulse sequence. The improvement of the SNR obtained by the coding gain for this cyclic coding is the same as for Simplex coding, given by [104, 105]:

$$C_{gain} = \frac{L_C + 1}{2\sqrt{L_C}} \tag{4.3}$$

Figure 4.2 shows the improvement attained in terms of SNR when Simplex and cyclic coding are deployed in BOTDA sensors compared to a conventional single pulse BOTDA scheme.

As stated, cyclic coding offers the great advantage of achieving reduced measurement time. This is possible due to the fact that the code sequence is cyclic, there is no need to launch different sequences of pulses. In this case, the first sequence is simply repeated in

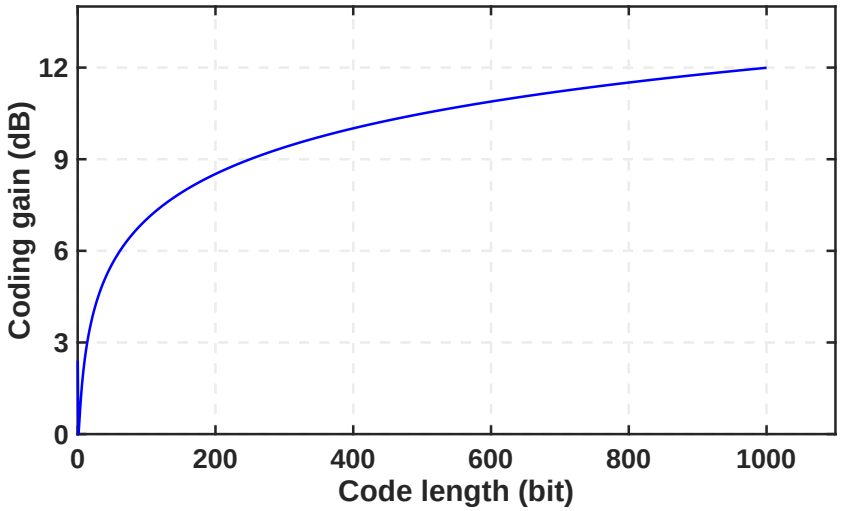

Figure 4.2: SNR enhancement in the BOTDA measurement as a function of the code length.

a continuous loop, providing fast averaging. The possible code lengths, L_C, to be used in the recurrence equation can be chosen between any prime number, giving rise to numerous combinations. In contrast to the Simplex code generation method that the code length has to be a number given by $2n-1$, in cyclic coding there are a higher number of possible code lengths that can be used.

As said in the introduction of this chapter, there are three important limitations that have to be taken into account in BOTDA sensors that deploy any of these coding techniques. The first one is the power fluctuation of the coded pump wave, which can be avoided if flat coded pump pulses are generated. The second constraint is the pump pulse depletion that is mitigated when the dithering is applied to the probe wave signal. However, the nonlinear amplification constraint caused by the accumulative Brillouin gain when long codewords are deployed is still limiting their performance.

4.3. Fundamentals of linearization method in mono-color cyclic coding

As explained in chapter 2, the Brillouin gain experienced by the probe wave does not depend linearly on the pump pulse power, but exponentially. This means that, when relative short codewords are deployed, the assumption of linearity is valid and the decoding process works properly. On the contrary, if the code length exceeds a certain threshold, the accumulated gain induced by the pulse sequence for optical frequencies close to the Brillouin gain peak becomes so large that the linearity approximation is no longer satisfied, turning to an exponential increment. This nonlinearity becomes a problem in coding

techniques because of the fact that linear amplification is a fundamental requirement of the decoding process to work properly. Therefore, since the onset of the nonlinear amplification is directly related to the length of the code, the maximum achievable coding gain in BOTDA sensors is limited.

Let's consider a single-pulse BOTDA sensor to explain the fundamental requirement of linearity. As mentioned, in order to retrieve the distributed measurand (T^{a} or ε) along the sensing fiber, it is necessary to determine the local Brillouin gain experience by the probe wave at every position, $G(z, \Delta\nu)$. So, based on the SBS interaction upon the probe wave described in chapter 2, it is possible to express the detected probe intensity variation, ΔP_S, observed in the receiver due to the interaction with the pump pulse at a certain location z along the fiber with the following equation:

$$\begin{aligned}\Delta P_S(z, \Delta\nu) &= P_{S_{in}} \cdot \exp(-\alpha L) \cdot \exp\big(G(z, \Delta\nu)\big) - P_{S_{in}} \cdot \exp(-\alpha L) \\ &= P_{S_{in}} \cdot \exp(-\alpha L) \cdot \Big[\exp\big(G(z, \Delta\nu)\big) - 1\Big]\end{aligned} \tag{4.4}$$

where $P_{S_{in}}$ is the intensity of the probe wave injected into the fiber and $G(z, \Delta\nu)$ the Brillouin gain at position z, which is defined as follows:

$$G(z, \Delta\nu) = \int_{z}^{z+\Delta z} \frac{g_B(\Delta\nu)}{A_{eff}} P_{P_{in}}\, exp(-\alpha z)\, dz \tag{4.5}$$

where $P_{P_{in}}$ is the intensity of the pump pulse and Δz is the spatial resolution determine by the pulse duration.

Then, if we assume as explained previously that Brillouin gain, $G(z, \Delta\nu)$, is small and the Brillouin sensor operates in small signal regime, the Eq. (4.4) can be simplified to:

$$\Delta P_S(z, \Delta\nu) \approx P_{S_{in}} \cdot \exp(-\alpha L) \cdot G(z, \Delta\nu) \tag{4.6}$$

Therefore, the Brillouin gain in a single-pulse BOTDA configuration can be approximately considered to depend linearly on the gain provided by single pulses.

So far, the method of retrieving the Brillouin gain in pulse-coded BOTDA sensors has relied, as in single-pulse BOTDA techniques, on the measurement of the power amplitude variation experienced by the probe wave when interacting with particular codeword sequences of pulses in the fiber. Thus, the resultant probe wave variation, $\Delta P_{S_T}(z, \Delta\nu)$, can be expressed as the sum of all the gain contributions of the pump pulses interacting

with the probe wave at a certain position z:

$$\Delta P_{S_T}(z,\Delta\nu) = P_{S_{in}} \cdot \exp(-\alpha L)\left[\exp\left(\sum_{i=1}^{L_C} G_i(z_i,\Delta\nu)\right) - 1\right]$$

$$\approx P_{S_{in}} \cdot \exp(-\alpha L)\sum_{i=1}^{L_C} G_i(z_i,\Delta\nu) \tag{4.7}$$

where $G_i(z_i,\Delta\nu)$ is the gain provided by each of the pulses with position i in the coded sequence at a location z_i along the fiber. Notice that the Brillouin gain contributions of the coded pulses, $G_i(z_i,\Delta\nu)$, are identical to the Brillouin gain, $G(z,\Delta\nu)$, for the single-pulse case. However, in order for the decoding process to work properly, the last approximation in Eq. (4.7) has to be valid, which is only satisfied if $\sum_{i=1}^{L_C} G_i(z_i,\Delta\nu)$ is small. As it has been already explained, contrary to the single-pulse case, in coding techniques the resultant total Brillouin gain increases with the code length and the small signal assumption becomes unreasonable. This makes the recovery of $G(z,\Delta\nu)$ from the measured ΔP_{S_T} for each codeword to fail because of the decoding process intrinsically requires that the resultant Brillouin gain provided by multiple pulses accumulates linearly. Altogether, this linearity requirement constrains the maximum code length that can be deployed in BOTDA sensors and, with it, the maximum achievable SNR enhancement and overall measurement range.

The main target of this chapter is to describe the research accomplished during this thesis to permit to overcome this deleterious limitation, and thus, obtain a further increase of the SNR by launching longer code sequences without undergoing nonlinear amplification. Basically, the proposed method is based on using a linearized version of the detected probe wave variation. This is attained calculating the natural logarithm of the detected probe wave, P_{S_T}, and subtracting the DC component. The linearized variation of the probe wave signal generated due to its interaction with a given codeword is given by:

$$\Delta P'_{S_T}(z) \equiv \ln\left[P_{S_T}(t)\right] - \ln\left[P_{S_{in}}\exp(-\alpha L)\right] \tag{4.8}$$

From this definition, it is easy to demonstrate that working with $\Delta P'_{S_T}$ instead of ΔP_{S_T}, provides linearity to the coded signal no matter what the total gain experienced by the

probe is:

$$\Delta P'_{S_T}(z,\Delta\nu) = \ln\left[P_{S_{in}}\exp(-\alpha L)\exp\left(\sum_{i=1}^{L_C} G_i(z_i,\Delta\nu)\right)\right] - \ln\left[P_{S_{in}}\exp(-\alpha L)\right]$$

$$= \sum_{i=1}^{L_C} G_i(z_i,\Delta\nu) = \sum_{i=1}^{L_C} \Delta P'_{S_i}(z,\Delta\nu) \tag{4.9}$$

where $\Delta P'_{S_i}(z,\Delta\nu)$ is the linearized probe wave power variation due to interaction of the probe wave with the i-th pulse of the code.

Apart from this really simple modification, the measurement process is similar to established procedures for other coding techniques. First, $P_{S_T}(z,\Delta\nu)$ is detected for the different codewords and $\Delta P'_{S_T}(z,\Delta\nu)$ calculated for each of them, according to Eq. (4.8). Then, decoding is performed. For instance, for Simplex or cyclic simplex coding, this involves the application of the inverse code matrix.

As mentioned in the introduction of this chapter, in addition to amplification non-linearity, the other main constraint faced by pulse coding in BOTDA is NLE due to the depletion of the pump pulses. In fact, these effects are exacerbated in BOTDA sensors deploying coding because successive pulses in a sequence interact with probe wavefronts that have been previously amplified by the rest of the pulses in the sequence [56]. Therefore, the increasing power of the probe wave induces a larger energy transfer from the pump pulses to the probe wave when providing gain, and hence, increase pump depletion. As a result, decoding errors are experienced because the relative amplitudes of the pulses in a sequence are altered along the fiber and do not correspond with the ones employed in the decoding process. As explained previously, this constraint has been addressed by deploying a method to reduce pump depletion that is based on introducing a wavelength modulation or dithering to the probe wave [56]. This configuration setup will be deployed in this research as well to compensate the impairments of NLE.

The fundamentals of the BOTDA sensor deployed in this research are schematically depicted in Fig. 4.3, where the optical waves involved in the technique are shown. As it is highlighted in the figure, the optical frequency of the probe waves is modulated following a saw-tooth shape. Additionally, this FM is synchronized to the pump pulses, so that, a pulse sequence experiences the same wavelength of the probe waves at any given location.

The dithering of the probe wave technique requires a reordering of the acquired data to retrieve the distribution of the BGS along the fiber [56]. However, when coding is applied, it has to be considered that multiple pulses are launched into the fiber in a code sequence, so, some extra considerations have to be considered to correctly retrieve the

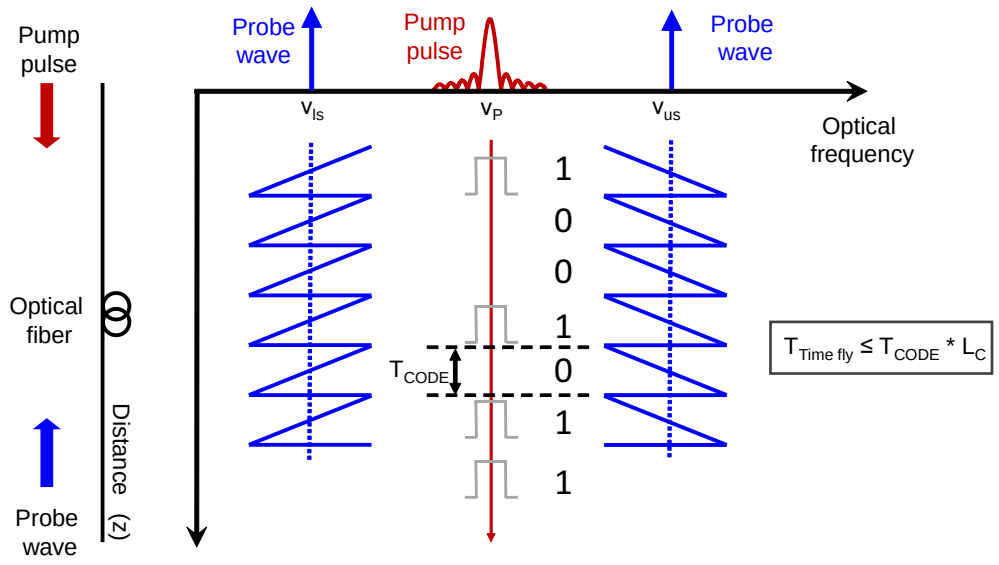

Figure 4.3: Fundamentals of the combined technique using dithering of the probe wave and cyclic coding.

signal. When cyclic coding is implemented, all codewords (pulses) of a sequence must fit simultaneously inside the fiber, being aware of not injecting more pulses than the codeword length. Thus, for a given fiber length, the code period needs to be modified depending on the code length. Finally, to properly decode the signal and retrieve the BGS of the fiber, the frequency shift of the probe waves must be compensated by reordering the decode matrix [56].

4.4. Experimental setup

Figure 4.4 depicts the BOTDA setup deployed during this research work to evaluate the performance of the proposed coding linearization method. This is a conventional dual-probe BOTDA setup that also incorporates the probe dithering method to mitigate first and second order NLE [56]. Similarly to other BOTDA sensors, a distributed feedback laser (DFB) laser of 1550-nm was employed as a light source, whose output was divided by a coupler into two branches. In the upper branch, a SOA optical switch, with an ER around 50 dB, was used to shape the pump pulses. This SOA was driven by an AWG that was configured to generate the coded sequence of pulses. Then, an EDFA was used to amplify the pulses to 20 dBm, which corresponds to the MI threshold. In order to compensate the Brillouin gain polarization dependence, a PS was deployed before injecting the pump signal into the sensing fiber to randomize its polarization. Pulses of 20-ns duration were generated for the experimental measurements, leading to a spatial

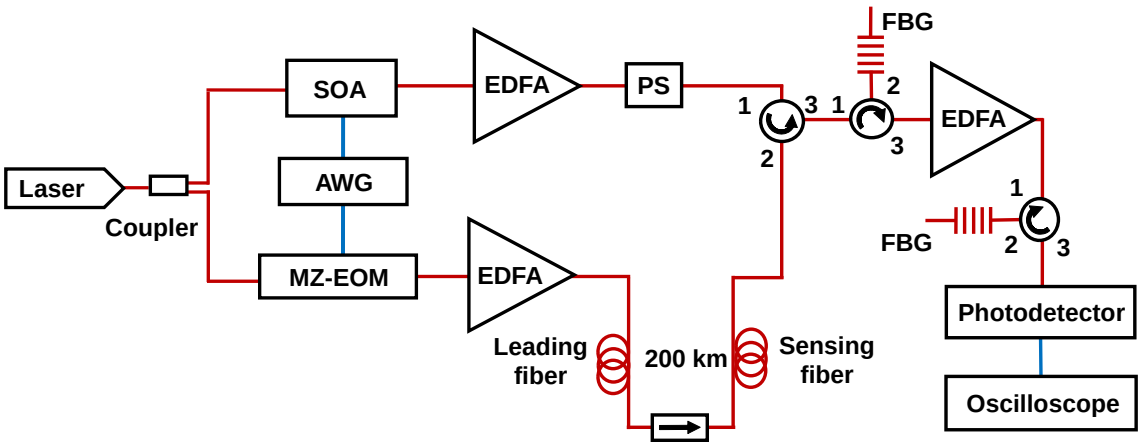

Figure 4.4: Experimental setup for the BOTDA sensor.

resolution of 2 m for the distributed measurements.

In the lower branch, a dual-probe wave was generated using a MZ-EOM that was driven by another output of the AWG. In order to implement the modulation of the probe wave frequency or dithering, the AWG generated a microwave tone whose instantaneous frequency was modulated following a saw-tooth shape with a peak-to-peak frequency deviation of 160 MHz and a period of 4 μs. As explained, this FM has shown to provide two enhancing effects [87]. First, it increases the effective Brillouin threshold of the sensing fiber, allowing to inject a total probe wave power (per sideband) of 13 dBm, much larger than the 7 dBm of Brillouin threshold measured without dithering. The second effect is the reduction of first and second order NLE thanks to the spreading in a large frequency range of the Brillouin interaction induced by the dual-probe wave upon the pulse [87].

A total of 200 km of SMF in a loop configuration were deployed; the first 100 km were used as leading fiber to bring the signal to the start of the sensing fiber. Then, the second 100 km of fiber were connected to use them as sensing fiber. One hotspot was placed at the beginning of the sensing fiber and another one at the end in order to determine the distortion induced by the nonlinear amplification and its reduction when the proposed solution is applied. Two portions of 80-m length of the sensing fiber were introduced in temperature-controlled thermal baths in order to maintain stable the temperature of the hotspots.

Finally, the probe wave was detected in an EDFA-preamplified receiver that includes two narrow-band FBGs that were used to filter out one of the probe sidebands and the Rayleigh backscattering originated from the pump wave.

4.5. Experimental results

The experiments started by measuring the amplitude of the pump pulses injected in the fiber, after their amplification in the EDFA, in order to ensure that we had a flat power pump pulses sequence. Fig. 4.5 depicts the amplified sequence of pulses for a code length of $L_c = 251$. This gives information regarding the amplitude distortion introduced by the EDFA transient response, which is crucial to derive amplitude weighting values to be used in the code matrix so as to ensure correct decoding. In fact, the decoded response was found to be very sensitive to errors in the determination of this weighting due to the fact that the detected signal level at the end of the fiber was extremely low, as it will be shown later. The maximum variation in the amplitude of the pulses in the cyclic sequence was found to be around 2.5% when $L_c = 251$ was deployed. Even though the distortion is very small, the corrective factors were applied in the decoding process to ameliorate this detrimental effect.

Since the probe wave power launched into the fiber was risen to 13 dBm (per sideband) and long codewords were tested ($L_C = 251$), it was necessary to analyze the possible impairments brought by the pump pulse depletion. To do this, the depletion induced by the probe wave on the pump pulses sequences after traveling across the fiber was measured. Fig. 4.6 shows the general trends that the depletion increases along the pulse sequence and that shorter sequences lead to smaller depletion, as it had been observed in previous works [56]. Nevertheless, observe that the deployment of the probe dithering method makes depletion negligible from a practical point of view.

After the characterization of the pulses and ensuring NLE do not limit the performance of the BOTDA sensor, full BOTDA measurements were performed on the fiber link.

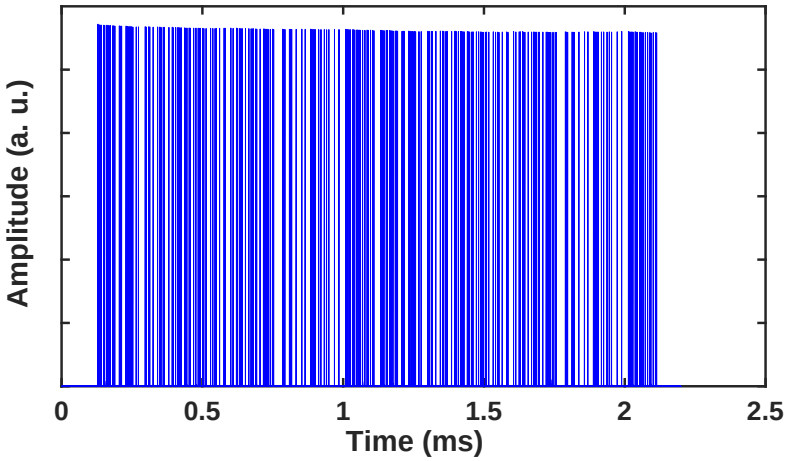

Figure 4.5: Cyclic pulse sequence for a code length of $L_c = 251$.

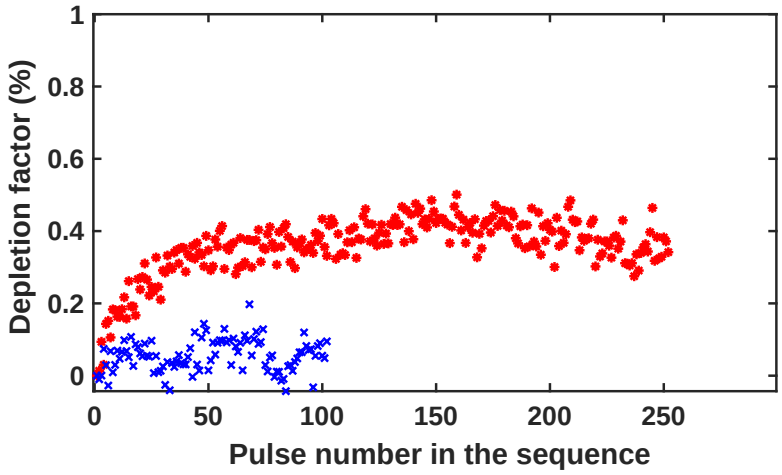

Figure 4.6: Depletion of the different pulses in a code sequence for code lengths of $L_c = 101$ (blue) and $L_c = 251$ (red).

Firstly, the measuring system was evaluated for different code lengths, $L_C = 101$ and $L_C = 251$, without applying the linearization method. Fig. 4.7 (a) depicts the decoded probe power variations measured along the fiber for a frequency difference between the pump and probe near the BFS. Notice that, as the code length is increased, the retrieved decoded signal displays an increasing amplitude error compared to that of a single-pulse BOTDA. This abnormal increment of power observed in the decoded signal is caused by the interaction of the probe wave with the successive pulses of the code sequence. This is particularly more visible at locations close to the pulse entry in the fiber, which is where the pump pulse have larger power, and thus, the energy transfer due to SBS interaction is higher. The distortion observed in these measurements is originated by the nonlinear amplification and, as it will be shown, errors in the determination of the BFS will appear. These errors not only appear at the begining of the fiber, but also after a certain distance of the sensing fiber.

On the contrary, Fig. 4.7 (b) highlights the decoded probe wave power variation when our simple processing technique is deployed to linearize the response. Observe that the resultant probe power variation for increased code length becomes equivalent to that with no coding and the linearity error is eliminated altogether. This fact is clearly observed in the inset of Fig 4.7 (b), where a detailed view of the Brillouin gain traces at the end of the sensing fiber are shown. All the traces overlap and it is clearly visible that noise is reduced when larger codewords are deployed, improving the SNR of the measurement and allowing to observe a usable signal at the end of the sensing fiber.

Furthermore, the Brillouin gain spectra in the first hotspot were measured and compared, with and without the linearization method, to determine the measurement error

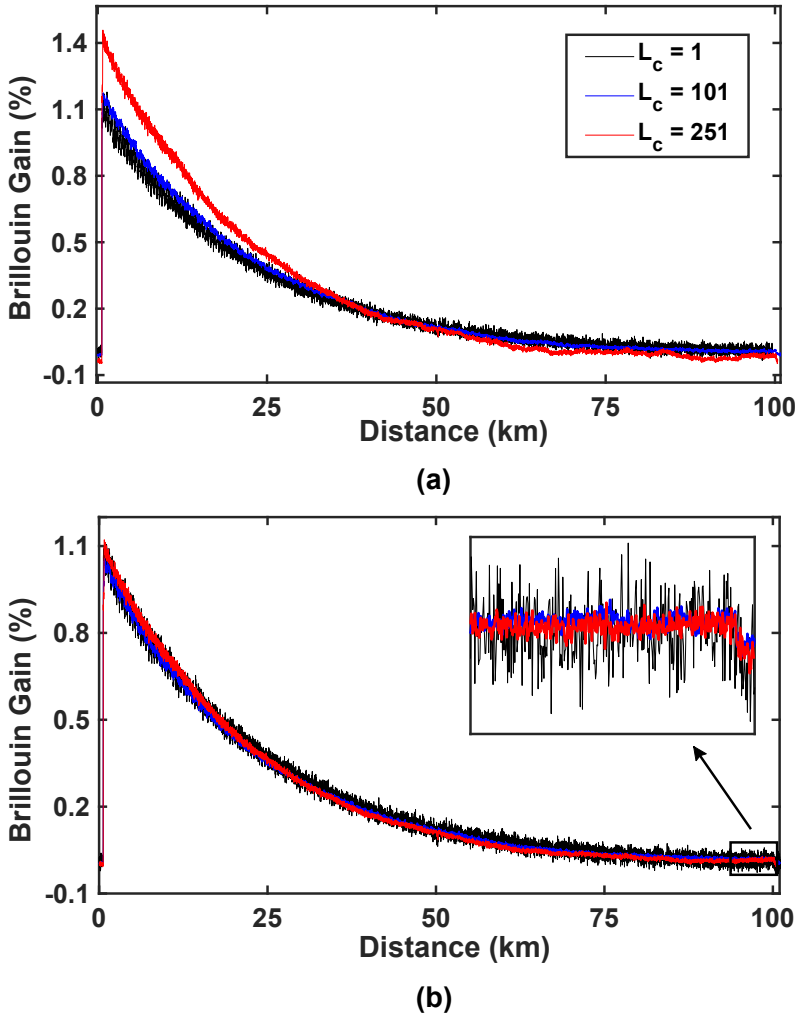

Figure 4.7: Brillouin gain of the probe along the fiber (a) without and (b) with linearization of the sensor response for three different code lengths.

induced by the nonlinear amplification. Fig. 4.8 (a) displays the normalized spectra measured in the hotspot at the start of the sensing fiber without deploying the linearization. This figure depicts that the deviation of linearity when deploying coding with long codewords leads to a BFS measurement error. As it is observed, the increased amplitude measured for the probe wave distorts the measured spectrum that, compared to that measured with no coding, is narrowed and skewed towards the BFS of the fiber outside the hotspot. This leads to a measurement error of approximately 2 MHz. However, as shown in Fig. 4.8 (b), the proposed linearization method completely compensates this effect and the spectrum for the pulse-coded BOTDA are seen to coincide with this of the single-pulse sensor, just with less noise due to the coding gain.

Then, the effects of the distortion induced by the nonlinear amplification were studied for this experiment by measuring the distributed BFS of the sensing fiber. Fig. 4.9

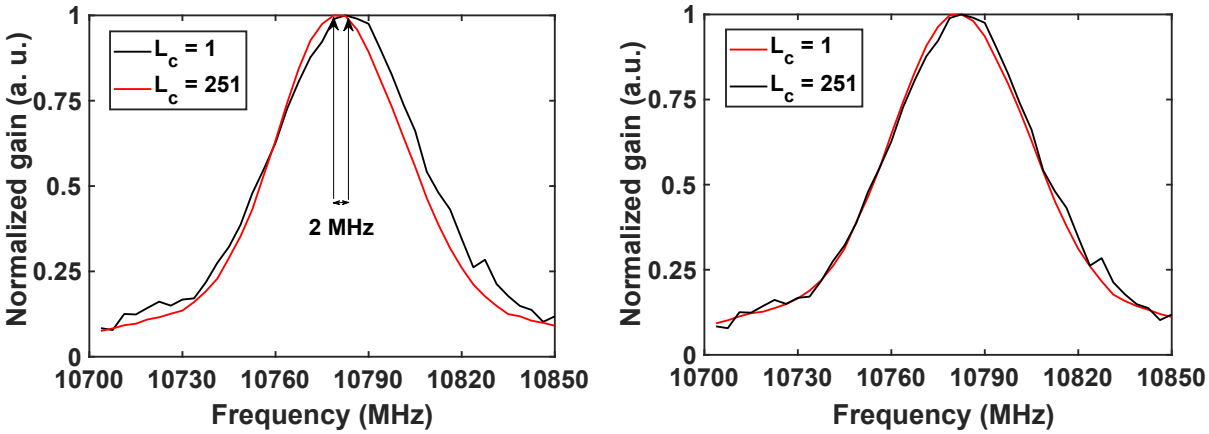

Figure 4.8: Brillouin spectra measured at the hotspot near the start of the fiber (a) without and (b) with linearization of the sensor response.

depicts the comparison of the BFS obtained along the sensing fiber by applying or not the proposed response linearization technique for a code length of $L_c = 251$. As it is observed, the improvement of the retrieved BFS is notorious. In case the linearization is not applied, the BFS results obtained from $z = 55$, returns large measurement errors. On the contrary, if the linearization method is deployed, the BFS obtained shows a good response until the end of the sensing fiber. Notice that this link is made of two fiber spools with slightly different average BFS. Fig. 4.9 (b) shows a zoom of the BFS obtained from the measurement with $L_C = 251$ at both hotspots. It can be seen that for the system without linearization, there is an approximately 2-MHz error in the measured BFS at the first hotspot for increasing code length, which is due to the spectral biasing depicted in Fig. 4.8 (a). This measurement error increases strongly after 55 km, however, this error is successfully corrected altogether by deploying the linearization method. For the second hotspot, just the BFS linearized result is shown because without linearization the Brillouin spectrum at that location was completely distorted.

As it is observed, the measuring system offers good performance for long-range measurements when the linearization method is deployed, enhancing the response with respect to coding systems undergoing nonlinear amplification. In order to experimentally demonstrate the enhanced performance of the proposed sensor, two more measurements were performed. The first one is shown in Fig. 4.10, which displays an additional measurement of the sensing fiber swapping the two fiber ends. Observe that, the BFS value obtained for both measurements is similar, although, with increasing noise due to the reduction of SNR, as expected. Note that, in this measurement, there is a worsening of the performance from z=85 km of the sensing fiber, where there is a slight deviation of the BFS from its true value with oscillation and biasing introduced. However, this error was nei-

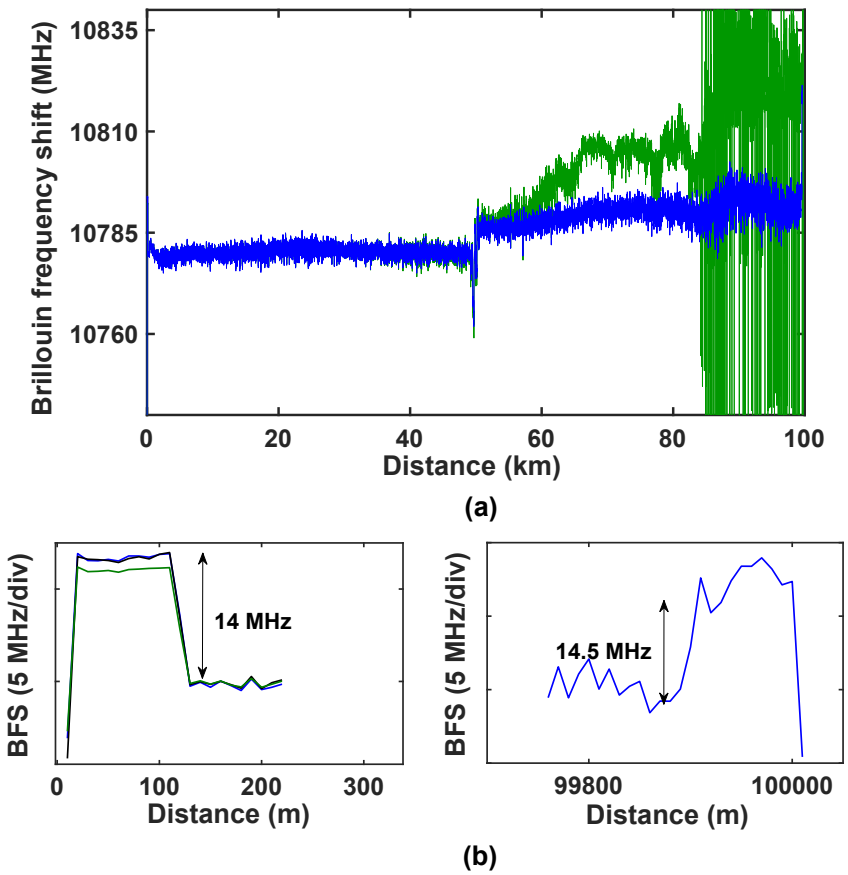

Figure 4.9: BFS measured along the fiber for $L_c = 251$ with coding linearization (blue) and without linearization (green). (b) BFS measured at the two hotspots for: $L_c = 1$ (no coding) (black), $L_c = 251$ without linearization (green) and $L_c = 251$ with linearization (blue).

ther due to NLE, nor to nonlinear effects such as SPM or MI affecting the pulses. This was confirmed by repeating the measurements after reducing either the pump or the probe wave power and simultaneously increasing the number of averages to maintain the SNR of the detected signal. Identical BFS distributions were obtained in all cases independently of the pump and probe power.

After deep research of the origin of this small detected variation of the BFS, it was observed that residual errors in the amplitude weighting of the pump pulses sequences introduced in the decoding process could be a reason for these slight variations on the decoded signal. Even though the corrective factors were introduced in the decoding process, the variation of the relative power of the coded pump pulses at the output of the EDFA along with the extremely small detected signal observed at the end of the sensing fiber were limiting the ultimate performance of the deployed sensor. Finally, the last result attained that demonstrates the improvements of the combination of cyclic coding, dithering of the probe wave and the linearization technique is the uncertainty of

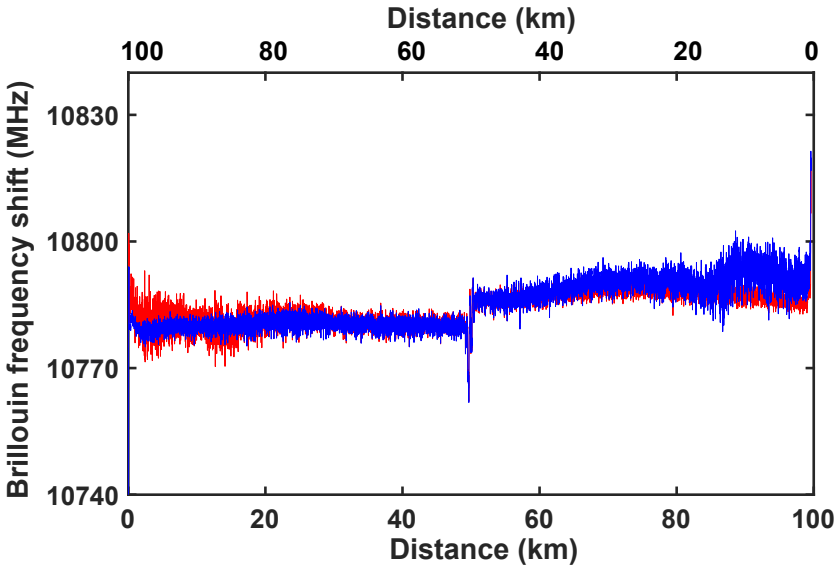

Figure 4.10: BFS measured along the fiber for $L_c = 251$ with coding linearization and swapping the two fiber ends.

BFS measurements obtained along the fiber. Fig. 4.11 depicts the calculated standard deviation of 8 consecutive measurements, showing an average accuracy of 4 MHz at the end of the sensing fiber. A remarkable performance is obtained assuming a 85-km sensing link, with an average measurement precision better than 4 MHz for 16000 trace averages and 2-m spatial resolution, obtaining a figure-of-merit of 4400, while if linearization method is not applied the figure-of-merit is 84.

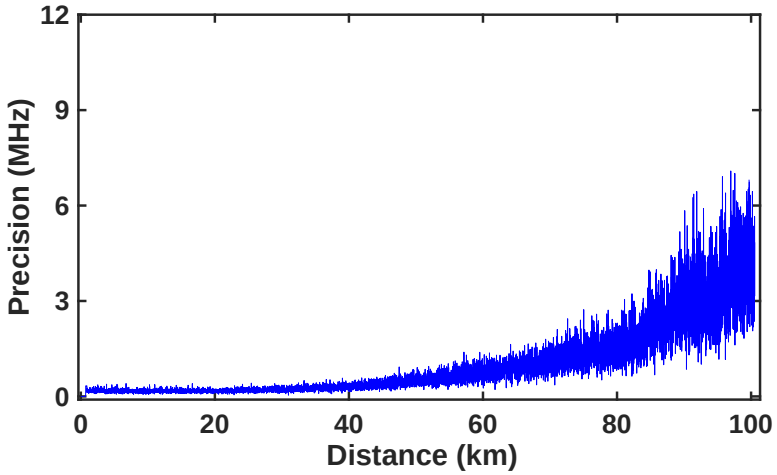

Figure 4.11: BFS measurement precision along the fiber (standard deviation of 8 consecutive measurements).

4.6. Conclusions

In this chapter of the dissertation, we have studied one of the constraints that still limiting the performance of BOTDA sensors with coding techniques. This is the non-linear amplification experienced by the probe wave when long sequences of pulses are deployed, which limits the code length that can be deployed. A limited code length directly constrains the improvement of the SNR in coding techniques, so that, the nonlinear amplification has been investigated and addressed with the aim of improving the SNR in BOTDA sensors.

As a result, a simple method to compensate the detrimental effects of the nonlinear amplification has been devised and presented. The implementation of this solution solves the non-linearity experienced by the probe, mitigating the impairments and the distortion observed in the decoded BGS for long codewords, allowing to deploy longer codes and thus, enhancing the performance of BOTDA sensors. Moreover, the proposed solution does not require any setup modification, since it is based on a postprocessing of the detected data.

The experiments of this work have demonstrated a proof-of-concept of the linearization method, deploying a BOTDA sensor that combines a frequency modulated dual-probe wave configuration and mono-color cyclic coding. The assambled setup along with the linearization process has proved the validity of the method and also the capability of performing long-range measurements.

Finally, as a result of the research fulfilled in chapter 4, a paper has been published in the Optics Letters journal with the manuscript title of: “Pulse coding linearization for Brillouin optical time-domain analysis sensors”. by Mariñelarena, et al.

CHAPTER 5

Contributions to slope-assisted BOTDA sensors

5.1. Introduction

As it has been mentioned in chapter 2, one of the main constraints of BOTDA sensors is the measuring time, which in many cases does not allow to perform dynamic measurements of strain and/or temperature due to the large time consumption of the BGS scan process. In order to overcome this limitation, several dynamic BOTDA configurations have been proposed during the last years as introduced in chapter 2. Most of the dynamic measurement techniques are based on the frequency discriminator principle, which are denominated as SA-BOTDA sensors [20, 21, 106, 107].

Thanks to numerous research contributions, dynamic BOTDA techniques have been demonstrated to be a very powerful technology to provide fast strain or temperature measurements, with the aim of providing the structural health monitoring of particular assets that require real-time monitoring. For instance, aircraft wing monitoring or wind turbine blade tests, among others. In most of these cases, this type of structure requires short lengths of monitoring fiber, allowing to increase the pump pulse peak power above typical maximum levels as far as nonlinear effects are not induced. However, a recent research work has demonstrated that there was a previously unknown effect in SBS interaction that induces a change on the BGS linewidth when the pump pulse power is large [108, 109]. This unexpected finding has shown that the Brillouin linewidth experiences a broadening effect when the pump pulse peak power is increased. This effect induces a BGS distortion in BOTDA sensors and, consequently, errors in the determination of the BFS when employing SA-BOTDA techniques based on the direct-detection method, which retrieves

the information from the BGS slope [108, 110].

As explained in chapter 2, an alternative SA-BOTDA dynamic measuring technique tolerant to NLE and Brillouin gain variations was recently presented by our research group [27, 28]. It is the self-heterodyne detection BOTDA sensor with phase-modulated probe wave (referred in this thesis from now on as dynamic BOTDA or D-BOTDA). In this measuring system, the probe wave signal is detected using a coherent-detection method after the propagation along the fiber, and the detected RF signal is demodulated to baseband for further processing. Then, the phase-shift of the detected RF signal is retrieved, which was found to be dependent on the BFS experienced by the probe wave. The D-BOTDA sensor offers the important advantage of providing fast strain or temperature measurements with high accuracy, high spatial resolution and tolerant to Brillouin gain variations to some extent. However, before this thesis work, there was no information about the detrimental effects that high Brillouin gain variations may generate in D-BOTDA sensors.

The first part of this chapter is focused on describing the study of the response of D-BOTDA measuring systems to Brillouin gain changes, in similar way to the research recently presented for conventional direct-detection SA-BOTDA sensors [108, 110]. As it will be shown, it has been found that a narrowing of the Brillouin RF phase-shift spectrum is induced when high power pump pulses are deployed, inducing errors in the BFS measurements.

Apart from the mentioned measurement time constraint, both types of SA-BOTDA sensors, direct-detection and dynamic BOTDA sensors, have another important limitation that restricts their features, which is the dynamic measurement range. As it has been explained in chapter 2, the SA-BOTDA techniques, and specifically the D-BOTDA sensor, has a limited dynamic measurement range, determined by the linear region of the RF phase-shift spectrum. This linear region of the spectrum depends inversely on the pulse duration, hence the dynamic range can be extended if the pulse duration is shortened. However, when the pulse duration is shortened, the SNR of the measuring system is also reduced and the accuracy rapidly worsens. Thus, there is an important trade-off among these features of the measuring system: dynamic range, spatial resolution and accuracy.

In order to overcome this second limitation, several solutions have been studied and presented to extend the dynamic range of SA-BOTDA sensors, although, none has been successfully applied to D-BOTDA setups. So, the second part of this chapter is focused on introducing and explaining the research accomplished during this thesis to develop alternative measuring systems to enhance the dynamic measurement range in D-BOTDA sensors. In particular, two different methods have been proposed and experimentally

demonstrated that successfully extend the dynamic measuring range. Finally, a comparison between these two presented techniques is provided to analyze their performance.

The chapter is organized as follows. Firstly, the Brillouin gain linewidth broadening effect in direct-detection BOTDA sensors when high peak power pump pulses are deployed is studied and presented. Then, the gain dependence of the Brillouin RF phase-shift spectrum shape in D-BOTDA is theoretically and experimentally studied is section 5.3. The gain dependence of both investigated methods is compared in terms of the amount of spectrum shape change when increasing Brillouin gain. Afterward, two proposals to extend the dynamic range in D-BOTDA sensors are introduced, explained and theoretically and experimentally demonstrated in secton 5.4. Finally, the performance of these two devised techniques to enhance the dynamic range is compared and discussed.

5.2. Brillouin gain linewidth broadening in direct-detection BOTDA sensors

In order to evaluate the effects that the dependence of large Brillouin gain has over the Brillouin gain linewidth, first, we started by studying how the experimental response of direct-detection BOTDA sensors to Brillouin gain variations is. Fig. 5.1 depicts the experimental scheme used for the initial measurements. A conventional BOTDA setup with a single-probe wave was assembled in the laboratory to perform BGS measurements in different conditions and analyze the response.

A DFB was deployed as a light source to generate the pump and probe signals. A coupler was used to divide the optical signal and, one of the DFB outputs was directly used as a probe wave, while the second one was employed to form optical pump pulses with a MZ-EOM biased at minimum and driven by microwave pulses. A FBG was tuned

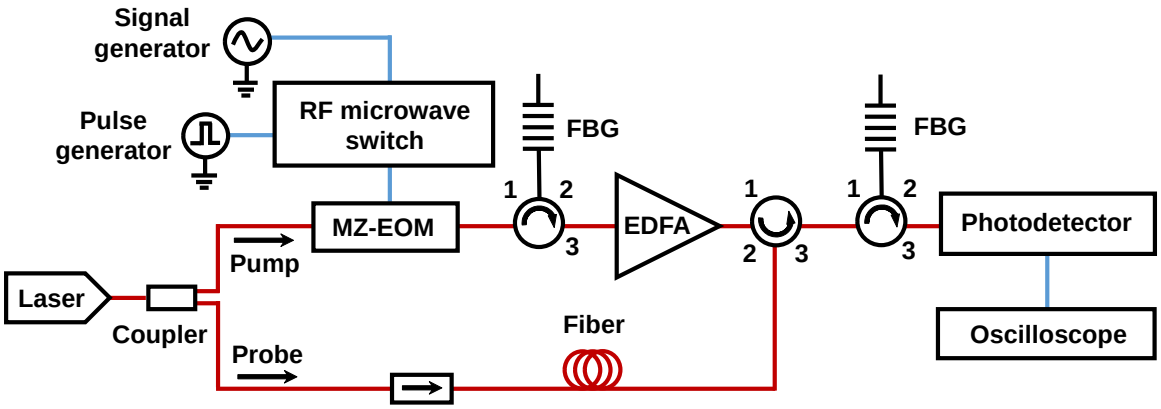

Figure 5.1: Experimental setup for the conventional direct-detection BOTDA sensor.

to filter out one of the two pump sidebands and a high-power EDFA was deployed to amplify the pulses up to 4-W-peak power. The peak pump pulse power was controlled with an attenuator and measured in the time domain using a calibrated PD. In the lower branch, the probe wave was injected into the fiber after adjusting its polarization state to optimize the Brillouin interaction along a 30-m SMF deployed as sensing fiber. Once the probe signal has exited the sensing fiber, the undesired spectral components are filtered out with a FBG prior to the detection in a PD and acquisition in an oscilloscope.

In order to analyze how the Brillouin linewidth broadens, the BGS has been measured for different pulse powers and pulse duration configurations. For instance, Fig. 5.2 (a) and (b) show the Brillouin linewidth broadening for 11-ns and 30-ns pump pulses when the gain is risen up to 1.8 dB and 6.7 dB, respectively. These spectra have been measured by sweeping the frequency separation between the pump and probe in the setup of Fig. 5.1. All these measurements have been normalized to the probe power with no Brillouin interaction to obtain the Brillouin gain by applying the natural logarithm to the normalized data.

Observe that, the BGS linewidth obtained when 11-ns duration pulses are deployed is larger than the one for 30-ns duration pulses. This is because the former pulse has a duration closer to the acoustic phonon lifetime, leading to a wider pulse spectrum, and thus, broaden BGS. This is a well-known effect since the effective Brillouin gain spectrum results from the convolution of the intrinsic Brillouin spectrum and the pump pulse spectrum. The FWHM widths were measured, giving rise to 86 MHz and 45 MHz, respectively. Notice also that the BGS linewidth obtained for 30-ns pulses tends to a Lorentzian profile, while that for 11-ns pulses is more similar to a Voigt or Pseudo-Voigt

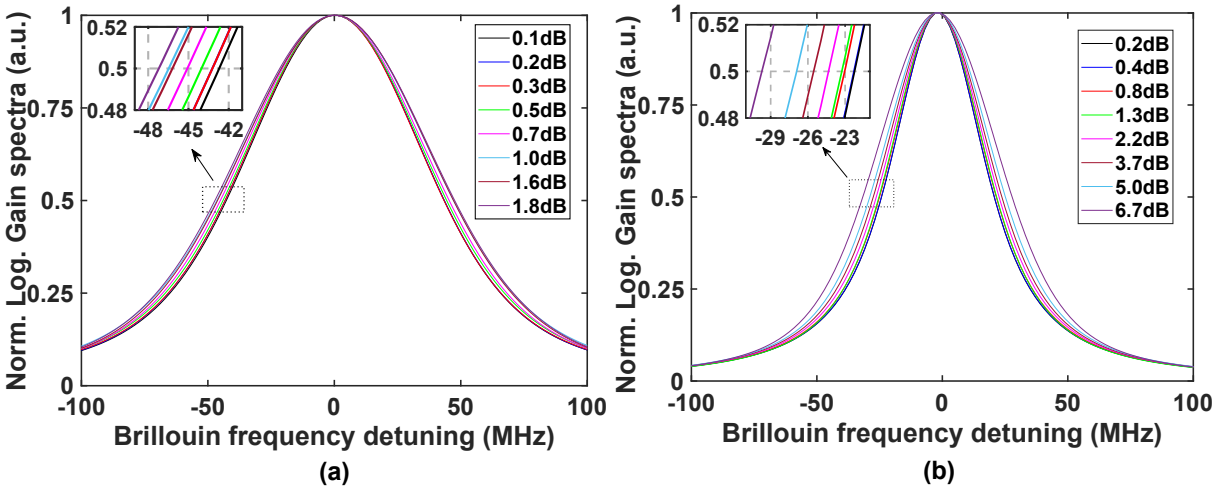

Figure 5.2: Experimental Brillouin gain spectra for (a) 11-ns and (b) 30-ns pulse duration and different Brillouin gains.

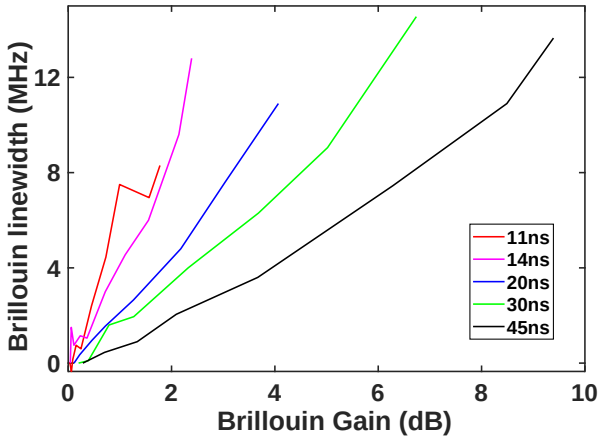

Figure 5.3: Brillouin linewidth broadening for different pulse durations when gain is increased.

profile.

Apart from the notorious broadening effect related to the pulse duration, it has been also observed that the spectra in Fig. 5.2 progressively broaden when the Brillouin gain is increased, as it was found in previous research [108]. For instance, 11-ns pump pulses generate 4-MHz broadening spectra if the Brillouin gain is risen 1 dB, whereas pulses of 30 ns duration lead to broadening the BGS 2.2 MHz. The BGS broadening effect has been analyzed for different pulse durations (from 11 to 45-ns length), showing a lower broadening of the Brillouin linewidth when short pulses are deployed, as it is depicted in Fig. 5.3. In general terms, the linewidth broadening agrees well with the results previously presented [108], confirming the existence of the broadening effect. It is important to remark that this experimental demonstration has been performed using a different BOTDA experimental setup, reducing any possible origin of the linewidth broadening effect due

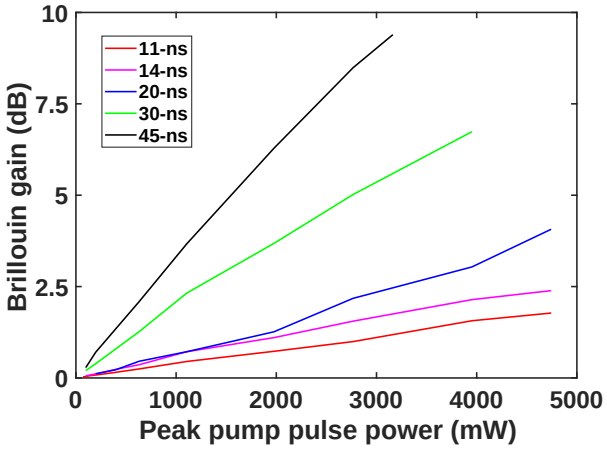

Figure 5.4: Brillouin gain generated in relation to the peak pulse power injected to the fiber for different pulse lengths.

to unintended experimental conditions.

Finally, Fig. 5.4 represents the peak pump pulse power employed for the experimental measurements. Note that, longer time pulses require less power to generate the same gain on the probe than shorter pulses, which is due to the fact that the interaction length between both signals, probe and pump pulse, is larger when longer pulses are deployed. As a result, observe that lower peak power is required to obtain high Brillouin gain when long pulses are deployed.

5.3. Brillouin RF phase-shift linewidth narrowing in dynamic BOTDA sensors

As mentioned, one of the objectives of the research presented in this chapter is to investigate the influence that increasing Brillouin gain has in Dynamic-BOTDA (D-BOTDA) sensors. Once the Brillouin gain dependence has been demonstrated in direct-detection SA-BOTDA sensors, we study and evaluate the gain influence in D-BOTDA sensors. As it has been introduced in chapter 2, the detection process in D-BOTDA sensors involves the interplay of several waves and, and in the same way as in conventional SA-BOTDA sensors, some influences on the spectral shape are expected to be observed when the gain is risen. In this particular slope-assisted configuration setup, the RF phase-shift spectrum of the retrieved signal is used for sensing, so, if this measuring system is also subjected to detrimental effect due to gain variations, changes would be observed on the RF phase-shift spectrum slope.

In this section of the chapter, the experimental setup deployed for the gain dependence study is firstly described. Then, the experimental measurement results are shown and analyzed. Afterward, the analytical results of the BGS shape changes when increasing gain are represented and discussed. Finally, the measurement errors induced by this effect are shown.

5.3.1. Experimental setup

Figure 5.5 depicts the experimental setup deployed for the D-BOTDA sensor used in this experiment. It is basically the same scheme as the conventional setup described previously with the only difference of the generation of a phase-modulated probe wave. This is formed using a phase-modulator located in the lower branch, and then the probe wave is injected into the fiber to counter-propagate the pump pulse and generate the Brillouin amplification in the fiber. After the propagation along the sensing fiber, the probe wave is

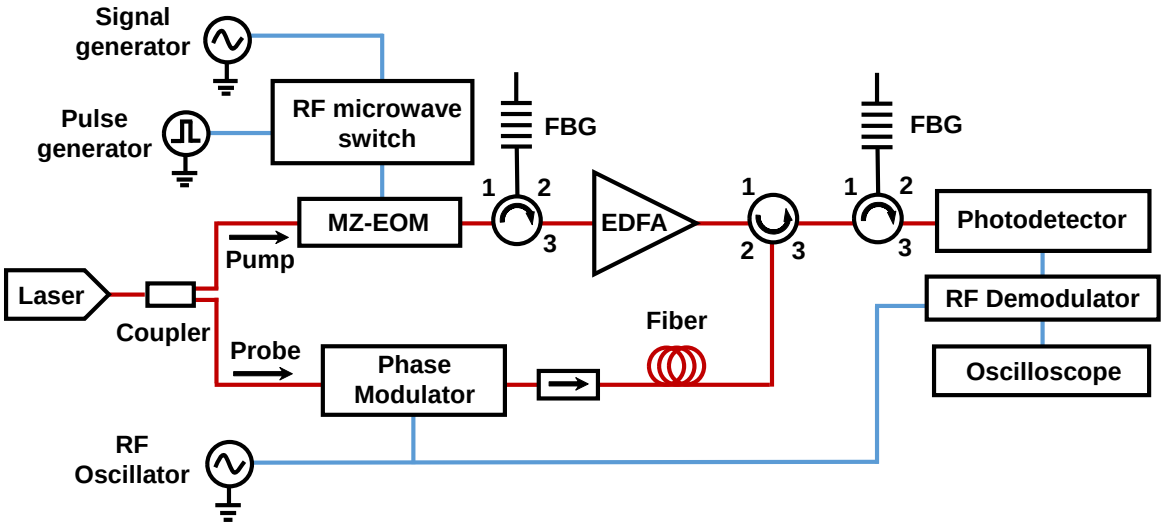

Figure 5.5: Experimental setup for the D-BOTDA sensor.

directed to the receiver where a coherent self-heterodyne detection is performed. Finally, the resultant RF-signal is processed with a RF-demodulator to obtain baseband signals that are captured in the oscilloscope.

5.3.2. Experimental results

In order to evaluate the response of D-BOTDA sensors to large gain variations, experimental measurements of the RF phase-shift spectra for increasing Brillouin gain were performed for 11-ns and 30-ns pulses. Fig. 5.6 (a) and (b) depict the different measured spectra for 11-ns and 30-ns pulses respectively. Similarly to the direct-detection BOTDA results, the retrieved RF phase-shift spectra are wider for 11-ns pulses than the ones for 30-ns pulses. This is again, due to the broadening effect of the measured Brillouin spectrum resulting from the convolution of the pulse spectrum and the intrinsic Brillouin gain. Apart from this, in both cases, gain dependence of the RF phase-shift spectrum shape is again observed. However, in this case, contrary to previous observations, the resultant measured spectra get narrower when the gain is increased.

This unexpected narrowing of the RF phase-shift spectrum has been evaluated assuming as reference the RF phase-shift values that correspond to the frequencies determined by the FWHM of the amplitude spectrum obtained in the direct-detection measurements when deploying small gain, see Fig. 5.2. For instance, in Fig. 5.6 (a), the upper-frequency limit of the FWHM is fixed to 43 MHz, which is given by the Brillouin linewidth of 11-ns length pulses obtained in section 5.2, where a FWHM of 86 MHz was measured. So, the frequency range that we analyze for 11-ns pump pulses is ±43 MHz. While for pump pulses of 30 ns is only ±22.5 MHz. Then, the small gain measurement curve of the

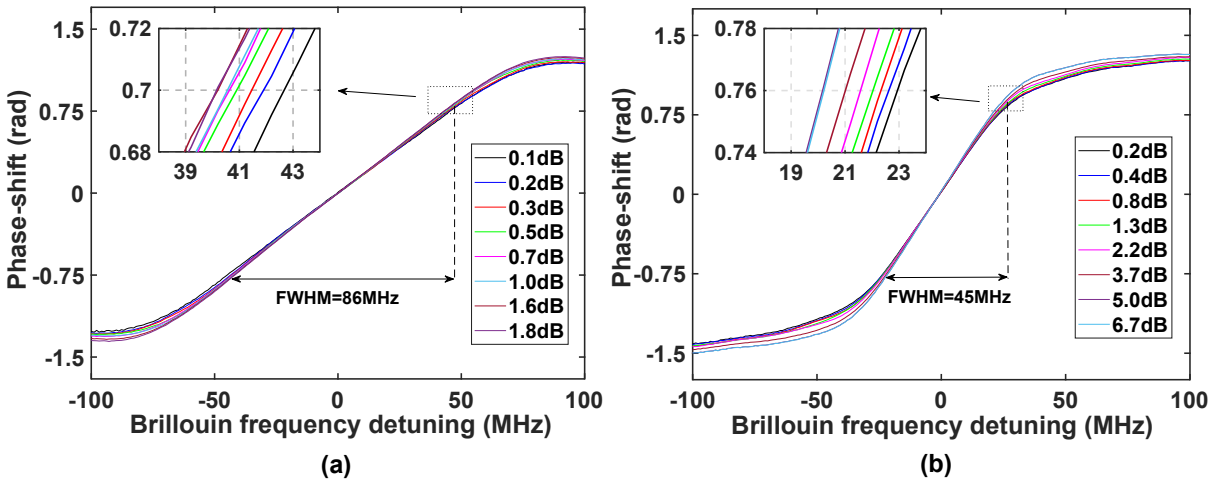

Figure 5.6: Experimental RF phase-shift spectra for (a) 11-ns and (b) 30-ns duration pulses when gain increases from, 0.1 to 1.8 dB and from 0.2 to 6.7 dB respectively.

RF phase-shift spectrum is taken as reference, black line, which determines the reference value, given by the intersection with the 43 MHz frequency detuning. In this case, the resultant phase-shift reference value is around 0.705 rad. Then, in order to obtain the spectral narrowing, the frequency difference between the initial FWHM frequency and the new frequencies at which are obtained the RF phase-shift reference values are calculated. This process is repeated for each measurement as the Brillouin gain is increased.

The narrowing of the RF phase-shift spectra in D-BOTDA sensors is depicted in Fig. 5.6 (a) and (b), which has been quantified using the explained evaluation method. The resulting narrowing when the gain is increased to 1 dB, is about 2 MHz for 11-ns length pulses, whereas for 30-ns pulses, the spectrum narrows by 0.7 MHz.

Notice that the frequency region defined by the FWHM of the Brillouin gain amplitude spectrum matches quite well with the linear region of the RF phase-shift spectrum curves, as it can be seen in Fig. 5.6 (a) and (b). Therefore, the FWHM frequency range is considered as a good estimator of the BFS dynamic measurement range for D-BOTDA setups. These limits are marked in the figures with an arrow and dashed-straight lines. As mentioned, the FWHM values selected for the evaluation of the RF phase-shift narrowing have been calculated from the Brillouin amplitude spectra obtained in the direct-detection BOTDA sensor study presented in section 5.2.

So far, it has been proved that RF phase-shift spectra shape narrows when the Brillouin gain is increased. Now, it is time to analyze how this effect depends on the pulse duration and gain amplitude.

Figure 5.7 highlights the phase-shift narrowing dependence on the pulse duration. Similar experimental measurements were accomplished for different pulse durations (11 ns,

14 ns, 20 ns, 30 ns and 45 ns) and the narrowing of the spectra was calculated as a function of the Brillouin gain. Like observed in direct-detection BOTDA measurements, the general trend of the phase-shift spectrum narrowing effect is to inversely depend on the pulse duration. In particular, if both dependence effects are compared, conventional SA-BOTDA sensor and D-BOTDA sensor, it is clear that the gain influence on RF phase-shift spectrum measured in D-BOTDA sensors is much smaller than on the Brillouin gain spectrum measured in direct-detection BOTDA sensors, demonstrating that the former system is more tolerant to gain variations than the latter.

It is interesting to remark that in a previous research work carried out by our research group [27], a moderate maximum peak power of 26 dBm was deployed in a similar setup, leading to 0.5 dB peak Brillouin gain. Extrapolating this gain from the data in Fig. 5.7, it is concluded that a narrowing of the RF phase-shift of the order of 1 MHz was induced in those measurements. However, the narrowing of the spectrum was comparable to the measurement uncertainty of those experiments, and hence, it was not visible in the results. This means that, D-BOTDA sensors are susceptible to the narrowing effect only if the peak pump pulse power deployed is highly increased. Moreover, notice that this effect will be only feasible in short lengths of fiber, where high pump pulses can be deployed without generating nonlinear effects such as MI.

Apart from the proposed evaluation method of the RF phase-shift spectrum shape distortion, another parameter that can be used to quantify the RF phase-shift spectrum narrowing is the variation of the linear region slope. As it is well-known, this parameter is directly linked to dynamic measurements that rely on the slope-assisted technique, that translates any modification of the measured phase-shift into BFS changes. This means that, if there is a narrowing/broadening of the RF phase-shift spectrum, the slope will

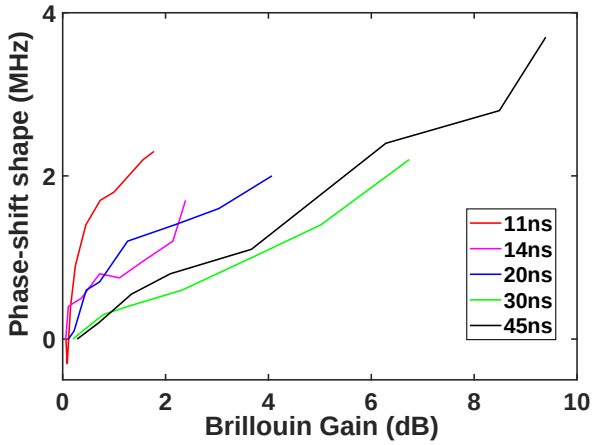

Figure 5.7: RF phase-shift shape narrowing for different pulse lenghts when gain is risen.

increase/decrease.

Figure 5.8 depicts the slope changes at the center of the RF phase-shift spectrum as a function of the peak Brillouin gain for different pulse duration. Observe that the dependence of the slope change on the gain is approximately linear for every pulse duration, except for pulses of 45 ns, which differs from the rest of the curves. This abnormal result is due to the interplay of the narrowing and the broadening effects that occur simultaneously when the gain is increased. Since the broadening of the Brillouin linewidth effect is less significant for long pulses, as demonstrated in section 5.2 and depicted in Fig. 5.3, the compensation of the narrowing effect observed in D-BOTDA sensor is more efficient with short pulses, while the compensation is significantly lower for 45-ns pulses, inducing this abnormal response on the slope change. The compensation of the narrowing effect will be explained in detail in the following section.

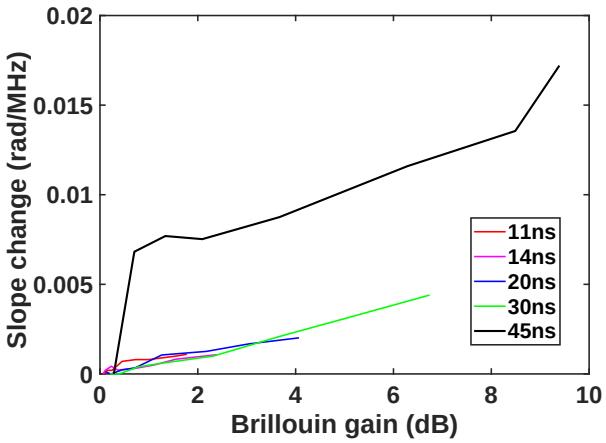

Figure 5.8: Experimental RF phase-shift spectrum slope change due to Brillouin gain.

5.3.3. Analytical model for RF phase-shift spectrum narrowing effect

As it has been shown, experimental results have confirmed that RF phase-shift spectrum shape is dependent on the Brillouin gain level when D-BOTDA sensors are deployed. In particular, a narrowing effect of the spectra instead of a broadening effect is observed. This unexpected response has been also investigated using an analytical model that represents the RF phase-shift value as a function of the frequency detuning and Brillouin linewidth. The expression to represent the RF phase-shift spectrum, θ_{RF}, employed in this study was derived with help of the phasorial diagram presented in Fig. 2.8:

$$\theta_{RF} = \arctan\left(\frac{G_{SBS}\cdot\sin(\varphi_{SBS})}{G_{SBS}\cdot\cos(\varphi_{SBS})-1}\right) \tag{5.1}$$

And replacing Eq. (2.18a) and Eq. (2.18b) into Eq. (5.1), the resultant expression for θ_{RF} is obtained:

$$\theta_{RF}(\Delta\nu) = \arctan\left(\frac{exp\left(g_B\frac{\Delta\nu_B^2}{\Delta\nu_B^2+4\Delta\nu^2}\right)\cdot\sin\left(-g_B\frac{2\Delta\nu_B\Delta\nu}{\Delta\nu_B^2+4\Delta\nu^2}\right)}{exp\left(g_B\frac{\Delta\nu_B^2}{\Delta\nu_B^2+4\Delta\nu^2}\right)\cdot\cos\left(-g_B\frac{2\Delta\nu_B\Delta\nu}{\Delta\nu_B^2+4\Delta\nu^2}\right)-1}\right) \tag{5.2}$$

This expression was used to evaluate the RF phase-shift narrowing effect, calculating the response of θ_{RF} for different peak Brillouin gain values and assuming that long duration pump pulses were deployed. To do this, a typical $\Delta\nu_B$ value of 33 MHz was selected and the pump pulse spectrum was approximated by a Lorentzian function (pulses longer than 50 ns). In these initial measurements, $\Delta\nu_B$ was regarded as constant and independent of gain. Fig. 5.9 (a) depicts the calculated narrowing effect of the RF phase-shift spectrum as the Brillouin gain increases. Fig. 5.9 (b) represents the variation of the θ_{RF} slope for different logarithmic gain values. Similarly to the results observed in the experimental measurements of section 5.3.2, see Fig. 5.7, the gradient of the slope change follows a linear trend for increasing gains.

However, as it has been demonstrated in section 5.2, in real-case scenarions Brillouin linewidth can not be considered a constant value if Brillouin gain is modified. So, the

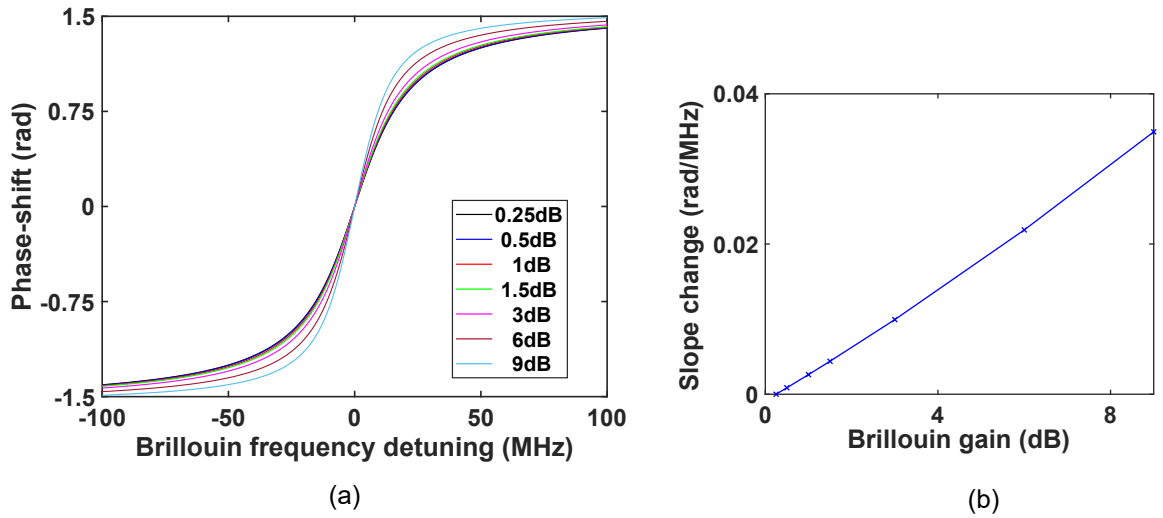

Figure 5.9: (a) Calculated phase-shift narrowing for long pulses using expression 5.2 under the influence of gain increment. (b) Dependence of the slope of θ_{RF} on logarithmic gain.

analytical model obtained in Eq. (5.2) must be completed by incorporating the dependence of $\Delta\nu_B$ on Brillouin gain. This dependence was introduced by taking advantage of the following expression, which was derived in [108, 109]:

$$\Delta\nu_B \approx \frac{1}{2\pi\tau_p} + \frac{3g_0}{4\pi T} \tag{5.3}$$

where τ_p is the phonon lifetime, T is the time duration of the pulse employed for each measurement and g_0 is the maximum peak Brillouin gain given in [dB].

Therefore, similar calculations of the RF phase-shift spectra were performed for increasing values of gain, taking into account the linewidth broadening given by Eq. 5.3. Fig. 5.10 (a) depicts the reevaluation of the model, showing a reduction of the narrowing effect, while the change of the slope of θ_{RF} with gain is indeed, clearly reduced, as shown in Fig. 5.10 (b). The reduction of the narrowing is understandable because of the fact that both effects, the broadening of the Brillouin linewidth observed in direct-detection BOTDA setups, and the narrowing of the RF phase-shift observed in D-BOTDA sensors, produce a counteracting influence over the RF phase-shift linewidth. While the former effect broadens the spectral shape, the latter one narrows the spectrum.

Finally, notice also that these calculated slope changes agree well with the experimental results obtained for 45-ns length pulses presented in Fig. 5.8. Thus, these calculated results confirm either the existence of the RF phase-shift narrowing effect and also the reliability of the analytical model for long duration pulses.

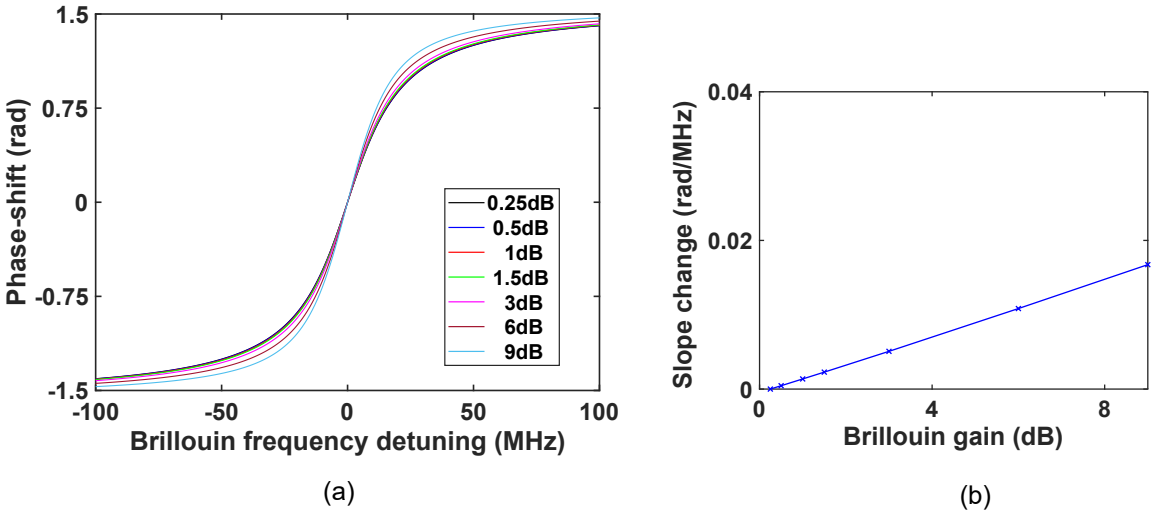

Figure 5.10: (a) Calculated phase-shift narrowing for long pulses using expression 5.2 under the influence of gain increment and Brillouin linewidth broadening. (b) Dependence of the slope of θ_{RF} on logarithmic gain.

5.3.4. Phasorial explanation of the RF phase-shift spectrum narrowing effect

In order to provide a further explanation of the narrowing effect experienced by the RF phase-shift spectra when the gain is increased, a phasor representation of the expression Eq. (2.19) has been employed. As explained in section 2.2.1, this equation conveys the fact that the detection of the probe wave is the result of the interference of two RF signals. The first one coming from the beating of the optical carrier with the lower sideband, and the second one coming from the beating of the optical carrier and the upper sideband of the phase-modulated probe wave. Without Brillouin gain, both RF signals have opposite phase and equal amplitude, and hence, they destructively interfere, canceling one another. On the contrary, when there is Brillouin interaction, one of the RF signals changes its amplitude and phase due to the SBS interaction. Fig. 5.11 represents the two interfering RF signals by two phasors (in blue). The detected RF signal is shown as another phasor (in red) that is the result of the addition of these two interfering phasors. The phase of this resultant phasor, θ_{RF}, is the RF phase-shift that is measured in the D-BOTDA sensor.

Two examples of detected signals for increasing gain are depicted. Notice that, when Brillouin gain is increased, the phasor affected by Brillouin interaction increments its amplitude (Brillouin gain, G_{SBS}) and phase (Brillouin phase-shift, φ_{SBS}), leading to the blue dashed-line phasor instead of the blue solid-line phasor. The resultant red dashed-line phasor has a larger θ_{RF} than the lower-gain red solid-line phasor. If we translate this θ_{RF} behavior to one particular RF phase-shift spectrum curve, it means that the RF phase-shift value detected for a particular detuning frequency grows with gain, which implies that the RF phase-shift spectrum slope increases, hence, the spectrum shape becomes narrower with gain, as it has been observed experimentally and through previous calculations.

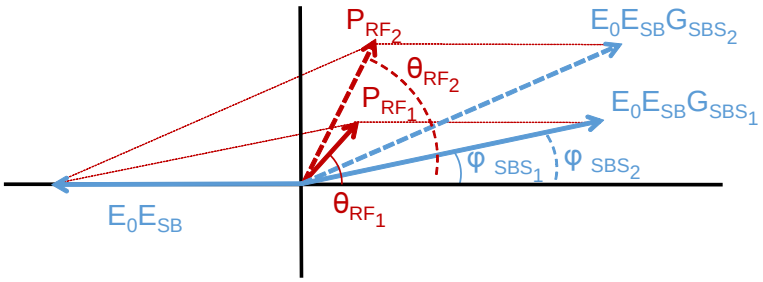

Figure 5.11: Phase-modulated probe wave phasorial representation in a D-BOTDA sensor.

5.3.5. Calculated results and discussion

So far, along this chapter of the thesis, it has been experimentally demonstrated that indeed, there is a Brillouin linewidth dependence on the gain for direct-detection SA-BOTDA sensors, as well as a dependence of the RF phase-shift spectra on the Brillouin gain in D-BOTDA sensors. The experimental results have been correlated with the analytical model calculations that have also proved the existence of the narrowing effect for pump pulses longer than 50 ns.

In this new section, the analytical model is used to calculate the RF phase-shift spectral dependence on the Brillouin gain when shorter pulses are deployed. The calculations will be compared to the experimental results shown in section 5.3.2. However, as it has been mentioned before, the model in Eq 5.2 is only valid for long duration pulses (> 50 ns). This is because of the fact that the Brillouin gain spectra have no longer a Lorentzian shape when shorter pulses are deployed, and thus, this approximation is not valid anymore.

So, in order to accurately calculate the spectral shape of the RF phase-shift spectrum when shorter pulses are deployed, again, the general model of Eq. (5.1) was used. Although in this case, the gain was represented as the convolution of the intrinsic Brillouin gain spectrum (Lorentzian) with the pulse spectrum, which is assumed to have a Gaussian profile. As a result of the convolution, the calculated gain spectrum follows a Faddeeva profile [111], which displays a better fit to the gain spectra measured in section 5.2 when short pulses were deployed.

The process of calculating the RF phase-shift spectra in this section is as follows: firstly, the experimental results obtained from Brillouin gain spectra in section 5.2 are fitted using the Faddeeva profile. Then, from this fitting, the necessary parameters for the model calculations as a function of the pump pulse power for each pulse duration are obtained. These parameters are the Lorentzian and Gaussian linewidth and the peak gain. Finally, the RF phase-shift spectra for each measurement condition are calculated using the analytical model and the parameters previously obtained.

Figure 5.12 (a) and Fig. 5.13 (a) show the calculated RF phase-shift spectra as a function of gain for 11-ns and 30-ns pulses. As it is expected, the retrieved spectra show a narrowing effect for the increasing gain, as before. In these calculations, in the same way as the study shown in section 5.3.3, these results are obtained assuming that there was no gain dependence of the Brillouin linewidth. This means that Brillouin gain spectrum linewidth parameters, Lorentzian and Gaussian linewidths, were fixed to those observed for small gain and just the peak gain was modified.

Thus, the change observed in the shape of these spectra (narrowing), is just due to

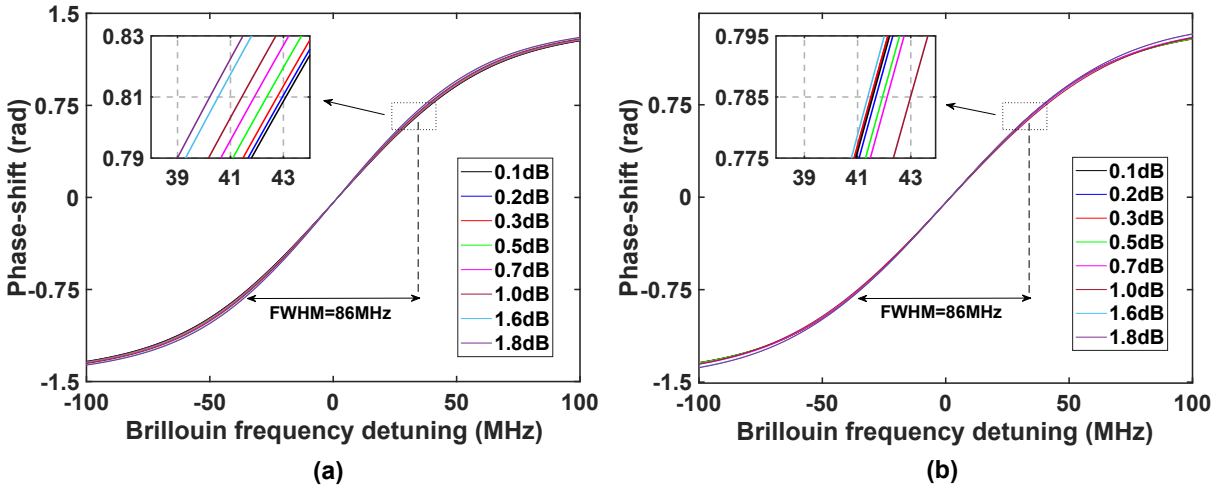

Figure 5.12: Calculated phase-shift narrowing for 11-ns pulses considering (a) only gain increment; (b) gain increment and Brillouin linewidth broadening.

the nature of the interference between detected waves, which is conveyed by Eq. (2.19), as it has been explained with the phasor scheme. In this case, the spectral linewidth broadening effect presented in section 5.2 is not considered and there is no contribution. Notice that, looking into the narrowing obtained in Fig. 5.12 (a) and Fig. 5.13 (a), it is found that the narrowing is slightly larger than the one observed in the experimental results, plotted in Fig. 5.6 (a) and (b). This difference is due to the fact that Brillouin linewidth broadening has not been taken into account and there is no compensation of the narrowing. However, in order to consider the real scenario, the Brillouin linewidth broadening must be introduced in the model to recalculate the spectral response with increasing gain. Fig. 5.12 (b) and Fig. 5.13 (b) highlight the calculated results, where it is

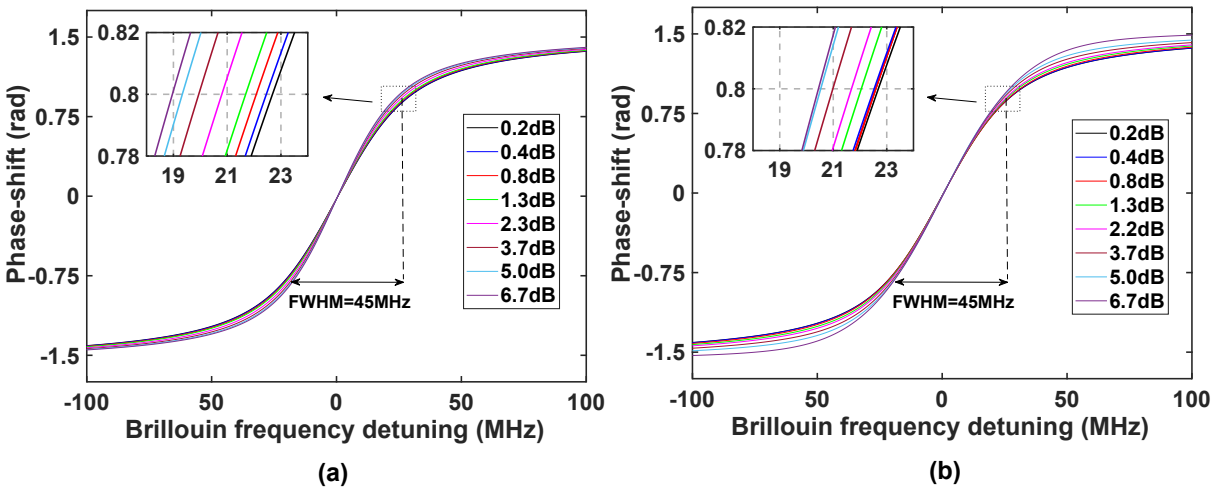

Figure 5.13: Calculated phase-shift narrowing for 30-ns pulses considering (a) only gain increment; (b) gain increment and Brillouin linewidth broadening.

observed a reduction of the narrowing effect, as expected, and hence, agreeing well with the results obtained in the experiments.

Therefore, the presented experimental results and analytical calculations demonstrate the natural trend to narrow of the RF phase-shift spectra for increasing gain in D-BOTDA sensors. Moreover, an important finding was attained with this work, which is the compensation of the narrowing effect to some extent by the Brillouin linewidth broadening effect observed when the gain is increased. Indeed, this is the reason why the Brillouin gain variations are less deleterious in D-BOTDA sensors than in conventional direct-detection SA-BOTDA sensors.

5.3.6. Measurement error originated by the gain dependence of the RF phase-shift in D-BOTDA sensors

Every BOTDA monitoring system, even those requiring a short length of sensing fibers, will deploy the maximum tolerable peak pump pulses to attain its best performance. As it has been demonstrated and explained along this chapter, any increment of the pump pulse power leads to rising the Brillouin gain, and thus, a broadening of the Brillouin gain spectrum and a narrowing of the RF phase-shift spectrum in case a D-BOTDA sensor is used. If an important broadening/narrowing is induced, it can generate a significant distortion of the spectrum, leading to errors in dynamic operation, as it has been already demonstrated for the direct-detection SA-BOTDA sensors [108, 112]. In this section, a study of the measurement errors induced in the determination of the BFS for increasing gain for D-BOTDA sensors is presented. This analysis is accomplished using the experimental measurements previously shown.

In order to provide a quantified measurement error, it is necessary to perform an initial calibration of the RF phase-shift spectrum for this type of dynamic sensors. This is because when dynamic measurements are performed, a value of θ_{RF} is dynamically obtained, which is directly translated to BFS changes by using the θ_{RF} versus frequency detuning calibration curve previously obtained.

Figure 5.14 schematically depicts how the error as a function of detuning frequency and Brillouin gain is calculated for given measurement conditions. The calibration of the RF phase-shift spectra can be performed at either low pump pulse power, small Brillouin gain, or high pump pulse power, high Brillouin gain. The blue trace represents the first RF phase-shift spectrum curve, and the red one is another RF phase-shift spectrum curve obtained when the Brillouin gain has been increased. Then, using either of the calibration curves, the frequency difference between both curves that corresponds for the reference

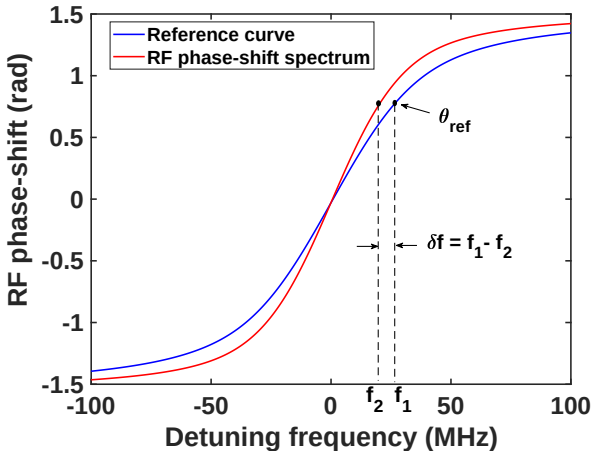

Figure 5.14: Measurement error calculation example.

θ_{RF} value is calculated. This frequency difference represents the error for the measurement subjected to a different Brillouin gain. For instance, in Fig. 5.14, for a particular reference value of $\theta_{RF_{ref}}$, there is a frequency mismatch between the $\Delta\nu$ value that the two of these spectra provide this $\theta_{RF_{ref}}$, equal to $\delta f = f_1 - f_2$. The measurement error is calculated by simply subtract these two values of $\Delta\nu$.

There is an alternative way of calculating this measurement error, which is based on using the RF phase-shift spectrum slope change. However, this method is not as accurate as the one explained before, particularly for regions away from $\Delta\nu = 0$ where the RF phase-shift spectrum deviates from linearity. So, this option was discarded in this study.

Therefore, based on the defined error calculation method, it is clear that the error will be dependent on the frequency detuning. This means that, in dynamic measurements, if there is a big change of BFS along the fiber, the measurement errors will be more significant in those fibers than for uniform sensing fibers. Fig. 5.15 (a) and (b) depict the error for 11-ns and 30-ns pulses when Brillouin gain is modified. In these graphs the RF phase-shift spectrum measured with low Brillouin gain has been taken as a reference. Notice that, when the detuning between the BFS and the probe wave frequency is small, the resultant error is very small. This is because of the fact that the narrowing of the RF phase-shift spectrum close to $\Delta\nu = 0$ is very small. Contrary, the error grows as the frequency detuning increases.

In contrast, Fig. 5.16 shows the measuring error calculations taking as reference curve the RF phase-shift spectrum measured when the maximum Brillouin gain is employed. In this case, the graphs show that the measurement errors are slightly more linear in the FWHM region. Furthermore, the error magnitude tends to be smaller due to the fact that

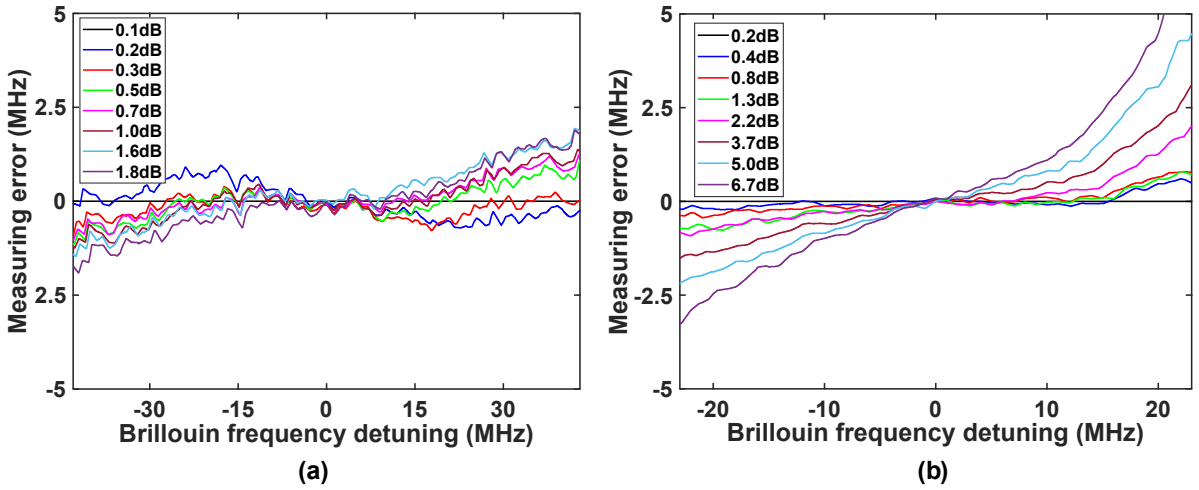

Figure 5.15: Measuring error in D-BOTDA sensor when Brillouin gain is modified and low gain spectrum is used for calibration (a) 11-ns and (b) 30-ns pulses.

the high gain curve has a slightly larger linear region, so, taking this as a reference for calibration, the comparison to the rest of measurements (lower gains) improves; hence, reducing the error.

These graphs can be used to calculate the trade-offs among the different parameters involved in a particular D-BOTDA sensor measurement, i.e., the desired BFS dynamic measurement range, maximum tolerable BFS error, and pump pulse power. For instance, if it is assumed that the low gain spectrum curve is taken as reference and the working pump peak power is 20 dBm, the dynamic strain measurements performed with 1.1-m spatial resolution will provide a maximum accuracy of 20 $\mu\epsilon$ (1 MHz) and a total dynamic measurement range of 1720 $\mu\epsilon$ (86 MHz). Then, from Fig. 5.15 (a) it is deduced that, Brillouin gain should be kept below 0.5 dB to satisfy the mentioned measurement requirements. This means that, looking at Fig. 5.4, the pump pulse power should be lower than 30.5 dBm, otherwise, the error experienced with respect to the lower gain spectrum curve at the FWHM detuning frequency would exceed 1 MHz.

On the other hand, if the measurement requirements are 3-m spatial resolution, an accuracy of 20 $\mu\epsilon$ and a dynamic measurement range of 760 $\mu\epsilon$ (45 MHz), it is possible to affirm from Fig. 5.15 (b) that the Brillouin gain should be kept below 1.3 dB, and hence, the peak pump pulses below 28 dBm. Notice that, as it has been previously mentioned, short duration pump pulses permit to deploy higher amplitude pulses, which is because of the fact that the Brillouin gain induced to the probe is lower for shorter pulses.

Finally, it is important to remark that the pump pulse power limitation imposed by the RF phase-shift spectrum narrowing effect is only significant if the power level limit is below the threshold imposed by other nonlinear effects such as MI, as presented in Fig. 4

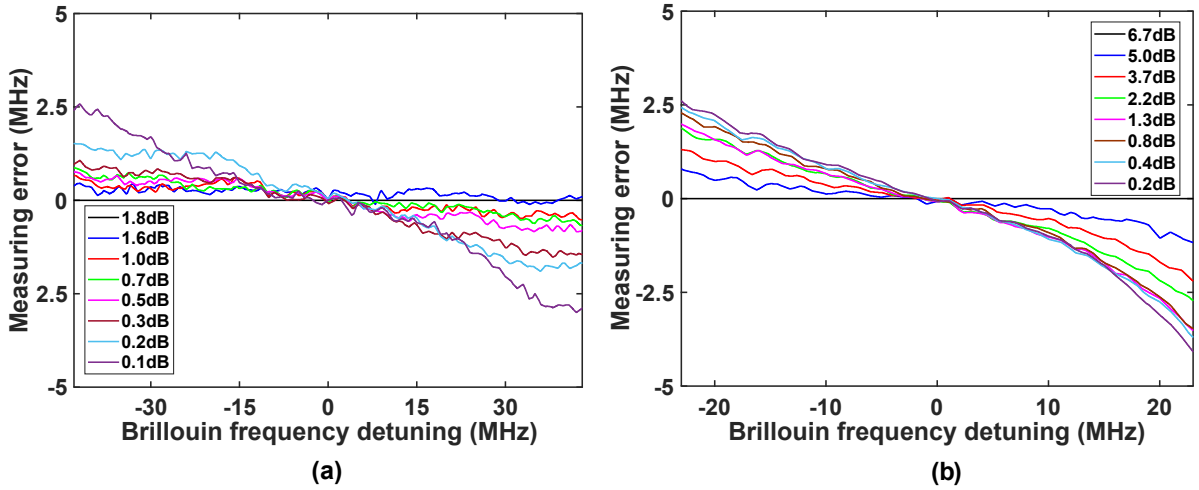

Figure 5.16: Measuring error in D-BOTDA sensor when Brillouin gain is modified and high gain spectrum is used for calibration (a) 11-ns and (b) 30-ns pulses.

in [36]. For instance, if the measurement conditions previously described are assumed, the pulse peak power of 30.5 dBm for 11-ns pulses, MI will limit the maximum link length to 2 km. In contrast, if 28 dBm pump peak power and 30-ns length pulses are deployed, MI will limit the maximum link length to 5-km [36]. Therefore, for measuring structures larger than 2-km length, MI will be the most limiting factor, instead of the error generated by the RF phase-shift spectrum shape change due to its dependence on the Brillouin gain in D-BOTDA sensors.

5.4. Extension of the dynamic range in dynamic BOTDA sensors

As it has been mentioned in the introduction of this chapter, another fundamental limitation of dynamic DOFS based on the SA-BOTDA technique is the limited dynamic range that they can offer. In direct-detection SA-BOTDA sensors, the dynamic range is determined by the linear region of the slope of the BGS, which directly depends on the BGS linewidth. For instance, if a 10-ns duration pump pulse is deployed to perform the measurements, the usable width of the BGS slope is typically around 50 MHz. Thus, taking into account the 20 $\mu\varepsilon$/MHz strain coefficient, the dynamic range turns to be about 1000 $\mu\varepsilon$, which is insufficient for many structural health monitoring applications.

Diverse solutions have been presented during the last years to overcome this constraint and extend the dynamic range of this type of sensor. One approach is based on switching the probe wave frequency in several steps within a given range, so that, multiple BGS slopes can be interrogated sequentially [106, 107, 113]. However, the measurement time

increases proportionally to the number of frequency steps, as multiple scans are required. Another option is to deploy short pump pulses with the aim of broadening the BGS shape [62].

There is still a strong demand from the industry to further extend the dynamic range of SA-BOTDA sensors to be able to perform dynamic strain measurements with a wide dynamic range. For example, in the wind turbine industry, blade certification tests require strain measurements over ± 10000 $\mu\varepsilon$, which far exceeds the current limit of SA-BOTDA sensors. It is important to stress that most of these proposals are implemented only for conventional direct-detection SA-BOTDA sensors. In contrast, the dynamic range of the D-BOTDA sensors that has been recently devised by our research group has not been enhanced yet.

Based on this need, part of this thesis work has been focused on deploying a theoretical and experimental study to enlarge the dynamic range of D-BOTDA sensors. As a result, two different techniques that allow to extend this range have been developed and demonstrated. In particular, the first method is based on the generation of pump pulses containing multiple frequency components simultaneously, so as to synthesize a phase-shift slope that extends over a larger frequency region. The second technique used to improve the dynamic range involves the shortening of the pulse duration that lead to the broadening of the Brillouin gain linewidth, and thus, the linear region of the RF phase-shift slope, providing a larger measurement region in D-BOTDA sensors. Therefore, in this section of the chapter, both of these methods are introduced and a preliminary validation of the systems is fulfilled using an analytical model to represent the spectral response. Then, an experimental demonstration to prove the enhanced performance of both techniques is presented. Finally, the results of the proposed techniques are compared and discussed.

5.4.1. Fundamentals of multi-spectral components pump pulses method

As mentioned, the first technique investigated to enlarge the dynamic range of D-BOTDA sensors involves the simultaneous generation of multiple frequency components of the pump pulses. The pump signal is conditioned in terms of power level and frequency separation of the different pump components previous the launch into the sensing fiber. Then, the multiple pump pulses interact with one of the sidebands of the phase-modulated probe wave injected from the other end of the fiber. As it is highlighted in Fig. 5.17, multiple Brillouin spectra are generated on the probe wave induced by the interaction with the

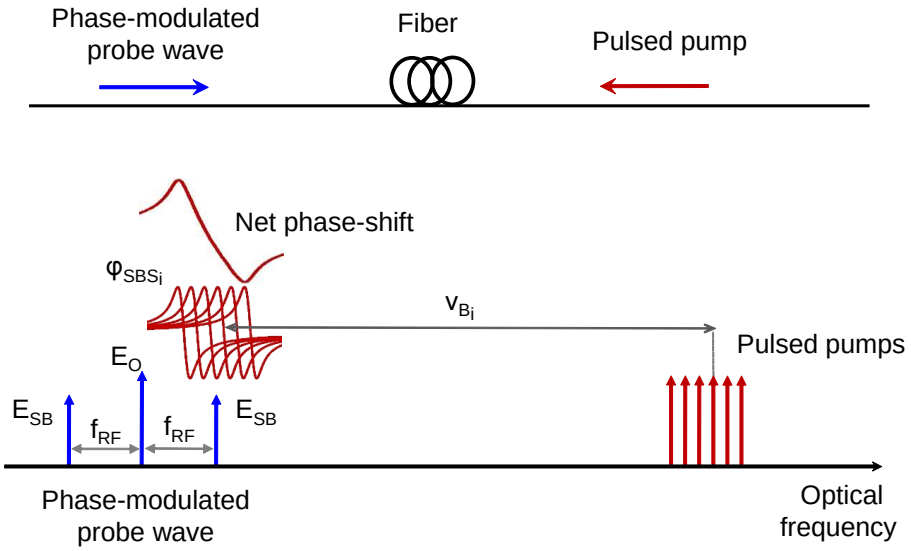

Figure 5.17: Scheme of the working principle of the multi-frequency components pump technique.

different pump components. The phase-shift spectra overlap and give rise to an extended phase-shift spectrum, showing a much wider shape, and thus, extending the dynamic range.

As shown, the working principle of this technique is just based on the addition of the n different Brillouin gain contributions generated by each of the pump pulse components during the propagation of the probe along the sensing fiber. So, the resultant Brillouin gain of the multiple pump pulse components can be expressed as the sum of the different exponential gain contributions:

$$H_{SBS_T}(\Delta\nu, z) = H_{SBS_1} H_{SBS_2} H_{SBS_3} ... H_{SBS_n} = exp\left(\sum_{i=1}^{n} g_{B_i}(\Delta\nu_i, z) \right) \tag{5.4}$$

where $H_{SBS_T}(\Delta\nu, z)$ is the resultant complex BGS at position z of all the contributions given by the n spectral components of the pump pulses. $H_{SBS_i}(\Delta\nu, z)$ represents the $i-th$ complex Brillouin gain defined in Eq. (2.17), while $g_{B_i}(\Delta\nu_i, z)$ is the complex exponential Brillouin gain at position z induced by the $i-th$ spectral component.

Then, if the pump pulse duration employed in the measuring system is assumed to be significantly longer than the phonon lifetime (>10 ns), the pulse spectral shape can be approximated by a Lorentzian shape, as explained in the previous section. Thus, the Brillouin gain response can be defined as follows:

$$H_{SBS_T}(\Delta\nu, z) = exp\left(\sum_{i=1}^{n} g_{B_i} \frac{\Delta\nu_B}{\Delta\nu_B + 2j\Delta\nu_i}\right) \tag{5.5}$$

where g_{B_i} is the peak gain of the Brillouin interaction induced by the $i-th$ spectral component and $\Delta\nu_i$ is de frequency detuning with respect to the $i-th$ spectral component of the pump.

So far, Eq. (5.5) has been derived to represents the complex Brillouin gain for the multi-spectral component pump pulses technique when pulses longer than the phonon lifetime are deployed. However, apart from improving the dynamic range of SA-BOTDA sensors, a requirement of this investigation was to propose techniques with high spatial resolution, as dynamic sensing usually requires high spatial resolution. Therefore, this research work was demonstrated deploying pump pulses with a duration equal or shorter than the phonon lifetime ($\leq$10 ns). This means that $g_{B_i}(\Delta\nu, z)$ will show a broader spectrum curve, giving rise to a wider linear region, as shown in the previous section, and thus, enhancing the dynamic range of the sensor. So, in order to obtain an equation for the representation of the total gain induced by short duration pump pulses, the approach previously explained was considered, which relies on modeling $g_{B_i}(\Delta\nu, z)$ with a Faddeeva profile (see section 5.3.5).

First, Brillouin amplitude and Brillouin phase-shift spectra were calculated using the analytical model to analyze the proposed method. Fig. 5.18 (a) represents the calculated Brillouin amplitude spectra when pump pulses with one, four and six spectral components are counter-propagated to the probe wave. In this case, it was assumed that 10-ns pulses were deployed, so, the amplitude spectra were calculated modeling $g_{B_i}(\Delta\nu, z)$ as a Faddeeva profile with a FWHM of 90 MHz.

In order to optimize the performance of the multi-spectral component technique, it is necessary to adjust the frequency detuning between the different frequency components of the pump signals equal to the 60 % of the FWHM frequency range of its gain spectrum. This is just to attain a correct overlap of the gain contributions and optimize the extension of the phase-shift range, obtaining a wider and uniform linear region. Note that this frequency detuning depends on the Brillouin linewidth of the spectrum, and thus, on the pulse duration. The resultant BGS_T is broadened and its peak is flatten as the number of spectral components in the pulse increases. Moreover, the peak amplitude of the gain spectrum is increased due to the addition of the multiple gain contributions. However, note that the slope region of the amplitude spectrum is not broadened, maintaining a similar shape as initially; hence, the multi-component pump technique would be useless for extending the dynamic range in direct-detection SA-BOTDA sensors, since the slope

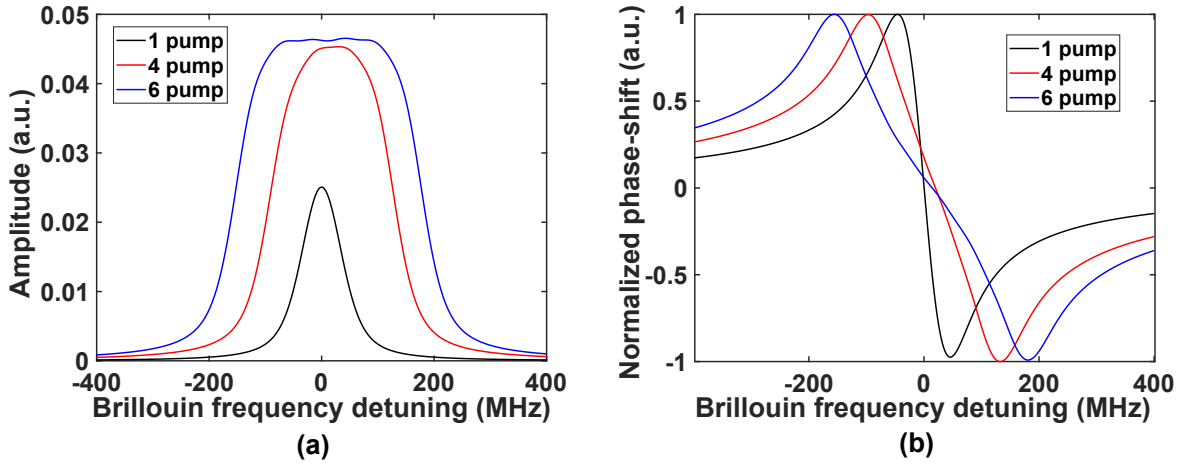

Figure 5.18: Calculated results of the Brillouin amplitude spectra for different number of pump pulse frequencies. Brillouin gain linewidth of 90 MHz and a frequency difference between tones of 55 MHz were deployed.

of the gain spectrum is not been modified and extended with this method.

In contrast, Fig. 5.18 (b) depicts the Brillouin phase-shift spectra obtained for the different number of pump pulse components. As it can be seen, the slope region of the spectra has been broadened due to the overlap of the phase-shift spectra induced by each spectral component of the pump pulse. Thus, these results hint that the proposed broadening method is valid to extend the dynamic range of SA-BOTDA sensors that rely on Brillouin phase-shift measurements, such as the D-BOTDA sensor.

Once the preliminary calculated results confirmed that the multi-spectral pump components technique can be a possible method to extend the dynamic range in D-BOTDA sensors, the research was focused on evaluating analytically the spectral response of D-BOTDA sensors when deploying this technique. The expression that represents the detected RF signal was already presented in chapter 2, see Eq. (2.19). From this equation and the phasorial diagram shown in Fig. 2.8, the amplitude of the detected RF signal is directly derived when multiple pump pulse components are deployed (the RF phase-shift spectrum was derived in Eq. (5.1)):

$$|P_{RF}| = E_0 E_{SB} \sqrt{\left[G_{SBS}\left(\cos\left(\varphi_{SBS}\right) - 1\right)\right]^2 + \left[G_{SBS}\sin\left(\varphi_{SBS}\right)\right]^2} \tag{5.6}$$

where G_{SBS} and φ_{SBS} are the amplitude and phase-shift of the total Brillouin gain spectrum generated by all the pump spectral components.

Figure 5.19 (a) and Fig. 5.19 (b) show the calculated spectral broadening obtained with the multiple pump pulse components technique when the D-BOTDA sensor scheme

is deployed. This calculation was performed using Eq. (5.1) and Eq. (5.6) and assuming a Faddeeva profile for the Brillouin gain. Notice that, similarly to the Brillouin phase-shift spectra, the RF phase-shift spectra shape becomes wider, providing a larger slope region, what means that the dynamic range is enhanced. As it is observed, the slope is not purely linear, as it is the result of the self-heterodyne detection process of the phase-modulated probe wave. However, this is not an important issue because this slope can be calibrated and used for dynamic measurements as long as it has a monotonically increasing behavior.

With regard to the amplitude spectrum, again, a broadening and an increment of the peak amplitude is observed. The latter is going to result in an enhancement of the accuracy, due to the SNR increasing. Observe that the detected RF amplitude spectrum shape shown in Fig. 5.19 (a) slightly differs with the Brillouin gain spectrum shape shown in Fig. 5.19 (a). This is basically due to the slight affectation of the modulated probe wave carrier with the Brillouin interaction, which appears just after the heterodyne detection process of the RF signal [27].

Apparently, this method proposed to enhance the dynamic range could provide arbitrarily large dynamic range by simply adding sufficient spectral components to the pump pulse. However, as it will be shown in the next sections, experimental results have demonstrated that nonlinear cross Kerr-effect interactions limit the number of spectral components that can be used in this technique [17, 33, 36].

5.4.2. Fundamentals of the pulse shortening method

The second technique that is proposed in this thesis to enhance the dynamic range of D-BOTDA sensors is based on shortening the length of the pump pulses injected into

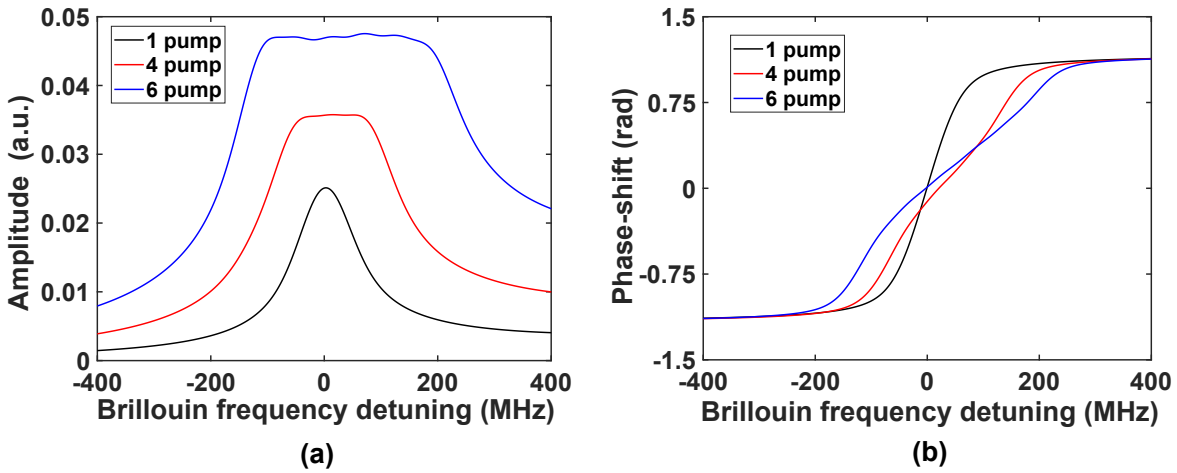

Figure 5.19: Calculated results of the RF amplitude spectra for different number of pump pulse components.

the fiber. Fig. 5.20 schematically depicts the working principle of the pulse shortening method. This technique relies on the inverse dependence of the Brillouin gain linewidth on the pulse duration, as observed in Fig. 5.20. Basically, when the pump pulses generated are shorter than 20 ns, the BGS linewidth, $\Delta\nu_B$, is approximately given by $1/T$ [108].

Like in section 5.4.1, the spectral Brillouin gain and phase-shift curves are analytically calculated using Eq. (5.4) to analyze the response of direct-detection BOTDA sensors to this second method. In this case, the linewidth parameters of the Faddeeva profile are previously calculated depending on the length of the pulse deployed. A Faddeeva profile has been used since the method was evaluated for short pump pulses, from 3-ns to 10-ns. Fig. 5.21 (a) and Fig. 5.21 (b) show the broadening of the Brillouin gain and Brillouin phase-shift spectra when different pulse durations are used.

Similarly, the broadening of the Brillouin amplitude and phase-shift spectra due to the shortening of the pump pulses has been analytically demonstrated in D-BOTDA sensors analyzing the response of the detected RF signal. Fig. 5.22 (a) and Fig. 5.22 (b) represent the broadening of the RF amplitude and RF phase-shift spectra as the pump pulses are shortened. As it is observed, the RF phase-shift spectrum broadens, providing a larger linear region of the phase-shift and enhancing also the dynamic range of this type of sensors.

Therefore, it has been demonstrated that the shortening of pulses technique also allows to extend the slope region of the RF phase-shift spectrum employed in D-BOTDA sensors. However, there is a disadvantage, the inherent broadening of the RF amplitude spectrum observed in Fig. 5.22 (a), reduces the peak gain and also the SNR, making the system

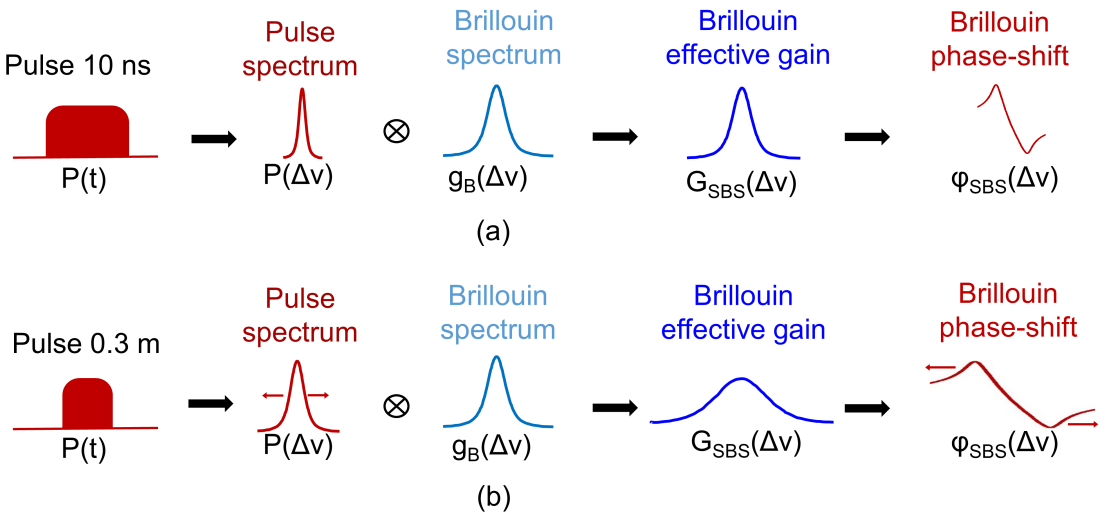

Figure 5.20: Fundamentals of the multi-frequency components pump technique.

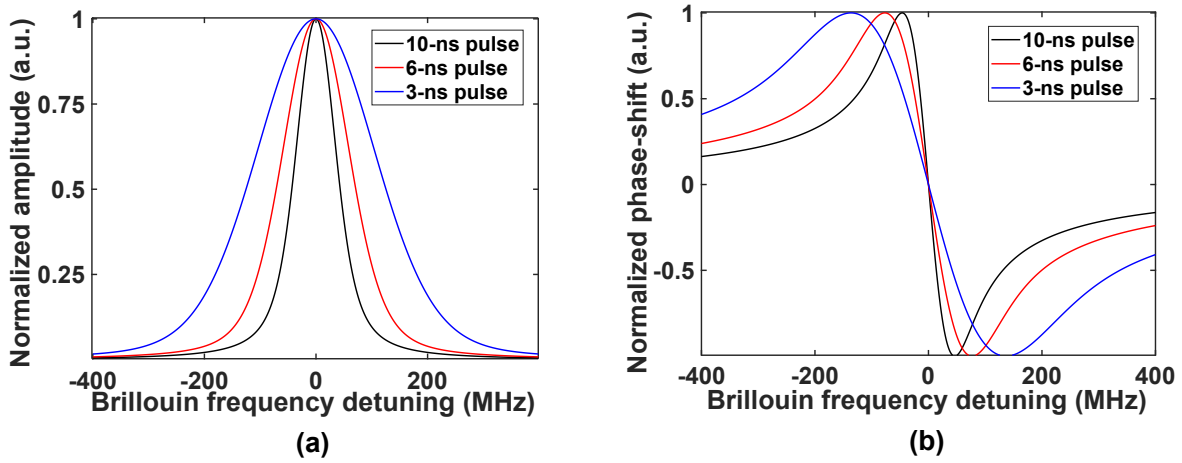

Figure 5.21: Calculated results of the RF amplitude spectra for different number of pump pulse components.

more susceptible to noise.

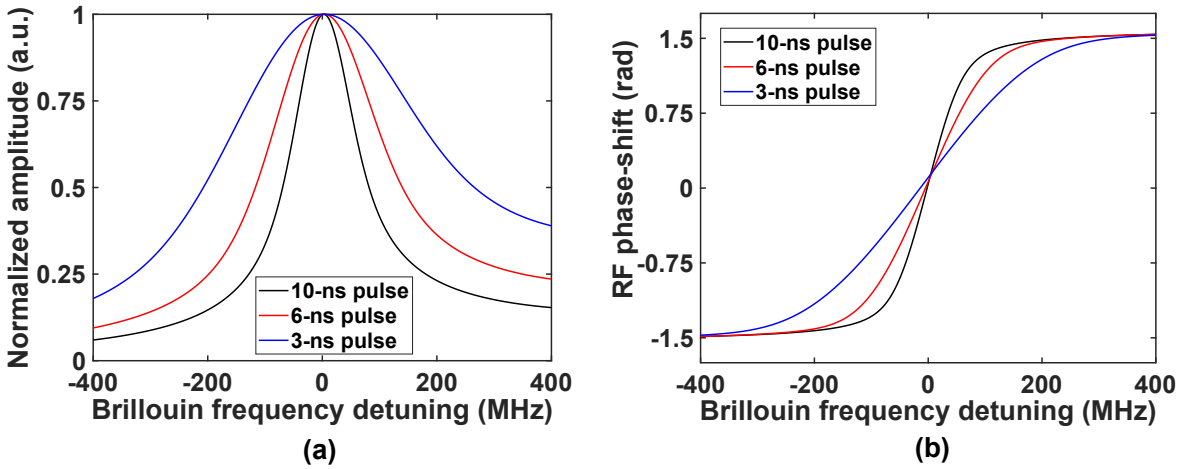

Figure 5.22: RF amplitude spectra broadening depending on the pulse duration.

5.4.3. Experimental setup

Figure 5.23 depicts the experimental setup deployed for this research, which is basically the similar scheme to the D-BOTDA setup described in section 5.3.1, with a slight modification on the generation process of the pump signal depending on which technique is deployed.

The pulsed microwave signal is generated in different ways depending on the technique employed. The left-hand side of Fig. 5.24 shows the experimental setup deployed for the generation of the microwave signal used in the multi-component pump technique. An AWG is used to generate the multiple RF tones at an intermediate frequency, which then are up-converted to the BFS band, using a mixer and a local microwave oscillator. Finally,

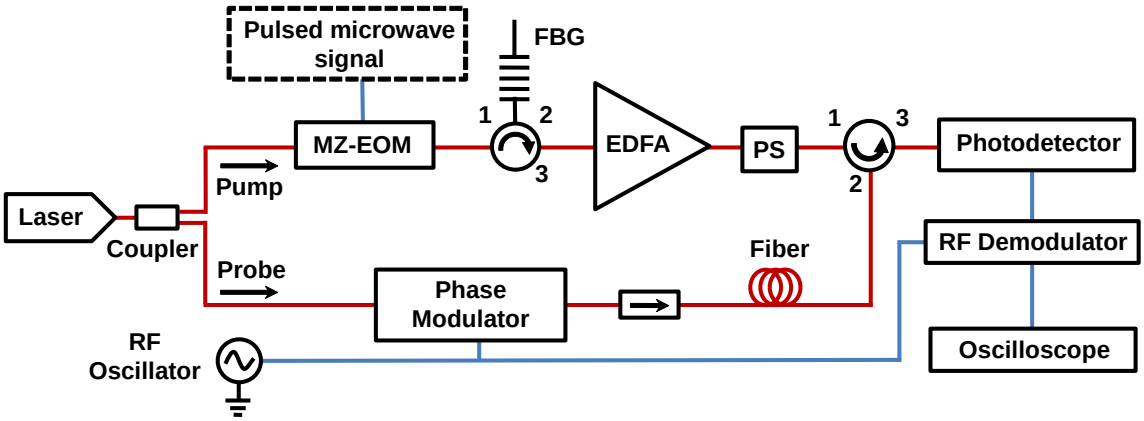

Figure 5.23: Experimental setup deployed for the extension of the dynamic range in coherent BOTDA sensors.

this microwave signal is pulsed using a RF switch that is driven by a pulse generator and applied to the MZ-EOM. The pulsed microwave signal generation of the pulse-shortening method is simpler, as it can be seen in the right-hand side of Fig. 5.24. An AWG that directly forms very short microwave pulses has been deployed, replacing the mixer and the microwave switch from the first setup. Then this pulsed microwave signal drives the MZ-EOM.

Apart from the microwave signal generation, the rest of the setup is the same as the presented one in section 5.3.1. In these particular experiments, the power of the phase-modulated probe wave sidebands was set to -4 dBm, a safe enough power level to avoid NLE in this system [29]. After interacting with the pump pulses in the sensing fiber via SBS, the resultant probe wave was directed to a receiver and the RF signal obtained was demodulated and captured in a digital oscilloscope employing 4000 averages.

5.4.4. Experimental results

In order to demonstrate the enhanced performance of the proposed techniques to overcome the constraint of the limited dynamic range undergone by D-BOTDA sensors, experimental measurements using both methods were performed and their dynamic range

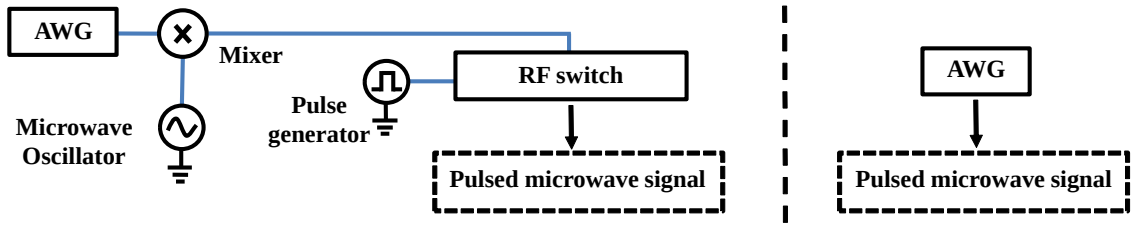

Figure 5.24: Microwave signal generation for the two presented techniques: multiple component pulse method (left-hand side) and shortening of pulses method (right-hand side).

was compared. In this section, a discussion of their advantages and disadvantages is also presented.

In order to quantify the dynamic range, the linearity of the RF phase-shift spectra slope was considered as a reference to measure the maximum and minimum frequencies that determine the linear region of the slope.

Multi-spectral components pump pulses method

Like the previous analytical study, experimental measurements were carried out deploying 10-ns-length pulses with one, four or six spectral components. Fig. 5.25 (a) and Fig. 5.25 (b) show the experimental RF amplitude and RF phase-shift spectra measured as a result of using each of these pump configuration. The depicted spectra, as well as the extension range results that will be provided later, were measured at 1-km fiber distance, which is a long-enough fiber distance to cover typical applications that require dynamic BOTDA sensors. The pump peak power of each spectral pump pulsed component was adjusted to 16 dBm and their frequency difference was set to 55 MHz, which approximately corresponds to the 60 % of the FWHM of the gain spectrum linewidth.

Observe that, as it was expected, the broadening of the RF amplitude and RF phase-shift spectra increases with the number of frequency components generated in the pump. Notice also that the general shape of the RF phase-shift spectra measured experimentally and that shown in the calculations of Fig. 5.19 are very similar, confirming and validating the preliminary results. The small differences between analytical and experimental results stem from the fact that, as it was explained before, the complex BGS depends on the pulse spectrum, and it can only be approximately modeled as the convolution of Gaussian and Lorentzian profiles. Moreover, sometimes, optical fibers have more than one acoustic mode, so that, the spectrum can be slightly altered.

As a result of this enhanced technique, the dynamic range is more than doubled when increasing the number of spectral components of the pump pulse. For instance, when the number of components is increased from one to four, the dynamic range broadens from 130 MHz to 300 MHz (from ± 1300 $\mu\varepsilon$ to ± 3000 $\mu\varepsilon$ assuming again a 20 $\mu\varepsilon/$MHz strain coefficient). Whereas if six spectral components are deployed, the dynamic range is tripled, reaching around 400 MHz (± 4000 $\mu\varepsilon$). Moreover, as it has been mentioned before, the maximum peak amplitude of the detected RF amplitude spectrum increases when pulses with multiple frequencies are launched. In particular, the SNR is enhanced 1.7 dB when four spectral components are generated, and 2 dB when six components are used.

As stated before, it could seem that there is no limitation with the number of pump

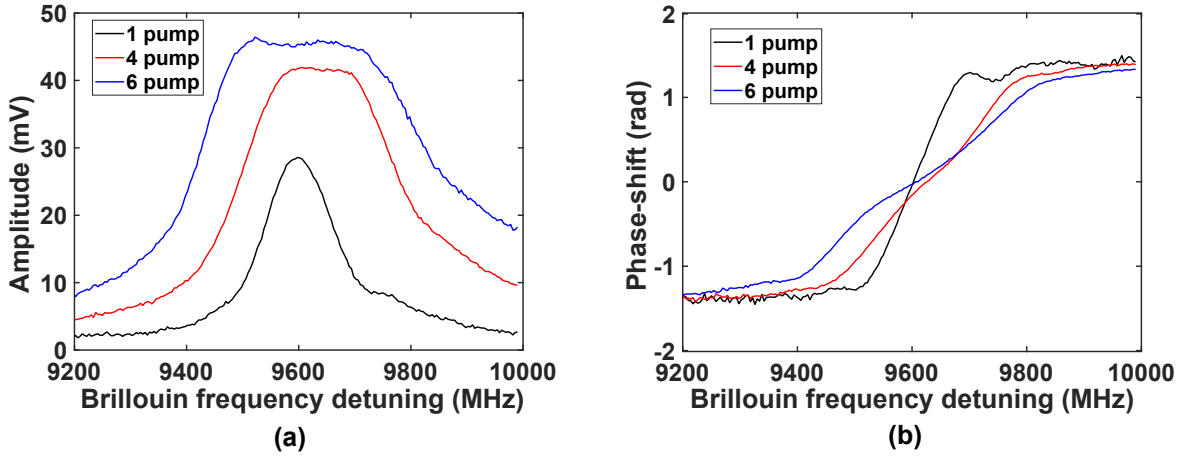

Figure 5.25: Experimental results of the RF amplitude spectra for different number of pump pulse frequencies.

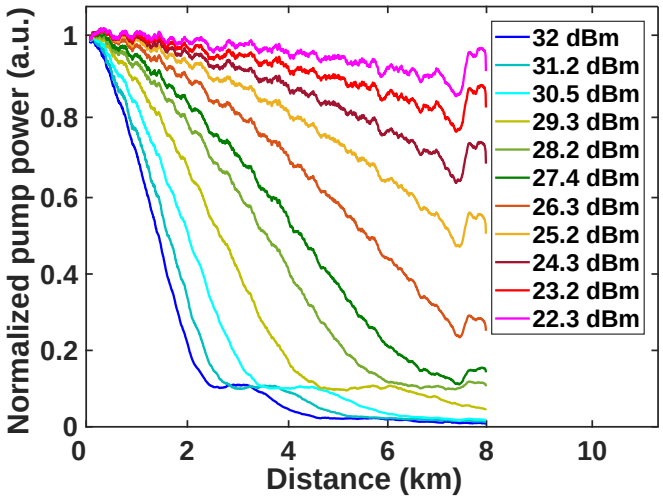

Figure 5.26: Evolution of pump power along the fiber for a pulse with a single frequency component.

pulses that can be injected to the fiber, nevertheless, there is an important limitation that affects the multi-component pulse technique. Since multiple pump pulses are injected simultaneously into the fiber, the maximum peak pump pulse power has to be reduced due to the onset of MI and FWM nonlinear effects [36, 33, 17]. MI and FWM are directly dependent on the pump power injected into the fiber, inducing depletion of the pump power along the fiber that reduces the interaction between the probe and pump waves. This depletion limits the performance of the system due to the reduction of the pulse power, and hence the SNR.

Figure 5.26 depicts the normalized Brillouin gain experienced by the probe when different levels of pump peak power are injected into an 8-km spool of sensing fiber. All traces have been normalized to the peak power, while losses due to fiber attenuation have

been compensated. Notice that this figure shows only the pump power depletion due to MI along the fiber for a single spectral component pump pulse of 10-ns length. As it has been explained, there is a dependence of the pump depletion with the pump peak power injected to the fiber. In particular, the pump depletion becomes more severe as the pump peak power is increased [36]. For instance, if a 22-dBm pump peak power is deployed, the pump depletion experienced at the second kilometer of the sensing fiber is negligible. In contrast, if a 28-dBm peak power is considered, which is the equivalent pump power to the deployment of four-components pump pulses of 22 dBm, the pump depletion experienced is nearly 20%. Observe that near the end of the traces shown in Fig. 5.26, there are some variations in the signal level that are not due to FWM or MI, but due to a BFS change in the sensing fiber cause by the use of different fiber spools for this final section of the sensing fiber.

Figure 5.27 depicts how the pump depletion just analyzed is worsened as additional frequency components are added to the pump signal. This particular measurement was performed deploying 26-dBm peak power pump pulses. In order to analyze the penalty of employing this technique, the critical pump power is used, which is defined as the maximum pump power that can be launched into a given length of fiber before the pump depletion becomes larger than 10% at the end of the fiber. Note that, if only one spectral component is generated, the maximum allowed sensing fiber is around 3 km. In contrast, if four or six-components pump pulses are deployed, the maximum fiber length that can be monitored is shorter than 200 m and 150 m, respectively.

Figure 5.28 represents the mentioned critical pump power as a function of the fiber length and the number of frequency components in the pump pulse. The resultant penalty

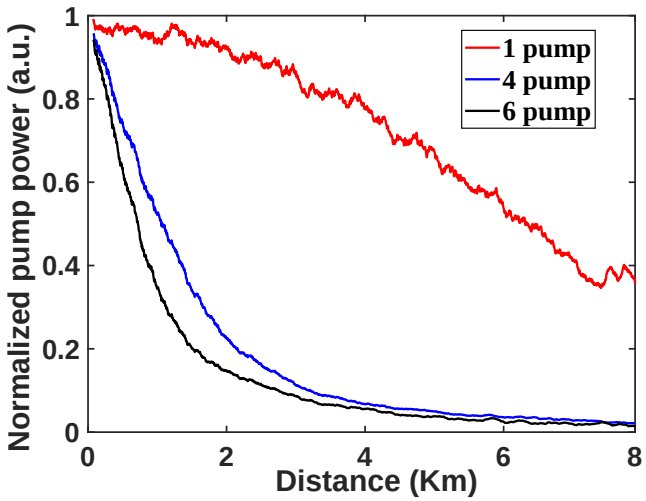

Figure 5.27: Pump power depletion along the fiber for different number of pulse spectral components each with of 26 dBm peak power at the start of the fiber.

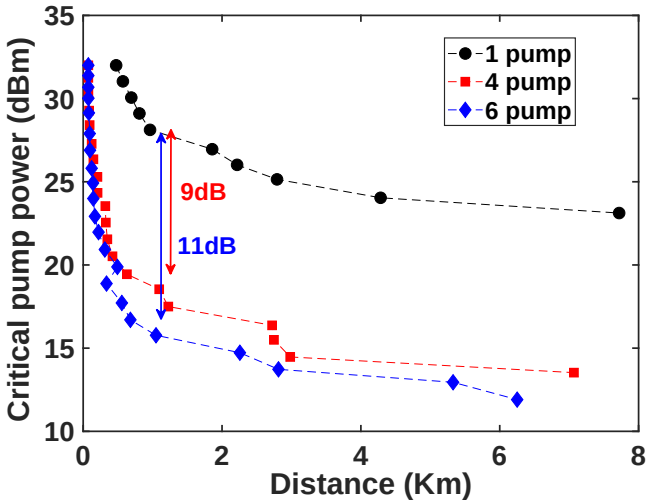

Figure 5.28: Critical pump peak power depending on the distance for different number of pump pulse frequencies.

in terms of power for the use of four and six-component pump pulses is around 9 dB and 11 dB, respectively. The SNR degradation is partially compensated with the increasing RF amplitude spectrum level, due to the overlap of the multiple gain spectra generated by the pump components. Table 5.1 show the results for the different situations. The enhancement of the detected signal for both multi-component pump cases is 1.7 dB and 2 dB; hence, the net penalty of this method is 7.3 dB (four-component) and 9 dB (six-component), respectively.

Apart from the pump power limitation, another difficulty faced on the multiple component pump pulses method relies on its practical implementation. It was found that the generation of a closely-spaced set pure microwave pulses requires a significantly more complex setup, increasing the cost of the sensor and difficulting the deployment itself. Unavoidable spurious components generated in the microwave components, particularly the mixer, were found to contribute to the critical pump power penalty. Despite these drawbacks, the multi-component pump pulse method provides a significant enhancement in

Number of spectral components	1	4	6
Dynamic range	130 MHz	300 MHz	400 MHz
SNR penalty	-	7.3 dB	9 dB

Table 5.1: Dynamic range enhancement and SNR penalty for the multi-spectral components pump pulses method.

the dynamic range with a power penalty that is tolerable for most short-distance dynamic strain measurement applications.

Pulse shortening method

Regarding the second dynamic range enhancement technique, the pulse shortening method, we have experimentally measured the broadening of the RF phase-shift spectra with different pump pulse durations injected into the sensing fiber. Fig. 5.29 (a) and Fig. 5.29 (b) depict the resultant RF amplitude and phase-shift spectra measured at 1-km fiber distance when using 10-ns, 6-ns and 3-ns pulses. As it is observed, the RF phase-shift spectrum slopes are extended, obtaining more than a fourfold extension of the dynamic range when a 3-ns pulse is used in comparison to a 10-ns pulse. In particular, the dynamic range has been enlarged from 130 MHz ($\pm$1300 $\mu\varepsilon$) to 500 MHz ($\pm$5000 $\mu\varepsilon$).

The shortening of pump pulses provides an additional advantage, which is the potential enhancement of the spatial resolution. As the length of the pulses generated is shortened to 3-ns duration, the spatial resolution obtained in this system is enhanced to 30 cm. Another important advantage with respect to the multiple component pump pulse technique is that there is no critical pump power penalty due to the onset of nonlinear effects. This is because of the fact that in the shortening of pulses method, there is only one pump pulse component injected into the fiber, and thus, the total amount of pump power is not increased as before.

However, despite the lack of the pump power constraint, the amplitude of the RF gain spectrum is reduced due to the shortening of the interaction time between the probe wave and the pump pulse, and with it, the noise in the RF phase-shift spectrum is increased. Fig. 5.29 (a) depicts the retrieved BGS for 3-ns, 6-ns and 10-ns pulses. Observe that their

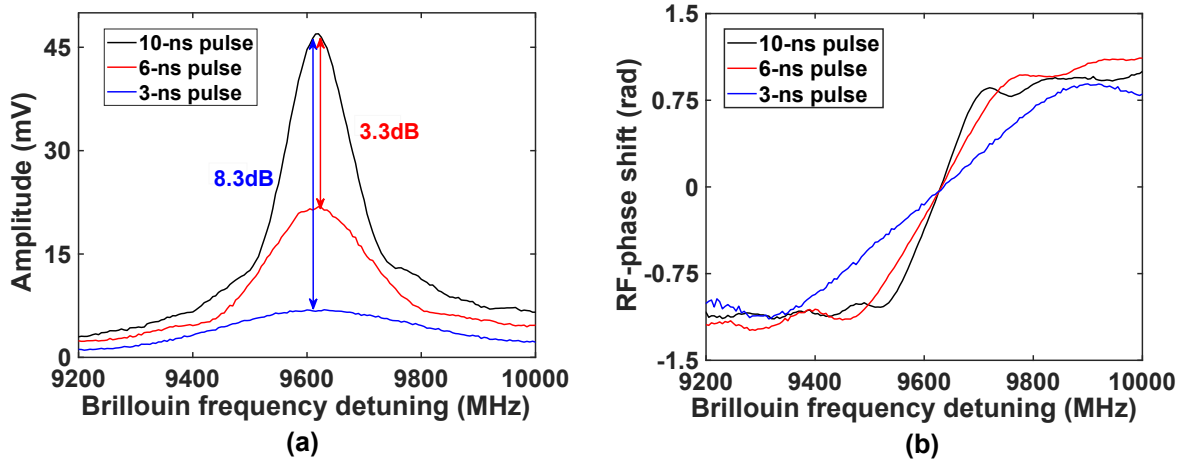

Figure 5.29: Experimental amplitude spectra when short pulses are employed.

amplitudes are scaled as mentioned, showing an power penalty with respect to the 10-ns case equal to 8.3 dB and 3.3 dB, respectively. Thus, this method also experiences a SNR penalty when short duration pump pulses are deployed, which is shown in Table 5.2 along with the dynamic range enhancement attained with each configuration.

As it is well-known, the SNR of the detected signal in BOTDA sensors is directly proportional to the root square of the number of averages [19], thus, if the SNR penalty caused by using a shortened pulse is 8.3 dB, the number of averages should be increased about 45 times to maintain the system performance. Then, as the measurement time is directly proportional to the number of averages, this means that the time measurement increases 45 times as well.

Pulse duration	10 ns	6 ns	3 ns
Dynamic range	130 MHz	200 MHz	500 MHz
SNR penalty	-	3.3 dB	8.3 dB

Table 5.2: Dynamic range enhancement and SNR penalty for the pulse shortening method.

5.5. Conclusions

In the first part of the research work presented in this chapter, it has been demonstrated that the RF phase-shift spectrum measured in D-BOTDA sensors based on a phase-modulated probe wave is indeed gain dependent in large gain scenarios. We have found that the phase-spectrum becomes narrower when the Brillouin gain is increased. However, in any case, this dependence has been shown to be less significant than that found in conventional direct-detection BOTDA sensors for the gain spectrum broadening.

The impairments induced by the narrowing effect of the RF phase-shift spectrum when increasing gains is deployed have been studied. It has been found that the error generated on the measuring system due to the Brillouin gain variation is dependent on the pump pulse duration and on the detuning frequency between the probe frequency and the BFS of the fiber.

From a practical point of view, it is found that this systematic error is not a serious limiting factor given the pump pulse power that is normally deployed in realistic application scenarios. Furthermore, this effect has significance only in very short fibers, because for longer lengths, nonlinear effects such as MI, SPM or Raman scattering impose a more

stringent limitation to the pump power that can be deployed.

In addition, in the second part of this chapter, we have investigated different methods to extend the dynamic range of D-BOTDA sensors. Two different solutions have been presented and experimental measurements have demonstrated between a threefold and fourfold enhancement of the dynamic range in both cases. In addition, both methods display a power penalty of the same order, but with different origins. The enlargement of the dynamic range achieved, makes both solutions suitable for application in a multitude of dynamic strain and vibration measurements in the structural health monitoring field, where the SNR penalties incurred by this application are not very significant because the lengths of fiber involved are usually small.

Regarding the comparison of the two methods, their relative performance seems to slightly favor the pulse shortening over the multi-component pump method, particularly because of the spatial resolution enhancement that it provides. Moreover, the RF phase-shift spectrum slope obtained with the pulse shortening technique shows a better linearity than the one obtained with the multi-component pump method.

It has been found that the improvement of the proposed techniques are mostly limited by the performance of the available components in the setup, particularly on the practical implementation of the electronic circuits involved in generating the microwave pulses. Generating a lowcost multi-tone microwave signal seems relatively easier and cheaper than a very narrow microwave pulse with very small rise time. In fact, a possible middle ground could be found by combining both methods: use a moderate number of spectral components in the pulse but shorten its duration so that each spectral components induces a broad spectrum that overlaps to provide a large overall dynamic range.

Lastly, as a result of the research done in this chapter of the thesis, two papers were published in international journals. The first one was published in Jounal of Ligthwave Technology with title “Gain dependence of the phase-shift spectra measured in coherent Brillouin optical time-domain analysis sensors”, Mariñelarena et al. While the second publication was published in IEEE Photonics Journal with the title “Enhancement of the Dynamic Range in Slope-Assisted Coherent Brillouin Optical Time-Domain Analysis Sensors”, Mariñelarena et al.

CHAPTER 6

Structural health monitoring of solar trackers using distributed optic fiber sensors

6.1. Introduction

As it has been presented in previous chapters, several proposals to enhance the performance of DOFS obtained during the realization of this thesis have been presented. Setup proposals and fundamental findings that contribute to enhance DOFS have been theoretically and experimentally demonstrated. In this sense, important advancements have been achieved to reach the ultimate limits of BOTDA sensors to attain their best features in terms of measurement range, spatial resolution, accuracy and measurement time.

Thanks to the great effort and commitment of the research community during the last years, DOFS are currently gaining paramount importance on the maintenance and safety of many industry assets. The capability of performing distributed and dynamic measurements of different measurands over large structures such as dams, bridges, oil or gas pipelines, wind turbine blades, etc., is turning this technology out to be in demand and necessary solution to improve the efficiency and security of this type of infrastructures and assets.

Thus, before concluding the research of this thesis, it was desired to bring to the field part of the contributions accomplished during this thesis research. In particular, the main goal was to implement, install and deploy a DOFS to monitor a real asset under

environmental conditions that could damage it. Eventually, this objective was met thanks to a research project named "Desarrollo de Seguidor Solar Bifila con sensorizacion de los efectos del viento WINDSOLAR" (0011-1365-2017-000122). This project was funded by the Navarre Government and was carried out as a collaboration of the Public University of Navarre and STI Norland S.L. company, which is focused on the renewable energy industry sector.

Basically, the main target of the Windsolar project was to find an alternative and additional monitoring solution to improve the current methods used to control the state of PV solar trackers. The objective of this complementary monitoring system is mainly the characterization of the effects of wind over the solar tracker structures. This is an important goal due to the fact that nowadays, installation of solar trackers is expanding to locations all around the world and the long-term reliability of solar trackers is being critical due to unpredictable environmental conditions.

So, the research work accomplished for the Windsolar project was focused on designing, developing and implementing a novel measuring system based on using the previously described D-BOTDA sensor to allow dynamic monitoring of the effects of wind on PV solar trackers. As a result, we have devised a system that permits to dynamically measure distributed bending strain along large structures and, for the first time to our knowledge, also distributed torsional strain. This project will permit to monitor in real-time the mechanical behavior of the whole structure and obtain valuable information to improve the tracker's design and increase safety, lifetime and energy production of solar parks. In addition, the real-time monitoring system will serve to develop alternative stow strategies that rely on the measurements of the actual state of the structure at any given time instead of using the speed of wind as an indicator.

In this chapter of the thesis, the measuring system developed for bending and torsion measurements is presented and described. A procedure devised for the instrumentation of the optical fiber along the structures to obtain the desired measurands is also explained. Then, preliminary experimental measurements performed in laboratory facilities are presented in order to validate the measuring system. Finally, field installation of the proposed measuring method in a solar plant is described in detail.

6.2. Effect of wind in solar trackers and its monitoring

As it is well-known, renewable energies are growing very fast during the last years and are bound to keep increasing their volume and production in order to reduce pollution,

global warming and fossil fuels consumption. Among the different renewable energies, solar energy, and in particular, PV solar energy, is the one that, nowadays, is growing faster all around the world, and it is expected to increase up to 65 times by 2050 [114].

The main component of PV systems is the solar tracker, which is basically composed by a set of long steel beams where solar panels are attached. Fig. 6.1 displays a real picture of a solar tracker and part of a solar plant. These large structures that can reach up to 60 meters length are actuated by motors to optimize the angle of incidence of the incoming sunlight on the solar panels. In a real scenario of PV solar parks, plenty of these large solar trackers are assembled row after row to reach up to several GW energy production capacity.

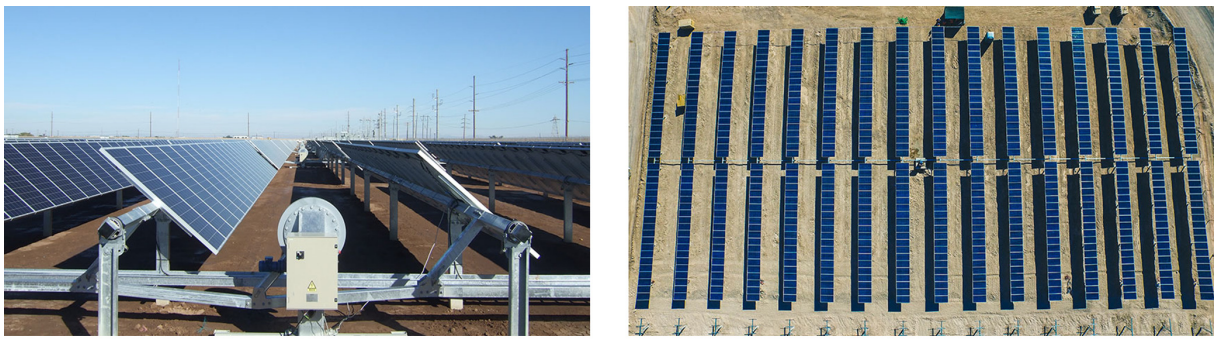

(a) (b)

Figure 6.1: Picture of (a) PV a solar tracker and (b) solar plant with multiple solar trackers installed.

However, there is a critical problem that solar parks' developers are facing nowadays. As mentioned previously, the installation of solar trackers is extending worldwide and their structures are undergoing uncontrolled climate adversities, in particular, wind effects, which are impairing the reliability of solar trackers. In this regard, it has been found that nearly 50% of the solar power plant insurance claims related to tracker failures are due to the effects of wind [115].

Therefore, the effects of wind are of paramount importance on the design of solar trackers. This is mainly because dynamic loads experienced by their structures during aeroelastic instability events due to wind effects can lead to more than five times the static wind load [116]. This means that, even though several approaches are usually taken into account to evaluate wind loading for solar trackers designs, these are neither robust enough nor complete. The reason for this limitation is that the current methods, such as the use of building codes and static wind tunnel testing, only provide static load information and do not account for dynamic amplification effects. Furthermore, it has

been shown that the traditional stow policy of positioning solar trackers at 0 degrees, or flat stow, is the most dangerous position during a wind event because it can lead to torsional instability. Fig. 6.2 depicts a representation of a failure solar tracker due to the effects of wind.

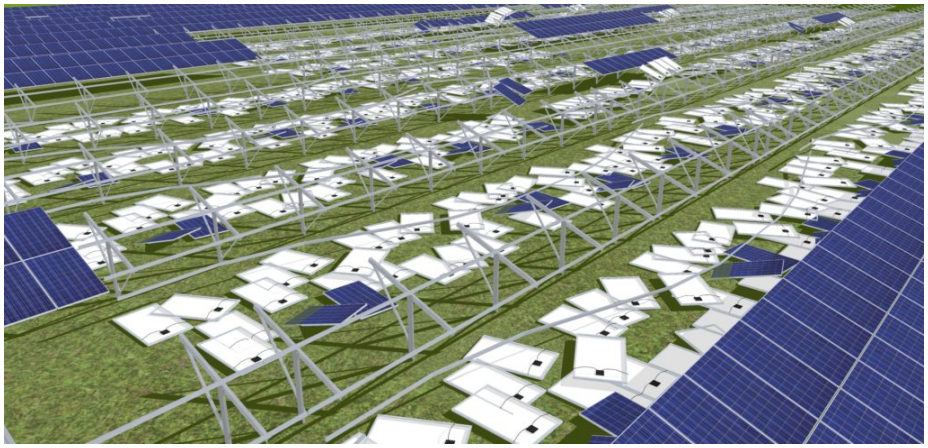

Figure 6.2: Failured PV a solar tracker due to wind effects (Why PV Structures Collapse: Five contributing factors, DNV-GL).

Thus, it is clear that it is necessary to develop an additional monitoring system to complement the current wind load evaluation methods and computational fluid dynamic models of solar trackers. This was the main reason for developing the Windsolar project. Its objective was to devise a measuring system to allow measurements in real-time of the mechanical state of the structure when it is subjected to wind loads. The acquired data will serve to correctly predict the dynamic performance of the structures under wind effects.

There are different options that could be implemented to develop a structural health monitoring system to measure bending and torsion strain in PV solar trackers. For instance, one option is to use the conventional electric strain gauge sensors, that can be installed in different positions to measured local strain variations. However, strain gauges are difficult to install infield because they require power supply and control wiring, which implies a complex deployment of cables. Furthermore, strain gauges are electrical sensors that are prone to experience interference or lightning strikes.

A more convenient alternative is to use FBG optical fiber sensors. This technology provides similar information to strain gauges with the great advantages of being purely passive, not power supply is needed, and that they can be interrogated remotely, even from several kilometers distance [15]. However, similarly to strain gauges, FBGs only measure the strain of the structure at the location where they are fixed. This is an important issue

because the application of monitoring the structural behavior of solar trackers requires a large number of measurement positions to characterized the response of the whole structure to wind effects. Moreover, in solar plants, wind conditions are complex and the effects generated on solar trackers are different depending on the location of each tracker, so, multiple units of solar trackers are necessary to be simultaneously monitored. This means that a large amount of FBGs should be installed and monitored, which is an important inconvenient as FBG interrogators are limited in the number of simultaneous FBGs that can be monitored, especially for dynamic measurements. Therefore, FBG technology has an important drawback because of the fact that, the cost and complexity of the measuring system would rapidly increase.

Thus, the most convenient monitoring solution for this research project is to deploy DOFS [2]. In particular, BOTDA sensors are the most adequate for this application because they can provide thousands of measurement positions along a single optical fiber cable fixed to long structures. However, the most popular BOTDA sensors, the direct-detection BOTDA sensors, have been limited to just static measurements. This is due to the fact that the scanning process of the BGS requires large measurement time, as it has been explained in chapter 2. In contrast, the D-BOTDA sensor described in chapter 2 and 5, allows to perform dynamic real-time measurements of strain with up to thousands of full simultaneous measurements per second for all positions in the fiber. So that, optical fiber cable can be deployed along multiple solar trackers and the strain of all of them can be simultaneously monitored in real-time with high accuracy and high spatial resolution. Altogether, this is the reason why the D-BOTDA sensor has been used to carry out the monitoring on solar trackers.

6.3. Distributed bending and torsional strain measurements in beams

As it has been already described, a solar tracker is formed by a set of multiple long steel beams composing a central torque beam, to which PV solar panels are attached. This central torque beam generally undergoes the effects of wind, that induce bending and torsion over this long structure. In order to theoretically study and understand the behavior of a structure subjected to bending and torsion stresses, it has been studied how a rectangular cross-section beam behaves when bending and torsion are generated. Then, it will be possible to determine the best solution for monitoring this type of structure using DOFS.

Figure 6.3 schematically represents a square-cross section beam of size d. It is assumed

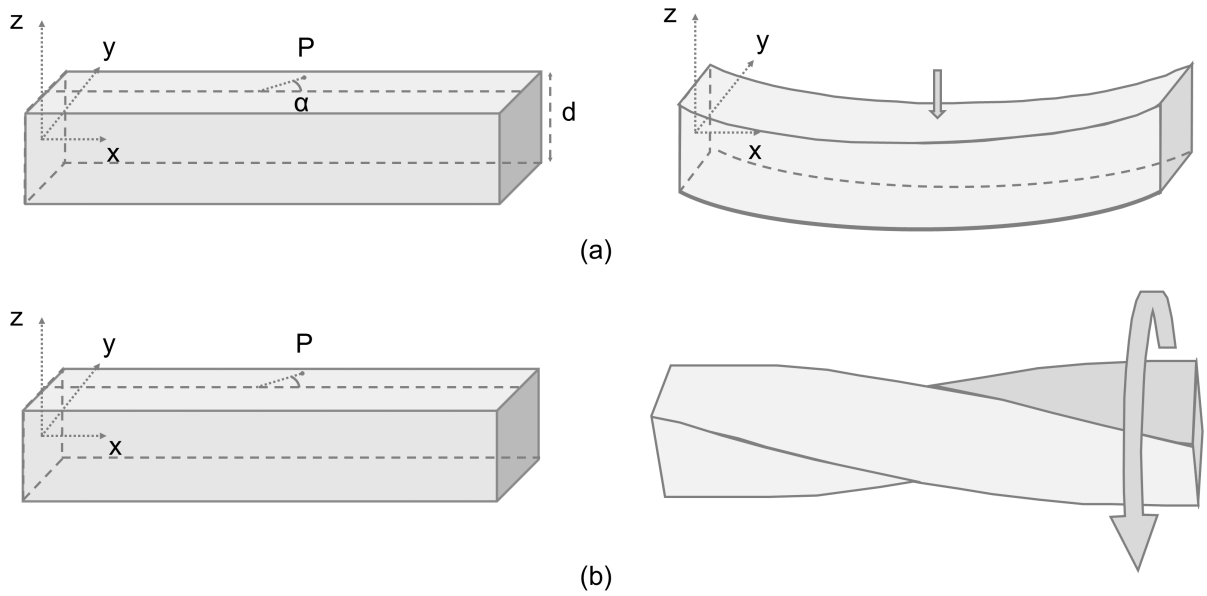

Figure 6.3: Scheme of deformed rectangular shaped beams due to (a) vertical displacement and (b) torsional twist angle. Blue color line shows the neutral axis of the beam.

that bending and torsion moments can be generated in either directions of y and z axes, inducing bending and torsion strain, respectively. Based on Euler-Bernoulli beam theory and classical Saint-Venant's theory, it is possible to derive equations to represent the strain experienced by a beam subjected to bending and torsion, and thus, obtain the strain undergone at any position of the beam [117]. In order to do this study, it is considered plane strain, that is the cross-section shape of the beam is maintained constant, which means that there is neither stress nor strain in the axial direction of the beam, x. Thus, bending and torsion strain is only induced in the two perpendicular directions to the axial direction of the beam, y and z axes. Then, using Hooke's law and Young's elastic modulus (E) of the material, the plane strain observed at a certain position along the axial direction of the beam is given by the following strain tensor [117]:

$$\varepsilon_{ij} = \begin{bmatrix} \varepsilon_x & \varepsilon_{yx} & 0 \\ \varepsilon_{xy} & \varepsilon_y & 0 \\ 0 & 0 & 0 \end{bmatrix} = \begin{bmatrix} \frac{\sigma_x}{E} & \frac{\tau}{2G} & 0 \\ \frac{\tau}{2G} & -\frac{\gamma\sigma_x}{E} & 0 \\ 0 & 0 & 0 \end{bmatrix} \tag{6.1}$$

where G and γ are the shear modulus, and the Poisson's ratio, respectively, being characteristic parameters of the beam's material. σ_x and τ are bending stress and shear stress at a given cross-section of the beam, which are obtained from the classical beam theory

of Euler-Bernoulli and Saint-Venant:

$$\sigma_x = -\frac{M_z}{I_z} y + \frac{M_y}{I_y} z \,, \tag{6.2}$$

where y and z are the coordinate distances from the neutral axis to the testing position P, while I_z and I_y are the moment of inertia of the beam's cross-section in both axes and M_y and M_z the bending moment in both directions. From this equation, it is clear that bending stress, and thus, bending strain, increase their magnitudes as the distance from the testing position to the neutral of the beam rises, while it is zero if the testing position is located in the neutral axis.

Similarly, the shear stress due to torsion can be expressed as follows:

$$\tau = \frac{M_T}{W_T} \,, \tag{6.3}$$

with W_T torsion resistant modulus and M_T moment of torsion [117].

In order to obtain the strain at certain position, P, located in the normal plane to the axial direction, it is necessary to define the directional vector to represent the resultant strain in a given position of the beam [117]:

$$\vec{r} = \begin{bmatrix} l \\ m \\ 0 \end{bmatrix} = \begin{bmatrix} sin(\alpha) \\ cos(\alpha) \\ 0 \end{bmatrix} \tag{6.4}$$

where α is the angle formed by the neutral of the beam at plane XY and the testing position P. The normal strain generated at point P by each bending moment and torsion moment in both principal directions is calculated as follows:

$$\varepsilon_p = [\varepsilon \cdot \vec{r}] \cdot \vec{r} \tag{6.5}$$

and introducing Eq. (6.1) and Eq. (6.4) we obtained an expression for the strain at position P:

$$\varepsilon_p = \left(\begin{bmatrix} \frac{\sigma_x}{E} & \frac{\tau}{2G} & 0 \\ \frac{\tau}{2G} & -\frac{\gamma \sigma_x}{E} & 0 \\ 0 & 0 & 0 \end{bmatrix} \cdot \begin{bmatrix} sin(\alpha) \\ cos(\alpha) \\ 0 \end{bmatrix} \right) \cdot \begin{bmatrix} sin(\alpha) \\ cos(\alpha) \\ 0 \end{bmatrix} \tag{6.6}$$

Then, calculating the product of the matrix, the following equation is obtained:

$$\varepsilon_p = \frac{\sigma_x}{E}\sin^2\alpha + \frac{\tau}{G}\sin\alpha\cos\alpha - \frac{\gamma\sigma_x}{E}\cos^2\alpha \tag{6.7}$$

where it is possible to substitute Eq. (6.2) and Eq. (6.3) to express the strain at position P as a function of the bending and torsion moments generated on the beam:

$$\varepsilon_p = \left(\frac{sin^2\alpha - \gamma\cos^2\alpha}{E}\right)\left(-\frac{M_z}{I_z}y + \frac{M_y}{I_y}z\right) + \left(\frac{sin\alpha\cos\alpha}{G}\right)\left(\frac{M_T}{W_T}\right) \tag{6.8}$$

From this expression, it is possible to obtain the strain generated at any position of a beam that is subjected to bending and torsion moments. Based on this equation, particular deployment for the optical fiber employed as sensing element was devised to optimize, independently, the measurements of strain induced by bending and torsion moments. In particular, three different optical fiber layouts were defined to measure independently the three different stresses, the strain induced by bending moments in both axis, M_y and M_z, and the strain induced by torsion shear, M_T. To do this, a square cross-section beam of size d was considered, as shown in Fig. 6.4. In this figure, the layout of the optical fiber that has been devised is depicted.

Firstly, in case of measuring strain induced by bending moment in the z axis, M_z, it is necessary to deploy two optical fibers longitudinally to the axial direction, that is with angle $\alpha = 0°$. Then, the distance y to the neutral axis should be maximum, in this case equal to half cross-section distance, $\pm d/2$, while the distance z should be zero. Therefore, the two optical fibers must be fixed to the outer surfaces of the lateral faces of the beam, right on the middle of each face, as shown in Fig. 6.4 with lines f_1 and f_2. Notice that f_2 is hidden in the rear part of the beam.

Solving the Eq. (6.8) with the parameter values of α, y and z, a pair of strain values are obtained, corresponding to the strain undergone in the both lateral faces of the beam by fibers f_1 and f_2:

$$\varepsilon_1(x) = \frac{\gamma}{E}\left(\frac{M_z(x)}{I_z}\right)\left(\frac{d}{2}\right) \tag{6.9a}$$

$$\varepsilon_2(x) = \frac{\gamma}{E}\left(\frac{M_z(x)}{I_z}\right)\left(-\frac{d}{2}\right) \tag{6.9b}$$

where $M_z(x)$ is the moment of bending applied to the beam in direction z for the position x along the axial direction. Notice that the strain for the two fibers is equal in amplitude but with opposite sign. This is due to the fact that one of the fibers experiences compression, while the second one experiences tension.

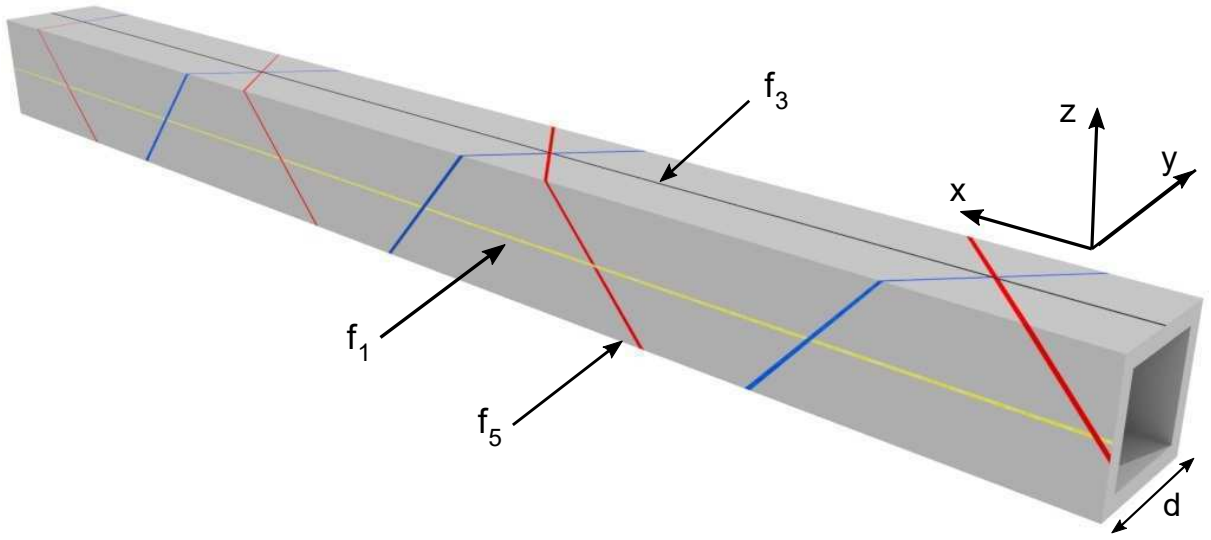

Figure 6.4: Instrumentation of beams with optical sensing fiber to measure bending and torsional moment distribution. The red, blue, yellow and back lines represent the optical fiber fixed to the beam.

During this study, it was found that with the simple subtraction of the strain measured with these two optical fibers it was possible to perform bending moment measurements tolerant to common mode effects that both fibers undergo during the measuring process, like temperature variation effects. As far as the assumption of having a uniform distribution of temperature in opposite faces of the beam is considered, the subtraction process will allow to cancel the strain contributions that are common for both fibers without interfering the bending measurement. Therefore, it is possible to obtain bending moment measurements tolerant to common mode effects like temperature induced effects, by just calculating the strain difference of the two deployed fibers, f_1 and f_2:

$$M_z(x) = \frac{\varepsilon_1(x) - \varepsilon_2(x)}{d \cdot \gamma} EI_z \tag{6.10}$$

If bending on the y axis has to be measured, the fiber layout proposed is basically the same, with the only difference of the distances from the neutral to the fiber location. In this case, these distances are $y = 0$ and $z = \pm d/2$. Therefore, two optical fibers must be longitudinally disposed along the upper and bottom faces of the beam, as shown in the figure with lines f_3 and f_4 (f_4 is hidden again by the beam). The resultant strain is given by:

$$\varepsilon_3(x) = -\frac{\gamma}{E}\left(\frac{M_y(x)}{I_y}\right)\left(\frac{d}{2}\right) \tag{6.11a}$$

$$\varepsilon_4(x) = -\frac{\gamma}{E}\left(\frac{M_y(x)}{I_y}\right)\left(-\frac{d}{2}\right) \tag{6.11b}$$

Calculating the strain difference of the two optical fiber, the bending moment on the y axis is deducted, canceling again any common mode introduced in the measurement as previously explained:

$$M_y(x) = -\frac{\varepsilon_3(x) - \varepsilon_4(x)}{d \cdot \gamma} EI_y \tag{6.12}$$

With respect to the distributed torsion moment measurement, which is the first time to our knowledge to be performed, the optical fiber layout is slightly different. Lines f_5 and f_6 highlight the two optical fibers used for the torsion measurements. In this case, in order to maximize the contribution of the torsional moment in Eq. (6.8), the optical fiber should describe a 45° angle with the axial direction. So, the proposed configuration is to deploy two optical fibers describing a helical shape in opposite directions, crossing one another along the structure and forming 45° angle with the x axis. The strain obtain at position x for each of these two fibers can be derived from Eq. (6.8) as:

$$\varepsilon_5(x) = \frac{0.5}{G}\frac{M_T(x)}{W_T} \tag{6.13a}$$

$$\varepsilon_6(x) = -\frac{0.5}{G}\frac{M_T(x)}{W_T} \tag{6.13b}$$

The deployment of two optical fibers with the described layout allows to perform distributed measurements of torsion moment tolerant to common mode variations such as temperature effects or thermal expansions. However, this is not the only advantage of this measuring method. Calculating the difference of the strain measured with f_5 and f_6, it is possible to successfully obtain torsion moment measurements independently of simultaneous bending moments induced to the beam. This is just because of the fact that both optical fibers experience the same bending strain when they are evaluated at the same position x along the axial direction of the beam. Note that the helical deployment of the fibers along the axial direction of the shaft, forces to fix them on the four faces of the beam, varying the distance to the neutral axis. Therefore, the bending strain experienced by these two optical fibers deployed along the 4 faces of the shaft, induces alternate amplitude bending strain due to the variation of the distance from the sensing fiber to the neutral of the shaft, increasing its amplitude as the position is closer to the

far end of the shaft. However, both optical fiber experience similar bending strain at a given section of the beam, allowing to cancel the bending effect when both measurements are subtracted. Thus, from Eq. (6.13b), torsion moment can be calculated from the experimental measurements of local strain measured with the two optical fibers:

$$M_t(x) = W_T \cdot G \cdot \big(\varepsilon_5(x) - \varepsilon_6(x)\big) \tag{6.14}$$

Notice that, from the theory of torsion in square beams, it is known that torsion moment is defined as follows [117]:

$$M_t(x) = W_T \cdot G \cdot \theta(x) \tag{6.15}$$

where θ is the shear angle at position x. From these two equations it is possible to conclude that the shear angle is:

$$\theta(x) = \varepsilon_5(x) - \varepsilon_6(x) \tag{6.16}$$

6.4. Laboratory tests

In the previous section, a novel optical fiber deployment method has been devised to allow performing distributed bending strain measurements and, for the first time, distributed torsional strain measurements along any type of beam using an optical fiber. A theoretical derivation has shown that either, bending and torsional moments, can be obtained by measuring the local strain with an optical fiber disposed following some defined layouts along the beam.

In this section, the capability of the proposed measuring system to monitor bending and torsion strain in beams, particularly, in a solar tracker beam is demonstrated. In order to validate the method, preliminary measurements are performed at the laboratory facilities with a D-BOTDA sensor prototype developed by our research group during the last years. This equipment employs the SA-BOTDA configuration previously presented in the introduction and in chapter 5, based on a phase-modulated probe wave and self-heterodyne detection, which relies on the measurement of the RF phase-shift [27].

6.4.1. Experimental measurement setup at laboratory facilities

In this subsection, the procedure followed to glue the sensing fiber on the beam and the laboratory measurements of bending and torsional strain along a 3.4-m length section

of stainless steel torque beam are explained. This solar tracker sample with a 10-cm rectangular cross-section was provided by the STI Norland S.L company.

Initially, the 3.4-m length beam was instrumented using an acrylate-coated SMF, which was fixed to the beam following the layout described in section 6.3. For this purpose, a two-component epoxy was used to glue the fiber to the beam, ensuring good strain transfer. This procedure is shown in Fig. 6.5 (a). Once the six optical fiber sections (four for bending and two for torsion) were bonded to the surface, all these sensing fiber sections were spliced together to obtain a single fiber loop. Then, the two optical fiber connections of the sensing fiber were connected to the D-BOTDA interrogator. In total, nearly 14-m length fiber was glued to the beam; 6 m were used to measure bending and 8 m were used for torsion.

Then, the instrumented beam was fixed to a mechanical test bench, as it is shown in Fig. 6.5 (b). In order to apply controlled bending and torsion moments to the shaft, a pulley and jack system was attached to the far end of the beam, while the other end was anchored to a rigid support.

Apart from the optical fiber cable deployed for the distributed strain measurements, 4 FBGs were also bonded to the beam close to the anchored end of the shaft. The measurements of the FBGs permit to have an additional strain measurement at a given cross-section of the beam for comparison purposes. Two of these FBGs were glued in opposite faces following the axial direction of the beam. The other two FBGs were bonded forming 45°angle with the axial direction. Thanks to this particular layout, bending and torsional strain variations were allowed to be obtained, respectively.

As mentioned, in order to perform distributed measurements of strain along the sens-

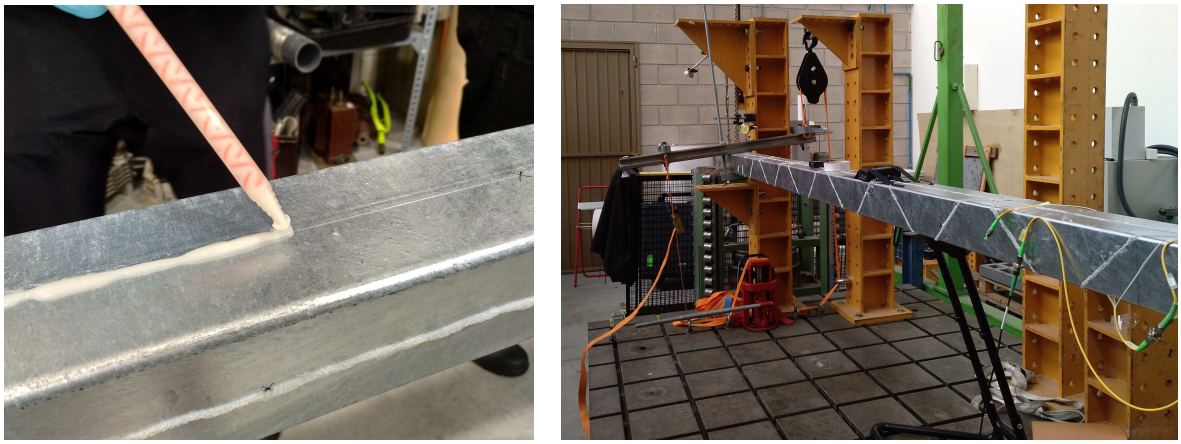

(a) (b)

Figure 6.5: Pictures during (a) fiber bonding process and (b) torsional strain measurements.

(a) (b) (c)

Figure 6.6: Optical fiber interrogators employed in the experiments: (a) D-BOTDA, (b) OFDR and (c) FBG interrogator.

ing fiber, a prototype of D-BOTDA interrogator was employed, allowing dynamic measurements of strain along several kilometers of optical fiber. Moreover, apart from the D-BOTDA sensor, a FBG interrogator (Micron Optics Hyperion) was used to measure the static and dynamic response of the FBGs installed on the beams. The results obtained from the FBGs were correlated with the distributed measurements obtained with the D-BOTDA sensor for the position were the FBGs were located. Finally, a third optical interrogator was employed to measure and compare the distributed strain measured with the D-BOTDA along the sensing fiber. This is the Optical Frequency Domain Reflectometry (OFDR) system from LUNA Technologies (model OBR4600). However, this interrogator only allows to perform static measurements, and, moreover, the sensing range is limited. Hence, it was only used to perform static measurements in the laboratory facilities to correlate the results and help to validate the proposed measuring system. Fig. 6.6 depicts the three optical fiber interrogators employed in these experiments.

6.4.2. Static measurements

Static measurements were initially performed using the different optical interrogators to demonstrate the capability of the D-BOTDA to measure bending and torsional strain along the instrumented beam. The D-BOTDA interrogator was configured to carry out static measurements by implementing a sweep of the frequency difference between the pump and probe waves to scan the BGS. These measurements were performed with a 20-cm spatial resolution obtained by deploying optical pump pulses of 20 ns duration. The results were compared with the other two optical fiber interrogators' results.

Bending tests

Initially, measurements of the bending strain along the sensing fiber longitudinally deployed were performed for different vertical displacements. Fig. 6.7 (a) highlights the strain measured along the two fiber sections bonded to the bottom and upper surfaces of the beam using the D-BOTDA interrogator. In particular, the first section shown in the

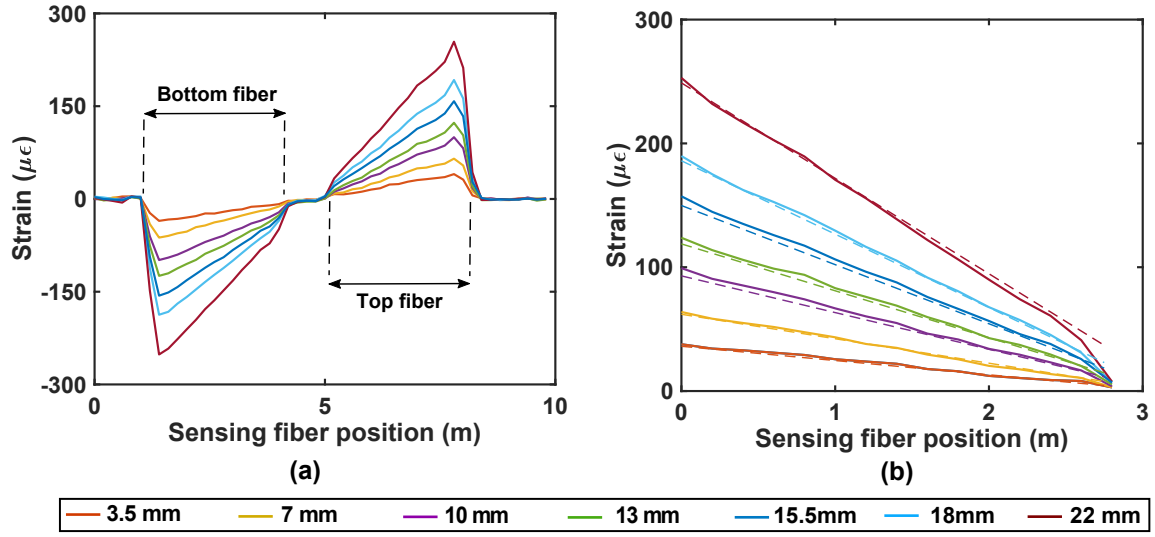

Figure 6.7: Bending strain measured with the D-BOTDA for several displacements applied at the far end of the beam: (a) distributed strain along sensing fiber and (b) differential strain of 2 sections measured compared to the theoretical model.

graph corresponds to the bottom face and the second one to the top face. Measurements were performed when the beam was subjected to several displacements at the loose end of the shaft. Observe that the two fiber sections along the sensing fiber are clearly discerned. Both of them have a similar length, approximately 2.8 m. Notice that, the amplitude of the strain measured in these two sections is symmetric in distance and have opposite sign. This is due to the fact that the first section of the sensing fiber is glued to the bottom face of the beam that undergoes compression, whereas the second one is bonded to the top face of the beam that experiences tension. The rest of the sensing fiber depicted in the figure with negligible strain corresponds to the fiber cable that connects the different bonded sections. Finally, note that the strain measured at positions near the anchored end of the beam (initial and ending part of the fiber) is larger, as it is expected by the theoretical behavior of beams.

Figure 6.7 (b) depicts the subtraction of the strain measured with the two fiber sections bonded in opposite sides of the beam. In this figure, apart from the experimental results, the strain calculated using the theoretical model of a cantilever beam for each of the vertical displacements are shown. As it is depicted, very good agreement is obtained with slight differences attributed to the effects of gluing the fiber and non-uniform strain transfer from the beam surface to the sensing fiber. Remember that, by subtracting the strain measured in opposite faces of the beam, the effects of temperature variations on the measurements are canceled, including thermal expansion.

Similar measurements were performed using the OFDR from Luna Technologies as it

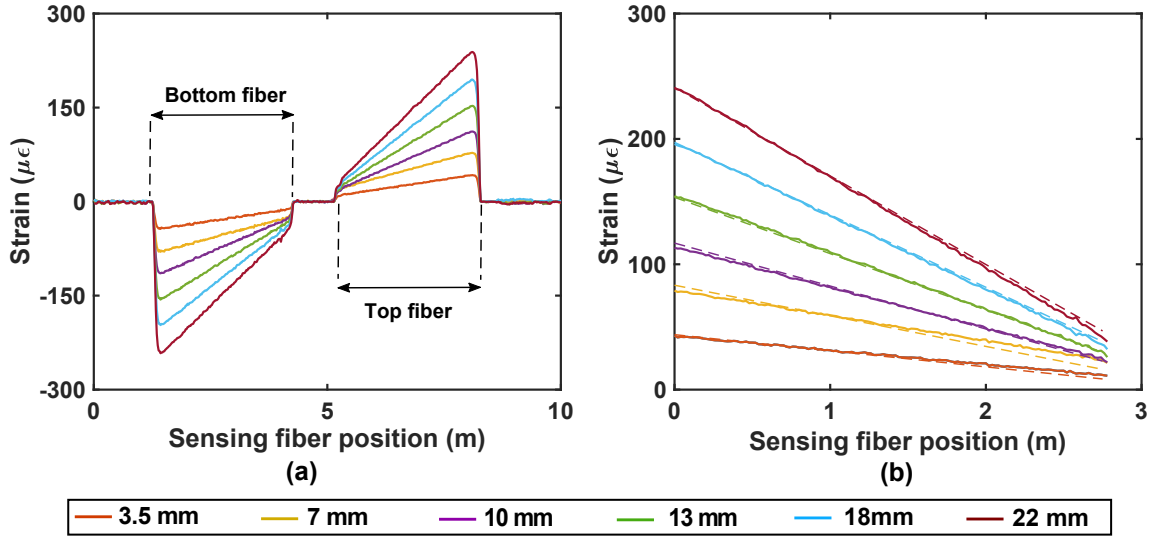

Figure 6.8: Bending strain measured with the OFDR for several displacements applied at the far end of the beam: (a) distributed strain along sensing fiber and (b) differential strain of 2 sections measured compared to the theoretical model.

is depicted in Fig. 6.8. Observe that the experimental measurements of the strain along the sensing fiber are pretty similar to the ones acquired with the D-BOTDA, even though, the spatial resolution selected was 2 cm. Likewise, the subtraction of the strain measured in the two fiber sections match with the theoretical calculations, confirming the reliability of the measuring system to obtain the bending strain.

Finally, Fig. 6.9 shows the comparison of the bending strain versus the vertical displacement applied at the far end of the beam measured with the FBGs and the two distributed optical fiber interrogators. The strain measured with the D-BOTDA and the OFDR correspond to the position where the FBGs were located. Moreover, the strain

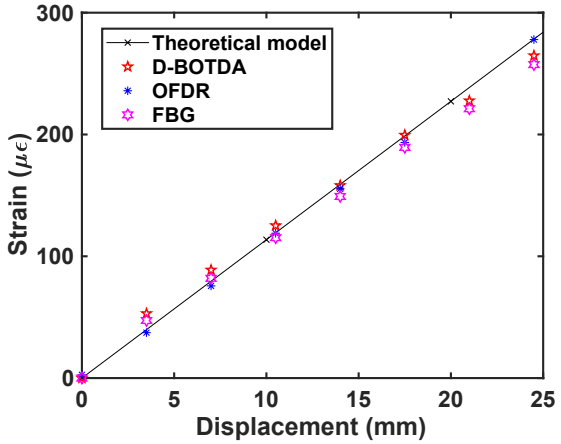

Figure 6.9: Experimental and calculated bending strain dependence on the vertical displacement of the loose end of the beam.

calculated with the theoretical model for each of the displacements applied to the beam is also plotted. As it is observed, the experimental results attained match with the theoretical calculations, showing very good agreement to the theoretical model.

Torsion tests

Then, measurements of torsional strain along the fiber bonded to the beam describing 45°angle with the axial were carried out when different torsional angles were generated. Fig. 6.10 (a) displays the strain measured with the two optical fibers deployed to measure torsion, obtaining the strain for several twist angles generated at 1-m distance from the anchored end of the tested beam. Similarly to the bending measurements shown previously, two different sections are visible along the sensing fiber, each one corresponding to one of the fibers cables deployed describing the helical shape. Notice that the strain measured along the glued fiber sections is fairly uniform and of opposite signs, as expected from theory. As before, this is due to the fact that the first section is experiencing compression and the second one tension.

Similarly, Fig. 6.10 (b) depicts the subtraction of the strain measured with the two fiber sections. Again, experimental results are compared to the strain calculated obtained using the theoretical model, showing excellent agreement. This measurement is also tolerant to common mode variations like temperature changes or thermal expansion effects, as explained before.

The OFDR was also used to performed distributed measurements of the strain gen-

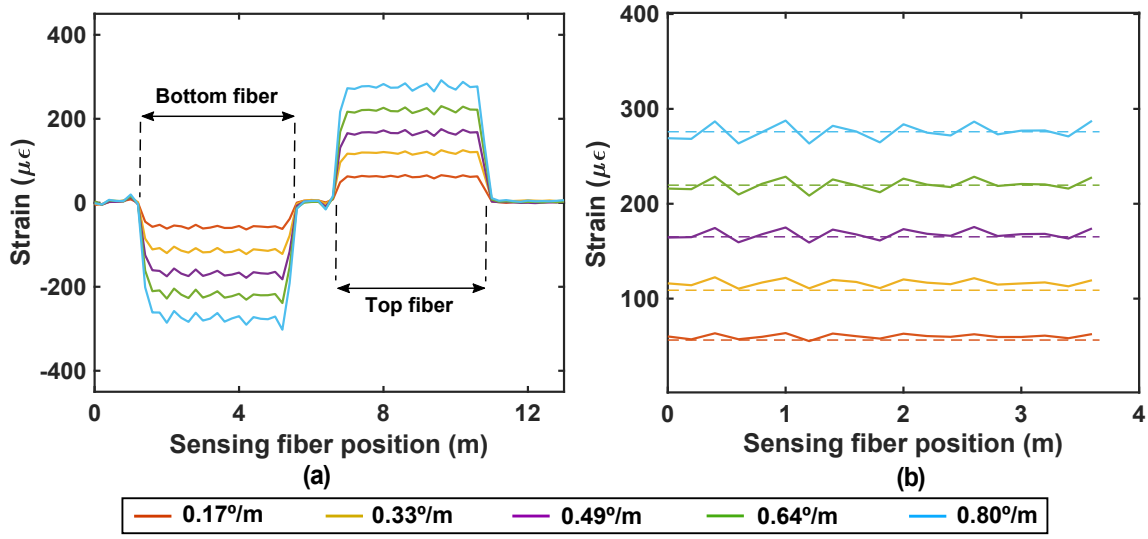

Figure 6.10: Torsional strain measured with the D-BOTDA for several torsion moments applied at the far end of the beam: (a) distributed strain along sensing fiber and (b) differential strain of 2 sections measured compared to the theoretical model.

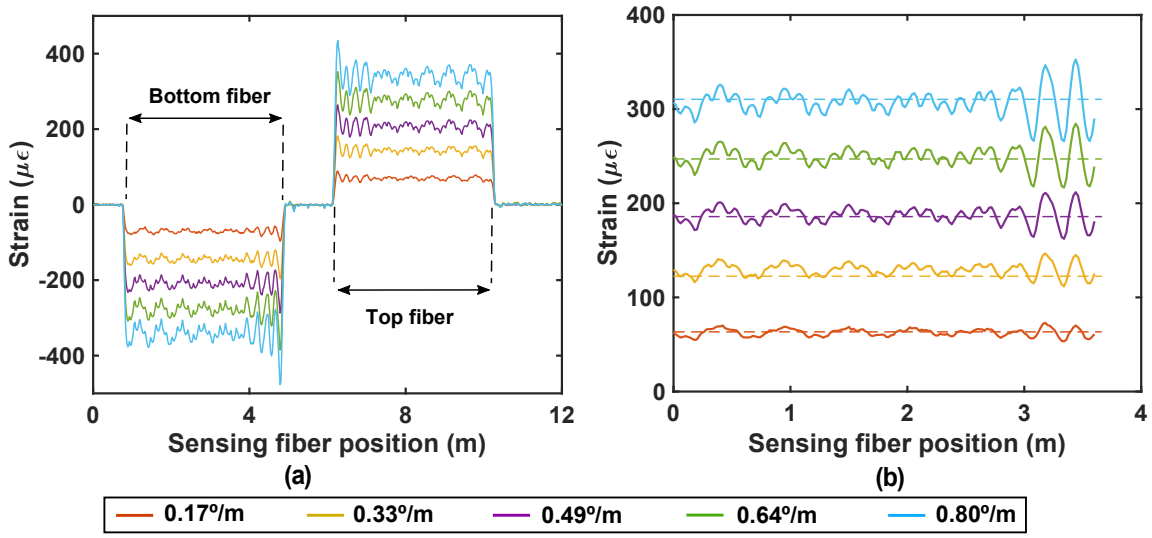

Figure 6.11: Torsional strain measured with the OFDR for several torsion moments applied at the far end of the beam: (a) distributed strain along sensing fiber and (b) differential strain of 2 sections measured compared to the theoretical model.

erated by the torsional moments as it is shown in Fig. 6.11. In this case, a small ringing on the amplitude of the measured strain can be observed in the measurements. This small strain variations seems to be due to an alteration of the cross-section shape of the beam, caused by the pulleys system used for inducing torsion on the beam; the non-ideal anchoring system of the beam to the bench could also have some unexpected effect. Nevertheless, these oscillations are reduced once the strain measured in the two sections is subtracted, as it is shown in Fig. 6.11 (b). This figure highlights the comparison of the experimental strain measured for different torsional moments and the calculated results using the theoretical model. Again, good agreement is obtained.

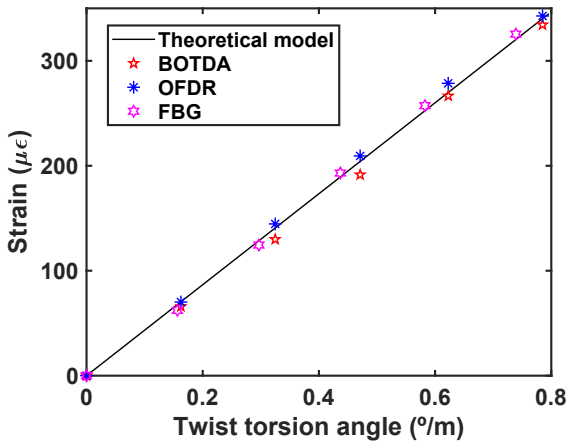

Figure 6.12: Experimental and calculated torsional strain dependence on the torsion moment applied at the loose end of the beam.

Finally, Fig. 6.12 represents the measured strain when different torsional angles are applied at a 1-m distance from the anchored end of the shaft. Notice that it follows a linear dependence as it is expected. Moreover, all the sensors' measurements match with the calculated values, showing a good agreement between experimental results and theoretical calculations.

Torsion strain measurements tolerant to bending variations

As mentioned and analytically demonstrated in section 6.3, the proposed measuring system permits to monitor the torsional strain at any section of a beam independently to any bending effect that could be induced during its monitoring. As explained and shown in Eq. (6.14) and Eq. (6.16), the resultant torsional strain difference obtained from the subtraction of the strain measured in the two fibers deployed at 45° angle, permits to obtain the shear angle and torsion moment avoiding any strain contribution due to bending.

In order to experimentally demonstrate this capability, three different distributed strain measurements were performed changing the bending moment applied to the beam, while the torsional state was maintained equal. Then, the strain measured along the two fiber sections was subtracted and the difference between the two optical fibers was calculated to analyze the performance of the proposed feature. Fig. 6.13 (a) depicts the distributed strain measured along the sensing fiber for three different bending moments induced to the beam. Observe that the two fiber sections show a very similar average strain along the sensing fiber for the three situations. This uniform strain contribution corresponds to the strain induced by the torsion moment. Contrary, a variable strain amplitude is detected along the sensing fiber when bending moments are applied. Note that the amplitude of this oscillating strain increases as the bending is increased (black line). This change of strain follows a sinusoidal shape along the fiber distance, alternating the sign around the average level and increasing its amplitude as the sensing fiber gets closer to the anchored end. This is because the helical deployment of the optical fiber along the 4 faces of the shaft induces alternate amplitude bending strain due to the variation of the distance from the sensing fiber to the neutral of the beam, depending on the fiber position.

Then, Fig. 6.13 (b) shows the resultant strain obtained from the subtraction of the strain of the two fiber sections, showing a fairly uniform strain value along the sensing fiber and reducing the sine shape strain contribution. Note that after subtracting the two fiber sections strain, there is a residual ringing amplitude strain along the sensing fiber, which is again due to the alteration of the beam shape caused by the jack and pulley

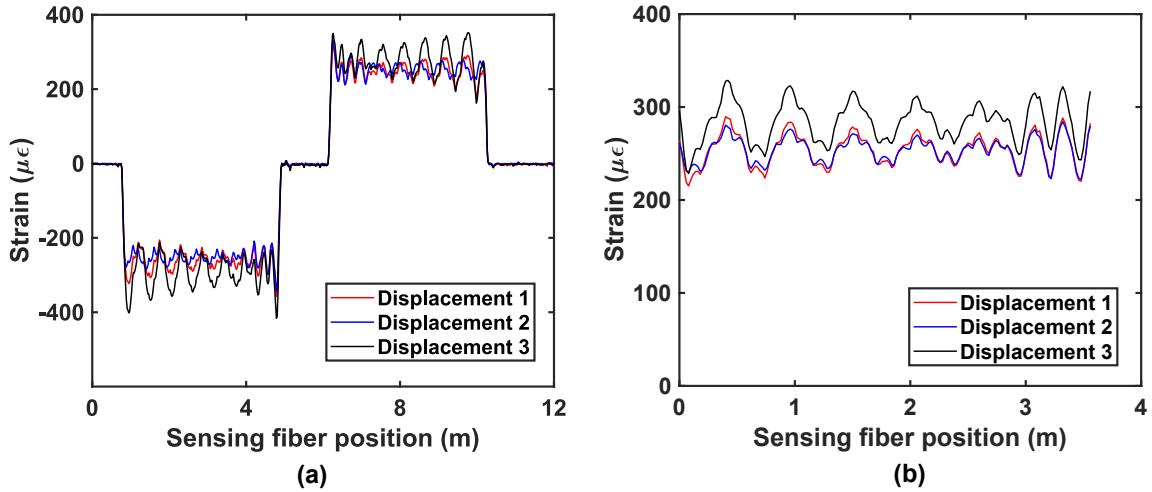

Figure 6.13: Measured torsional strain in the beam for a certain torsional angle and different bending displacements: (a) distributed strain along sensing fiber and (b) differential strain of 2 measured sections.

system, as explained previously.

In order to verify the tolerance to bending strain, the reduction of the peak-to-peak strain amplitudes observed for the different measurements near the pulley position, before and after subtracting the two fiber sections strain has been quantified. In the former case, the peak-to-peak variation strain increased from 47 $\mu\varepsilon$ to 80 $\mu\varepsilon$ and 131 $\mu\varepsilon$, when displacement 2 and 3 were applied. On the contrary, when the subtraction of the two fiber sections is calculated, the peak-to-peak strain variation with respect to the reference measurement is incremented only by 10 and 26 $\mu\varepsilon$, respectively. This result shows an important compensation of the ringing amplitude, confirming a good performance of the proposed technique. The residual increment of the ringing amplitude is again caused by the alteration of the beam shape.

Observe that, in both figures, the measurement for the third bending displacement (black line) shows a slightly higher strain offset respect to the other two measurements, showing a larger average strain level, while the ringing amplitude is similar. This offset is due to the lack of accuracy of the pulley system to obtain exactly the same torsion in different measurements. In this particular case, the torsion moment induced to the beam was slightly higher than for the other two measurements and, as a consequence, a higher average strain was measured. Nevertheless, the amplitude of the ringing shown in Fig. 6.13 (b) is similar, confirming that the bending strain contribution is canceled with the subtraction process.

Therefore, the proposed measuring system, thanks to the devised method of deploying the optical fiber cables and the subtractions of the measured strain of the two fiber

sections, allows to provide torsional strain measurements tolerant to common mode and bending effects.

6.4.3. Dynamic test

Once the performance of the D-BOTDA sensor has been demonstrated for static measurements of bending and torsional strain, we proceeded to perform dynamic measurements at the laboratory facilities to validate the measuring system for dynamic measurements.

In order to dynamically evaluate the D-BOTDA interrogator, the same instrumented shaft was manually excited at the far end of the structure, where the pulleys and jack system was previously located. Alternating displacements at frequencies in the few-Hz range were manually applied to generate bending and torsional moments and, simultaneously, measurements with the D-BOTDA and FBGs interrogators were performed.

Figure 6.14 depicts the bending strain measured along a 75-s measurement. During this measurement time, several manual stimulations were conducted at the far end of the beam with the aim of evaluating the response of the measuring system. Firstly, two events of manual constant torsion were induced, followed by a free vibration of the shaft after releasing it from a torsional state. Then, manual alternating-sign torsion events were successively applied, at around 1-Hz frequency. Finally, another two events of constant bending were generated, followed by a new free vibration of the beam after releasing it from a bending state.

As it is observed, the response of the D-BOTDA sensor and the FBGs match perfectly,

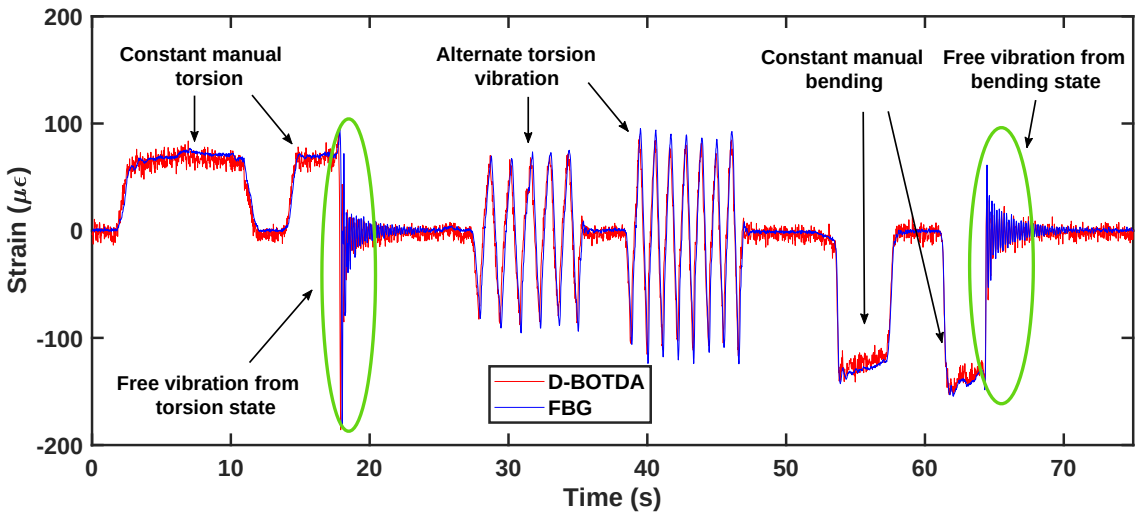

Figure 6.14: Measured strain of the bending fiber along time when dynamic stimulation is applied to the beam.

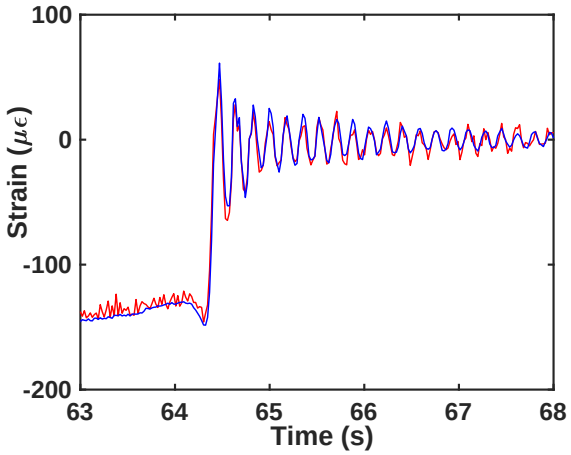

Figure 6.15: Bending strain vibration measurement when the shaft is released from a bending state.

showing a similar response even when the beam is subjected to alternate torsion variation. Notice that, when the strain is measured in the optical fiber deployed longitudinally, the measurement returns either the strain contribution of bending and torsion. This is because the mechanical test bench and the stimulations applied to the beam did not allow to independently stimulate these two deformation modes. So that, bending measurements also show strain due to torsion moments.

Figure 6.15 highlights the period of time when the beam is released from the constant bending state and it freely vibrates, acquiring perfectly the resonance frequency and the decay of the strain amplitude. The measurements of both interrogators, distributed and FBGs shows very good agreement and from both the bending resonance frequency is retrieved, which is approximately 5.77 Hz.

Likewise, the torsional strain was also acquired with both measuring systems for the same period of time, as it is displayed in Fig. 6.16. Again both interrogators offer a very similar response, confirming the good reliability of the D-BOTDA sensor for dynamic measurements. At this point, it is important to highlight the fact that torsional strain measurements are indeed tolerant to bending moments. Therefore, observe that, when a constant bending moment is applied (from second 55 to 65), the resultant strain is nearly canceled thanks to the subtraction process presented previously. A residual strain is observed at this time due to the fact that the excitation applied to the beam was manually and it was not possible to generate only bending, but also torsion was applied. Again, Fig. 6.17 shows in detail the strain measured during the free vibration event created when releasing the beam from the torsional state. The resonance frequency acquired with both measuring systems is 5.67 Hz.

Therefore, in summary, it has been experimentally demonstrated that the proposed

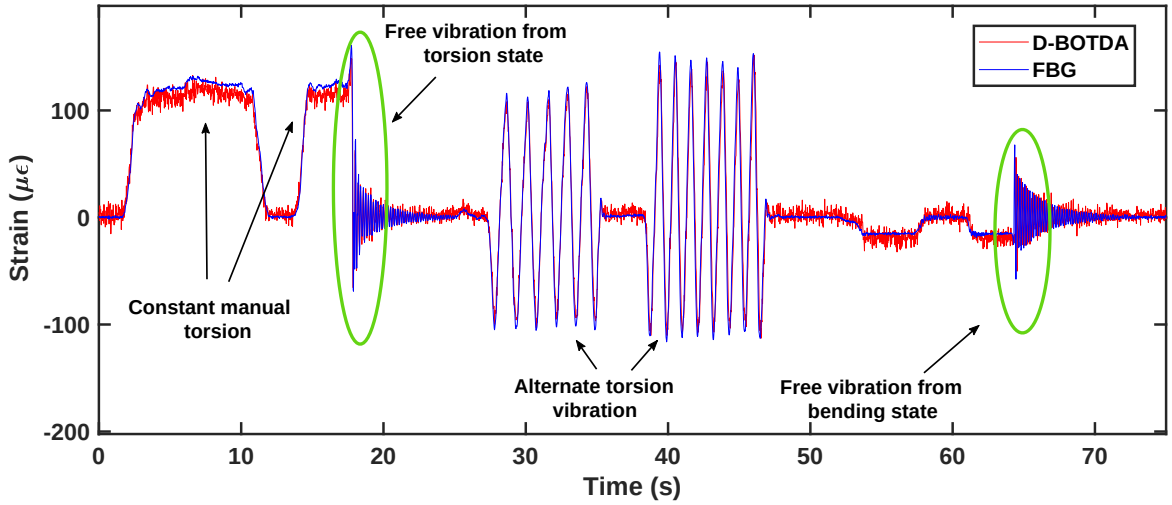

Figure 6.16: Measured strain of the torsional fiber along time when dynamic stimulation is applied to the beam.

measuring system provides good performance and reliability to dynamically monitor the strain induced in solar tracker beams due to either bending and torsion moments. This is, for the first time to our knowledge, the first measuring system capable of obtaining distributed torsional strain measurements and, moreover, in a dynamic configuration. Hence, it is possible to conclude that the devised system is ready for the installation in a real scenario and monitor the effect of wind over a whole PV solar tracker located in a solar plant.

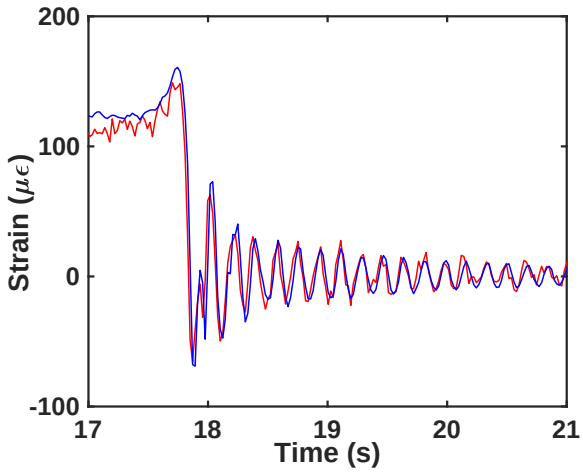

Figure 6.17: Torsional strain vibration measurement when the shaft is released from a torsional state.

6.5. Field installation

As mentioned at the beginning of this chapter, the Windsolar project has the aim of monitoring the effects of wind on solar trackers in a real scenario. So far, we have introduced the measuring system and equipment to be used. Moreover, experimental results obtained in the laboratory have confirmed the validity of the proposed solution. To conclude, in this section, the installation of the measuring system in a solar tracker property of STI Norland S.L. company is presented.

In order to perform in field experiments, a single-axis PV solar tracker was decided to monitor. As explained before, a solar tracker is composed of several beams similar to the one employed for the laboratory tests. This means that multiple beams were necessary to be instrumented and monitored. The solar tracker to be monitored is part of a solar plant located in the south of Navarre (Bardenas Reales), as it is depicted in Fig. 6.18. Observe that the localization of the solar tracker (marked in red) is placed at around 1.5 km far away from the solar park control building, where the D-BOTDA and FBG interrogators were supposed to be installed and kept. In order to be able to connect

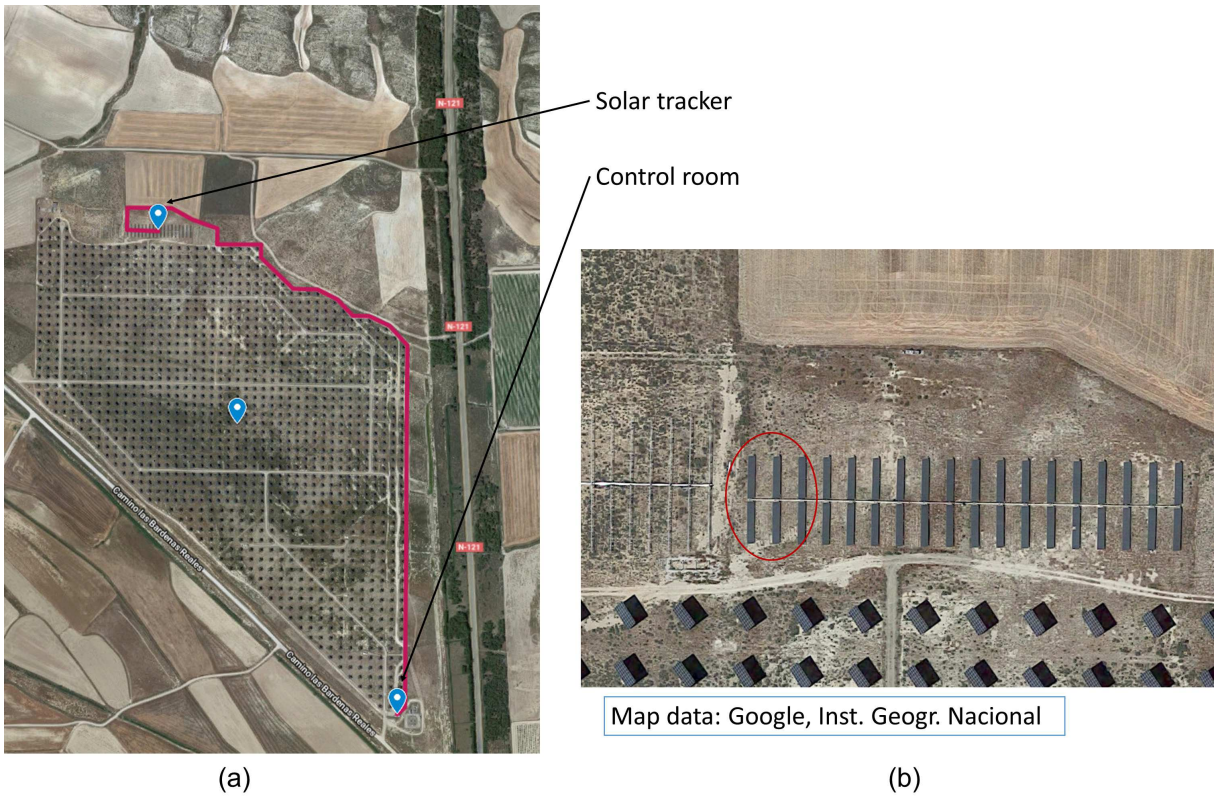

Figure 6.18: (a) Localization of the solar plant and (b) zoomed view of the specific emplacement of the solar tracker to be monitored.

Figure 6.19: (a) Fiber bonding process in laboratory facilities and (b) solar tracker beam after curing process.

both interrogators to the sensing fiber of the solar tracker, an armored fiber optic cable connecting the control building and the solar tracker emplacement was necessary to be deployed. As it is highlighted in the figure (red line), a communications optical cable was disposed along the perimeter area of the solar plant to reach the desired location.

The optical fiber installation process was initiated with the instrumentation of the solar tracker beams to be monitored, following the procedure outlined in section 6.4. Specifically, there were five of these beams, reaching a total length of 33 m length structure. Fig. 6.19 shows the glueing process of the optical fiber, for which it was necessary a detailed cleaning of the surfaces and careful disposal of the fiber to follow the layout described previously. Every section of the solar tracker was instrumented with optical fiber cables to measure bending and torsional strain. A two-component epoxy was used to glue the fiber and ensure a good strain transfer.

After the curing process, see Fig. 6.19 (b), all the sections were packed and taken to the field. The solar tracker structure was fully assembled as shown in Fig. 6.20 and

Figure 6.20: Pictures during solar trackers and solar panels installation.

Figure 6.21: (a) Fiber Bragg gratings sensors installed in solar tracker junctions. (b), (c) PV solar tracker after optical fiber installation.

Fig. 6.21. During this process, it was necessary to coordinate the mounting process with STI Norland in order to solve several incidences regarding the protection of the bonded optical fiber. For instance, Fig. 6.20 (b) shows that special parts were installed on the edges of the beams to provide a safe distance from the solar panels clamps to the sensing fiber, so the fiber is not damaged.

After assembling the whole structure, FBGs were glued in specific locations to monitor some critical beam positions determined by STI Norland. In particular, junctions between solar tracker beams were monitored along with the crank strain, temperature of the beams and other critic parts of the structure. Afterward, all bonded fiber sections glued for distributed measurements were spliced together in a single loop and directed to a fiber optic cable connection enclosure installed by the solar tracker. Then, the sensing fiber loop connectors of distributed sensing and FBGs arrays were spliced to the communications optical fiber cable that connects to the interrogators. Finally, some preliminary measurements were performed to ensure the correct operation of all elements in the monitoring system.

6.6. Conclusions

In this chapter of the thesis, a new measuring system capable of dynamically monitor bending and torsion in long structures has been devised, presented and experimentally demonstrated. A measuring method that requires a particular optical fiber deployment layout has been proposed to allow the system to measure distributed bending and torsional strain. The measuring system designed in this research work has shown to perform strain measurements tolerant to common mode variations. In particular, the torsional strain measurements are independent on any bending variations during the measurement process.

Experimental measurements of bending strain and torsional strain generated in a rectangular 3.4 m beam were performed with a D-BOTDA sensor in the laboratory facilities. The results were correlated with measurements carried out simultaneously with the FBGs and OFDR interrogators to demonstrate the correct performance of the devised measuring system. A theoretical model was developed to analytically calculate the expected bending and torsional strain along the beam and was compared to the experimental results, showing good agreement.

Dynamic measurements of bending and torsional strain have been performed in the laboratory with a D-BOTDA sensor demonstrating that the proposed dynamic interrogator is able to detect the resonance frequency of the beam when the structure is externally stimulated, showing a good agreement with the FBGs results and confirming the reliability of the presented system.

An in-field 30-m length PV solar tracker has been instrumented following the described procedure to allow the measurements of bending and torsional strain. Then, the whole solar tracker was assembled in a solar plant and the installation of the required communication optical fiber cable and equipment was completed.

CHAPTER 7

Enhanced linearly-configured BOCDA sensor

7.1. Introduction

As it has been already explained during previous chapters of this thesis, DOFS may be deployed using diverse configurations. The most explored and deployed ones are those based on the time-domain analysis configuration, the well-known BOTDA sensors, which have been deeply studied during this thesis. Several solutions have been proposed and demonstrated during the last years and during the realization of this thesis to enhance the capabilities offered by BOTDA sensors: large sensing range, high accuracy and fast acquisition time are some of their main features. However, due to the fundamentals of the SBS interaction in BOTDA systems, there are some limitations that cannot be overcome, and hence, constrain their performance. In particular, the spatial resolution and the measurement access to random positions along the sensing fiber cannot be freely selected.

Contrary to BOTDA sensors, BOCDA sensors offer the advantage of being much more suitable when measurements with higher spatial resolution are needed. The working principle of BOCDA sensors is based on using two continuous waves and the coherent interaction between them along the sensing fiber, offering the capability to perform distributed measurements with spatial resolution of the order of millimeters. In addition, it is possible to arbitrarily select multiple points along the sensing fiber and perform the measurements at only the selected points. These are two features that characterize BOCDA sensors, which cannot be obtained with BOTDA sensors.

Numerous approaches have been presented during the last years to overcome several constraints of this type of sensors. As mentioned in chapter 2, among these contributions, the LC-BOCDA scheme has been recently devised, which allows single-ended access to

the sensing fiber, reducing the complexity of the practical deployment of the setup. This technique is a great alternative to the use of BOCDR methods, which is another type of single-ended measurement technique, although, with lower SNR [118].

However, during the research of this thesis, an important limitation of LC-BOCDA sensors has been found, which is related to the maximum amplitude of the FM of the pump and probe waves that can be deployed in these sensors. This parameter determines the spatial resolution and the number of sensing points (or resolving points), and hence, the measurement range. The main objective of this chapter is to present and demonstrate a proof-of-concept for a new LC-BOCDA configuration based on a dual-probe wave and correlation-order control to nearly double the limit of maximum modulation frequency deployed to generate the pump and probe waves. This research contribution permits to enhance the performance of LC-BOCDA sensors by increasing the number of resolving points.

During this chapter, a brief introduction to recent research contributions in BOCDA sensors is firstly presented, particularly, the compensation of the uncorrelated gain induced in BOCDA sensors and the recently devised LC-BOCDA sensor configuration, which allows a simplification of the sensing fiber installation. Then, the proposed LC-BOCDA sensor configuration is described along with the experimental setup. Finally, the performance of the enhanced measuring technique is demonstrated and the experimental results are shown and discussed.

7.2. Recent progress in BOCDA sensors

Since the first BOCDA sensor configuration was proposed in 1999, multiple advancements and diverse techniques have been presented to improve their performance, capabilities and simplicity. In this sense, one of the most important contributions was the scheme devised to reduce the detrimental effect caused by the uncorrelated gain generated by all the sensing positions where the correlation between both waves is low. Another significant advancement is the deployment of the novel BOCDA setup that allows to perform single-ended access measurements, the LC-BOCDA.

7.2.1. Compensation of uncorrelated gain in BOCDA sensors

As it has been explained in chapter 2.2.3, BOCDA sensors are based on the SBS interaction of two continuous waves along the sensing fiber. The measured output spectrum of a BOCDA sensor is given by the two-dimensional convolution integral between the intrinsic BGS and the pump-probe wave beat spectrum. Fig. 7.1 (a) shows the propaga-

tion pump and probe optical waves and the resultant shape of the local Brillouin spectra obtained along the sensing fiber due to the SBS interaction. Observe that the resultant Brillouin gain is only efficient in those positions of the fiber where the correlation between both waves is high. Fig. 7.1 (b) depicts the shape of the output spectra of the BOCDA signal for two given sensing position. In particular, Fig. 7.1 (b.1) displays the local Brillouin spectrum obtained at a CP position when the BFS of the sensing fiber is uniform, showing a Lorentzian profile (red line) added to a broadened background signal. Whereas, Fig. 7.1 (b.2) shows the BOCDA spectrum shape when a strain is induced to the CP fiber position. Note that, the Lorentzian signal contribution, red line, is now up-shifted, while the Brillouin gain contribution of all the non-correlated fiber positions, remains equal, showing a severely broadened spectrum.

As it is observed, the BOCDA output spectrum obtained at the end of the fiber has an important background noise level, which is due to all the gain contributions of the uncorrelated positions of the sensing fiber, and on top of this noise, there is a tower-like signal spectrum. The tower-shaped component at the top of the background noise corresponds to the Brillouin gain generated at the CP positions. This uncorrelated gain deteriorates the dynamic range of distributed BFS measurements due to the broadening of the detected signal linewidth. Note that, when the measured position at the CP has

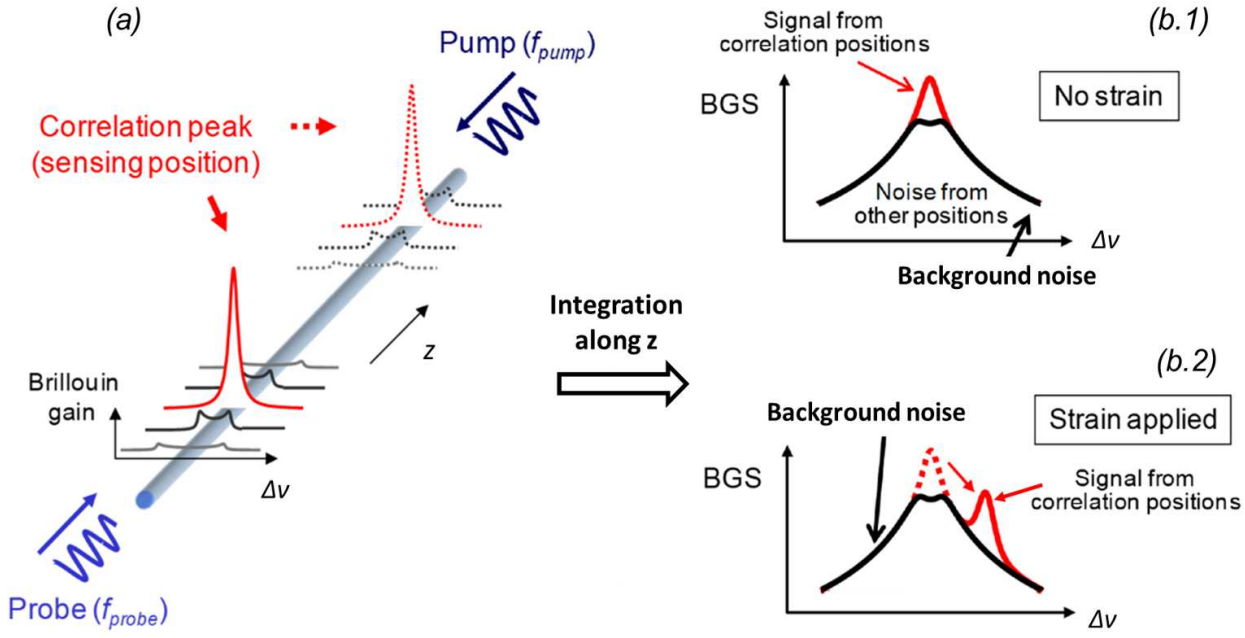

Figure 7.1: (a) Spectral shape induced locally along the optical fiber by the BOCDA principle. (b.1) BOCDA output spectrum obtained by the integration of the spectra generated at each position along the fiber when strain is not applied and (b.2) when it is applied. © 2019, Appl. Sci. [4]

a different BFS with respect to the rest of the fiber positions, the frequency of the BGS peak is shifted and the background noise could reach higher signal amplitude than the desired signal, as it is shown in Fig. 7.1 (b.2). Hence, errors on the determination of the BFS of the sensing fiber can be experienced [119].

Since the BOCDA sensors were presented for the first time, several solutions have been proposed to overcome the important drawback of the background noise spectrum. One of them is the intensity modulation (IM) scheme that mitigates the detrimental effects caused by the FM modulation on the LD [119, 75]. This technique is based on controlling the averaging time of the LD power spectrum shape. The disadvantage of this solution is the complexity of the measurement scheme.

Another way to reduce the background noise is to deploy the differential measurement scheme [76]. This technique lies on the generation of phase modulation in either the pump or probe signals to suppress the carrier and broaden the local BGS spectrum. Fig. 7.2 (a) and Fig. 7.2 (b) show, for instance, the resultant BOCDA output signal using a conventional configuration and a phase-modulated scheme, respectively. As it has been mentioned before, the BOCDA signal is obtained by the integral of the convolution between a local BGS, that shows a Lorentzian profile, and the local beat spectrum between the pump and probe waves. Note that, when the phase modulation is applied, the shape of the local BGS is spread out and the resultant BOCDA signal appears with the sharp BGS peak significantly attenuated. In contrast, the signal due to the uncorrelated positions remains similar to the conventional configuration. Then, by calculating the difference between the BOCDA spectra of the two detected signals, with and without phase modulation, the background noise spectrum is highly reduced and it is nearly negligible. As a result, the detected signal shows a sharp BGS peak corresponding just to the CP signal. Fig. 7.2 (c) highlights the resultant differential spectrum. As a result of the deployment of this technique, a reduction of the background noise level is obtained, leading to a significant amelioration of the dynamic range constraint, and indeed, to an enhancement of the spatial resolution of BOCDA systems [76, 120].

An additional advantage of the differential measurement method is that the practical implementation of this technique does not require a complex setup. It can be easily deployed using a lock-in detection system applied for the signal processing of ordinary BOCDA systems [66, 121]. Phase modulation can be applied to either the pump or probe waves. This modulation is turned-on and off by a switching control with a frequency f_L, as shown in Fig. 7.2 (d), where it is represented the RF signal applied to the phase modulator. Then, using a lock-in amplifier (LIA) synchronized with a reference frequency f_L, it is possible to easily obtain the differential measurement of the BGS. As mentioned,

this technique has allowed to significantly enhance the spatial resolution and dynamic range of BOCDA sensors [76, 120].

7.2.2. Linearly-configured BOCDA systems

As it has been shown along this thesis, BOCDA and BOTDA sensors are typically built up in loop configurations in order to counter-propagate probe and pump waves along the sensing fiber to induce SBS interaction. These schemes permit to obtain a much larger signal and SNR than other Brillouin reflectometry techniques. However, sometimes the

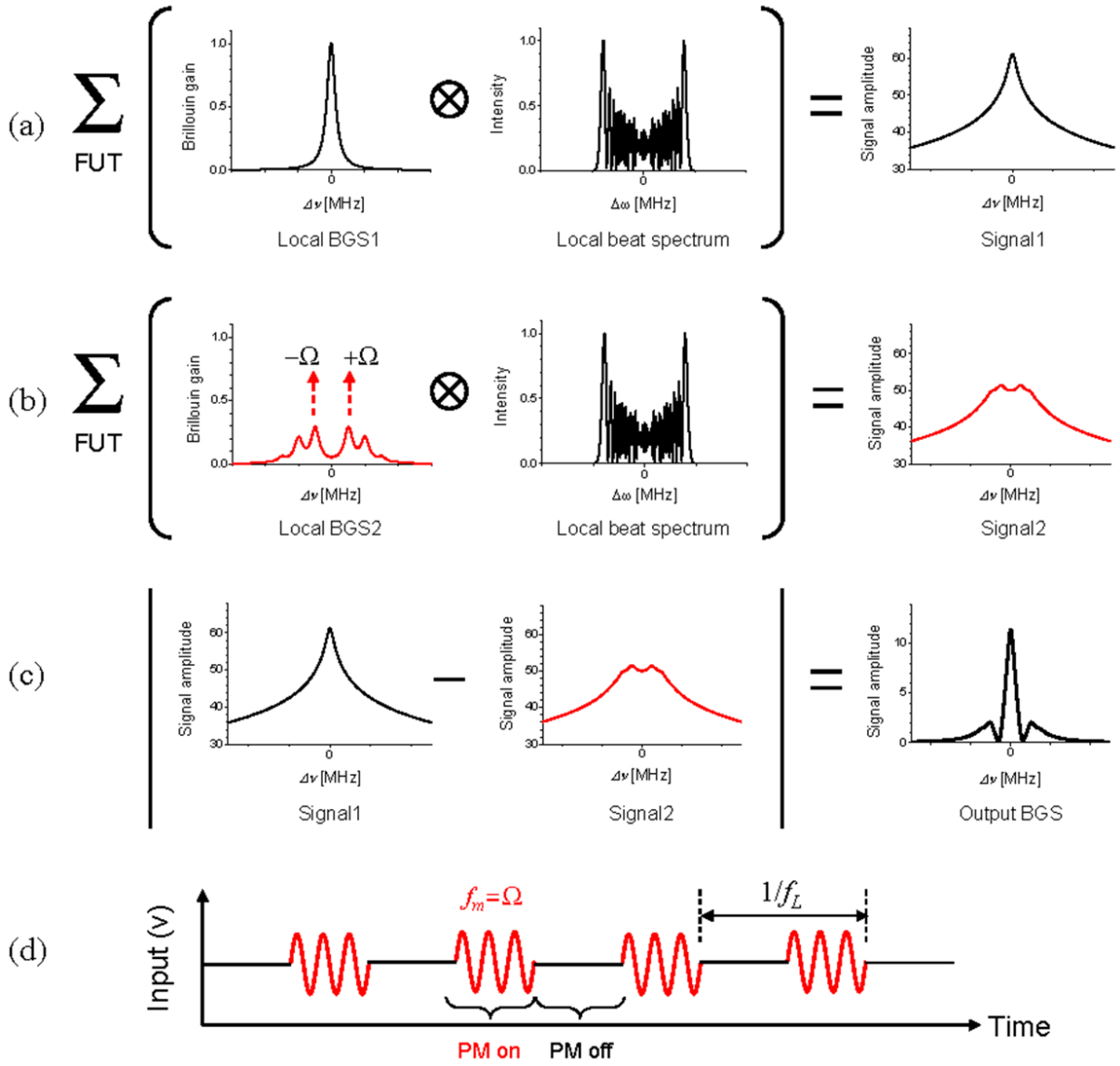

Figure 7.2: (a) BOCDA output signal using a conventional probe wave. (b) BOCDA signal spectrum using a phase-modulated pump wave. (c) Differential measurement after calculating difference between (a) and (b). (d) RF signal used for the phase modulation in the differential measurement. © 2012, Opt. Express [76].

single-ended access can be advantageous over the loop configuration due to the simplicity of their setups and the reduction of costs, mainly due to the shorther length of fiber that needs to be installed. For this reason, several proposals have been also presented during the last years to allow BOCDA systems to monitor with single-ended access to the sensing fiber [85, 120, 86].

In this sense, in 2008, a linear configuration of a BOCDA sensor was proposed applying beat lock-in detection together with a narrowband optical filter [85]. The working principle of a LC-BOCDA is based on generating modulated pump and probe waves and inject both of them into the sensing fiber from one direction, as displayed in Fig. 7.3. Then, after their propagation, both waves are reflected at the end of the fiber and propagated backward, so, the outgoing optical signal will counter-propagate the incoming waves, giving rise to SBS interaction between the counter-propagating pump and probe waves.

In order to develop the first LC-BOCDA system, it was necessary the combination of a beat lock-in detection system, two intensity modulators and, an additional function generator with a complex signal processing used to acquire the BGS [85]. However, this type of BOCDA system still had an important drawback. As the pump wave is reflected and detected along with the probe wave, a remaining pump signal is still reaching the lock-in detection system, even after filtering out with a FBG. The detection of the un-filtered pump wave induces a considerable amount of noise offset due to intensity variations caused by the detection of the remaining pump wave. Apart from the noise detrimental effect, during the propagation of these two optical waves, two different SBS interactions take place in the sensing fiber, giving rise to two different CP, as shown in the table of Fig. 7.3. The first CP is generated by the outgoing pump wave that interacts with the incoming probe, which has been previously reflected at the end of the fiber. Whereas the second CP is generated by the outgoing probe wave and the reflected incoming pump wave. In order to avoid measurement errors due to simultaneous detection of both CPs,

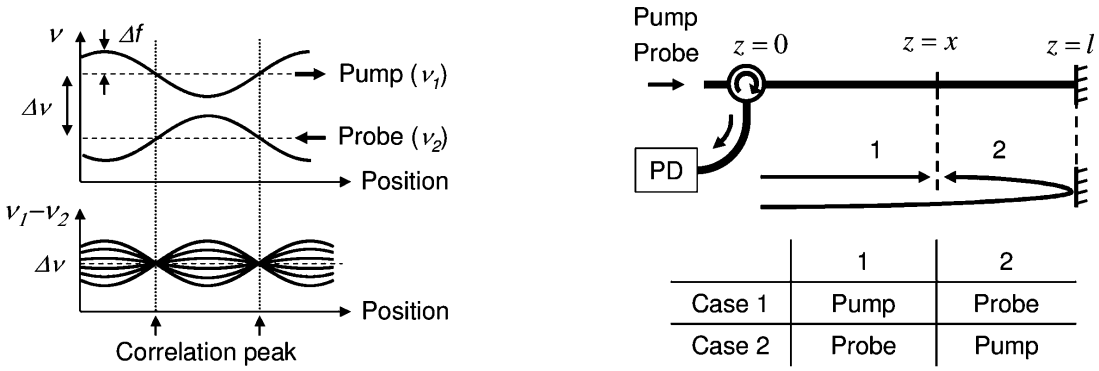

Figure 7.3: Fundamentals of the LC-BOCDA systems. © 2008, IEEE [85].

the distance between the CPs had to be doubled, halving the nominal sensing fiber range in linear configuration BOCDA sensors.

An alternative method to deploy a linear configuration of a BOCDA system is the use of two polarization beam splitters and a polarization maintaining fiber as sensing fiber to separate the pump and the probe. However, the complexity of the setup makes difficult the implementation of this solution [86].

Lately, an improved LC-BOCDA sensor configuration has been presented that enhances the spatial resolution and dynamic range of these sensors, and moreover, solves the constraint of the simultaneous detection of the two CPs, allowing to double the measurement range [120]. This solution combines the initial LC-BOCDA setup with two advancements recently presented: the differential measurement technique, which enhances the spatial resolution and dynamic range of BOCDA sensors and, the weak reflectivity at the end of the fiber, which permits to solve the measurement range shortening in linear configuration by using Fresnel reflected end [85].

7.3. Fundamentals of the enhanced linearly-configured BOCDA sensor

As explained, there have been presented several proposals and advancements to improve BOCDA sensors using linear configurations. However, during the realization of this thesis, it has been found that there is an important limitation that restricts the performance of this type of sensors, which is the limited Δf that can be deployed. This constraint does not allow to improve the spatial resolution, Δz, nor the number of sensing points, N, of BOCDA sensors, which are defined as follows [66]:

$$\Delta z = \frac{c \cdot \Delta\nu_B}{2\pi n \cdot f_m \cdot \Delta f} \tag{7.1a}$$

$$N \equiv \frac{Range}{\Delta z} = \frac{\pi \cdot \Delta f}{\Delta\nu_B} \tag{7.1b}$$

where $\Delta\nu_B$ is the Brillouin gain bandwidth, c is the speed of light, n is the group index of the optical fiber, and f_m is the modulation frequency of the light source, respectively. Observe that, the spatial resolution could be enhanced by increasing f_m, although, in that case, the measurement range would proportionally decrease because of the reduction of the CP distance given by Eq. (2.24).

Based on the research work done in this thesis, it has been found that the origin of the

limited Δf, is the frequency overlap of the pump and probe waves spectra that occurs if a Δf larger than $\nu_B/2$ is deployed to dither the LD. Due to this frequency overlap, the maximum value of Δf that can be deployed in LC-BOCDA sensors is practically limited to half of the Brillouin frequency of the sensing fiber $\nu_B/2$. Fig. 7.4 highlights the overlap effect between the pump and probe spectra if $\Delta f > \nu_B/2$. Whenever the modulation frequency amplitude exceeds $\nu_B/2$, the reflected pump wave at the overlapped frequency cannot be filtered out by an optical filter, and hence, it is detected in the PD along with the probe wave, resulting in a significant distortion of the retrieved signal [85].

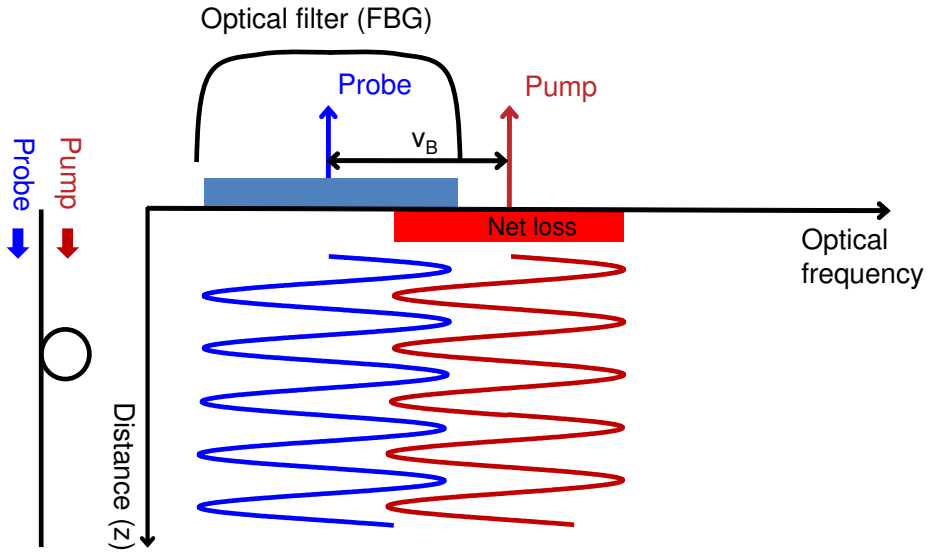

Figure 7.4: Spectral overlap in the single-probe wave LC-BOCDA scheme.

We have found that, the overlap of the pump and probe wave spectra and the non-ideal filtering of the pump wave, originates two problems. The first problem is described in Fig. 7.5. As it is observed, when both optical waves are injected into the sensing fiber and reflected at the far end, there is a first SBS interaction between the incoming probe and the outgoing pump wave at CP_1 (Case 1). Apart from this, there is an additional Brillouin loss interaction that takes place at CP_2, where the incoming pump wave is depleted by a strong outgoing probe wave (Case 2). This Brillouin loss experienced by the pump wave (CP_2) is simultaneously detected in the PD, giving rise to a false CP, that it will be called ghost peak. Consequently, the SBS gain and loss signals from both CPs are simultaneously detected, leading to a distorted measurement of the BGS.

Notice that the depletion of the pump at CP_2 is always present as long as the length of the sensing fiber is long enough to have a second CP after the reflection. However, it only has a deleterious effect if Δf is large enough to lead to spectral overlap between the pump

and probe components, so that, it cannot be completely filtered out. Note that there is also some depletion of the pump wave by the incoming probe wave at CP_1, although it is negligible compared to that at CP_2 because of the reduced power of the probe after being reflected at the end of the fiber.

It is worth mentioning that the signal amplitude obtained by the LIA used in LC-BOCDA sensors is proportional to the pump and probe waves power. Therefore, it can be deduced that the SBS gain from CP_1, and SBS loss from CP_2, lead to the same signal amplitude, regardless of the injected power of the outgoing pump and probe waves. This is an important constraint that induces an ambiguous detection of the BGS, and hence, errors on the determination of the sensing fiber BFS.

The second problem induced by the mentioned pump and probe waves overlap and its non-ideal filtering, is the detrimental effect caused by the simultaneous detection of both modulated waves in the PD. Since both waves are modulated with the same modulation frequency, f_m, and the fiber length in the signal generation process is different for each wave, the relative phase between both waves changes when the CP position is swept. Thus, depending on the relative phase value, a beating frequency interference can be generated at the receiver and added to the detected signal as a beating noise signal.

Therefore, in order to overcome these constraints, an alternative configuration of

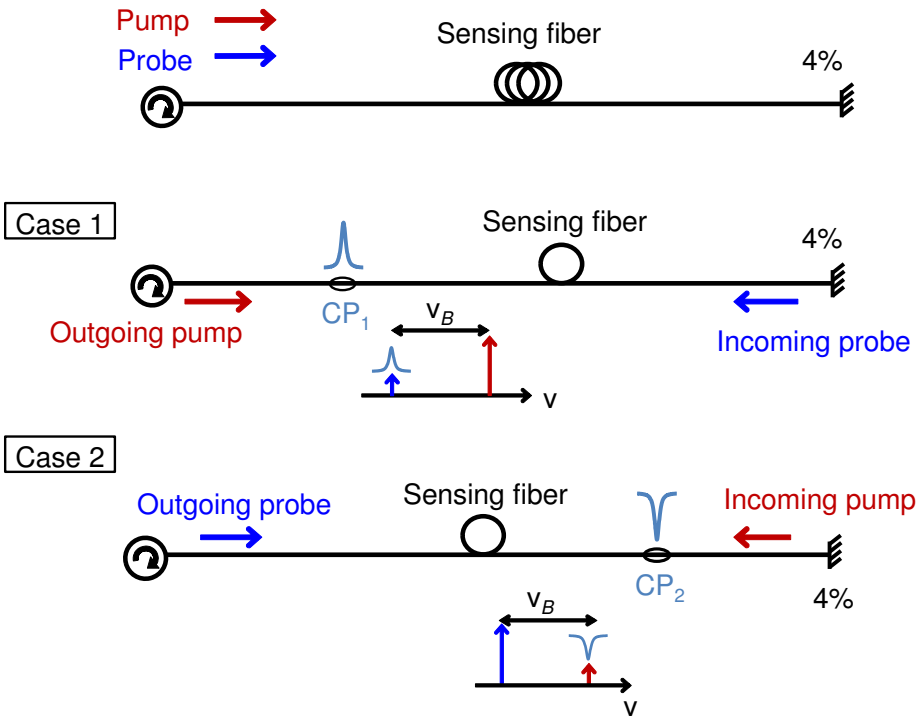

Figure 7.5: Fundamentals of the generation of the SBS interactions in LC-BOCDA systems.

the previously explained LC-BOCDA sensor was devised during a research collaboration between the Public University of Navarre and Chung-Ang the University of Seoul, in South Korea. This method is based on a dual-probe wave LC-BOCDA system and correlation-order control that allows to nearly double the limit of maximum Δf from the previous $\nu_B/2$ to almost ν_B. On the one hand, the dual-probe wave that is generated by double-sideband modulation of the optical source signal solves the detrimental effects induced by the Brillouin depletion of the reflected pump wave. On the other hand, the control of the correlation order avoids beating noise due to the spectral overlap between the pump and probe waves at the receiver.

Figure 7.6 depicts the working principle of the proposed technique. As it can be observed, a dual-probe wave is generated to compensate the Brillouin loss generated on the pump in conventional LC-BOCDA systems. This is a similar solution to the one already applied in BOTDA systems to reduce NLE [88]. Specifically, both optical waves are injected together into one end of the sensing fiber and propagated to be reflected at the cleaved far-end of the fiber. As it is schematically depicted in the figure, both sidebands of the probe interact with the pump wave. The Brillouin loss experienced by the pump wave due to the interaction with the lower-frequency sideband of the probe wave is compensated by the gain provided by the upper-frequency sideband. This combination of SBS interactions allows to obtain a net gain and loss on the pump wave equal zero, compensating the first one of the two problems generated by the spectral overlap, as it is depicted in Fig. 7.6. The validity of this solution to overcome this constraint has been experimentally demonstrated, as it will be shown in section 7.4.3.

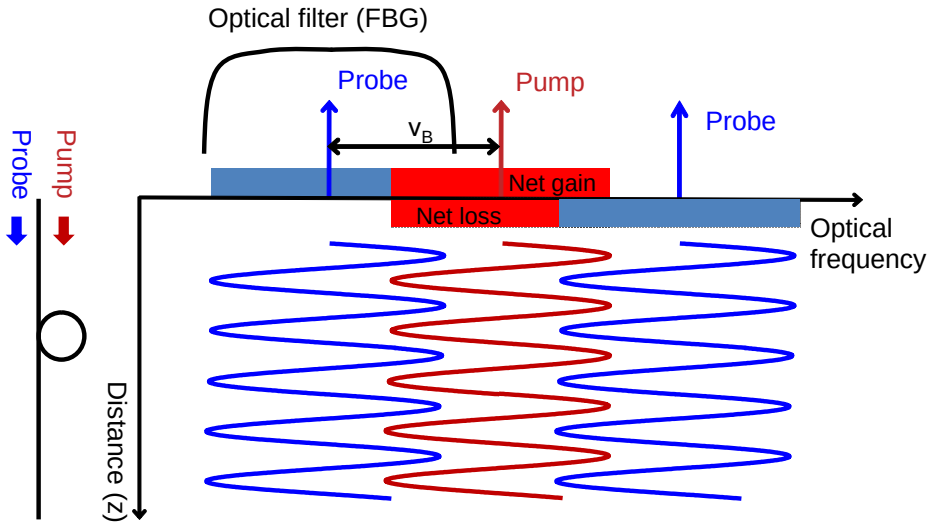

Figure 7.6: Spectral overlap in a dual-probe wave LC-BOCDA scheme.

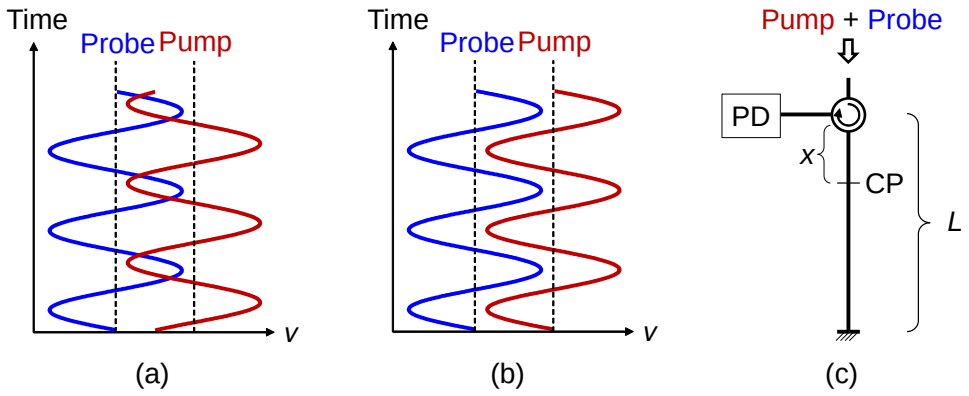

Figure 7.7: Optical frequency change in time of the pump and probe waves detected by the PD when their FM is (a) out-of-phase, or (b) in-phase. (c) Schematic of the LC-BOCDA with a CP at position x.

The second detrimental effect brought by the spectral overlap is highlighted in Fig. 7.7. This limitation is caused when pump and probe waves reach simultaneously the PD after their propagation along the sensing fiber. If both waves reach the receiver out-of-phase, they mix and the resultant beat frequency can lie within the bandwidth of the PD as schematically shown in Fig. 7.7 (a).

The occurrence of this beat noise is dependent on the relative phase of the sinusoidal waves modulating the pump and probe optical frequencies. Their beat signal may generate an important interference on the detected BGS and completely distort the detected spectrum. Moreover, since the Brillouin gain is small in BOCDA systems, this beating signal causes a significant noise to the obtained BGS, even though lock-in detection is applied.

The resultant beating frequency of pump and probe waves at the PD is dependent on their relative phase and it can be expressed as follows:

$$f_{beating} = \Delta f_0 \pm 2\Delta f \cdot cos\left(2\pi f_m t \pm \frac{\Delta\phi}{2}\right) \cdot sin\left(\frac{\Delta\phi}{2}\right) \tag{7.2}$$

where $\Delta\phi$ is the phase difference between the outgoing pump and incoming probe at CP, when both modulated signals arrive at the PD and Δf_0 is the static frequency difference between both waves, commonly set equal the BFS, ν_B. From this expression, it is deduced that, if $\Delta\phi$ is small, $f_{beating}$ will be always out of the PD bandwidth, because the second part of the expression is close to zero. However, if $\Delta\phi$ increases its value, due to for example the fiber scanning process, the resultant $f_{beating}$ can lie within the PD bandwidth, generating the detrimental interference in certain positions of the fiber.

In order to avoid this constraint, it has been devised a method by controlling the modulation of both waves and the correlation order, so that, they always arrive "in-phase" at the receiver and the beating frequency is out of the PD bandwidth, as depicted in Fig. 7.7 (b). Let's consider the situation as it is shown in Fig. 7.7 (c), where the sensing position, CP, is located at position x within the total fiber length, L. As it is well known, the phase difference, $\Delta\phi$, of the modulated pump and probe waves at the CP is always zero in BOCDA systems (by the definition of CP). So that, $\Delta\phi$ at the PD is determined by the round trip path length, $2n(L-x)$, which, in order to suppress beat noise, should be made to be close to 2π to ensure that both waves still have similar phase. Therefore, the resultant phase difference is as follows:

$$\Delta\phi = \frac{4\pi n f_m}{c}(L-x) = 2\pi \pm \Delta\theta \tag{7.3}$$

where $\pm\Delta\theta$ is a margin in the phase difference between the pump and probe waves within which the suppression of the beat noise is secured by ensuring that their beat frequency is out of the PD bandwidth. The physical meaning of the tolerable margin can be also understood in Fig. 7.8 where the red and blue solid curves represent variation in time of the pump and probe optical frequencies, respectively. While blue dashed curves correspond to the probe wave with maximum and minimum allowable phase delay that this signal can tolerate without generating the detrimental beat noise. For instance, let's consider the pump and probe frequencies given by the solid lines at a given time, t_0. For this particular condition, both waves are in-phase, $\Delta\phi = 0$, and beat noise is negligible. However, there exists a phase delay range determined by the phase margin (blue-dashed lines), in which, the probe wave can be delayed $\pm\Delta\theta$ without generating beat noise. This means that, for all these $\Delta\phi$ range, the beating frequency lies out of the PD bandwidth.

The condition to locate a CP at a given position x along the sensing fiber using the LC-BOCDA is related to the path length difference between the outgoing pump and incoming probe waves, which is given by the following equation:

$$2n(L-x) + n \cdot D = m\frac{c}{2f_m}, \tag{7.4}$$

where D is the length of the delay fiber and m is the order of CP, respectively. From Eq. (7.3) and Eq. (7.4), an equation for the order of the CP, m, that should be selected to obey the phase margin restriction yields:

$$m = \left[\frac{2\pi \pm \Delta\theta}{2\pi}\right] \cdot \left[2 + \frac{D}{L - x}\right]. \tag{7.5}$$

Note that, in order to allow measurements of a given length of sensing fiber, L, it will be necessary to deploy a dummy fiber at the end of the fiber under test of at least similar length, to permit the whole scan of the desired sensing fiber, as it will be explained in detail in the next section.

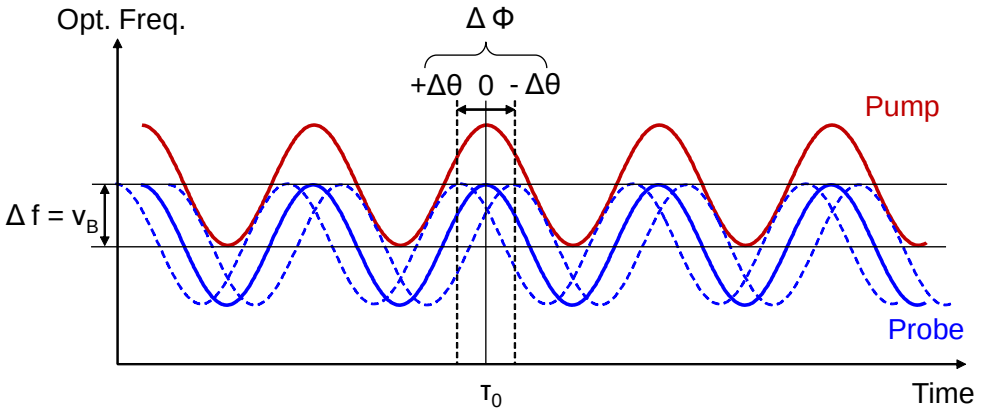

Figure 7.8: Optical frequency of pump and probe waves with the maximum phase difference to avoid beat noise at the PD.

7.4. Experimental setup and measurements

In order to demonstrate the enhancement of the proposed LC-BOCDA technique and compare its performance with the conventional LC-BOCDA sensor, two different configurations of LC-BOCDA were assembled. A conventional single-probe LC-BOCDA sensor setup was built for the later, while a dual-probe wave LC-BOCDA setup was assembled for the former. In this section, the experimental setup is described, and then, the correlation order control method devised to solve the beating noise is experimentally demonstrated. Finally, experimental results of the enhanced LC-BOCDA technique are shown.

7.4.1. Experimental setup

Figure 7.9 shows the experimental setup of the two LC-BOCDA sensor configurations deployed to demonstrate the improvement of the proposed scheme: the conventional and the enhanced LC-BOCDA sensor setup. A 1550-nm distributed feedback LD was used as a light source. The current of this device was driven with a sinusoidal RF signal in

order to modulate the wavelength of the emitted light. Then, the output signal of the LD (13-dBm power) was divided into two branches using a 3-dB coupler.

The upper branch of the setup was used to generate the probe wave. Initially, a single-sideband suppressed-carrier (SSB-SC) modulation was generated using a MZ-EOM to study the performance of the conventional single-probe LC-BOCDA sensor. Once the measurements using single-probe configuration were fulfilled, a DSB-SC modulation using a dual-parallel MZ-EOM was generated to evaluate the performance of the devised dual-probe LC-BOCDA sensor. In both configurations, the modulators were driven by a 25-dBm RF signal, which was generated by a microwave sweep synthesizer (MSS) used to scan the frequency detuning between the pump and probe and the BFS of the fiber, $\Delta\nu$, for each position of the sensing fiber. In order to suppress the polarization dependence of the Brillouin interaction, a polarization switch (PSW) was deployed before injecting the probe wave into the fiber.

In the lower branch, a phase modulation at a fixed frequency, Ω, was applied to the pump wave to implement the differential measurement scheme [76]. In order to be able to perform the differential measurement, the electrical signal used to drive the phase modulator had to be switched on and off. Then, the pump wave was launched to a 5-km delay SMF, so a high-order CP was obtained to easily scan the sensing fiber. Finally, both signals, pump and probe, were combined using a 3-dB coupler and amplified by a high output power (27 dBm) EDFA. The amplified signal, formed by a 21-dBm peak power pump and 22-dBm peak power probe wave, was launched to a 68-m SMF. Two strained sections of 30-cm length with a separation of 30-cm fiber between them were

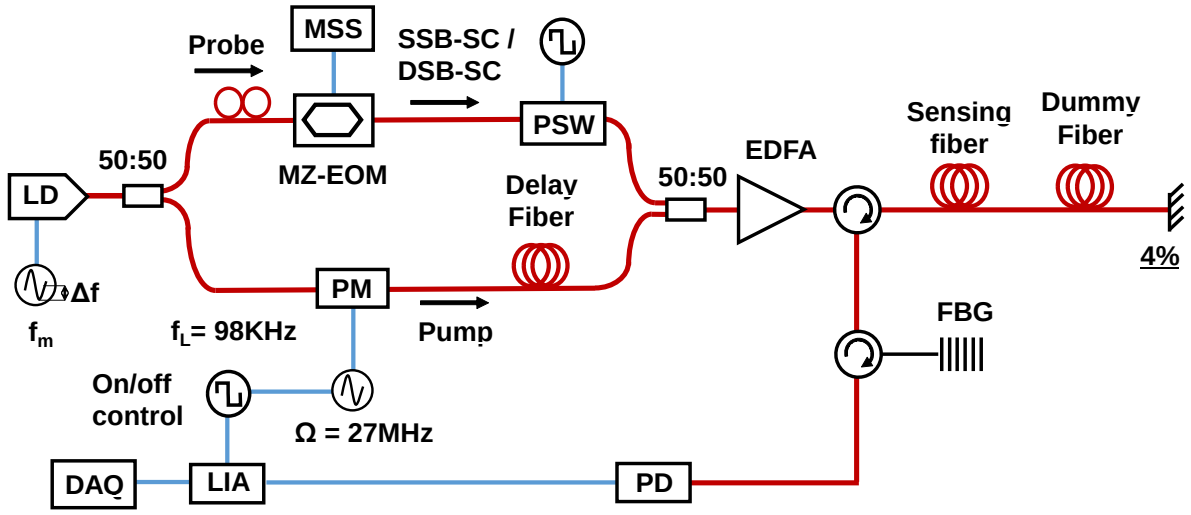

Figure 7.9: Experimental setup of the LC-BOCDA system using the differential measurement scheme. PM: phase modulator.

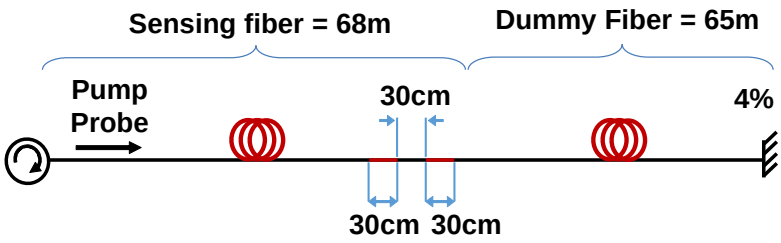

Figure 7.10: Scheme of the 68-m length sensing fiber where two test strained sections of 30 cm were deployed and dummy fiber.

deployed near the end of the sensing fiber as shown in Fig. 7.10. After the 68-m length sensing fiber, another 65-m-length dummy fiber was deployed to overcome the second problem that arises from the spectral overlap of pump and probe waves, the beat noise, as mentioned before. Then, at the far end of the dummy loop, the fiber was cleaved to induce a weak reflection to the sensing signal.

After the propagation of the optical signals along the sensing fiber, a FBG was used to suppress the ASE and reduce the pump wave component prior to detection in a 125 MHz bandwidth PD and further processing in a LIA and acquisition in a scope. For the acquisition of the BGS at every position of the fiber, the differential measurement technique was applied, which is based on detecting the amplitude difference of the probe wave signal with the phase modulation switched on and off [76]. The amplitude of the probe wave signal for the different positions in the sensing fiber was measured by sweeping the frequency difference from 10.3 to 11.3 GHz around the BFS of the fiber, which was around 10.8 GHz. The RF sweeping time for a single polarization state at a certain position was 0.1 s.

Figure 7.11 depicts the spectra of the optical waves before and after the optical filter in the detector for the dual-probe LC-BOCDA with $\Delta f = 9$ GHz. Note that the higher-frequency sideband of the dual-probe wave spectrum is almost completely suppressed by the FBG, so that, its contribution to the detected signal becomes negligible. On the contrary, the pump wave cannot be completely filtered out because part of its spectral components overlap with the probe wave and lie within the FBG bandwidth. Hence, part of the pump wave signal is detected and it is added to the detected probe signal, leading to its corruption.

7.4.2. Control of the CP order to cancel the beat noise

Figure 7.12 displays the fundamentals of the correlation order method devised to avoid the detrimental effects caused by the interference between the detected probe and pump

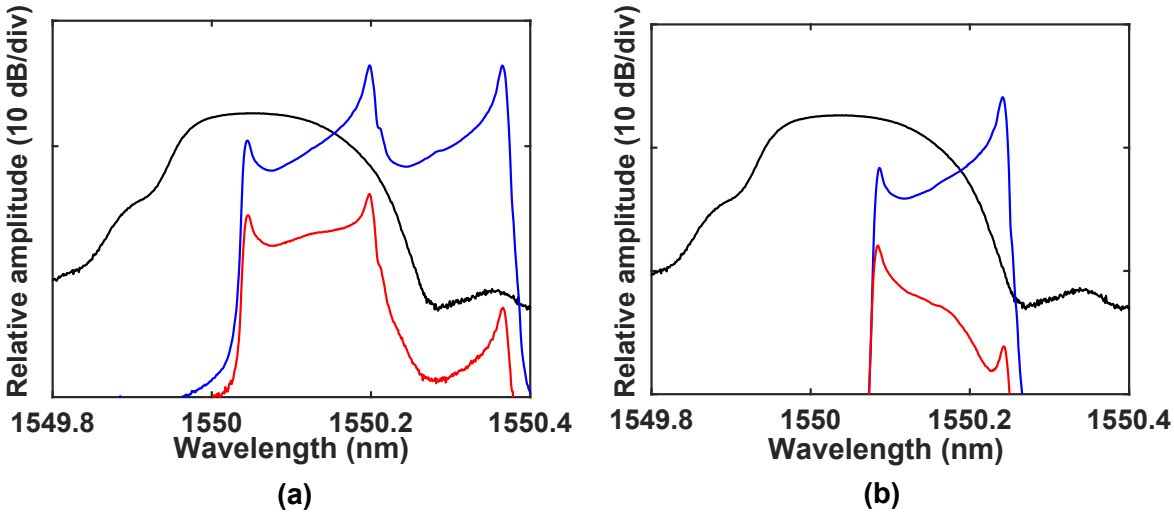

Figure 7.11: Optical spectra of the (a) dual-probe and (b) pump waves before (blue line) and after (red line) optical filtering for $\Delta f = 9$ GHz. The transfer function of the FBG is also highlighted (black line).

waves in the PD. The correlation order technique should satisfy the condition stated in Eq. (7.5). To fulfill this requirement, it is necessary to connect a dummy fiber of approximately similar length to the sensing fiber, in this case 65 m length, to the end of the current sensing fiber. Then, the order of the CP should be adjusted to avoid the beat noise. Notice that, in Eq. (7.5), it is possible to keep the same correlation order, m, while sweeping the position x of the sensing fiber by varying the phase difference, $\Delta\phi$, within the limits imposed by $\pm\Delta\theta$; i.e. tuning of f_m according to Eq. (7.3). However, when the position x is further shifted and $\Delta\phi$ exceeds the limit of phase margin, $\Delta\theta$, it is required to change the order of CP by ± 1 to satisfy Eq. (7.5). Following this procedure, a continuous fiber position sweep is attained without experience any beat noise. Note that, for a PD with 125 MHz bandwidth and a modulation frequency equal to $\nu_B = 10.8$ GHz, the margin is about $\pm\pi/3$, and becomes larger as Δf decreases.

Let's consider the example of Fig. 7.12 (a), where f_{m1} represents the modulation frequency that has to be deployed to measure the position P_1 is the fiber. This particular f_m, has associated a certain correlation order, m, based on Eq. (7.5). Notice that, in this case, the phase difference between the incoming and outgoing waves is zero as the round trip path length is equal to 2π, shown in red solid lines. If the position to be measured is shifted to P_2, the value of f_m must be changed, and thus, the phase difference between the two waves changes, as shown with red dashed lines. In this particular situation, if $\Delta\phi$ exceeds $\pm\pi/3$, as in Fig. 7.12 (a), the beating frequency will lie within the PD bandwidth and beat noise will appear with the detected probe wave. On the contrary, if the correlation order control method is employed, as shown in Fig. 7.12 (b), the distance

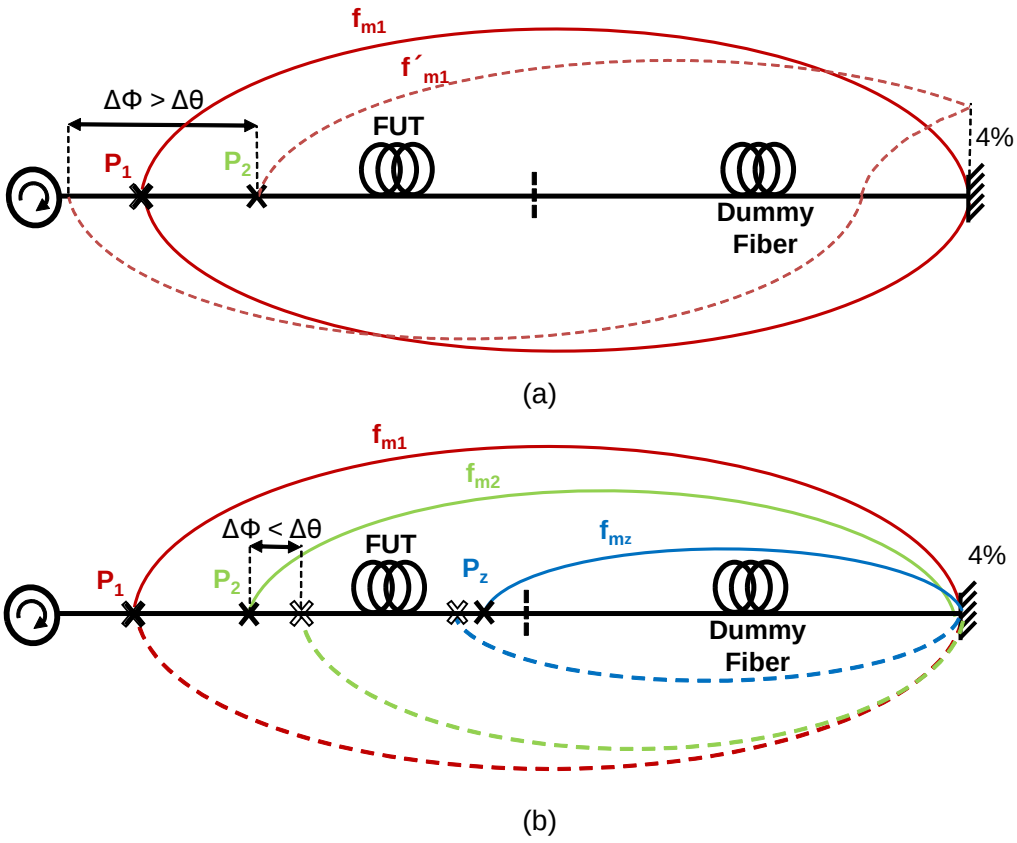

Figure 7.12: Correlation order adjustment during the CP order control process.

between CPs is reduced and the f_{m2} can be recalculated to adjust the CP to the measuring position P_2 maintaining $\Delta\phi$ withing the margin and allowing to retrieve the BGS signal without beating noise.

In our test measurement, a total fiber length of $L = 133$ m was deployed, including the 65-m length of dummy fiber. So, in order to obtain a continuous scan of all the sensing positions, from $x = 0$ to $x = 68$, the order of CP was varied from 16 to 25.

Figure 7.13 depicts a sample BGS measurements when the sensing position in the sensing fiber was scanned with 15 cm steps. Severe interference can be appreciated for the conventional measurement technique when the correlation order control technique is not applied. In contrast, a complete cancellation of this impairment is achieved when the proposed method for simultaneous control of f_m and the CP order is used.

7.4.3. Experimental measurements

In order to validate the proposed method, measurements using either, single or the dual-probe wave LC-BOCDA sensor configuration were performed to compare both setups and demonstrate the benefits of the latter. Fig. 7.14 shows the normalized gain spectra

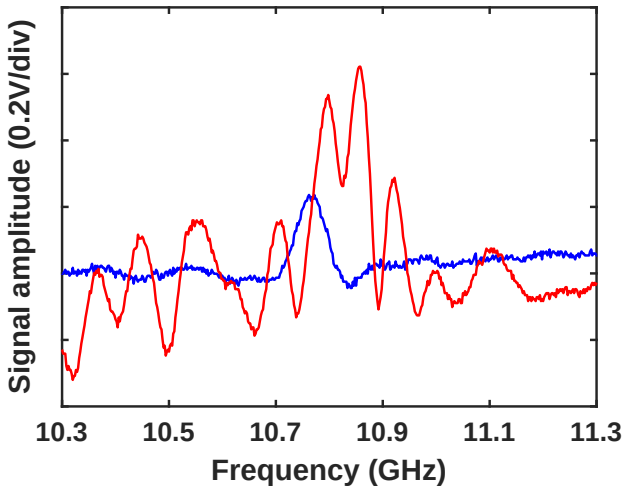

Figure 7.13: (a) Sensing fiber scanning procedure when the method for simultaneous control of the CP order and the modulation frequency is not deployed (b) and when it is deployed.

acquired using the single-probe configuration, where the first problem brought by the spectral overlap between pump and probe, the generation of a ghost peak, is highlighted. The output signal of the BOCDA system was acquired and normalized when the CP was located in one of the strained sections for Δf equal to 5 GHz, 7 GHz and 9 GHz. As a result, multiple gain peaks are simultaneously observed in the measurement. For instance, the higher-frequency main peak, is the result of the SBS interaction that occurs at the CP position where the strain was applied. This Brillouin gain is generated by the interaction between the outgoing pump and the incoming probe wave. A second lower-frequency peak (ghost peak), appears as a result of the interaction between the incoming pump and the outgoing probe. This secondary BGS peak is centered in a different frequency because this CP is located in a fiber position where strain was not applied, so, the BFS observed is different.

Particularly, the ghost peak is caused by the depletion that the high power probe wave induces on the counter-propagating pump wave. Its amplitude is dependent on the amount of the frequency overlap. This means that the larger the frequency overlap, the bigger the ghost peak amplitude detected, as shown in Fig. 7.14. This confirms that the conventional single-probe LC-BOCDA is not tolerant to the spectral overlap of the pump and probe waves. And hence, it is severely limited in terms of the maximum Δf that can be deployed.

Observe that, apart from the two main peaks, there are additional side lobes in the measured spectra. These undesired gain contributions are due to the intrinsic shape of the BGS when the differential measurement technique is deployed [76]. The amplitude of

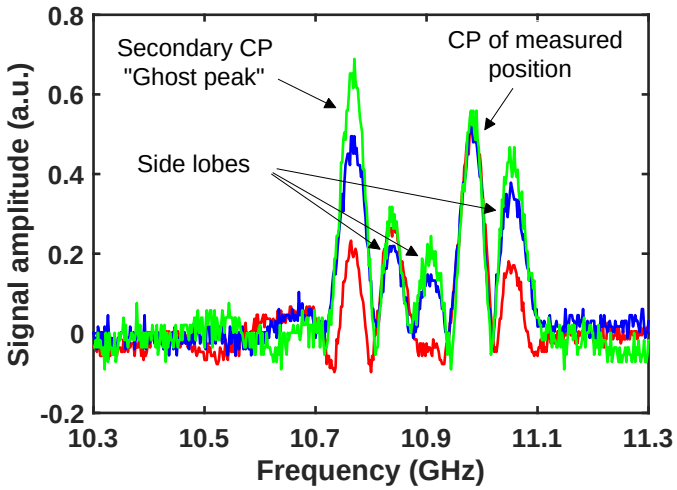

Figure 7.14: BGS measured using single-probe wave configuration for different Δf of 5 GHz (red line), 7 GHz (blue line) and 9 GHz (green line).

these side lobes is always lower than the main peaks, therefore, they do not significantly perturb the determination of the BFS measurement. Notice that, even when there is no overlap between probe and pump, for Δf= 5 GHz, a small ghost peak was detected simultaneously to the BGS peak of the CP measured. This is due to the non-ideal filtering of the pump wave by the FBG, which is not selective enough to completely filter out the pump. This means that even if there is no spectral overlap between pump and probe for that Δf, there is still some remaining pump wave reaching the receiver and distorting the measurement.

Finally, note that the amplitude of the ghost peak has the same polarity than the BGS peak generated by the main CP. Actually, it would have been expected to obtain an opposite polarity due to the Brillouin loss experienced by the pump at the second CP. This change of sign is explained by the fact that the LIA was operated in an amplitude mode (or R-mode), which just gives the modulus of the detected signal.

On the contrary, Fig. 7.15 represents the BGS measured when the dual-probe wave configuration is deployed and the same measurement conditions than Fig. 7.14 are tested. Observe that, in contrast to the single-probe configuration, the correct BGS is measured without any additional ghost peak, even when there is a big overlap between the pump and probe waves. As it has been explained in section 7.3, this is possible due to the fact that the proposed dual-probe wave modulation allows compensating the Brillouin loss induced by the lower-frequency sideband of the probe wave. Thanks to the higher-frequency probe wave sideband, an additional SBS interaction takes place at the second CP. Here, the outgoing higher-frequency sideband probe induces Brillouin gain on the incoming pump

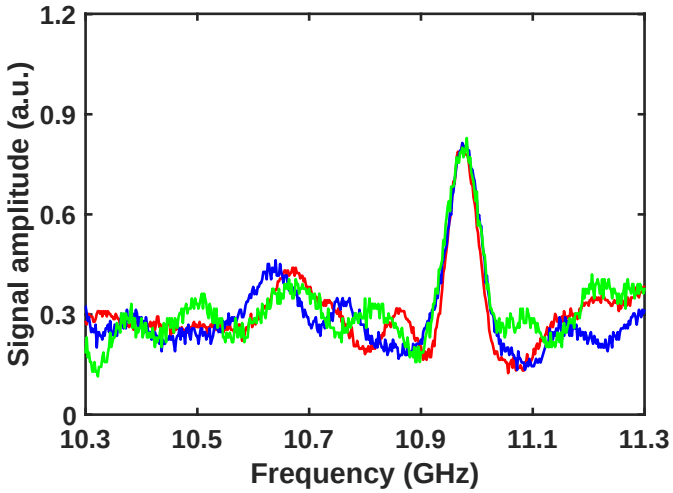

Figure 7.15: BGS measured using dual-probe wave configuration for different Δf of 5 GHz (red line), 7 GHz (blue line) and 9 GHz (green line).

wave. So that, the net Brillouin gain-loss induced in the pump wave is zero and, its amplitude remains invariable, leading to a retrieval of an undistorted BGS even though Δf is $> \nu_B/2$

In order to experimentally validate the proposed enhancement for the LC-BOCDA technique, distributed measurements of the BGS were performed along the sensing fiber. To do this, the modulation frequency of the LD was swept from 0.69 to 1.09 MHz, giving rise to a measurement range d_m equal to 98 m.

Note that, due to different modulation frequency amplitudes were used to compare the performance of both setups, the nominal spatial resolution was also different for each of the situations, giving rise to around 27 cm when $\Delta f = 5$ GHz and 15 cm when $\Delta f = 9$ GHz. Since the spatial resolution deployed for the measurements was different, the amplitude of the detected BGS was also different. Hence, for comparison, all the measured BGS in Fig. 7.14 and Fig. 7.15 were normalized to the amplitude of the BGS peak in the strain section for Δf equal 9 GHz.

Figure 7.16 (a) depicts the peak amplitude of the BGS measured with the conventional single-probe configuration along the sensing fiber distance. As it is observed, the peak amplitude fluctuates depending on the location along the sensing fiber, which is due to the influence of the ghost peak gain contribution. In contrast, when $\Delta f > 5$ GHz, there are significant amplitude fluctuations. Whereas, Fig. 7.16 (b) shows the same measurements when the dual-probe LC-BOCDA configuration is deployed. In this case, the measured BGS amplitude remains fairly stable and the fluctuations are considerably smaller along the fiber thanks to the compensation of the pump wave loss.

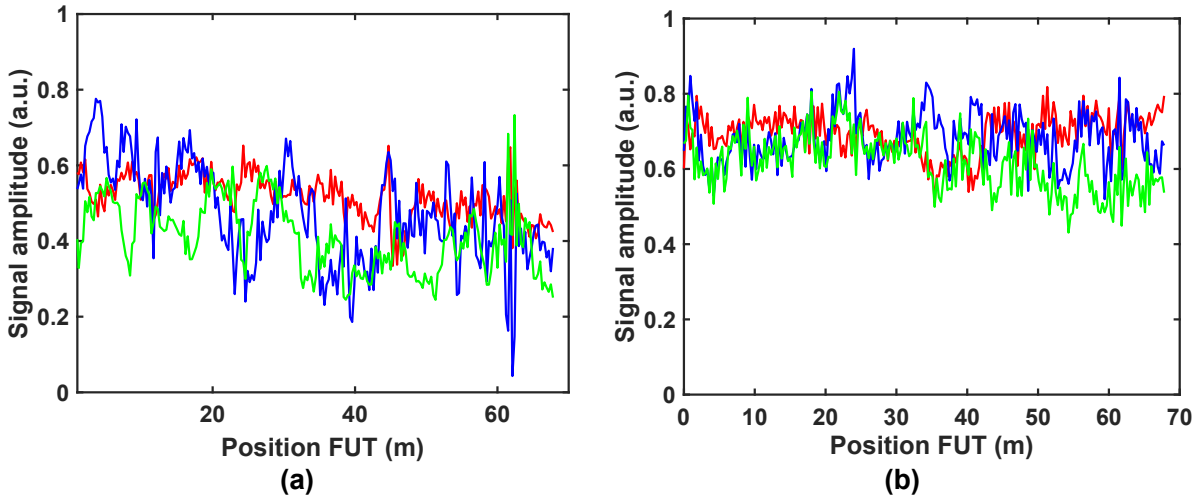

Figure 7.16: BGS amplitude along the sensing fiber using (a) single-probe wave and (b) dual-probe wave scheme for different Δf of 5 GHz (red line), 7 GHz (blue line) and 9 GHz (green line).

The standard deviation, σ_d, of the acquired amplitude of the BGS peak was calculated in both systems, showing a reduction of σ_d when dual-probe wave system was used with modulation amplitudes of 7 and 9 GHz. For instance, when the dual-probe wave configuration is used, σ_d is reduced from 0.13 and 0.09 to 0.07 and 0.075, respectively. In contrast, if the modulation amplitude, Δf, is equal to 5 GHz, σ_d is nearly the same for both systems, 0.06 and 0.054, as expected. For these measurements, the amplitude was also normalized to take into account the change of the spatial resolution due to the different Δf.

Finally, distributed measurements of the BFS were performed along the sensing fiber using both LC-BOCDA setups to experimentally demonstrate the enhanced performance of the proposed technique. In order to calculate the Brillouin frequency for each position of the fiber using the distributed BGS measurements, a Lorentzian profile fit was applied only to the highest peak of the detected signal, as generally adopted in BOCDA systems.

Figure 7.17 (a) shows the resultant distribution of the BFS for the conventional scheme, the single-probe wave. As it is observed, the retrieved BFS of the sensing fiber shows multiple errors in the determination of the BFS when there is a spectral overlap between pump and probe waves, specially for Δf equal to 7 and 9 GHz. These errors, as previously explained, are due to the detrimental effects of the ghost BGS peak, which distorts the real BGS signal. In contrast, if the dual-probe wave scheme is deployed, the BFS is accurately obtained without errors for any Δf, as it is highlighted in Fig. 7.17 (b), confirming that the proposed technique permits to extend Δf over the previous limit, $\nu_B/2$.

Figure 7.18 shows a zoomed view of Fig. 7.17 (b), with the distribution of BFS around

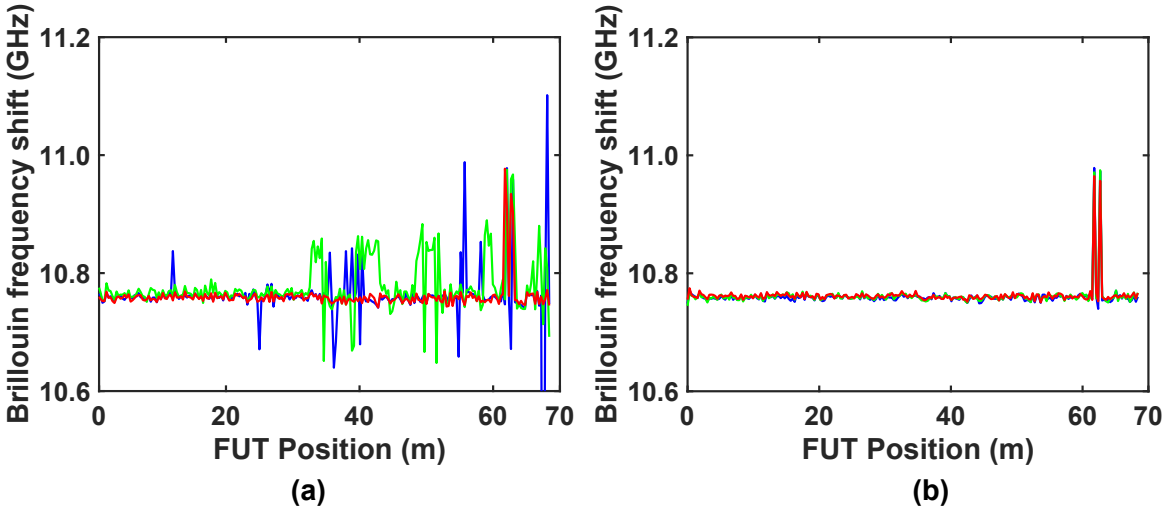

Figure 7.17: Measured BFS along the sensing fiber using (a) single-probe wave and (b) dual-probe wave configuration for different Δf of 5 GHz (red line), 7 GHz (blue line) and 9 GHz (green line).

the strained sections in the sensing fiber, confirming that the applied strain is correctly measured even when Δf equal to 9 GHz is used. A variation of the Brillouin frequency of 197 MHz is observed at the strained sections with Δf of 9 GHz and 203 MHz with 5 GHz and 7 GHz, which matches well with the theoretical value for the applied strain of 4000 $\mu\epsilon$, considering a strain coefficient of $\sim$0.05 MHz/$\mu\epsilon$. The deviation of the strain estimation is within the uncertainty of this type of sensors [85].

Finally, different strain values were applied to the fiber section that was being measured, increasing the strain gradually from 0 to nearly 6000 $\mu\epsilon$. Fig. 7.19 depicts the variation of BFS as a function of the applied strain for the dual-probe LC-BOCDA. As

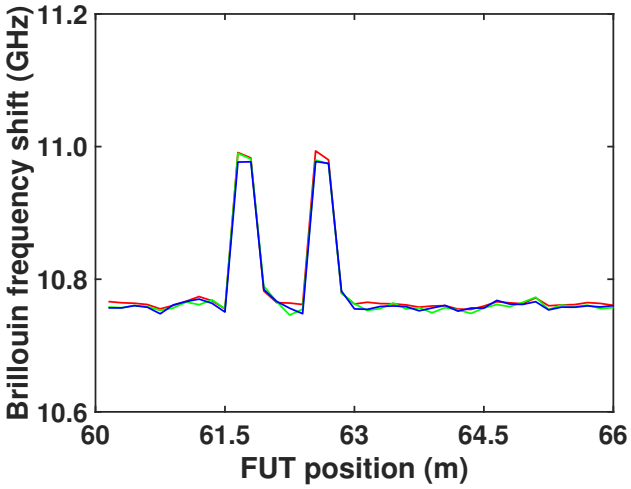

Figure 7.18: Zoomed view of the measured BFS of Fig. 7.17 (b).

it was expected, excellent agreement with the linear dependence is obtained for all Δf.

To conclude, it should be noted that all the experimental results presented in this research were performed using a maximum modulation frequency amplitude of 9 GHz, which is due to two reasons. The first one is the limited selectivity of the FBG available for the experiments, which could not completely filter out the lower probe wave sideband, and, the second one, was the practical limitation of the deployed LD to generate a modulation amplitude beyond 9 GHz.

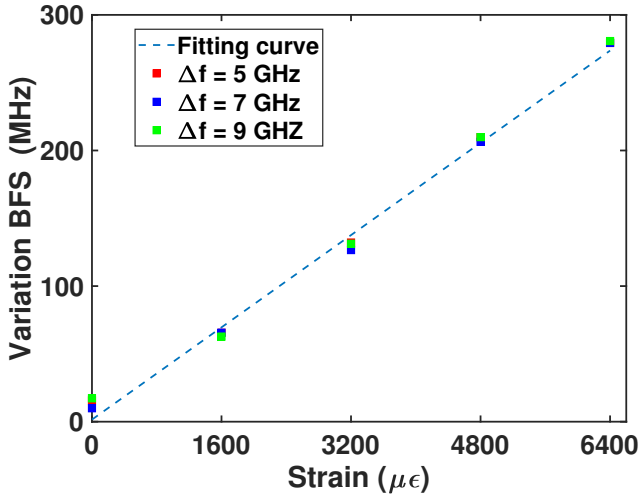

Figure 7.19: Measured BFS (symbols) and fitting curve (blue-dashed line) according to strain measured by the dual-probe wave for different Δf of 5 GHz, 7 GHz and 9 GHz.

7.5. Conclusions

In this chapter of the dissertation, we have studied the limitations of the LC-BOCDA sensor and in particular the limitation imposed by the spectral overlap of the pump and probe wave when the FM of the LD exceeds $\nu_B/2$. It is found that there are two impairments caused by the overlap of the spectra that constrains the performance of LC-BOCDA sensors. The first one is the detection of a second CP due to the Brillouin loss experienced by the pump wave when interacts with the probe. The second problem has been found to be caused by the simultaneous detection of both modulated waves in the PD.

Two complementary solutions are proposed to solve the impairments and mitigate the detrimental effects. These are based on deploying a dual-probe wave and implementing a control of the correlation order. The dual-probe wave configuration, like in its previously use in BOTDA sensors, is deployed for the generation of simultaneous gain and loss

interactions upon the pump to compensate each other and avoid the first of the problems. This makes the pump amplitude to remain unaltered when it meets the outgoing probe in the secondary CP that appears in the sensing fiber due to the reflection of the pump wave at its end. Therefore, no signal is detected from this unwanted interaction even when the spectral overlap between the pump and probe does not allow to filter out the former before detection. Equally, the control of the correlation order ensures that there are not undesirable mixing terms due to the beating of the pump and probe spectral components even in situations in which both waves arrive simultaneously to the receiver.

Finally, experimental measurements are carried out to confirm the proposed enhanced configuration and measuring method. Indeed, it is demonstrated that the proposed technique permits to increase the modulation amplitude from the former limit of 5 GHz to at least 9 GHz, which corresponds to a nearly two-fold enhancement in either the spatial resolution or the number of resolving points in the BOCDA system. The ultimate limit for Δf would be equal to the BFS of the fiber. This limit was not reached in the experiments just due to the FM limitations of the LD and optical filtering limitations.

Lastly, as a result of the research described in this chapter of the dissertation, a paper has been published in the international Jounal of Ligthwave Technology with the manuscript title of: “Dual-probe linearly-configured BOCDA system with enlarged modulation amplitude”, by Mariñelarena et al.

CHAPTER 8

Conclusions and open lines

8.1. Conclusions

In this dissertation different solutions have been presented to contribute with the enhancement and development of DOFS based on SBS. In particular, alternative schemes and measuring methods are proposed to solve impairments that constrain the performance of BOTDA and BOCDA sensors. Moreover, a new measuring system based on deploying a dynamic BOTDA sensor is presented for structural health monitoring of PV solar trackers structures. The conclusions are grouped according to the objectives of the thesis.

Contributions to BOTDA sensors

Two contributions to mitigate the impairments induced in BOTDA sensors are presented. The proposed solutions allow to mitigate the distortion and the measurements experienced in this type of sensors when limited ER pump pulses are deployed in BOTDA sensors and long code sequences are generated in coding techniques.

In chapter 3, a simple technique to reduce the NLE originated by the deployment of pump pulses with limited ER in BOTDA sensors has been presented. The method is based on introducing a wavelength modulation to the common optical source used for the pump and probe waves. This technique has demonstrated that is able to compensate the different types of NLE related to the ER of the pump pulses. In particular, it is found that the NLE originated by the distortion of the measured probe gain due to

the increment depletion of the trailing pedestal of the pump pulse caused by the probe wavefronts that have been previously amplified by the pump pulse are compensated. It is demonstrated that the proposed method mitigates and nearly cancel the distortion of the measured probe gain originated by the distorted trailing pedestal of the pulse by due to the transient response of the EDFA. In addition, it is experimentally proved that this technique solves first and second-order NLE. In summary, the presented technique allows to compensate all NLE and, moreover, it increases the Brillouin threshold. All of this is achieved with very little complexity added to the dual-probe wave setup, simplifying the deployment of this method. It has been also found that this technique allows to deploy MZ-EOM for high resolution measurements without undergoing the constraints induced by ER-related NLE.

In chapter 4, a solution has been presented for the BOTDA sensors that deploy coding techniques, which undergo nonlinear amplification when long sequences of pulses are generated to interact with the probe. It is based on a simple post-processing calculation applied to the detected probe signal. It has been demonstrated to compensate the nonlinearity observed when long codes are generated. Experiments performed along 200-km length sensing fiber proved the correct linearization. The distortion observed in the detected signal and subsequently decoded BGS is canceled and the measurement errors are mitigated. In summary, this contribution allows to optimize the pump power entering the sensing fiber without experiencing nonlinear amplification, and hence, improve the SNR and performance of BOTDA sensors. Is is demonstrated that the deployment of the dithering technique along with the proposed linearization process alleviate and cancel the two most important impairments of BOTDA systems that use coding techniques: the depletion of the pump pulses and the nonlinear amplification. The proposed solution can be applied in any BOTDA sensor that deploys other coding methods.

Contributions to D-BOTDA sensors

It is found that the RF phase-shift spectrum measured in D-BOTDA sensors depends on large Brillouin gain variations. The spectrum shows a narrowing effect when the Brillouin gain is highly increased. It is found that this dependence is less significant than the one observed in conventional direct-detection BOTDA sensors, where the gain spectrum broadens with the increasing gain. From this research work, we conclude that the measurement errors induced in dynamic measurements are dependent on the pump pulse duration and on the detuning frequency between the probe frequency and the BFS of the fiber. An important consideration concerning the measurement errors is that they

are only significant when large pump power is deployed, appearing indeed, only for short lengths of fiber, because for longer lengths, nonlinear effects such as MI, SPM are more limiting. Therefore, it is demonstrated that D-BOTDA sensors are tolerant to Brillouin gain variations to some extent, being only deleterious for very large gains.

The dynamic range of D-BOTDA sensors limits the practical applicability of these sensors due to the fact that many structural health monitoring measurements require the monitoring of large strain variations. Two different solutions have been presented and experimental measurements have demonstrated a threefold to fourfold enhancement of the previous dynamic range in D-BOTDA. In addition, it has been found that both methods display a power penalty of the same order, but with different origins. The improvement of the proposed techniques are mostly limited by the practical implementation of the electronic circuits involved in generating the microwave pulses. One of the proposed methods is based on deploying short-length of pulses, which has demonstrated a slightly better linearity and performance than the one based on the multi-component pump method. Moreover, we have found that the former provides higher spatial resolution with very little complexity added to the setup. Overall, both techniques have demonstrated to successfully extend the dynamic range being suitable for multitude of application that monitor large strain and vibrations in short length of fibers.

Contributions to BOCDA sensors

In chapter 7, the limitations faced by LC-BOCDA sensors when the FM amplitude of the LD is increased over the limit $\nu_B/2$ is investigated. It has been found that the spectral overlap between the probe and the pump waves generates two deleterious effects in the measurements that distort the detected signal and induce errors. The first one is the detection of a second CP due to the Brillouin loss experienced by the pump wave when interacts with the probe. The second problem has been found to be caused by the simultaneous detection of both modulated waves in the PD.

We have contribute to the enhancement of this technique by developing an alternative scheme and measuring method that mitigates the detrimental effects when larger Δf is deployed. A dual-probe wave LC-BOCDA sensor configuration has been proposed to compensate the impairment caused by the Brillouin loss interaction induced over the pump wave. It has been found that the correlation order needs to be controlled during the scanning process to avoid the beating frequency between the probe and pump waves detected simultaneously at the PD. Experimental measurements are carried out to confirm the proposed enhanced configuration and measuring method. With all these findings, the

proposed solution has demonstrated to nearly double the FM amplitude of LC-BOCDA, allowing to extend the number of resolving points in this type of BOCDA sensor.

Deployment of DOFS for structural health monitoring

Finally, a practical implementation of a D-BOTDA sensor to monitor the effects of wind in PV solar trackers has been accomplished. During this research, it has been found the dynamic monitoring of solar tracker structures is very important important to prevent them from collapses and damages. It is demonstrated a measuring method that is able, for the first time, to perform distributed measurements of the bending and torsional strain along a large structure. Dynamic torsional and bending moments can be obtained from the devised measuring system to improve and complement mechanical studies of the structures. The results retrieved from the proposed measuring system will allow to enhance the structural designs of solar trackers for the aeroelastic instability events. It has been found the possibility of performing bending and torsional strain measurements tolerant to common mode effects, such as temperature variations. In case of torsional measurements, the measuring system is, in addition, tolerant to simultaneous bending effects. This contribution demonstrates the capability of BOTDA sensors and, in particular, of the D-BOTDA sensors of performing distributed and dynamic measurements of strain in novel applications to complement the current monitoring methods.

8.2. Open lines

The following lines introduce the open research fields from the work carried out during this dissertation.

As it has been stated, NLE are one of the most important and limiting effects in BOTDA sensors and the proposed dithering method has demonstrated an important solution to all of them, in particular, to that one related to limited ER pump pulses. A significant enhancement has been demonstrated when limited-ER MZ-EOM are deployed, but further research should be focused on analyzing if ER-related NLE may be also significant even when using other high-ER devices. For instance SOAs, in such situations as ultra long range links or when deploying pulse coding techniques in which a large number of pulses are simultaneously launched into the fiber. Thus, it is of paramount importance that future research lines focuses on deploying this method in alternative schemes to reach the ultimate performance of BOTDA sensors.

A linearization technique proposed to solve the nonlinear amplification in coding tech-

niques has been successfully demonstrated within this thesis. Future work in this line can be carried out to reach the full potential of this methods technique in terms of measurement range, exploring different ways of deploying additional methods to obtain flat amplitude pulses at the output of the EDFA.

Dynamic measurements performed with BOTDA sensors is a promising field, as there are increasing number of industries that require DOFS for monitoring their assets. Since the research accomplished in this thesis has allowed to determined the error experienced when large pump power is deployed, further research work could be done to implement a calibration method to allow the compensation of this error by characterizing the measurement error. This would provide a further improvement in dynamic measurements. It should be study as well the combination of the two proposed techniques to extend the dynamic range to find a further enhancement to the D-BOTDA sensor performance.

Bibliography

[1] A. Hartog, "A distributed temperature sensor based on liquid-core optical fibers," *Journal of Lightwave Technology*, vol. 1, no. 3, pp. 498–509, Sep. 1983.

[2] A. H. Hartog, *An introduction to distributed optical fibre sensors*. CRC Press, 2017.

[3] R. Boyd, *Nonlinear Optics*, 3rd ed. Academic Press, 2007.

[4] K. Hotate, "Brillouin Optical Correlation-Domain Technologies Based on Synthesis of Optical Coherence Function as Fiber Optic Nerve Systems for Structural Health Monitoring," *Applied Sciences*, vol. 9, no. 1, p. 187, 2019.

[5] G. P. Agrawal, *Nonlinear Fiber Optics*, 5th ed. Academic Press, 2013.

[6] T. R. Parker, M. Farhadiroushan, R. Feced, V. A. Handerek, and A. J. Rogers, "Simultaneous distributed measurement of strain and temperature from noise-initiated brillouin scattering in optical fibers," *IEEE Journal of Quantum Electronics*, vol. 34, no. 4, pp. 645–659, April 1998.

[7] W. Zou, Z. He, and K. Hotate, "Investigation of Strain and Temperature Dependences of Brillouin Frequency Shifts in GeO_2 -Doped Optical Fibers," *Journal of Lightwave Technology*, vol. 26, no. 13, pp. 1854–1861, 2008.

[8] T. Horiguchi, T. Kurashima, and M. Tateda, "Tensile strain dependence of Brillouin frequency shift in silica optical fibers," *IEEE Photonics Technology Letters*, vol. 1, no. 5, pp. 107–108, 1989.

[9] T. Kurashima, T. Horiguchi, and M. Tateda, "Thermal effects of Brillouin gain spectra in single-mode fibers," *IEEE Photonics Technology Letters*, vol. 2, no. 10, pp. 718–720, 1990.

[10] ——, "Distributed-temperature sensing using stimulated Brillouin scattering in optical silica fibers," *Optics Letters*, vol. 15, no. 18, pp. 1038–1040, 1990.

[11] T. Horiguchi and M. Tateda, "BOTDA-nondestructive measurement of single-mode optical fiber attenuation characteristics using Brillouin interaction: theory," *Journal of Lightwave Technology*, vol. 7, no. 8, pp. 1170–1176, Aug 1989.

[12] A. Barrias, J. Casas, and S. Villalba, "A review of distributed optical fiber sensors for civil engineering applications," *Sensors (Switzerland)*, vol. 16, no. 5, 2016.

[13] A. Minardo, G. Porcaro, D. Giannetta, R. Bernini, and L. Zeni, "Real-time monitoring of railway traffic using slope-assisted Brillouin distributed sensors," *Applied Optics*, vol. 52, no. 16, pp. 3770–3776, 2013.

[14] M. Iten and A. Puzrin, "Botda road-embedded strain sensing system for landslide boundary localization," *SPIE Smart Sensor Phenomena, Technology, Networks, and Systems*, vol. 7293, 03 2009.

[15] *Streicker Bridge: a comparison between Bragg-grating long-gauge strain and temperature sensors and Brillouin scattering-based distributed strain and temperature sensors*, vol. 7981, 2011.

[16] T. Horiguchi, T. Kurashima, and M. Tateda, "A technique to measure distributed strain in optical fibers," *IEEE Photonics Technology Letters*, vol. 2, no. 5, pp. 352–354, May 1990.

[17] T. Horiguchi, K. Shimizu, T. Kurashima, M. Tateda, and Y. Koyamada, "Development of a Distributed Sensing Technique Using Brillouin Scattering," *Journal of Lightwave Technology*, vol. 13, no. 7, pp. 1296–1302, 1995.

[18] X. Bao, D. J. Webb, and D. A. Jackson, "32-km distributed temperature sensor based on Brillouin loss in an optical fiber," *Optics Letters*, vol. 18, no. 18, pp. 1561–1563, Sep 1993.

[19] M. A. Soto and L. Thévenaz, "Modeling and evaluating the performance of Brillouin distributed optical fiber sensors," *Optics Express*, vol. 21, no. 25, pp. 31 347–31 366, Dec 2013.

[20] R. Bernini, A. Minardo, and L. Zeni, "Dynamic strain measurement in optical fibers by stimulated Brillouin scattering," *Optics Letters*, vol. 34, no. 17, pp. 2613–2615, Sep. 2009.

[21] Y. Peled, A. Motil, L. Yaron, and M. Tur, "Slope-assisted fast distributed sensing in optical fibers with arbitrary Brillouin profile," *Optics Express*, vol. 19, no. 21, pp. 19 845–19 854, Sep. 2011.

[22] A. Motil, O. Danon, Y. Peled, and M. Tur, "Pump-power-independent double slope-assisted distributed and fast Brillouin fiber-optic sensor," *IEEE Photonics Technology Letters*, vol. 26, no. 8, pp. 797–800, Apr. 2014.

[23] A. Motil, A. Bergman, and M. Tur, "[invited] state of the art of brillouin fiber-optic distributed sensing," *Optics Laser Technology*, vol. 78, pp. 81 – 103, 2016, the year of light: optical fiber sensors and laser material processing. [Online]. Available: http://www.sciencedirect.com/science/article/pii/S0030399215002571

[24] X. Bao, J. Dhliwayo, N. Heron, D. J. Webb, and D. A. Jackson, "Experimental and theoretical studies on a distributed temperature sensor based on brillouin scattering," *Journal of Lightwave Technology*, vol. 13, no. 7, pp. 1340–1348, July 1995.

[25] C. L. Tang, "Saturation and spectral characteristics of the stokes emission in the stimulated brillouin process," *Journal of Applied Physics*, vol. 37, pp. 2945 – 2955, 08 1966.

[26] A. Zornoza, M. Sagues, and A. Loayssa, "Self-heterodyne detection for SNR improvement and distributed phase-shift measurements in BOTDA," *Journal of Lightwave Technology*, vol. 30, no. 8, pp. 1066–1072, 2012.

[27] J. Urricelqui, A. Zornoza, M. Sagues, and A. Loayssa, "Dynamic BOTDA measurements based on Brillouin phase-shift and RF demodulation," *Optics Express*, vol. 20, no. 24, pp. 26 942–26 949, 2012.

[28] J. Urricelqui, M. Sagues, and A. Loayssa, "BOTDA measurements tolerant to non-local effects by using a phase-modulated probe wave and RF demodulation," *Optics Express*, vol. 21, no. 14, pp. 17 186–17 194, 2013.

[29] L. Thévenaz, S. F. Mafang, and J. Lin, "Effect of pulse depletion in a Brillouin optical time-domain analysis system," *Optics Express*, vol. 21, no. 12, pp. 14 017–14 035, 2013.

[30] H. Iribas, J. Urricelqui, J. J. Mompó, J. Mariñelarena, and A. Loayssa, "Non-local effects in brillouin optical time-domain analysis sensors," *Applied Sciences*, vol. 7, no. 8, 2017.

[31] T. Shimizu, K. Nakajima, K. Shiraki, K. Ieda, and I. Sankawa, "Evaluation methods and requirements for the stimulated brillouin scattering threshold in a single-mode fiber," *Optical Fiber Technology*, vol. 14, no. 1, pp. 10 – 15, 2008.

[32] A. Domínguez-López, X. Angulo-Vinuesa, A. López-Gil, S. Martín-López, and M. González-Herráez, "Non-local effects in dual-probe-sideband Brillouin optical time domain analysis," *Optics Express*, vol. 23, no. 8, pp. 10 341–10 352, 2015.

[33] J. Urricelqui, M. Alem, M. Sagues, L. Thévenaz, A. Loayssa, and M. Soto, "Mitigation of modulation instability in Brillouin distributed fiber sensors by using orthogonal polarization pulses," in *Proceedings of SPIE*, vol. 9634, Oct. 2015, pp. 1–4.

[34] H. Iribas, J. Mariñelarena, C. Feng, J. Urricelqui, T. Schneider, and A. Loayssa, "Effects of pump pulse extinction ratio in Brillouin optical time-domain analysis sensors," *Optics Express*, vol. 25, no. 22, pp. 27 896–27 912, 2017.

[35] A. David and M. Horowitz., "Low-frequency transmitted intensity noise induced by stimulated brillouin scattering in optical fibers," *Optics Express*, vol. 12, no. 19, p. 11792–11803, 2011.

[36] M. Alem, M. A. Soto, and L. Thévenaz, "Analytical model and experimental verification of the critical power for modulation instability in optical fibers," *Optics Express*, vol. 23, no. 23, pp. 29 514–29 532, Nov 2015.

[37] D. Alasia, M. G. Herraez, L. Abrardi, S. Martin-Lopez, and L. Thevenaz, "Detrimental effect of modulation instability on distributed optical fiber sensors using stimulated brillouin scattering," in *Proceedings of SPIE*, vol. 5855, 2005.

[38] L. T. Stella M. Foaleng, "Impact of raman scattering and modulation instability on the performances of brillouin sensors," vol. 7753, 2011.

[39] M. N. Alahbabi, Y. T. Cho, T. P. Newson, P. C. Wait, and A. H. Hartog, "Influence of modulation instability on distributed optical fiber sensors based on spontaneous brillouin scattering," *J. Opt. Soc. Am. B*, vol. 21, no. 6, pp. 1156–1160, Jun 2004.

[40] M. Soto, M. Alem, W. Chen, and L. Thévenaz, "Mitigating modulation instability in Brillouin distributed fibre sensors," vol. 8794, 2013, p. 87943J.

[41] K. Wu, J. Li, Y. Zhang, W. Dong, X. Zhang, and W. Chen, "Multiple microwave frequencies measurement based on stimulated brillouin scattering with ultra-wide range," *Optik - International Journal for Light and Electron Optics*, vol. 126, no. 19, pp. 1935 – 1940, 2015.

[42] S. M. Foaleng, F. Rodríguez-Barrios, S. Martin-Lopez, M. González-Herráez, and L. Thévenaz, "Detrimental effect of self-phase modulation on the performance of Brillouin distributed fiber sensors," *Optics Letters*, vol. 36, no. 2, pp. 97–99, Jan 2011.

[43] W. Li, X. Bao, Y. Li, and L. Chen, "Differential pulse-width pair BOTDA for high spatial resolution sensing," *Optics Express*, vol. 16, no. 26, pp. 21 616–21 625, 2008.

[44] Y. Dong, L. Chen, and X. Bao, "Extending the Sensing Range of Brillouin Optical Time-Domain Analysis Combining Frequency-Division Multiplexing and In-Line EDFAs," *J. Lightwave Technol.*, vol. 30, no. 8, pp. 1161–1167, Apr 2012.

[45] Z. Yang, M. A. Soto, and L. Thévenaz, "Increasing robustness of bipolar pulse coding in Brillouin distributed fiber sensors," *Optics Express*, vol. 24, no. 1, pp. 586–597, Jan 2016.

[46] X. Angulo-Vinuesa, S. Martin-Lopez, J. N. no, P. Corredera, J. D. A.-C. non, L. Thévenaz, and M. González-Herráez, "Raman-Assisted Brillouin Distributed Temperature Sensor Over 100 km Featuring 2 m Resolution and 1.2 C Uncertainty," *J. Lightwave Technol.*, vol. 30, no. 8, pp. 1060–1065, Apr 2012.

[47] M. Soto, G. Bolognini, and F. Di Pasquale, "Optimization of long-range BOTDA sensors with high resolution using first-order bi-directional Raman amplification," *Optics Express*, vol. 19, no. 5, pp. 4444–4457, 2011.

[48] S. Martin-Lopez, M. Alcon-Camas, F. Rodriguez, P. Corredera, J. Ania-Castañon, L. Thévenaz, and M. Gonzalez-Herraez, "Brillouin optical time-domain analysis assisted by second-order Raman amplification," *Optics Express*, vol. 18, no. 18, pp. 18 769–18 778, 2010.

[49] J. Urricelqui, M. Sagues, and A. Loayssa, "Brillouin optical time-domain analysis sensor assisted by Brillouin distributed amplification of pump pulses," *Optics Express*, vol. 23, no. 23, pp. 30 448–30 458, Nov 2015.

[50] J. J. Mompó, J. Urricelqui, and A. Loayssa, "Brillouin optical time-domain analysis sensor with pump pulse amplification," *Optics Express*, vol. 24, no. 12, pp. 12 672–12 681, Jun 2016.

[51] X.-H. Jia, H.-Q. Chang, L. Ao, X.-L. Ji, C. Xu, and W.-L. Zhang, "BOTDA sensors enhanced using high-efficiency second-order distributed Brillouin amplification," *Optics Express*, vol. 24, no. 13, pp. 14 079–14 085, 2016.

[52] M. A. Soto, G. Bolognini, F. D. Pasquale, and L. Thévenaz, "Long-range Brillouin optical time-domain analysis sensor employing pulse coding techniques," *Measurement Science and Technology*, vol. 21, no. 9, p. 094024, 2010.

[53] M. Taki, Y. Muanenda, C. J. Oton, T. Nannipieri, A. Signorini, and F. D. Pasquale, "Cyclic pulse coding for fast BOTDA fiber sensors," *Optics Letters*, vol. 38, no. 15, pp. 2877–2880, Aug 2013.

[54] S. L. Floch, F. Sauser, M. Llera, and E. Rochat, "Novel Brillouin Optical Time-Domain Analyzer for Extreme Sensing Range Using High-Power Flat Frequency-Coded Pump Pulses," *Journal of Lightwave Technology*, vol. 33, no. 12, pp. 2623–2627, June 2015.

[55] S. Le Floch, F. Sauser, M. Llera, and E. Rochat, "Colour cyclic code for Brillouin distributed sensors," in *Proceedings of SPIE*, vol. 9634, 2015, pp. 963 431–963 431–4.

[56] H. Iribas, A. Loayssa, F. Sauser, M. Llera, and S. L. Floch, "Cyclic coding for brillouin optical time-domain analyzers using probe dithering," *Optics Express*, vol. 25, no. 8, pp. 8787–8800, Apr 2017.

[57] H. Iribas, "Contribution to the advancement of brillouin optical time-domain analysis sensors," *Thesis dissertation from Universidad Pública de Navarra*, 2018.

[58] D. Cotter, "Stimulated Brillouin Scattering in Monomode Optical Fiber," *Journal of Optical Communications*, vol. 4, no. 1, pp. 10–19, 1983.

[59] X. Bao, A. Brown, M. DeMerchant, and J. Smith, "Characterization of the Brillouin-loss spectrum of single-mode fibers by use of very short (¡10-ns) pulses," *Optics Letters*, vol. 24, no. 8, pp. 510–512, 1999.

[60] A. Brown, B. Colpitts, and K. Brown, "Distributed sensor based on dark-pulse Brillouin scattering," *IEEE Photonics Technology Letters*, vol. 17, no. 7, pp. 1501–1503, 2005.

[61] K. Kishida and C.-H. Li, "Pulse Pre-Pump-BOTDA technology for new generation of distributed strain measuring system," *Structural Health Monitoring and Intelligent Infrastructure, SHMII 2005*, vol. 1, pp. 471–477, 2006.

[62] Q. Cui, S. Pamukcu, W. Xiao, and M. Pervizpour, "Truly distributed fiber vibration sensor using pulse base BOTDA with wide dynamic range," *IEEE Photonics Technology Letters*, vol. 23, no. 24, pp. 1887–1889, Dec 2011.

[63] Y. Peled, A. Motil, and M. Tur, "Fast Brillouin optical time domain analysis for dynamic sensing," *Optics Express*, vol. 20, no. 8, pp. 8584–8591, Apr. 2012.

[64] A. Voskoboinik, O. Yilmaz, A. Willner, and M. Tur, "Sweep-free distributed Brillouin time-domain analyzer (SF-BOTDA)," *Optics Express*, vol. 19, no. 26, pp. B842–B847, 2011.

[65] J. Fang, P. Xu, Y. Dong, and W. Shieh, "Single-shot distributed Brillouin optical time domain analyzer," *Optics Express*, vol. 25, no. 13, pp. 15 188–15 198, 2017.

[66] K. Hotate, "Measurement of Brillouin gain spectrum distribution along an optical fiber using a correlation-based technique -proposal, experiment and simulation-." *IEICE Transactions on Electronics*, vol. E83-C, no. 3, pp. 405–411, 2000.

[67] *A correlation-based continuous-wave technique for measuring Brillouin gain spectrum distribution along an optical fiber with centimeter-order spatial resolution*, vol. 4185, 2000.

[68] Y. Kohno, M. Kishi, and K. Hotate, "Performance improvement in high-speed random accessibility of brillouin optical correlation domain analysis," in *Proceedings of the Sixth EuropeanWorkshop on Optical Fibre Sensors (EWOFS'2016), Limerick, Ireland*, vol. 9916, 31 May–3 2016, p. pp. 991630:1–991630:4.

[69] M. Tanaka and K. Hotate, "Application of correlation-based continuous-wave technique for fiber brillouin sensing to measurement of strain distribution on a small size material," *IEEE Photonics Technology Letters*, vol. 14, no. 5, pp. 675–677, May 2002.

[70] S. Ong, H. Kumagai, H. Iwaki, and K. Hotate, "Crack detection in concrete using a brillouin optical correlation domain analysis based fiber optic distributed strain sensor," in *Proceedings of the 16th International Conference on Optical Fiber Sensors (OFS-16), Nara Japan*, Oct 2003, pp. We–3.

[71] M. Imai, R. Nakano, T. Kono, T. Ichinomiya, S. Miura, and M. Mure, "Crack detection application for fiber reinforced concrete using bocda-based optical fiber strain sensor," *Journal of Structural Engineering*, vol. 136, no. 8, pp. 1001–1008, 2010.

[72] S. Ong, ., M. Imai, Y. Sako, Y. Miyamoto, S. Miura, and K. Hotate, "Dynamic strain measurement and damage assessment of a building model using a brillouin optical correlation domain analysis based distributed strain sensor," in *Proceedings of the 16th International Conference on Optical Fiber Sensors (OFS-16), Nara Japan*, Oct 2003, pp. We–2.

[73] Y. Kumagai, S. Matsuura, S. Adachi, and K. Hotate, "Enhancement of bocda system for aircraft health monitoring," in *2008 SICE Annual Conference*, Aug 2008, pp. 2184–2187.

[74] T. Yari, K. Nagai, M. Ishioka, K. Hotate, and Y. Koshioka, "Aircraft structural health monitoring using on-board bocda system," in *Proceedings of the 15th Annual International Symposium on Smart Structures and Materials and Nondestructive Evaluation and Health Monitoring, San Diego, CA, USA,*, vol. 6933, 2008.

[75] K. Y. Song, Z. He, and K. Hotate, "Effects of intensity modulation of light source on brillouin optical correlation domain analysis," *Journal of Lightwave Technology*, vol. 25, no. 5, pp. 1238–1246, May 2007.

[76] J. H. Jeong, K. Lee, K. Y. Song, J.-M. Jeong, and S. B. Lee, "Differential measurement scheme for Brillouin optical correlation domain analysis," *Optics Express*, vol. 20, no. 24, pp. 27 094–27 101, Nov 2012.

[77] Y. Mizuno, Z. He, and K. Hotate, "Measurement range enlargement in brillouin optical correlation-domain reflectometry based on temporal gating scheme," *Optics Express*, vol. 17, no. 11, pp. 9040–9046, May 2009.

[78] K. HOTATE, H. ARAI, and K. Y. SONG, "Range-enlargement of simplified brillouin optical correlation domain analysis based on a temporal gating scheme," *SICE Journal of Control, Measurement, and System Integration*, vol. 1, no. 4, pp. 271–274, 2008.

[79] K. Hotate and M. Tanaka, "Correlation-based continuous wave technique of fiber brillouin distributed strain sensing for smart materials with cm order spatial reso-

lution," in *Technical Digest. CLEO/Pacific Rim 2001. 4th Pacific Rim Conference on Lasers and Electro-Optics (Cat. No.01TH8557)*, vol. 1, July 2001, pp. I–I.

[80] K. Y. Song and K. Hotate, "Enlargement of measurement range in a Brillouin optical correlation domain analysis system using double lock-in amplifiers and a single-sideband modulator," *IEEE Photonics Technology Letters*, vol. 18, no. 3, pp. 499–501, Feb 2006.

[81] K. Y. Song, M. Kishi, Z. He, and K. Hotate, "High-repetition-rate distributed brillouin sensor based on optical correlation-domain analysis with differential frequency modulation," *Optics Letters*, vol. 36, no. 11, pp. 2062–2064, Jun 2011.

[82] K. Washiyama, M. Kishi, Z. He, and K. Hotate, "High speed bocda measurement of strain distribution by longitudinal sweep method," in *Proceedings of the 34th Progress in Electromagnetics Research Symposium (PIERS), Stockholm, Sweden,*, vol. 4A-3., Aug. 2013, p. 12–15.

[83] W. Zou, Z. He, and K. Hotate, "Distributed dynamic-strain sensing based on brillouin optical correlation domain analysis," in *Proceedings of the 8th Pacific Rim Conference on Lasers and Electro-Optics (CLEO PR 2009), Shanghai, China,*, vol. WE1-5, Aug. 2009, p. 30.

[84] K. Hotate, K. Abe, and K. Y. Song, "Suppression of signal fluctuation in brillouin optical correlation domain analysis system using polarization diversity scheme," *IEEE Photonics Technology Letters*, vol. 18, no. 24, pp. 2653–2655, Dec 2006.

[85] K. Y. Song and K. Hotate, "Brillouin optical correlation domain analysis in linear configuration," *IEEE Photonics Technology Letters*, vol. 20, no. 24, pp. 2150–2152, Dec 2008.

[86] W. Zou, Z. He, and K. Hotate, "Single-end-access correlation-domain distributed fiber-optic sensor based on stimulated Brillouin scattering," *Journal of Lightwave Technology*, vol. 28, no. 18, pp. 2736–2742, Sept 2010.

[87] R. Ruiz-Lombera, J. Urricelqui, M. Sagues, J. Mirapeix, J. M. López-Higuera, and A. Loayssa, "Overcoming nonlocal effects and Brillouin threshold limitations in Brillouin optical time-domain sensors," *IEEE Photonics Journal*, vol. 7, no. 6, pp. 1–9, Dec 2015.

[88] A. Minardo, R. Bernini, and L. Zeni, "A Simple Technique for Reducing Pump Depletion in Long-Range Distributed Brillouin Fiber Sensors," *IEEE Sensors Journal*, vol. 9, no. 6, pp. 633–634, June 2009.

[89] J. Urricelqui, M. Sagues, and A. Loayssa, "Synthesis of Brillouin frequency shift profiles to compensate non-local effects and Brillouin induced noise in BOTDA sensors," *Optics Express*, vol. 22, no. 15, pp. 18 195–18 202, 2014.

[90] A. Dominguez-Lopez, Z. Yang, M. A. Soto, X. Angulo-Vinuesa, S. Martin-Lopez, L. Thevenaz, and M. Gonzalez-Herraez, "Novel scanning method for distortion-free BOTDA measurements," *Optics Express*, vol. 24, no. 10, pp. 10 188–10 204, 2016.

[91] A. Minardo, R. Bernini, L. Zeni, L. Thevenaz, and F. Briffod, "A reconstruction technique for long-range stimulated Brillouin scattering distributed fibre-optic sensors: Experimental results," *Measurement Science and Technology*, vol. 16, no. 4, pp. 900–908, 2005.

[92] X. Hong, W. Lin, Z. Yang, S. Wang, and J. Wu, "Brillouin optical time-domain analyzer based on orthogonally-polarized four-tone probe wave," *Optics Express*, vol. 24, no. 18, pp. 21 046–21 058, Sep 2016.

[93] A. Zornoza, D. Olier, M. Sagues, and A. Loayssa, "Brillouin distributed sensor using RF shaping of pump pulses," *Measurement Science and Technology*, vol. 21, no. 9, 2010.

[94] S. A. V., G. A. Ferrier, X. Bao, and L. Chen, "Effect of the finite extinction ratio of an electro-optic modulator on the performance of distributed probe-pump Brillouin sensor systems," *Optics Letters*, vol. 28, no. 16, pp. 1418–1420, 2003.

[95] Y. Sun, J. Zyskind, and A. Srivastava, "Average inversion level, modeling, and physics of erbium-doped fiber amplifiers," *IEEE Journal on Selected Topics in Quantum Electronics*, vol. 3, no. 4, pp. 991–1007, 1997.

[96] K. Y. Ko, M. S. Demokan, and H. Y. Tam, "Transient analysis of erbium-doped fiber amplifiers," *IEEE Photonics Technology Letters*, vol. 6, no. 12, pp. 1436–1438, Dec 1994.

[97] J. Mompo, H. Iribas, J. Urricelqui, and A. Loayssa, "Second-Order Nonlocal Effects Mitigation in Brillouin Optical Time-Domain Analysis Sensors by Tracking the Brillouin Frequency Shift Profile of the Fiber," *IEEE Photonics Journal*, vol. 9, no. 5, 2017.

[98] M. D. Jones, "Using simplex codes to improve OTDR sensitivity," *IEEE Photonics Technology Letters*, vol. 5, no. 7, pp. 822–824, July 1993.

[99] M. A. Soto, S. L. Floch, and L. Thévenaz, "Bipolar optical pulse coding for performance enhancement in BOTDA sensors," *Optics Express*, vol. 21, no. 14, pp. 16 390–16 397, Jul 2013.

[100] M. Nazarathy, S. A. Newton, R. P. Giffard, D. S. Moberly, F. Sischka, W. R. Trutna, and S. Foster, "Real-time long range complementary correlation optical time domain reflectometer," *Journal of Lightwave Technology*, vol. 7, no. 1, pp. 24–38, Jan 1989.

[101] S. Le Floch, F. Sauser, M. Llera, M. A. Soto, and L. Thévenaz, "Colour simplex coding for Brillouin distributed sensors," in *Proceedings of SPIE*, vol. 8794, 2013, pp. 879 437–879 437–4.

[102] M. Harwit and N. J. Sloane, *Hadamard Transform Optics*. Academic Press, 1979.

[103] H. Y. Song and S. W. Golomb, "Some new constructions for simplex codes," *IEEE Transactions on Information Theory*, vol. 40, no. 2, pp. 504–507, March 1994.

[104] F. Baronti, A. Lazzeri, R. Roncella, R. Saletti, A. Signorini, M. A. Soto, G. Bolognini, and F. D. Pasquale, "SNR enhancement of Raman-based long-range distributed temperature sensors using cyclic Simplex codes," *Electronics Letters*, vol. 46, no. 17, pp. 1221–1223, August 2010.

[105] D. Lee, H. Yoon, P. Kim, J. Park, and N. Park, "Optimization of SNR Improvement in the Noncoherent OTDR Based on Simplex Codes," *J. Lightwave Technol.*, vol. 24, no. 1, p. 322, Jan 2006.

[106] D. Ba, B. Wang, D. Zhou, H. Zhang, Z. Lu, L. Chen, X. Bao, and Y. Dong, "Dynamic distributed Brillouin optical fiber sensing based on multislope analysis," in *Proceedings of SPIE*, vol. 9634, Sep. 2015.

[107] D. Ba, B. Wang, D. Zhou, M. Yin, Y. Dong, H. Li, Z. Lu, and Z. Fan, "Distributed measurement of dynamic strain based on multi-slope assisted fast BOTDA," *Optics Express*, vol. 24, no. 9, pp. 9781–9793, May 2016.

[108] A. Motil, R. Hadar, I. Sovran, and M. Tur, "Gain dependence of the linewidth of Brillouin amplification in optical fibers," *Optics Express*, vol. 22, no. 22, pp. 27 535–27 541, Nov. 2014.

[109] G. L. Keaton, M. J. Leonardo, M. W. Byer, and D. J. Richard, "Stimulated Brillouin scattering of pulses in optical fibers," *Optics Express*, vol. 22, no. 11, pp. 13 351–65, 2014.

[110] A. Motil, I. Sovran, and M. Tur, "The effect of the gain dependency of the linewidth of Brillouin amplification on double slope-assisted dynamic sensing techniques," in *Proceedings of SPIE*, vol. 9634, Sep. 2015, pp. 8–11.

[111] G. P. M. Poppe and C. M. J. Wijers, "More efficient computation of the complex error function," *ACM Transactions on Mathematical Software*, vol. 16, no. 1, pp. 38–46, 1990.

[112] A. Motil, R. Davidi, R. Hadar, and M. Tur, "Mitigating the effects of the gain-dependence of the brillouin line-shape on dynamic botda sensing methods," *Optics Express*, vol. 25, no. 19, pp. 22 206–22 218, Sep 2017.

[113] D. Zhou, Y. Dong, B. Wang, T. Jiang, D. Ba, P. Xu, H. Zhang, Z. Lu, and H. Li, "Slope-assisted BOTDA based on vector SBS and frequency-agile technique for wide-strain-range dynamic measurements," *Optics Express*, vol. 25, no. 3, pp. 1889–1902, Feb 2017.

[114] *Global Market Outlook for Solar Power*. SolarPower Europe, Jul 2018.

[115] K. Pickerel, "How the solar industry is responding to the increasing intensity of natural disasters," *Solar Power World*, Jan 2018.

[116] C. Rohr, P. A. Bourke, and D. Banks, "Torsional instability of single-axis solar tracking systems," in *Proceedings of the 14th international conference on wind engineering, Porto Alegre*, 2015, pp. 21–26.

[117] F. P. Beer, *Mechanics of Materials*, 7th ed. McGraw-Hill Education, 2014.

[118] Y. Mizuno, W. Zou, Z. He, and K. Hotate, "Proposal of brillouin optical correlation-domain reflectometry (BOCDR)," *Optics Express*, vol. 16, no. 16, pp. 12 148–12 153, Aug 2008.

[119] K. Y. Song, Z. He, and K. Hotate, "Optimization of brillouin optical correlation domain analysis system based on intensity modulation scheme," *Optics Express*, vol. 10, no. 14, pp. 4256–4263, Sep 2006.

[120] J. H. Jeong, K. H. Chung, S. B. Lee, K. Y. Song, J.-M. Jeong, and K. Lee, "Linearly configured BOCDA system using a differential measurement scheme," *Optics Express*, vol. 22, no. 2, pp. 1467–1473, Jan 2014.

[121] J. H. Jeong, K. Lee, K. Y. Song, J.-M. Jeong, and S. B. Lee, "Variable-frequency lock-in detection for the suppression of beat noise in brillouin optical correlation domain analysis," *Optics Express*, vol. 19, no. 19, pp. 18 721–18 728, Sep 2011.

List of publications

International journals

1. H. Iribas, J. Urricelqui, **J. Mariñelarena**, M. Sagues, and A. Loayssa, "Cost-effective Brillouin optical time-domain analysis sensor using a single optical source and passive optical filtering," *Journal of Sensors*, 2016, Art. no. 8243269, 2016.

2. **J. Mariñelarena**, J. Urricelqui, and A. Loayssa, "Gain dependence of the phase-shift spectra measured in coherent Brillouin optical time-domain analysis sensors," *Journal of Lightwave Technology* 34(17), pp. 3972–3980, 2016.

3. **J. Mariñelarena**, J. Urricelqui, and A. Loayssa, "Enhancement of the Dynamic Range in Slope-Assisted Coherent Brillouin Optical Time-Domain Analysis Sensors," *IEEE Photonics Journal*, Vol. 9 , Issue: 3, 6802710, June, 2017.

4. H. Iribas, J. Urricelqui, J.J. Mompó, **J. Mariñelarena**, and A. Loayssa, "Non-local effects in Brillouin optical time-domain analysis sensors," *Applied Sciences (Switzerland)*, vol. 7, no. 8, Art. no. 761, 2017.

5. H. Iribas, **J. Mariñelarena**, C. Feng, J. Urricelqui, T. Schneider, and A. Loayssa, "Effects of pump pulse extinction ratio in Brillouin optical time-domain analysis sensors," *Optics Express*, Vol. 25, Issue 22, pp. 27896-27912, 2017.

6. **J. Mariñelarena**, Y. H. Kim, A. Loayssa, and K. Y. Song, "Dual-Probe Linearly Configured BOCDA System With Enlarged Modulation Amplitude," *Journal of Lightwave Technology*, Vol. 36, Issue 22, pp. 5203-5209, 2018.

7. **J. Mariñelarena**, H. Iribas, and A. Loayssa, "Pulse coding linearization for Brillouin optical time-domain analysis sensors," *Optics Letters*, Vol. 43, Issue 22, pp. 5607-5610, 2018.

8. **J. Mariñelarena**, H. Iribas, J. Urricelqui, and A. Loayssa, "Compensation of non-local effects induced by the extinction ratio of pump pulses in Brillouin optical time-domain analysis sensors," *Optics Express*, Vol. 27, Issue 5, pp. 6310-6319, 2019.

Conference proceedings

1. J. Urricelqui, **J. Mariñelarena**, M. Sagues, and A. Loayssa. Phasorial DPP-BOTDA sensor tolerant to non-local effects. *Proceedings of SPIE*, volume 9157, Event: 23th Optical Fiber Sensors Conference (OFS'23), n. 96346O, Santander (Spain), 2014.

2. H. Iribas, J. Urricelqui, **J. Mariñelarena**, M. Sagues, and A. Loayssa, "Simplified Brillouin sensor for structural health monitoring applications based on passive optical filtering," *Proceedings of SPIE*, vol. 9634, Event: 24th Optical Fiber Sensors Conference (OFS'24), n. 96346O, Curitiba (Brazil), 2015.

3. **J. Mariñelarena**, J. Urricelqui, and A. Loayssa, "Gain dependence of measured spectra in coherent Brillouin optical time-domain analysis sensors," *Proceedings of SPIE*, Vol. 9916, Event: Sixth European Workshop on Optical Fibre Sensors (EWOFS'2016), Limerick, Ireland, 2016.

4. **J. Mariñelarena**, J. Urricelqui, and A. Loayssa, "Extension of the dynamic range in slope-assisted coherent BOTDA sensors," *Proceedings of SPIE*, Vol. 10323, Event: 25th Optical Fiber Sensors Conference (OFS'25), Jeju (Republic of Korea), 2017.

5. C. Feng, H. Iribas, **J. Mariñelarena**, T. Schneider, and A. Loayssa, "Detrimental effects in brillouin distributed sensors caused by EDFA transient," *Proceedings of CLEO*, Vol. 2017-January, pp. 1-2 San Jose, California, United States, 2017.

6. **J. Mariñelarena**, Kim, Y. H., Loayssa, A., Song, K. Y., "Dual-probe linearly configured BOCDA system with enlarged modulation amplitude", *Proceedings of SPIE*, Event: 26th International Conference on Optical Fibre Sensors (OFS'26) Lausanne, Switzerland, 2018.

7. Alayn Loayssa, J. Urricelqui, H. Iribas, **J. Mariñelarena**, J. Mompó, "Latest research on long-range Brillouin distributed sensing, *Proceedings of SPIE*, Vol. 10934, Event: Photonics West 2019 in San Francisco, 2019.

8. **J. Mariñelarena**, Mompó, J. J., Zurita, J., Urricelqui, J., Judez, A., López-Amo, M., Jiménez, S., Achaerandio, A., Loayssa, A., "Structural health monitoring of solar trackers using distributed fiber optic sensors", *Proceedings of SPIE*, Vol. 10970, Event: SPIE Smart Structures + Nondestructive Evaluation, Denver, Colorado, United States, 2019.

Book chapters

1. A. Loayssa, J. Urricelqui, H. Iribas, J.J. Mompó, and **J. Mariñelarena**, "Fiber-optic Brillouin distributed sensors: from dynamic to long-range measurements," In: *Sensors for Diagnostics and Monitoring*, CRC Press, K338070, ch. 2, 2018.